Design optimization of the $\bar{\text{P}}$ANDA Micro-Vertex-Detector for high performance spectroscopy in the charm quark sector

Dissertation
zur
Erlangung des Doktorgrades (Dr. rer. nat)
der
Mathematisch-Naturwissenschaftlichen Fakultät
der
Rheinischen Friedrich-Wilhelms-Universität Bonn

vorgelegt von
Dipl.-Phys. Thomas Würschig
aus
Dresden

Bonn, 2011

Angefertigt mit Genehmigung der Mathematisch-Naturwissenschaftlichen Fakultät der
Rheinischen Friedrich-Wilhelms-Universität Bonn

1. Gutachter : Prof. Dr. Kai-Thomas Brinkmann

2. Gutachter : Prof. Dr. Jochen Dingfelder

Tag der Promotion: 19. Juli 2011

Erscheinungsjahr: 2011

Kurzdarstellung

Das $\bar{\text{P}}$ANDA-Experiment ist eines der Hauptprojekte an der zukünftigen Beschleunigeranlage FAIR, die sich zurzeit an der GSI in Darmstadt im Aufbau befindet. Für die später dort durchgeführten Experimente werden Antiprotonen zum Einsatz kommen, die auf ein festes Target geführt werden. Hauptziel dieser Messungen wird die Untersuchung der starken Wechselwirkung im Charm-Quark-Sektor sein. In diesem Zusammenhang ist eine hochpräzise Spektroskopie hadronischer Systeme im entsprechenden Energiebereich unabdingbar. Der Mikro-Vertex-Detektor (MVD) als innerster Teil des Spurerkennungssystems spielt dabei eine wesentliche Rolle.

Das $\bar{\text{P}}$ANDA-Projekt hat die Anfangsphase rein konzeptioneller Studien bereits hinter sich gelassen. Basierend auf diesen Ergebnissen ist eine Optimierung der einzelnen Detektorsysteme einschließlich des MVDs erforderlich, um die Umsetzung des Vorhabens bis hin zu seiner Inbetriebnahme voranzutreiben. Um dies zu erreichen muss ein möglichst realistisches und umfangreiches Modell erarbeitet werden, welches sowohl den physikalischen Anforderungen genügt, als auch die ingenieurstechnische Umsetzung erlaubt. Diese Aufgabe steht im Mittelpunkt der vorliegenden Arbeit. Wesentliche Teile der präsentierten Studien werden dabei Einklang in den zu erstellenden technischen Abschlussbericht für den $\bar{\text{P}}$ANDA-MVD finden. Dieser Bericht ist der nächste Schritt auf dem Weg zum endgültigen Aufbau des Detektors.

Der erste Teil der Arbeit befasst sich zunächst mit den wesentlichen physikalischen Aspekten der Spektroskopie Charm-behafteter Systeme. Außerdem wird ein kompletter Überblick über den derzeitigen experimentellen Stand auf diesem Gebiet gegeben. Anschließend werden alle wichtigen Informationen zum $\bar{\text{P}}$ANDA-Experiment zusammengefasst. In den darauf folgenden Kapiteln werden die Grundkonzeption und zugehörige Hardware-Entwicklungen für den MVD vorgestellt. Diese liefern die wesentlichen Vorgaben für die durchgeführte Detektoroptimierung, welche im Hauptteil der Arbeit präsentiert wird. Darin wird auch die Ausarbeitung des detaillierten MVD-Modells bis hin zu seiner Implementierung in die Simulations-Software des $\bar{\text{P}}$ANDA-Experiments beschrieben. Im letzten Teil werden die Ergebnisse ausführlicher Simulationen zusammengefasst, die mit dem entwickelten Detektormodell durchgeführt worden sind. Diese beziehen sich sowohl auf Basisparameter des Detektors als auch auf die vollständige Simulation physikalischer Kanäle. Die erzielten Resultate bestätigen die Einhaltung aller Vorgaben, die für das gewünschte Detektorverhalten zur Erfüllung des physikalischen Kernprogramms notwendig sind.

Abstract

The $\bar{\text{P}}$ANDA experiment is one of the key projects at the future FAIR facility, which is currently under construction at GSI Darmstadt. Measurements will be performed with antiprotons using a fixed-target setup. The main scope of $\bar{\text{P}}$ANDA is the study of the strong interaction in the charm quark sector. Therefore, high precision spectroscopy of hadronic systems in this energy domain is a prerequisite. The Micro-Vertex-Detector (MVD) as innermost part of the tracking system plays an important role to achieve this goal.

At present, the $\bar{\text{P}}$ANDA project has exceeded the initial phase of conceptual design studies. Based on these results, an optimization of the individual detector subsystems, and thus also for the MVD, is necessary to continue the overall detector development towards its commissioning. Therefore, a comprehensive and realistic detector model must be developed, which on the one hand fulfils the physics requirements but on the other hand also includes feasible engineering solutions. This task is the main scope of the present work. The outcome of these studies will deliver important contributions to the technical design report for the $\bar{\text{P}}$ANDA MVD, which is the next step towards the final detector assembly.

In the first part of this work, main physics aspects of the charm spectroscopy are highlighted and a complete review of the experimental status in this field is given. Afterwards, all relevant details of the $\bar{\text{P}}$ANDA experiment are summarized. The conceptual design and associated hardware developments for the MVD are discussed separately in the following chapters. They deliver basic input for the performed detector optimization, which is presented in the central part. Furthermore, this section describes the development of a comprehensive detector model for the MVD and its introduction into the physics simulation framework of $\bar{\text{P}}$ANDA. The final part contains a compilation of extended simulations with the developed detector model. This includes the determination of basic detector parameters as well as the full simulation of physics channels. Obtained results demonstrate the compliance with all given requirements that warrant the desired physics performance.

Contents

Motivation

The physics of strong interactions is related to both, the nuclear force binding protons and neutrons to form the nucleus of an atom, and the formation of hadrons including the nucleons, which results from the interaction of quarks and gluons. Hence, it provides a link between macroscopic properties of matter on the one hand and underlying mechanisms of the interaction of its smallest elementary particles on the other hand.

While Quantum Chromo Dynamics (QCD) is able to describe physics phenomena at distances much smaller than the nucleon size, other theoretical approaches such as effective field theories or potential models are applied at large distances corresponding to the formation of hadrons. However, they do not deliver a consistent picture, i.e. the simultaneous description of all observed phenomena.

The study of the strong interaction in the charm quark sector potentially provides an interpolation between the two energy domains defined by the limiting scales of QCD. To date rather scarce experimental data is available in this regime. Most of the results were obtained with electromagnetic probes, which are intrinsically limited in the achievable precision for non-vector states as well as associated production cross sections. A suitable setup with hadronic probes would render possible high-resolution spectroscopy. Therefore $\bar{\text{P}}$ANDA, an antiproton experiment dedicated to charm physics, will be constructed at the future FAIR facility.

The $\bar{\text{P}}$ANDA project has left the initial phase of conceptual design studies, which are accumulated in a technical progress report and a physics performance report. As it is outlined there, the Micro-Vertex-Detector (MVD) as innermost part of the tracking system plays an important role for key points of the $\bar{\text{P}}$ANDA physics program. In particular, the vertex reconstruction needed for the identification of D mesons is intimately connected to the delivered hit points in the MVD, which are located very close to the decay vertices. The main scope of the present work is the development of a sophisticated detector model, which respects both physics requirements and the feasibility of engineering solutions. Compared to previous studies it is the next step needed towards the final detector assembly. Therefore, a realistic detector description is necessary, which includes all available input of the ongoing hardware developments. Moreover, detector simulations must be performed in order to evaluate basic detector properties and to check the impact of engineering solutions on the overall physics performance.

In the following, the structure of this work is briefly summarized:

In the introductory chapter, main aspects of the physics in the charm quark sector will be discussed and a detailed review on the present status of charmed hadrons will be worked out. After the discussion of common experimental techniques for charm production, the chapter closes with a short introduction to silicon tracking detectors and a general description of tracking algorithms.

The second chapter provides all important information about the $\bar{\text{P}}$ANDA experiment.

It summarizes main aspects of the physics program and describes the conditions under which it will be operated. At the end, the setup of the $\bar{\text{P}}$ANDA apparatus with its main subcomponents will be explained and concluding remarks on the detection concept will be given.

The third chapter explicitly summarizes the most important facts concerning the MVD. Main tasks and the conceptual design of the detector will be outlined.

Chapter four gives a status report of all hardware developments associated with the MVD. These deliver central input to the further detector optimization.

The central part of the present work is the development of a comprehensive detector model for the MVD, which is presented in chapter five. This chapter contains a description of the design optimization performed and all important data about the finalized detector model. Furthermore, the procedure applied to implement the detector model from technical projects into the physics simulation framework will be outlined.

The last chapter is dedicated to simulations. In the first part, special emphasis will be given to the elastic scattering process in antiproton-proton reactions. A careful study of this reaction is crucial for the MVD because it potentially has impact on technical specifications of different detector parts. Extensive detector simulations with the developed MVD model are then summarized in the second part of this chapter.

1 Introduction

The introduction starts with a short outline of physics aspects and underlying theories pertaining to the charm spectroscopy. A review of the present experimental status in this field is given in section 1.2. It includes established and newly discovered states in the charmonium sector, an updated list of confirmed D mesons with open charm and a brief summary on charmed baryons. Common techniques used to experimentally access all required information are outlined in section 1.3. Concluding remarks give a link between current and future applications. The remaining sections focus on technical aspects. Section 1.4 contains a description of basic principles and technologies used in silicon tracking detectors. Finally, general concepts of tracking algorithms are presented in section 1.5.

1.1 Physics in the charm sector

The identification of elementary particles and the description of fundamental forces between them is one of the basic concepts in modern physics. The systematic spectroscopy of associated compound objects is one of the main tools to test theoretical models and to get a deeper insight into the physics mechanisms beyond. Massive hadrons are composed objects made of quarks. They are characterized by their mass, their total width, which is related to the lifetime, their spin and other selected quantum numbers, which are conserved under special transformations. The fundamental force between quarks is described by the strong interaction, which introduces a colour field with gluons as associated exchange particles. Quarks and anti-quarks, respectively, carry three types of colour and anti-colour charges. The colour structure of gluons is more complex. They may be thought of as a combination of both colour and anti-colour. This special feature leads to a gluonic self-interaction which results in the confinement of quarks, i.e. the absence of free quarks. A characteristic of strongly bound systems is the creation of colourless objects. Mesons and baryons represent the minimum possible configuration. They consist of a quark-antiquark pair and three quarks, respectively. Nucleons, i.e. the proton and the neutron, form the ground states of baryonic systems.

All hadrons have a finite spatial extension, which is in the order of 10^{-15} m. It corresponds to the typical range of the strong interaction which is given by the nucleon size. The quantitative description of hadronic systems is complicated. Even though some of the problems can be reduced to a simplified model of valence quarks, other properties demand a deeper understanding of the inner structure of the system. Looking into detail, the hadronic object manifests itself as an intrinsic many-body system with a self-similar structure, which includes many gluons and quark-antiquark pairs apart from the valence quarks. As a consequence, main macroscopic properties of hadrons such as the mass or the total spin are generated dynamically. This feature is the reason behind the complex world of nuclear and hadron physics which is far from being completely understood.

Quark flavour	**u**p	**d**own	**c**harm	**s**trange	**t**op	**b**ottom
Charge [e]	2/3	-1/3	2/3	-1/3	2/3	-1/3
Mass	(1.7...3.3) MeV/c^2	(4.1...5.8) MeV/c^2	$1.27^{+0.07}_{-0.09}$ GeV/c^2	101^{+29}_{-21} MeV/c^2	172.0±2.2 GeV/c^2	$4.19^{+0.18}_{-0.06}$ GeV/c^2

Table 1.1: Estimated quark masses as given by the particle data group [1]. Only the value of the top quark mass refers to a direct observation. More details on the extraction of the quark masses can be found in a corresponding review [2].

Within the Standard Model (SM) of particle physics [4] there are three families of elementary quarks and antiquarks. The first one contains up and down quarks with an electric charge of $+2/3\,e$ and $-1/3\,e$, respectively. Among other hadrons, they are also the constituents of nucleons. The corresponding anti-quarks have the same mass but a conjugated electric charge. The quark flavour is a conserved quantity for the strong interaction. It can be broken in weak decays thus changing the flavour content of freely propagating quarks. The transformation is given by the so-called Cabibbo–Kobayashi–Maskawa matrix (CKM matrix), which defines the strength of flavour changes under weak interactions of quarks. Charm quarks belong to the second family. According to their conjugation they carry an electric charge of $\pm 2/3\,e$. Strange quarks are the associated partner in the second family. One major feature of elementary particles is the broken mass scale which also distinguishes between different quark flavours. While the up and down quarks are nearly massless, the estimated quark masses in the second family are considerably large. Moreover, the masses of the heavier charm quarks differ by one order of magnitude from those of the strange quarks. Values of estimated dynamical quark masses according to the particle data group (PDG) are listed in table 1.1. It should be noted that due to the confinement an absolute measurement of quark masses is not possible. Therefore, resulting values are model-dependent. For instance, the masses of the light u and d quarks in the simplified picture of valence quarks are defined as approximately one third of the nucleon mass, while in dynamical models they are considered as nearly massless. Details on the PDG quark masses listed in table 1.1 can be found in [2].

A theoretical framework for the strong interaction is provided by Quantum Chromodynamics (QCD) [4], which is part of the SM. It is a relativistic quantum field theory where quarks and gluons are the fundamental degrees of freedom. The gluonic interaction between the colour charges is mathematically described according to laws of the underlying symmetry defined by the non-Abelian gauge group SU(3). Due to the self-interaction of gluons the field equations in QCD are non-linear. In this context, one of the major challenges is the running coupling constant, α_s, whose strength depends on the distance between the strongly interacting objects involved. Thus, the quantitative understanding of QCD is based on the calculation of the scale dependence. It results in the asymptotic freedom of quarks at small distances or, equivalently, at an infinite large energy scale ($\alpha_s \to 0$) and the confinement due to the rapidly increasing coupling constant at large distances which corresponds to a low energy scale. An illustration of the running coupling constant is given in figure 1.1.

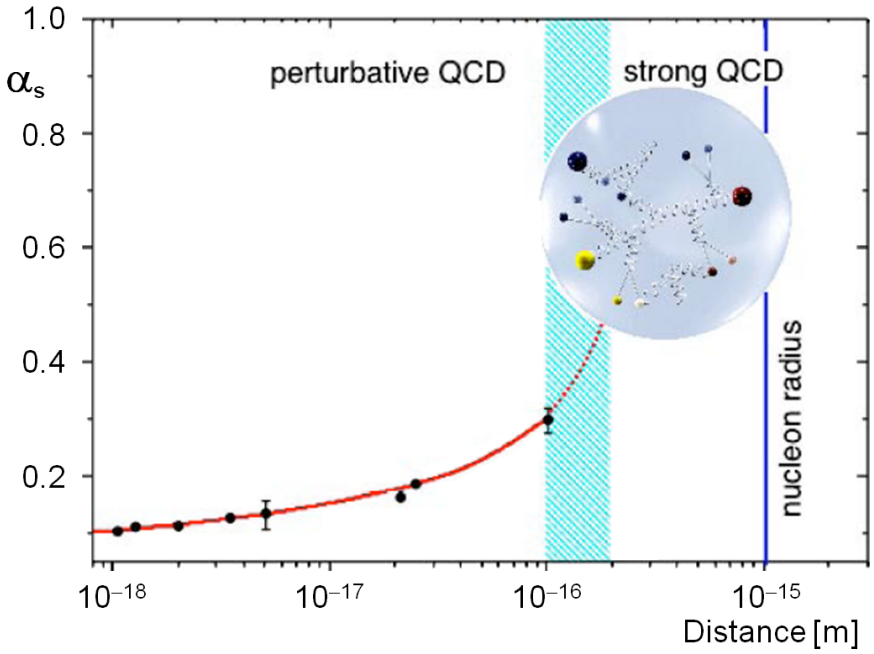

Figure 1.1: Coupling constant, α_s, of the strong interaction as a function of distance (taken from [3]). For small distances a perturbation theory can be applied in analogy to the QED. At larger distances comparable to the nucleon size the coupling constant diverges and quarks cannot be further separated. Here, the system can be approximated by effective models. The intermediate region, where both approaches potentially can be overlapped, is highlighted in cyan.

Based on the scale dependence it is possible to divide the field of strong interactions into the region of pertubative QCD (pQCD) and non-pertubative QCD. In the first case the coupling constant is small enough to apply perturbation theory. This approximation has been very successful in delivering a quantitative description of observed phenomena in high-energy physics. For instance, it allowed an accurate reproduction of electron-positron collisions, jet rates in electron-proton collisions , the τ lifetime or the decay of heavy mesons made of a bottom and an anti-bottom quark, which belong to the third quark family [5].

The low energy regime is connected to strong nuclear forces and hadronic resonances. Hence, the exploration of the hadron spectrum is a central issue in non-pertubative QCD. Common theoretical approaches into this field are lattice QCD (LQCD) and effective field theories (EFT). LQCD directly tackles the given field equations by means of numerical simulations. EFT is based on a scale separation applied at a specified energy range. Therefore, particular hierarchical structures of the systems under study are taken into account. Simplified field equations are obtained by the reduction to the low-energy degrees of freedom. A typical example for very low energies is given by Chiral Pertubation Theory (χPT) where the interaction can be approximated in expansions of the pion mass. A similar solution can be used selectively for some hadrons containing a heavy quark. The Heavy Quark Effective Theory (HQET) exploits the mass difference between light and heavy quarks and delivers

an expansion in terms of inverse heavy quark masses. However, all present results of QCD approaches does not suffice to fill the gap between the well explained high energy domain and the mostly incomplete picture for the transition region at an intermediate energy scale, which is related to hadronization.

A different approach to describe the quark-gluon structure of hadrons and thus to explain the associated spectrum is given by potential models. In contrast to the QCD calculations this method is purely phenomenological. It is based on the introduction of an effective quark potential which describes the fundamental behaviour of a bound quark-antiquark system by a Coulomb term for the short-range interaction and a linear term for the long range part. Depending on the special application additional terms are added considering relativistic effects, spin-spin or spin-orbit interactions between quarks. In this way it is possible to access long distance properties of the strong interaction. This also includes information on the coupling constant which may provide important input for further LQCD calculations. A third complementary method to extract more details on hadronic matter at a sub-nuclear level is derived from a suited modelling of the gluonic flux tube between bound quarks.

Theoretical approaches as discussed above are not only constrained to explain the spectrum of mesons and baryons. There are also attempts to extend the description from conventional hadrons to predictions on other, so far unexplored configurations, which are not excluded by first principles of QCD. Basically, there are two phenomena connected with exotic QCD states: one is the possible existence of multi-quark states which are not made out of two or three quarks, e.g. loosely bound molecules of two mesons, the other are gluonic excitations. The latter would manifest themselves in hybrids made from conventional QCD states with one additional gluonic degree of freedom or in glueballs, which are objects purely composed of gluons. While the existence of bound molecules could provide deeper insight into the interaction of quarks, glueballs and hybrids would deliver information about the long distance features of the QCD vacuum.

The standard modus operandi to access and validate fundamental principles of physical phenomena connected with strongly bound QCD objects is given by a systematic spectroscopy in the relevant mass region. For a complete description it is necessary to quantitatively extract information apart from the mass and the width of associated objects in the spectrum. Therefore, specific quantum numbers are introduced. They characterize intrinsic properties of the system and thus allow for an unambiguous assignment of individual states. In the first group there are dynamical variables such as the total spin S, the total orbital momentum, L, or the total angular momentum, J, of the system. Other quantities, i.e. the charge parity, C, and the spatial parity, P, are related to symmetry properties of the underlying theory of QCD. The flavour of involved valence quarks is considered e.g. by the isospin, I, which accounts for the configuration of light up and down quarks. Depending on the specific application there are also combinations of the above quantities, e.g. the G-parity defined as $G = (-1)^{L+S+I}$.

Hadron spectroscopy in the charm quark sector offers some unique opportunities. Bound states within this energy regime are characterized by the substitution of at least one light valence quark by a charm quark. Compared to the light quark sector, charmed hadrons have smaller total widths and the spectrum is less populated. These particular features facilitate the confirmation and unambiguous assignment of observed resonances because of

the reduced mixing between different states. Currently there are many theoretical predictions of exotic QCD objects within the relevant mass region of charmed hadrons. Some of these non-conventional QCD configurations are expected to have a clear assignment to be distinguished from conventional interpretations. Therefore, a precise spectroscopy in the charm sector will deliver important input to either confirm or disprove different models on non-conventional QCD bound states.

The existence of a bound charm quark defines an internal dynamics of the system which is beneficial for any theoretical attempt to describe the nature of strong interactions. It allows a non-relativistic treatment which can be used for EFT in parallel to quark-potential models. The direct link between both complementary approaches is crucial for a deeper understanding of fundamental QCD mechanisms at a larger scale at one hand and the hadronization on the other. Charmed mesons represent the minimum QCD configuration of such systems. They can be divided into charmonium states, which consist of one charm and one anti-charm quark, and D mesons where only one out of the two quarks is charmed and combined with a lighter up, down or strange quark. The two different configurations are the QCD analogue of positronium and hydrogen in Quantum Electrodynamics (QED), respectively. Therefore, non-relativistic potential models can be used to predict the associated mass spectrum.

A comparison of calculated level schemes for positronium and charmonium as well as the underlying potentials is shown in figure 1.2. The Coulomb term given in both systems determines the distance between excited states, which is proportional to $1/n^2$ with n being the main quantum number. The additional linear term of the quark potential related to the properties of strong interactions is absent in QED. As a consequence, the level schemes of positronium and charmonium are similar for lower-lying states ($n = 1$ and $n = 2$) but significantly differ for higher radial excitations. While the energy levels in case of positronium converge towards a dissociation threshold, the distance of adjacent levels in the charm spectrum does not tend to zero. Higher-lying charmonia are very sensitive to the linear term of the quark potential due to the relatively large extension of their wave functions, which is superior to heavier quarkonia. However, detrimental effects have to be considered in this energy region. They are related to the possible strong decay of charmonium states into two D mesons resulting in an increased particle width above the $D\bar{D}$ threshold. A precise knowledge about D mesons is thus mandatory to describe properly the coupling to different $D\bar{D}$ channels. As for charmonia, a threshold for the strong decay of D mesons into kaons and pions is defined in the associated spectrum.

Theoretical predictions do not only concern with the calculation of mass spectra but also include the extraction of associated particle widths and partial contributions of individual decay channels. The observation of e.g. a very narrow state close to one of the two meson thresholds in either of the charmed mesonic systems would be from particular interest because it eventually indicates long distance interactions of a strongly bound molecule or multi-quark systems. For a complete understanding, the decay pattern of charmed systems must be studied. Therefore, partial decay widths must be determined quantitatively. Important information are thus delivered e.g. by the magnitude of radiative decays and deexcitation of charmonia or the branching ratios of hadronic, semi-leptonic and leptonic decays. A systematic study of weak decays in the charm sector also enables complementary measurements of CKM matrix elements. Rare decays provide a fundamental test of

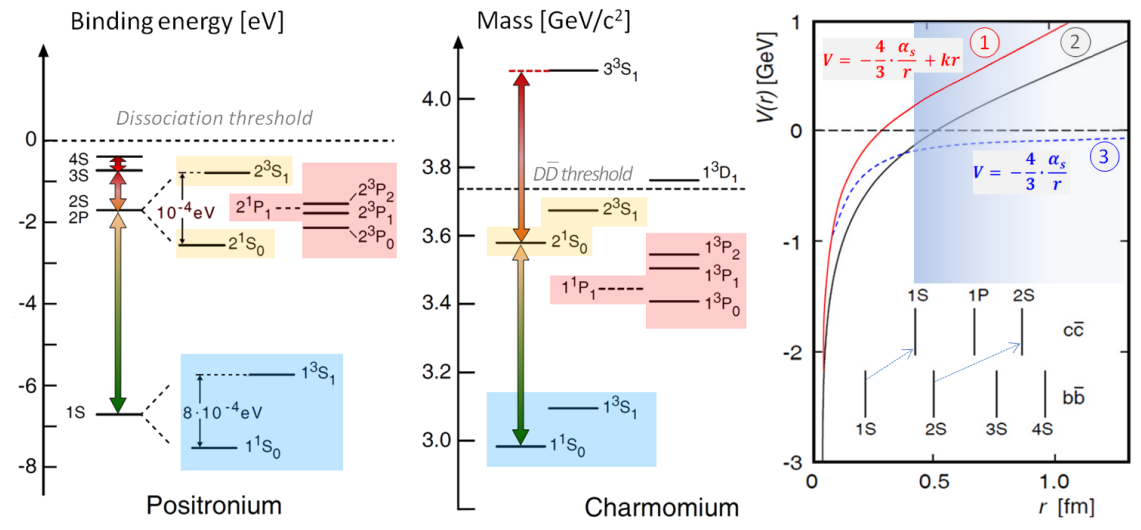

Figure 1.2: Level schemes of positronium (*left*) and charmonium (*middle*). Modified pictures refer to [4]. Both diagrams are scaled such that the distance between the $1S$ and the $2S$ level is equal. The level splitting in the positronium system is zoomed. Note that due to a different nomenclature of the first quantum number $2P$ states of positronium correspond to $1P$ states of charmonium. Dotted lines represent the dissociation of positronium and the open charm threshold for a strong decay into two D mesons, respectively. While the structure of the lowest levels $n = 1$ and $n = 2$ is very similar in both systems, the distance between higher-lying states is significantly different reflecting the linear term of the QCD potential. *Right*: Illustration of the quark potential model (1) consisting of the Coulomb term (3) and an additional linear term. Modified picture refers to [4] and [6]. (1) with $\alpha_s = 0.3$ and $k = 1\text{GeV/fm}$ and (2) with $\alpha_s < 0.3$ and $k \approx 1\text{GeV/fm}$ represent different approaches of the model. At the bottom, the corresponding mean charged radii of different quarkonia are plotted. They indicate a higher sensitivity of charmonia to the linear term of the quark potential.

SM predictions and may eventually deliver hints for physics mechanisms beyond. Another missing result needed to complete the experimental data is related to a precise study about CP violation in the charm sector which is associated with the possible mixing between a particle and its anti-particle. To date this phenomenon has been observed in several systems of neutral mesons. The CP violation in the charm sector is expected to be rather small, deviations bigger than predictions may require extensions of the SM. In any way, precise and complete experimental data on the CP violation in the domain of light and heavy quarks are prerequisite for theoretical attempts to understand the nature of this phenomenon.

1.2 Review of the present status

Charmed particles are well established in the hadron spectrum for more than 35 years. The first state, J/ψ, was discovered in 1974 ([7, 8]), ten years after the prediction of the c-quark. This observation was the starting point for extensive studies on charm flavour physics. In the following, a short overview of the present experimental status in the field of charm spectroscopy is given. It is subdivided into three main areas, namely the study of charmonium systems, the open-charm spectroscopy with D mesons and the analysis of charmed baryons. In all cases PDG data and reviews of the year 2010 are used to obtain an updated compendium [1]. These sources in particular delivered main input to the summary tables 1.2 - 1.5. For a qualitative classification of the current experimental status a customized scheme has been developed. Main criteria are the precision of mass and width of the state, the confirmation of main quantum numbers, the total percentage of all partial widths with respect to the total one and the number of all studied decay channels as well as the ones with a specified partial width. All details are listed in [9].

Furthermore, updated reviews apart from the PDG summary have been considered. Amongst them, the most recent publications on charmonium-like states are given in [10], [11] and [12]. A short outline of charmonia below and above threshold used for the reviews can be found in [13] and [14], respectively. Also an additional update for the D mesons presented in [15] and [16] has been included. Further information can be found in the detailed source citations within the respective references given above.

1.2.1 Charmonia and charmonium-like systems

In the first section of the review, established and observed systems in the charmonium region will be discussed. A summary of the associated mass spectrum is given in figure 1.3. Basically, conventional charmonia can be separated into spin-singlets and spin-triplets with a total quark spin of zero and one, respectively. The charmonium spectrum below the open-charm threshold is both experimentally and theoretically well established. Mass predictions of conventional potential models are in good agreement and deliver eight charmonia from what all states have been experimentally confirmed. In contrast, the situation above the open charm threshold is rather incomplete. So far only four charmonia could be confirmed but a lot of states, which are expected according to theoretical models, have not yet been seen. All of the established states above threshold are spin-triplets. Furthermore, a lot of new states have been discovered which do not seem to fit in the conventional scheme. The following brief review will start with the established charmonia below and above threshold. They are listed in the summary table 1.2. It is obvious that the parameters and decay pattern of the spin-triplets are measured with much higher precision than the ones for the spin-singlet states. This section will be completed by a discussion on the newly discovered X, Y and Z states.

The triplet S-wave states J/ψ and $\psi(2S)$ have been extensively studied in different reaction types and at various facilities. Experimental data on mass and width of both charmonia is in good agreement and determined with high precision. The PDG world average obtained by a combined fit of all measurements delivers an absolute uncertainty of only 10 keV for the J/ψ and 40 keV for the $\psi(2S)$. The particle widths can be quantified with a small relative error of around 3% even though the experimental determination is

Charmonium states							
Particle	Mass [MeV/c^2]	Width [MeV]	$I^G(J^{PC})$	Main decays	Γ_{Σ_i}/Γ [%]	N_{Γ_i} $^{N_{\text{abs}}}$ (N_{ch})	Exp. status
Spin triplets							
$J/\psi(1S)$	3096.916 ($\pm$0.011)	$92.9_{\times 10^{-3}}$ ($\pm$2.8)	$0^-(1^{--})$	Hadronic e^+e^- $\mu^+\mu^-$	87.7 $\pm$0.5 5.9 $\pm$0.1 5.9 $\pm$0.1	183 **147** (187)	***** *****
$\psi(2S)$	3686.09 ($\pm$0.04)	$304_{\times 10^{-3}}$ ($\pm$9)	$0^-(1^{--})$	Hadronic Letponic	97.9 $\pm$0.1 1.8 $\pm$0.1	135 **107** (135)	***** *****
$\chi_{c0}(1P)$	3414.75 ($\pm$0.31)	10.3 ($\pm$0.6)	$0^+(0^{++})$	Pionic $2K$-pions $(+X)$ Radiative	9.9 $\pm$1.0 7.1 $\pm$0.5 1.2 $\pm$0.1	65 **46** (65)	** *****
$\chi_{c1}(1P)$	3510.66 ($\pm$0.07)	0.86 ($\pm$0.05)	$0^+(1^{++})$	Radiative Pionic $2K$-pions $(+X)$	34.4 $\pm$1.5 5.3 $\pm$1.0 3.0 $\pm$0.7	48 **36** (48)	*** *****
$\chi_{c2}(1P)$	3556.20 ($\pm$0.09)	1.97 ($\pm$0.11)	$0^+(2^{++})$	Radiative Pionic $2K$-pions $(+X)$	19.5 $\pm$0.8 7.4 $\pm$1.1 3.9 $\pm$0.7	54 **41** (54)	*** *****
Open charm treshold							
$\psi(3770)$	3772.92 ($\pm$0.35)	27.3 ($\pm$1.0)	$0^-(1^{--})$	$D\bar{D}$ $\gamma\chi_{cJ}$	$93\ ^{+8}_{-9}$ 1.02 $\pm$0.2	79 **10** (91)	***(*) *****
$\psi(4040)$	4039 ($\pm$1)	80 ($\pm$10)	$0^-(1^{--})$	$D\bar{D}, D^*\bar{D}$, $D^*\bar{D}^*$	seen	13 **1** (22)	*****
$\psi(4160)$	4153 ($\pm$3)	103 ($\pm$8)	$0^-(1^{--})$	$D\bar{D}, D^*\bar{D}$, $D^*\bar{D}^*$	seen	14 **1** (23)	(*) *****
$\psi(4415)$	4421 ($\pm$4)	62 ($\pm$20)	$0^-(1^{--})$	Hadrons $D^0D^{*-}\pi^+$	dominant 10$\pm$4	4 **2** (16)	*****
Spin singlets							
$\eta_c(1S)$	2980.3 ($\pm$1.2)	28.6 ($\pm$2.2)	$0^+(0^{-+})$	Pionic $2K$-pions Kaonic	17.2 $\pm$6.8 10.3 $\pm$2.6 1.6 $\pm$0.6	32**19** (32)	** *****
$\eta_c(2S)$	3637 ($\pm$4)	14 ($\pm$7)	$0^+(0^{-+})$ quark model prediction	$K\bar{K}\pi$	1.9 $\pm$1.2	2 **1** (15)	***
$h_c(1P)$	3525.42 ($\pm$0.29)	< 1	$?^?(1^{+-})$ quark model prediction	$\eta_c\gamma$ $2\pi^+2\pi^-\pi^0$	seen	0 **0** (5)	**(*)

Table 1.2: PDG values (2010) of all established charmonia. Given ratios $\Gamma_{\Sigma_i}/\Gamma > 1\%$ (Γ ... full particle width) are obtained by a summation over decay channels with $\Gamma_i/\Gamma > 5 \cdot 10^{-4}$ (Γ_i ... partial decay width). N_{ch} corresponds to the total number of listed PDG decay modes. N_{abs} accounts for the number of decay channels with a known partial width. N_{Γ_i} includes in addition with N_{abs} decay modes for which only an upper limit is given. For the classification of the experimental status see [9].

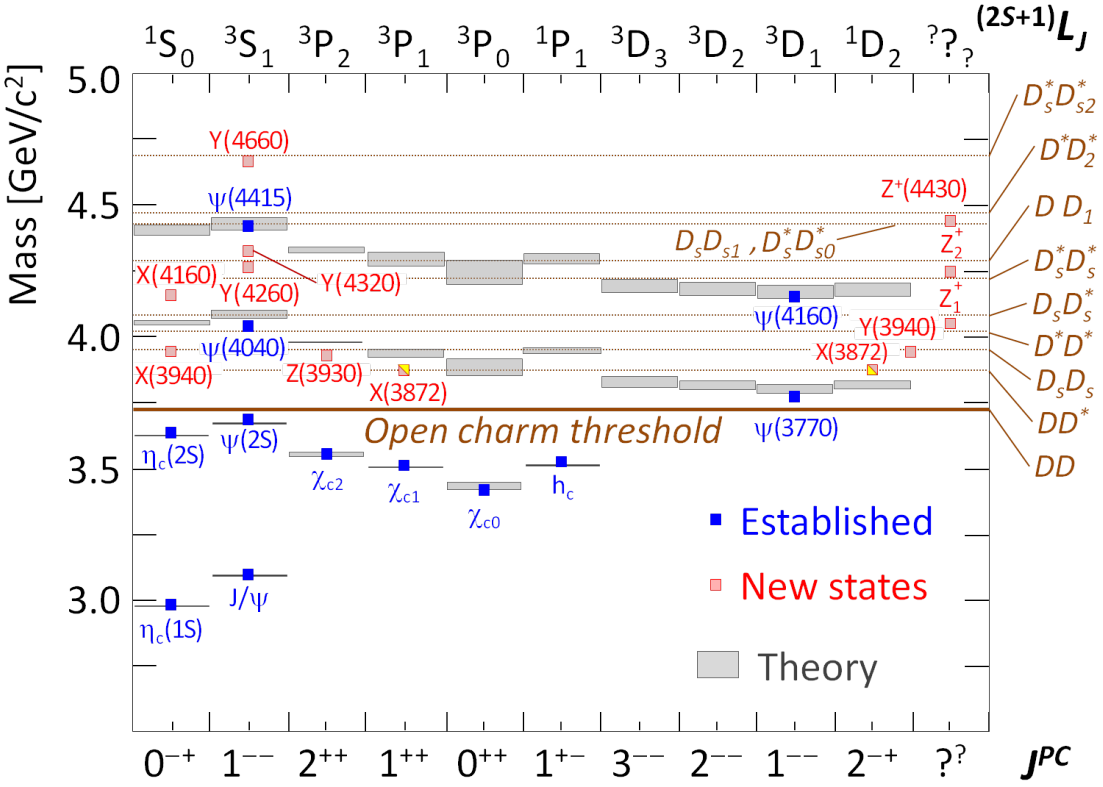

Figure 1.3: Mass spectrum of established charmonia and charmonium-like states. The spectroscopic notation $^{2S+1}L_J$ and the J^{PC} quantum numbers of the system are given at the top and the bottom, respectively. In addition, different $D\bar{D}$ thresholds are indicated. Further details on the plotted states can be found in table 1.2 and 1.3. Predicted masses of charmonia given by conventional potential models are highlighted in grey.

more difficult. Also the decay pattern of both S-wave states are well known. This can be seen by the large number of studied decay channels, which nearly describe the full particle widths. However, there are still remaining questions even on these well established states. The most challenging is the so-called ρ-π puzzle which concerns the ratio of the branching ratios for hadronic decays of the $\psi(2S)$ state compared to the J/ψ state. In some cases, e.g. for the decay into ρ-π, the measured ratio is more than one order of magnitude smaller than predicted.

Due to the given quantum numbers a direct formation of the triplet P-wave states $\chi_{cJ;\,J=0,1,2}$ is experimentally limited (for details see section 1.3). One alternative is the indirect production via a radiative decay of the $\psi(2S)$. Latest results on masses and total widths for both methods are in good agreement. The precision of the particle masses and the full widths is similar to the one for the S-wave states. In contrast, the restricted experimental access is reflected by a more incomplete picture of the decay pattern. A very specific decay mode is given by the two photon decay of the χ_{cJ} states, which is a pure

QED process and thus an interesting channel for theoretical models. The measured partial widths can be directly linked to higher-order relativistic and QCD radiative corrections.

The current situation for spin-singlet states, which are important for a proper description of the spin-spin interaction, is far from being competitive with the high precision data of the spin-triplets. In particular this accounts for the charmonium ground state η_c. It plays a key role for a test of potential models which either rely directly on its measured values or try to fit the mass difference between the J/ψ and the η_c. The η_c was first discovered in radiative decays of the J/ψ and the $\psi(2S)$. Since then various measurements with different reactions have been performed improving the precision of the η_c mass significantly to around 1 $\mathrm{MeV/c^2}$. This value is still one to two orders of magnitude higher compared to the obtained values of the triplet states. The uncertainty of the extracted total width remains rather large. Individual measurements considered for the PDG world average range from $7\,\mathrm{MeV/c^2}$ to $48\,\mathrm{MeV/c^2}$. Moreover, recent measurements seem to indicate a value above $25\,\mathrm{MeV/c^2}$, which is difficult to accommodate in quark models. In contrast, the measured radiative decay of the η_c into two photons is in good agreement with theoretical predictions.

Experimental data for the first radial excitation of the charmonium ground state, $\eta_c(2S)$, is restricted to only a few measurements with significantly larger errors on the particle mass and a wide spread of the individual data points. The situation is even worse in case of the associated particle width and results in a large relative error of 50% for the given PDG world average. The remaining spin-singlet state, h_c, has been observed last among the charmonium states below threshold and remains rather unexplored. Even though the mass of the h_c is known with high precision, only upper limits are given for the total width. Also an experimental confirmation of the quantum numbers according to the quark model prediction is still missing. A high resolution of the measured h_c parameters is important to determine the hyperfine splitting with the corresponding P-wave states, χ_{cJ}, of the spin-triplet. It is expected to be zero in lowest order pQCD calculations. Extracted values from experiments indicate that this condition is not strongly violated. However, results have a relatively large error.

For charmonium systems above the open-charm threshold, a decay into two D mesons is the predominant decay process and results in much larger particle widths. Due to the existence of different D mesons, there are several thresholds within the respective mass region of $3.72\,\mathrm{GeV/c^2}$ and $5.0\,\mathrm{GeV/c^2}$. A detailed discussion of the D meson spectrum is given in subsection 1.2.3. All established charmonia above threshold, namely the $\psi(3770), \psi(4040), \psi(4160)$ and $\psi(4415)$, are spin triplets which are experimentally easier to access. Even though all four states were discovered in early experiments, corresponding results of different measurements were partly inconsistent (cf. figure 1.10). Recently, a new measurement was performed and could solve most of the remaining problems [14]. Most precise data comes from an associated resonance scan with a global fit over the centre-of-mass energy region between 3.7 GeV and 5.0 GeV. In this way, masses and widths of the four charmonia are fully determined. While the absolute mass uncertainty stays below 5 MeV/c, the extracted particle widths have considerably larger errors ranging from 4% for the $\psi(3770)$ up to 32% for the $\psi(4421)$. A precise study of the decay pattern depends on the proper reconstruction of D mesons, which is experimentally demanding. Because there are different accessible open-flavour decay modes for the $\psi(4040)$, $\psi(4160)$ and $\psi(4415)$,

experimental data on partial decay widths is very limited. The situation is much better for the $\psi(3770)$, which is located only above the lowest $D\bar{D}$ threshold. Therefore, it is best suited to study the coupling strength of orbitally excited $c\bar{c}$ states to different decay channels without open charm such as $p\bar{p}$.

Based on the large data samples collected in B-factories a lot of new and unexpected charmonium-like states labelled as X, Y and Z [1] have been discovered since 2002. These findings revived interest in the field of charm spectroscopy. Most of the newly discovered states are very close to a $D\bar{D}$ threshold and seem not to fit in a conventional charmonium scheme because of their assigned quantum numbers, their charge or their extremely narrow width. So far, only the $X(3872)$ and the $Y(4260)$ have been included in the PDG summary table and thus can be regarded as basically established. A list of observed X, Y and Z states currently mentioned by the PDG and possible theoretical interpretations are given in table 1.3. It should be noted that there are further results indicating additional new states apart from the ones discussed in this review. Nevertheless, from the experimental point of view a lot of open questions remain and an independent confirmation of all announced observations is still missing. So far, results of different experiments do not sustain a consistent picture. In some cases they even deliver contradictory results (e.g. for the $Z^{\pm}(4430)$, cf. table 1.3).

Basically, theoretical interpretations of the XYZ states can be classified into six different groups. These are (1) an assignment as conventional charmonium, (2) a molecule state made of two mesons loosely bound by pion or gluon exchange, (3) a tetra-quark system formed by four tightly bound quarks, (4) a hybrid which includes an additional gluonic degree of freedom, (5) hadrocharmonium where a conventional $c\bar{c}$-state is coated by light hadrons or (6) the occurrence of threshold effects due to rescattering or channel coupling.

Amongst all XYZ states, the $X(3872)$ is experimentally best explored. It has been observed by various experiments and in different decay channels. There are two main decay modes: one via two pions and a charmonium (J/ψ), the other one via two D mesons. For the decay mode into $J/\psi\,\pi^+\pi^-$, a considerable large number of events could be reconstructed which even allowed an analysis of the angular distribution (see picture 1.9). However, a clear theoretical interpretation of this state is still missing. There are numerous publications with different theoretical explanations. Most popular interpretations feature either a loosely bound molecule or a tetra-quark system according to the favoured J^{PC} quantum numbers of 1^{--} and 2^{-+}, respectively.

The second established state is the $Y(4260)$, which has been found by three different experiments. It belongs to a family of new resonances observed in electron-positron annihilations into $J/\psi\,\pi^+\pi^-$ accompanied by initial state radiation thus fixing J^{PC} to 1^{--}. Other states with the same reaction type are e.g. the $Y(4350)$ and the $Y(4660)$. The $Y(4260)$ has been seen in three different decay channels and a significant number of events could be reconstructed exclusively. In contrast, experimental results on the $Y(4350)$ and the $Y(4660)$ are much less and main parameters are extracted only from a fit to the data.

The charged Z states represent probably the most speculative discoveries in the charm sector. Due to the non-zero net charge any charmonium interpretation is excluded. How-

[1] Due to the preliminary status in this field, different naming schemes can be found in literature. In this work the most common assignment suggested by [11] and [12] is used, which differs from the PDG conventions.

Observed charmonium-like X, Y, Z states						
State	Mass [MeV/c^2]	Width [MeV]	J^{PC}	Decay modes/ Seen in	Possible interpretation	N_{Evts} $N_{\mathsf{Ref}}(N_{\mathsf{Exp}})$
$\boldsymbol{X(3872)}$	3871.56 ± 0.22	< 2.3	$1^{++\star}$ $2^{-+\star}$	$\pi^+\pi^- J/\psi$ $D^0\bar{D}^{0*}$ $\gamma J/\psi, \gamma\psi(2S)$	Molecule, tetraquark $\{c\bar{c}\}$: χ'_{c1}, η_c(2S)	$\gtrsim$7500 $\pm$350 18(5)
$Z(3930)$	3929 ± 5	29 ± 10	2^{++}	$D\bar{D}$	$\{c\bar{c}\}$: $\chi_{c2}(2P)$	64 $\pm$18 1(1)
$X(3940)$	3942 (± 9)	37 ($^{+27}_{-17}$)	$0^{?+\otimes}$	$D\bar{D}^*$, not seen: $D\bar{D}$ or $\omega J\psi$	$\{c\bar{c}\}$: $\eta_c(3S)$	52 $^{+29}_{-16}$ 2(1)
$Y(3940)$	3915.5 (± 2.7)	28 ($^{+12}_{-10}$)	$?^{?+\triangledown}$	$\omega J\psi, \gamma\gamma$ not seen: $D\bar{D}^*$	Conventional $\{c\bar{c}\}$, hybrid	107 $\pm$26 4(2)
$X(4160)$	4156 ($^{+29}_{-25}$)	139 ($^{+110}_{-60}$)	$0^{?+\otimes}$	$D^*\bar{D}^*$, not seen: $D\bar{D}$	$\{c\bar{c}\}$: $\eta_c(4S)$	24 $^{+12}_{-8}$ 1(1)
$\boldsymbol{Y(4260)}$	4263 ($^{+8}_{-9}$)	95 (± 14)	$1^{--\diamond}$	$e^+e^-, \pi^0\pi^0 J/\psi$, $K^+K^- J/\psi$	$\{c\bar{c}\}$: 3^3D_1, hybrid	139 $^{+28}_{-27}$ 13(3)
$Y(4350)$	4361 (± 13)	74 (± 18)	$1^{--\diamond}$	$\pi^+\pi^-\psi(2S)$	Molecule, tetraquark hadro-$\{c\bar{c}\}$, hybrid	data fit 4(2)
$Y(4660)$	4664 (± 12)	48 (± 15)	$1^{--\diamond}$	$\pi^+\pi^-\psi(2S)$	Molecule, tetraquark hadro-$\{c\bar{c}\}$, hybrid	data fit 3(2)
$Z_1^{\pm}(4050)$	4051 ($^{+24}_{-40}$)	82 ($^{+50}_{-28}$)	$?^{??}$	$\pi^{\pm}\chi_{c1}(1P)$	Molecule, tetraquark hadro-$\{c\bar{c}\}$, hybrid	data fit 1(1)
$Z_2^{\pm}(4250)$	4248 ($^{+190}_{-50}$)	177 ($^{+320}_{-70}$)	$?^{??}$	$\pi^{\pm}\chi_{c1}(1P)$	Molecule, tetraquark hadro-$\{c\bar{c}\}$, hybrid	data fit 1(1)
$Z^{\pm}(4430)$	4443 ($^{+24}_{-18}$)	107 ($^{+110}_{-70}$)	$?^{??}$	$\pi^{\pm}\psi(2S)$ not seen: $\pi^{\pm}J/\psi$	Molecule, tetraquark hadro-$\{c\bar{c}\}$, hybrid	data fit 2(1), $\bar{1}(\bar{1})$

$\star$ ... favoured assignments in angular analysis, $\otimes$ ... double charmonium production (assignment not listed in PDG 2010), $\triangledown$ ... $C = ^+$ due to observed decay mode, $\diamond$ ... e^+e^- initial state radiation , $\bar{N}$ ... not seen

Table 1.3: Status of observed X, Y and Z states according to the PDG 2010. Only the $X(3872$ and the $Y(4260)$ are included in the summary table. N_{Evts} lists the number of assigned events. N_{Ref} and N_{Exp} correspond, respectively, to the number of published analyses on experimental results and the number of different experiments at which the state was observed. The naming refers to the convention suggested in [11, 12].

ever, all of them have been observed at the same facility and there are no independent confirmations by another experiment at the moment. Other states such as the $X(3940)$ and the $X(4160)$ have been obtained in a double-charmonium production studying the recoil mass spectrum against J/ψ. Due to this production mechanism the quantum numbers are partly fixed. Also in this case, there are only sparse experimental data available.

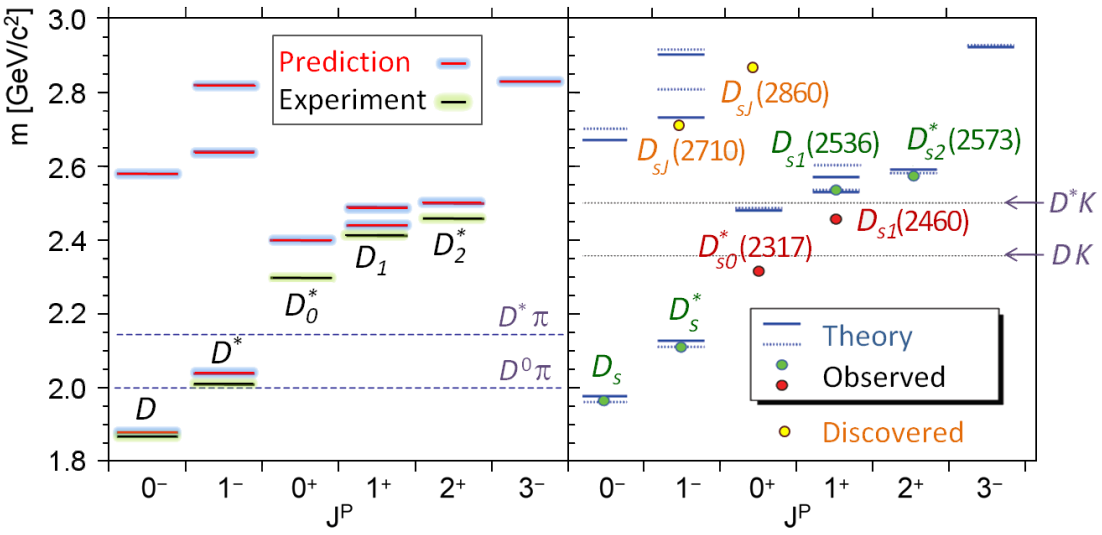

Figure 1.4: Mass spectrum of light (*left*) and strange (*right*) D mesons. Indicated theoretical predictions refer to [17] (solid line) and [18] (dashed lines).

1.2.2 Mesons with open charm

According to the constituent quark model, the lightest D mesons consist of a charm quark and an up or down quark. Considering all possible quark-antiquark combinations, there are two charged and two neutral D mesons. The mass difference of roughly 5 MeV/c^2 between the neutral and the charged states is related to the substitution of an up quark for a down quark. Moreover, two additional configurations with a mass shift of roughly 100 MeV/c^2 arise from the substitution of the light quarks with a strange quark. All six mesons are experimentally well established and extensively studied. Current PDG values are summarized in table 1.4.

The D meson ground states have a total quark spin of zero and a vanishing orbital momentum between the two quarks. A special feature is their relatively long lifetime. It is related to the restriction to weak decay modes and results in measurable decay lengths of 123 µm and 312 µm for neutral and charged D mesons, respectively. As a consequence, the experimental identification ("tagging") of D mesons via their secondary decay vertex becomes possible.

Even though the experimental status on the lowest-lying D mesons is one of the best in the charm quark sector, further improvements of the high-precision data are desirable because they still have potential impact on the study of the charmonium spectrum above threshold and the further exploration of excited D mesons. In both cases, main decay modes are strongly connected to properties of the ground state D mesons. In this context, given errors on e.g. the mass and the width are still slightly worse than for the lowest spin-triplet charmonium states. Another point is the determination of partial decay widths for selected exclusive channels. Even though the overall number of observed channels is remarkable, the sum of individual partial widths compared to the total one is only in the order of 60%.

D meson ground states							
Particle $\{q\bar{q}\}$	Mass [MeV/c^2]	$c\tau$ [µm]	$I(J^P)$	Main decays	Γ_{Σ_i}/Γ [%]	$N_{\Gamma_i}{}^{N_{\text{abs}}}$ N_{ch}	Exp. status
D^0, $\bar{D}^0$ $\{c\bar{u}\}, \{\bar{c}u\}$	1864.83 (±0.14)	122.9 (±0.4)	$\frac{1}{2}(0^-)$	*Hadronic* $K\pi, \ldots, K(4\pi)$ Pionic modes $2K, 2KX$ *Semi-leptonic* $K(\bar{l}\nu_l), K(\bar{l}\nu_l)\pi$	42.30 ±2.25 4.29 ±0.43 2.03 ±0.18 15.31 ±2.28	$255^{\mathbf{192}}$ (265)	**** *****
D^+, D^- $\{c\bar{d}\}, \{\bar{c}d\}$	1869.60 (±0.16)	311.8 (±2.1)	$\frac{1}{2}(0^-)$	*Hadronic* $K\pi, \ldots, K(4\pi)$ Pionic modes $2K, 2KX$ *Semi-leptonic* $K(\bar{l}\nu_l), K(\bar{l}\nu_l)\pi$ Strangeless	29.00 ±1.81 2.25 ±0.18 1.91 ±0.21 26.23 ±2.12 1.12 ±0.19	$123^{\mathbf{96}}$ (132)	**** *****
D_s^+, D_s^- $\{c\bar{s}\}, \{\bar{c}s\}$	1968.47 (±0.33)	149.9 (±1.2)	$0(0^-)$	*Hadronic* KX Pionic modes $2K, 2KX$ *Semi-leptonic* $(K, \phi, \eta)(\bar{l}\nu_l)$ *Leptonic*	2.48 ±0.45 22.94 ±7.32 37.10 ±6.96 6.15 ±0.43 6.18 ±0.44	$112^{\mathbf{85}}$ (112)	***(*) *****

Table 1.4: List of current PDG values (2010) of all ground state D mesons. Column labels are the same as in table 1.2 in spite of the particle width, which is replaced by the mean decay length $c\tau$. $\{q\bar{q}\}$ indicates the quark configuration. The experimental status is obtained according to [9].

Besides the ground states, several excited mesons with open charm have been confirmed in the D sector. Current PDG values for all excited states presently established are summarized in table 1.5. The corresponding mass spectra are shown in figure 1.4. In analogy to the charmonium spectrum there are thresholds for a strong decay of D mesons into two lighter mesons, which effect a broadening of the particle width. According to potential models the first excited states in both spectra are P-wave spin-singlets. However, while the D^* masses are determined very precisely, the quantum numbers need to be confirmed experimentally.

Considering all quark configurations there are four light D^* mesons and two oppositely charged D_s^*. Charged and neutral D^* mesons are separated by roughly 3 MeV, which is less compared to their ground states. The mass splitting between the S-wave and the P-wave singlets in both systems is very similar. It is in the order of 140 MeV/c^2 and 145 MeV/c^2 for light and strange D mesons, respectively. All P-wave spin-singlets in the D spectra are located very close above the $D-\pi$ threshold. Hence, the main decay modes are defined to be either radiative or hadronic into a D meson and a pion. Even though

Excited D mesons states							
Particle $\{q\bar{q}\}$	Mass [MeV/c^2]	Γ [MeV]	$I(J^P)$	Main decays	Γ_{Σ_i}/Γ [%]	N_{Γ_i} $N_{\text{ch}}^{N_{\text{abs}}}$	Exp. status
$D^*(2007)^0$	2006.96 (±0.16)	< 2.1	$\frac{1}{2}(1^-)^A$	$D^0\pi^0$ $D^0\gamma$	61.9 ±2.9 38.1 ±2.9	$2^{\mathbf{2}}$ (2)	*****
$D^*(2010)^\pm$	2010.25 (±0.14)	0.096 (±0.022)	$\frac{1}{2}(1^-)^A$	$D^0\pi^+$ $D^+\pi^0$ $D^+\gamma$	67.7 ±0.5 30.7 ±0.5 1.6 ±0.4	$3^{\mathbf{3}}$ (3)	* *****
$D_s^{*\pm}$	2112.3 (±0.5)	< 1.9	$0(?^?)^{B_1}$	$D_s^+\gamma$ $D_s^+\pi^0$	94.2 ±0.7 5.8 ±0.7	$2^{\mathbf{2}}$ (2)	****(*)
$D_0^*(2400)^0$	2318 (±29)	267 (±40)	$\frac{1}{2}(0^+)$	$D^+\pi^-$	seen	$0^{\mathbf{0}}$ (1)	***(*)
$D_{s0}^*(2317)^\pm$	2317.8 (±0.6)	< 3.8	$0(0^+)^A$	$D_s^+\pi^0$	seen	$0^{\mathbf{0}}$ (2)	**(*)
$D_1(2420)^0$	2422.0 (±0.6)	20.4 (±1.7)	$\frac{1}{2}(1^+)^A$	$D^*(2010)^+\pi^-$ $D^0\pi^+\pi^-$	seen seen	$0^{\mathbf{0}}$ (4)	****
$D_{s1}(2460)^\pm$	2459.5 (±0.6)	< 3.5	$0(1^+)$	$D_s^{*+}\pi^0$ $D_s^+\gamma$ $D_s^+\pi^+\pi^-$ $D_{s0}^*(2317)^+\gamma$	48.0±11.0 18.0 ±4.0 4.3 ±1.3 $3.7^{5.0}_{-2.4}$	$5^{\mathbf{4}}$ (5)	* *****
$D_{s1}(2536)^\pm$	2535.29 (±0.20)	< 2.3	$0(1^+)^C$	$D^*(2010)^+K^0$ $D^*(2007)^0K^+$	seen seen	$0^{\mathbf{0}}$ (6)	**(*)
$D_2^*(2460)^0$	2462.8 (±1.0)	42.9 (±3.1)	$\frac{1}{2}(2^+)^C$	$D^+\pi^-$ $D^*(2010)^+\pi^-$	seen seen	$0^{\mathbf{0}}$ (4)	****
$D_2^*(2460)^\pm$	2460.1 ($^{+2.6}_{-3.5}$)	37.0 (±6.0)	$\frac{1}{2}(2^+)^C$	$D^0\pi^+$ $D^{*0}\pi^+$	seen seen	$0^{\mathbf{0}}$ (4)	***(*)
$D_{s2}^*(2573)^\pm$	2572.6 (±0.9)	20 (±5)	$0(?^?)^{B_2}$	D^0K^+	seen	$0^{\mathbf{0}}$ (2)	***

A ... to be confirmed, $B_{1/2}$ ... mass + width consistent with 1^- / 2^+, C ... strongly favoured assignment for J^P

Table 1.5: PDG values (2010) of established excited D mesons. Column labels are the same as in table 1.2. The experimental status is obtained according to [9].

strong decays are not forbidden, resulting particle widths remain very small. To date an explicit measurement only exists for the light $D^{*\pm}$ meson. The absolute value of 96 keV is comparable to the one of the J/ψ but still has a relatively large error of 25%. In all other cases only upper limits for the D^* widths are given.

Additional D mesons with a total quark spin of one have been observed at higher masses. Actually three neutral, D_0^*, D_1 and D_2^{*0}, and two charged states, $D_2^{*\pm}$, are established in

the light D meson spectrum. Even though the quantum numbers need to be finally confirmed they seem to fit to conventional models. All states are very broad because they are located far above the $D\pi$ threshold and thus coupling to strong decay channels. As a consequence, their experimental study against the non-resonant background is experimentally challenging. However, a systematic deviation from theoretical predictions is obvious. This accounts in particular for the very broad $D^{*0}(2400)$ meson (see figure 1.4). Further precision measurements are necessary to decide if there is a significant discrepancy with model predictions or if possibly smaller corrections of the theoretical values deliver a better approach to the experimental data.

The situation for higher excited states in the D_s sector is much less understood and can be compared to some extent with the charmonium spectrum above threshold. Two broad charged states above the DK threshold, the $D_{s1}^{\pm}(2536)$ and $D_{s2}^{*\pm}(2573)$, can be assigned as members of the P-wave spin-triplet. However, the experimental status of both is rather poor and also their quantum numbers need to be confirmed experimentally. The associated masses are determined with a precision of better than $1\,\mathrm{MeV/c^2}$. The particle width for the $D_{s2}^{*}(2573)$ still has a large error. In case of the $D_{s1}(2536)$ only an upper limit of 2.3 MeV is given. However, compared to the value of 20 MeV obtained for the slightly heavier $D_{s2}^{*}(2573)$, this value seems to be surprisingly small. Moreover, the location of the $D_{s1}(2536)$ shortly above the D^*K threshold also features other theoretical interpretations e.g. as a possible candidate for a bound molecule.

Other exciting discoveries in the D meson spectrum are the $D_{s0}^{*}(2317)$ and the $D_{s1}(2460)$. Similar to the $D_{s1}(2536)$, both states have an unexpected small width and are located relatively close to the DK and D^*K threshold, respectively. They do not fit in the conventional spectrum of a heavy-light compound quark system and thus stimulated a controversial discussion about their nature. However, the experimental status remains rather incomplete. So far, only upper limits for the particle widths can be given and the experimental confirmation of their quantum numbers is pending. Further studies are needed to allow a validation of various theoretical models for these states, which include also non-conventional QCD configurations. Most recent discoveries in the D_s spectrum are the $D_{sJ}(2710)$ and the $D_{sJ}(2710)$. They still have to be confirmed and thus are not listed in the PDG table. For completeness, they are indicated in figure 1.4. At least one of them potentially seems to fit in a conventional scheme.

1.2.3 Charmed baryons

In the field of charmed baryons all predicted ground states with one charm quark are observed and in good agreement with predictions of the constituent quark model. In total there are 17 known states and four additional candidates that need a final confirmation. They include charmed hyperons where an additional strange quark is substituted for an up or down quark and a number of excited states. One of the interesting studies is the work on a detailed model on the narrow charm resonances near threshold which then could be expanded to the field of hyperons without charm flavour, e.g. the $\Lambda(1405)$, in order to clarify if some of them are either a three quark system or merely threshold effects. A schematic view of the SU(4) multiplets for baryons formed by u, d, s and c-quarks is shown in figure 1.5. Baryons with double or even triple charm content have not yet been discovered.

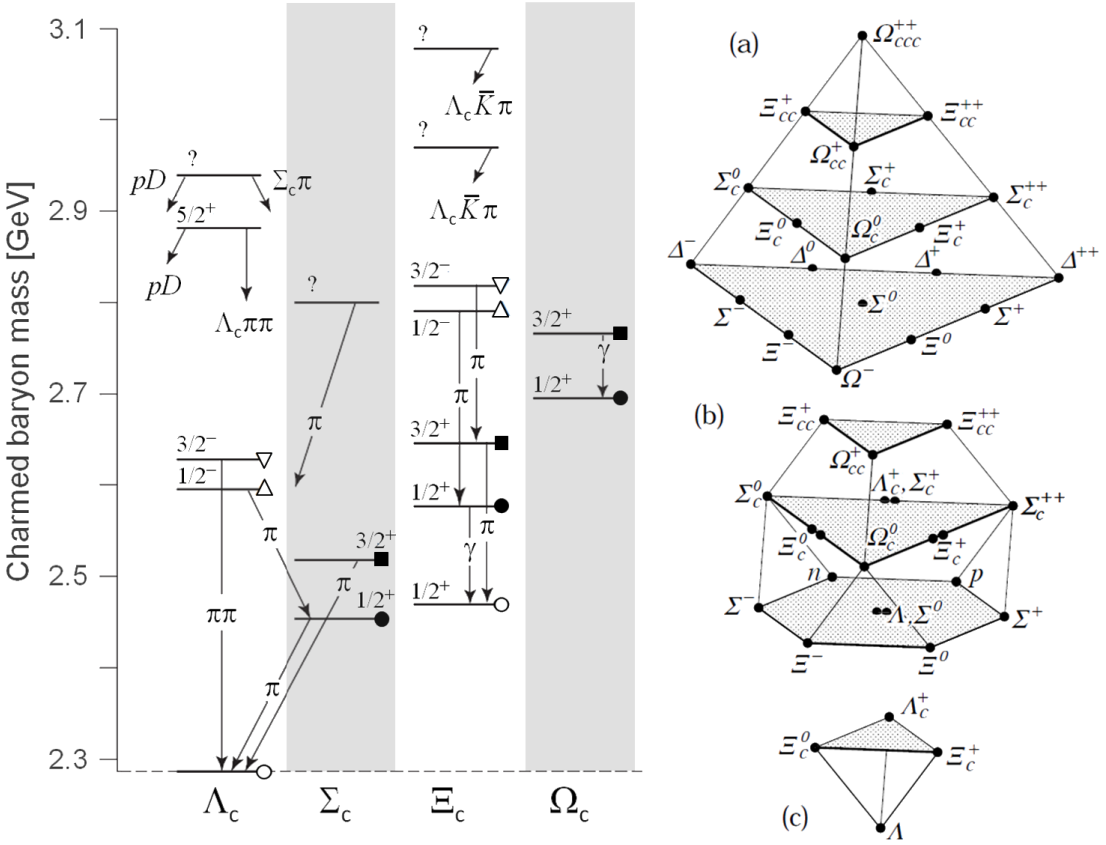

Figure 1.5: *Left*: Mass spectrum of known charmed baryons. To date only baryons with single charm flavour have been observed. J^P states tabbed with the same shape and the same fill belong to the same SU(4) and SU(3) multiplet, respectively. *Right*: SU(4) multiplets of baryons made of u, d, s, and c quarks: (a) The 20-plet with an SU(3) decuplet on the lowest level, (b) The 20'-plet with an SU(3) octet on the lowest level, (c) The $\bar{4}$-plet. In contrast to the depicted multiplets individual charge states are not shown separately in the mass spectrum. Pictures are adopted from [19].

1.2.4 Closing summary

The spectroscopy of charmed hadrons has delivered a huge number of new particles thus opening a complementary field to study the nature of strong interactions. Obtained results could successfully validate a lot of model predictions on conventional QCD configurations and stimulated further theoretical work due to unexpected observations.

So far, the measured spectrum of baryons with single charm flavour seems to be best understood. For charmed mesons the situation is less coherent. In some cases, namely the spin-triplet charmonium states below the open charm threshold and the ground states D mesons, experimental data is in a very good shape and allows profound tests of model predictions and QCD principles to the limits of the SM. The experimental status of other established states within the conventional charm spectrum still needs to be improved sig-

nificantly to reach the same quality level. In particular, this pertains to the charmonium spin-singlet states below the open charm threshold including the charmonium ground state $\eta_c(1S)$. Also the data on excited D mesons contains rather large errors or is partly incomplete.

Besides the well established conventional QCD states, a lot of open questions remain or were even posed by the observation of new states with unexpected properties. One characteristic is the deficient population of predicted charmed mesons above the threshold for strong decay modes. In contrast to this observation, a lot of newly discovered states do not seem to fit in the conventional scheme. All of them are located in the mass region above the threshold for a strong decay. In particular the XYZ puzzle within the charmonium mass region above the open charm threshold remains unsolved. In the D meson sector there are also several higher excited states whose nature is so far rather unexplored.

1.3 Experimental methods and applications

This section contains a short outline of different charm production mechanisms and associated measurements. In the second part, the main experiments relevant for the charm sector are summarized and an outlook to future applications is given.

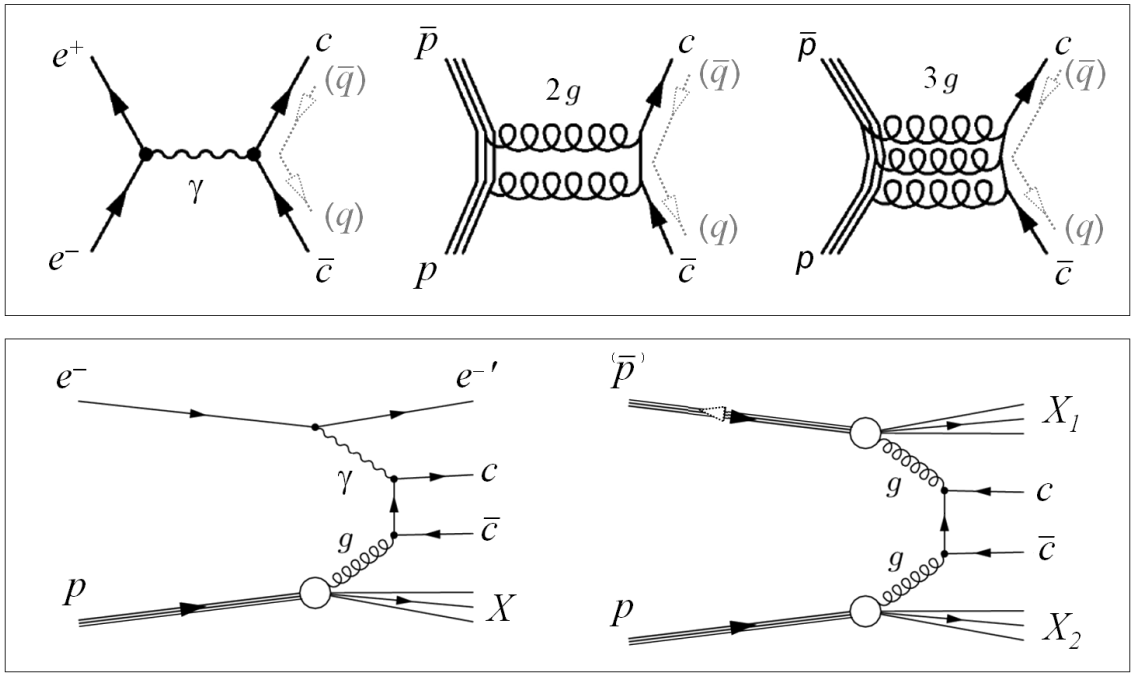

Figure 1.6: Feynman diagrams of different production mechanisms for charmed hadrons. Top: Formation in electron-positron (*left*) and antiproton-proton annihilation (*middle and right*). Bottom: Leading order process for the photoproduction (*left*) and the hadroproduction (*right*) in electron-proton and proton-(anti)proton collisions, respectively.

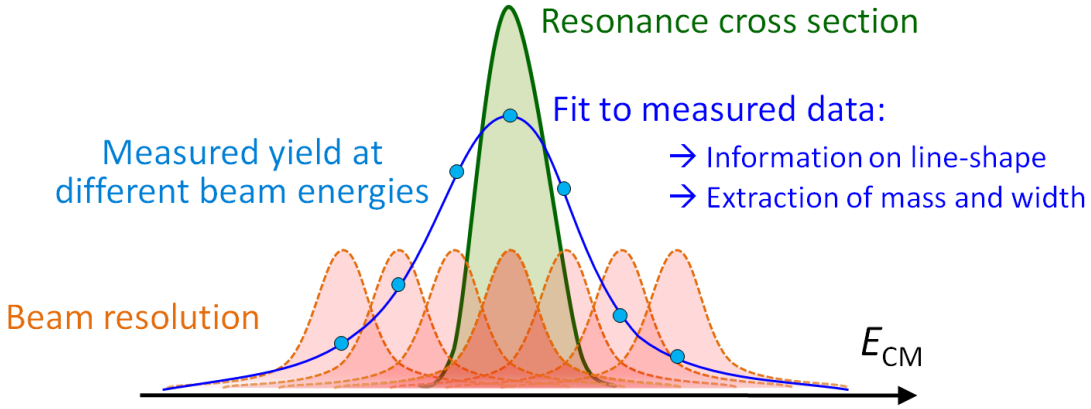

Figure 1.7: Schematic illustration of a resonance scan. Final results on the studied state are extracted from a fit to the measured yield obtained at different beam momenta. Assuming a suited and isotropic detection and reconstruction efficiency of the detector, the resolution is only driven by the beam quality, i.e. the resolution of the beam energy.

1.3.1 Common techniques for charm flavour production

For the study of charmed hadrons sufficient centre-of-mass energy must be available. Larger particle accelerator facilities are necessary to access the required mass region above $3\,\mathrm{GeV/c^2}$. There are different reaction channels for charm flavour production. They include electromagnetic or hadronic annihilations, the photoproduction in electron-proton collisions or the hadroproduction in proton-proton reactions. Feynman diagrams of the associated leading order QCD processes are shown in figure 1.6. All of them describe strong or electromagnetic mechanisms connected with a direct production in the reaction channel. Besides, weak decays of B mesons produced at higher centre-of-mass energy deliver another source of charmed hadrons which can be accessed by inclusive studies.

Basically, there are two experimental techniques for hadron spectroscopy. The first one is a direct formation of particles at rest within their resonant mass region, the second one is a production at higher centre-of-mass energy which delivers additional particles apart from the assigned bound states. While the production mode covers a larger dynamical range, the formation mode can be used for high-precision measurements. Due to flavour conservation in QCD only pairs of hadrons with open charm, i.e. one charm quark, can be produced directly.

Formation experiments in the charm quark sector are only feasible by means of annihilation reactions. Mass and width are extracted directly from the measured particle yield at different beam momenta. A schematic sketch of such a resonance scan is shown in figure 1.7. The experimental accuracy depends only on the resolution of the beam energy. Assuming high beam quality, a precise determination of the lineshape may eventually deliver additional information about the nature of the particle. For the study of open charm, i.e. D mesons, resonance scans must be performed over the respective mass region of the

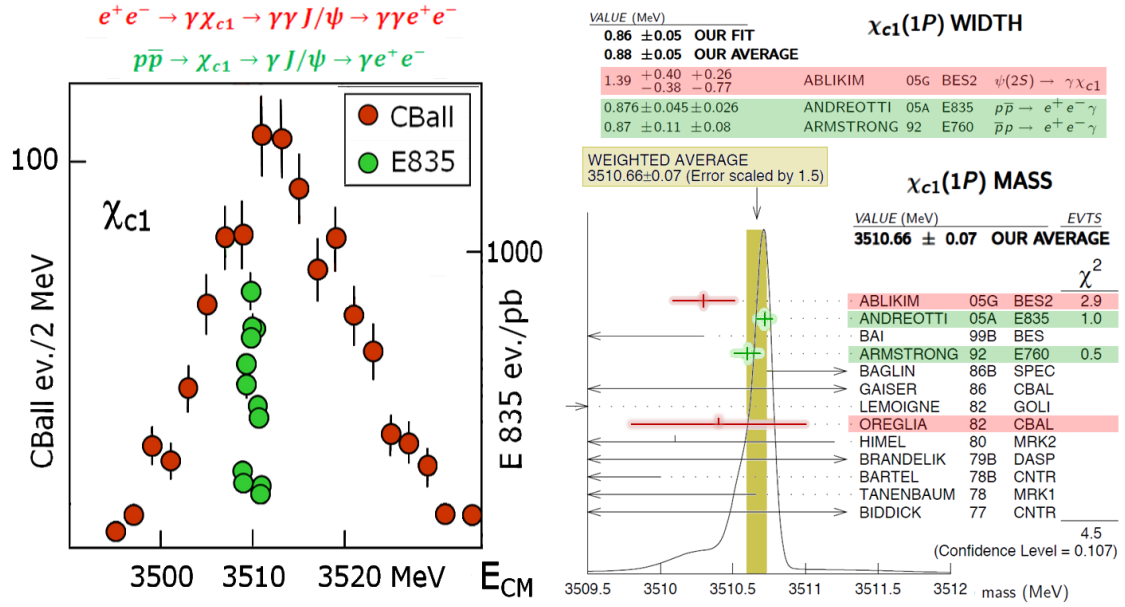

Figure 1.8: Comparison of the achievable precision in formation and production experiments shown exemplarily for the non-vector charmonium state $\chi_{c1}(1P)$. The given quantum numbers $J^{PC} = 1^{++}$ do not allow for a direct formation at electron-positron colliders. *Left*: Obtained mass spectra for e^+e^- (Crystal Ball [20]) and $p\bar{p}$ (E835 [21]) annihilations using an indirect production via a radiative decay of a higher charmonium and a direct formation, respectively. The particle yield is plotted against the centre of mass energy E_{CM} and scaled such that results of both measurements can be compared directly. *Right*: Present experimental data on the particle mass and width taken from the actual PDG summary table [1]. Formation experiments are highlighted in green, measurements at e^+e^- colliders in red. The precision of given parameters is clearly driven by formation experiments at $p\bar{p}$ machines.

two-particle threshold. In this case it is possible to obtain an excitation curve for either of the two charmed particles. However, the extraction of mass and width from the fitted excitation function depends on the complementary particle. Unambiguous results comparable to the ones for a direct formation of hadrons with hidden charm can be thus only obtained if the studied particle is formed together with its antiparticle. Otherwise, input parameters of the second particle must be given explicitly and the results of the fit are biased. Moreover, possible final state interactions or even resonant structures of both particles have to be taken into account and may complicate the analysis.

For the production of charmed hadrons there are no restrictions on the reaction type. Hence, either a direct creation in the initial process or a delayed generation in a subsequent decay of a short-lived B meson are possible. In contrast to the direct formation, results on mass and width of the particle are correlated with the intrinsic detector resolution of the experiment. However, production techniques render possible to exploit a wide range of the relevant mass region with one experimental setup and thus feature a high discov-

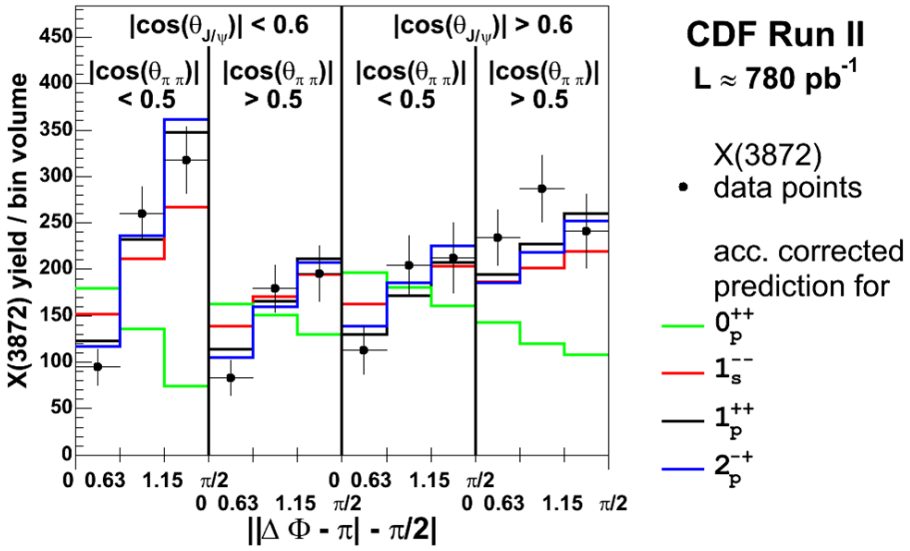

Figure 1.9: Analysis of quantum numbers in the angular distribution of the reconstructed particle yield shown exemplarily for the case of the charmonium-like state $X(3872)$. Results exclude quantum numbers of $J^{PC} = 0^{++}$ but favour an assignment of 1^{++} or 2^{-+}. The figure is taken from [22].

ery potential for so far unknown states. An accurate knowledge about the spectrum is prerequisite to perform resonance scans for selected hadronic systems. A comparison of the achievable resolution between direct formation and indirect production experiments is shown in figure 1.8.

Independent of the chosen reaction channel, a direct detection of charmed hadrons is excluded because of the very short lifetimes for these systems. Therefore, they must be reconstructed from the emitted particles in the final state. In this context, fully exclusive measurements are favourable because they feature a complete reconstruction of different decay modes and thus give access to the entire information concerning the intermediate charm state. The correct particle identification is needed i.a. to study the isospin structure or other flavour quantum numbers. It is also important for the determination of all corresponding four-momenta. They are needed for the extraction of the mass and the initial three-momentum of the charm state. The measurement of angular distributions gives insights to other dynamic quantities of the system such as the angular momentum or the total spin. One example is shown in figure 1.9. Inclusive methods may be needed for specific reactions with a very small production cross section in order to obtain sufficient statistics. Amongst others, a common approach is given by the calculation of missing masses or a combined mass of a subset of particles instead of the full reconstruction of all particles in the final states.

To date most data in charm spectroscopy has been delivered by electron-positron colliders and by antiproton-proton machines. Both feature the performance of formation measurements. One of the major disadvantages in electron-positron annihilations is the intrinsic limitation of formation experiments to vector states whose quantum numbers are fixed by

the intermediate virtual photon. Other states must be produced indirectly e.g. by a radiative deexcitation of higher charmonia or the weak decay of heavier mesons with b-quark content. All of these mechanisms suffer from significantly reduced cross sections and additional experimental restrictions given by the finite detector resolution. Such limitations can be overcome with antiproton-proton machines. Hadronic annihilations intrinsically provide the opportunity of a direct formation of any state. Different quantum numbers are accessible via intermediate states with the appropriate number of gluons and virtual quark-antiquark pairs. Challenges arise from the large hadronic background, which is much more critical compared to the relatively clean environment of leptonic electron-positron annihilations. Cross sections for the production of charmed hadrons are significantly smaller compared to other hadronic channels with a similar final state. Hence, a proper description and understanding of main background processes is mandatory.

Other initial channels based on electron-proton or proton-proton reactions do not allow a direct formation but only the production of charmed hadrons. Associated production mechanisms are relatively complex and thus impede a proper determination of the input channel in terms of quantum numbers involved. Moreover, even though the J/ψ was discovered in hadroproduction experiments, studies of charmed hadrons in this environment are considerably limited by large backgrounds.

If the experiment is performed at a very large centre-of-mass energy it is also possible to produce heavier B meson pairs in analogy to the $D\bar{D}$ production in the charm quark sector. In a weak decay of B mesons, charm flavour can be produced both by the transformation of the heavier bottom quark into a lighter quark as well as in the decay of the exchange boson. As a consequence, there are many possible decay channels with open or hidden charm. The inclusive study of B meson decays thus provides access to a lot of states in the charm spectrum with a relatively clean sample. It also features the search for new states, which manifest themselves in a possible resonant structure in reaction channels with established D mesons or charmonia. However, any direct formation of these states is excluded. Further restrictions on the achievable precision are given by the large excess energy released in the B meson decay, which is transferred to the decay products. Moreover, associated branching ratios for the subsequent production of a B meson and the following decay into one specific channel lead to a tremendous decrease of the achievable particle yield and enlarged systematic errors.

1.3.2 Experiments and future applications

The present accumulated data in the charm quark sector is based on a large number of individual experiments which have been performed during the last thirty years. First results were delivered by early experiments at electron-positron colliders e.g. at SLAC (Mark I-III, TPC, Crystal Ball) or DESY (DASP, PLUTO). Complementary studies in antiproton-proton collisions during the same period were performed at CERN (R704) and at Fermilab (E760, E835). In addition, experiments on the charm hadroproduction with pion beams were carried out at both facilities (WA82, SELEX, E791). Starting in the mid-seventies, all of the mentioned experiments were finished before the year 2000.

In the following years many measurements at new e^+e^- colliders such as the Cornell Storage Ring (CLEO, CLEO-c), the LEP at CERN, KEK-B in Japan (BELLE) or the BEPC collider in Beijing (BESII, BESIII) improved the knowledge about charmed hadrons. An

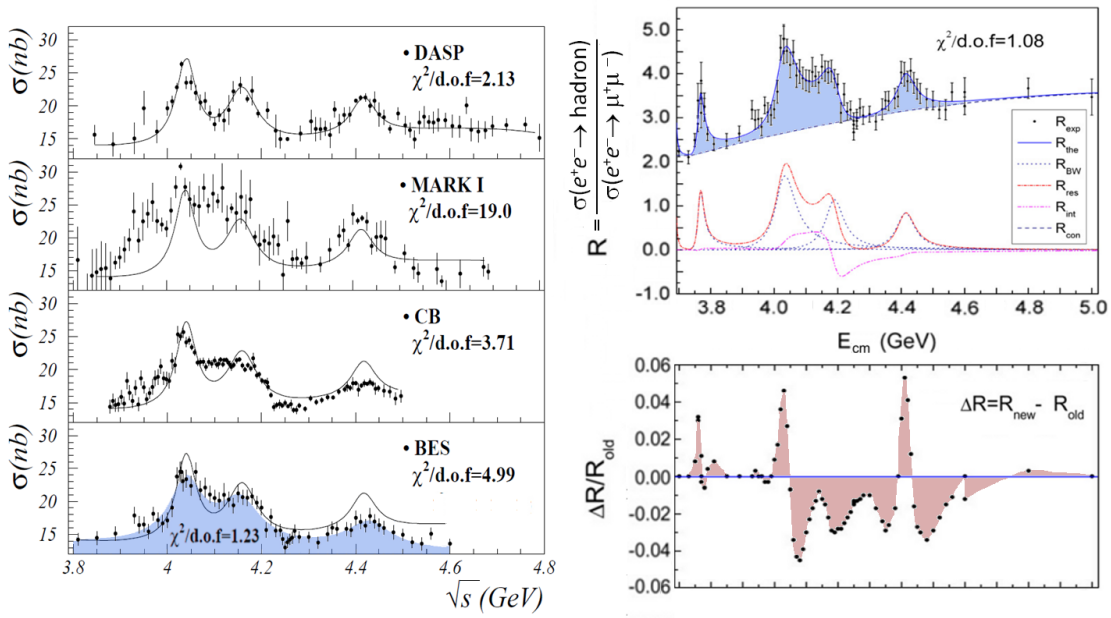

Figure 1.10: Experimental data on charmonium states above the $D\bar{D}$ threshold. To date there are no results from $p\bar{p}$ machines but only from e^+e^- colliders. All results are extracted only from measurements of total cross sections. Even though the observed resonances are indentified as well established charmonia, discrepancies between the different measurements and limiting factors on the precision of extracted values are obvious. *Left*: Total hadron cross sections obtained in various experiments covering the mass range of the $\psi(4040)$, $\psi(4160)$ and $\psi(4415)$. Picture taken from [23]. The common curve superimposed on all data sets and the filled curved at the bottom show the best fit of DASP and BES, respectively. *Right*: Updated results from BESII over the complete mass region above the $D\bar{D}$ threshold including the $\psi(3770)$ [14]. *Top*: Ratio R of the hadron compared to the muon production. The solid curve shows the best fit including all four resonances over a continuum background R_{con}. The Breit-Wigner contributions of each resonance, R_{BW}, the interference term, R_{int}, and the summed resonance fit, R_{res}, are shown explicitly below. Obtained results present the best data currently available. They mainly define the given PDG (2011) values. *Bottom*: Relative deviation of the updated, R_{new}, to the previous BES analysis, R_{old}, which is shown at bottom left.

example of the collected experimental data on charmonium states above the $D\bar{D}$ threshold is given in figure 1.10. Besides, upgrades of the existing accelerator facilities at SLAC and Fermilab enabled additional experiments on both e^+e^- (BaBar) and $p\bar{p}$ (CDF, D0) annihilations. In parallel, studies on the charm photoproduction in electron-proton collisions were performed at DESY (HERA). Amongst all listed experiment only BESIII did not stop data taking yet.

In summary, during the last decade a majority of accelerator facilities providing sufficient centre-of-mass energy for charm flavour production were built or updated with the emphasis

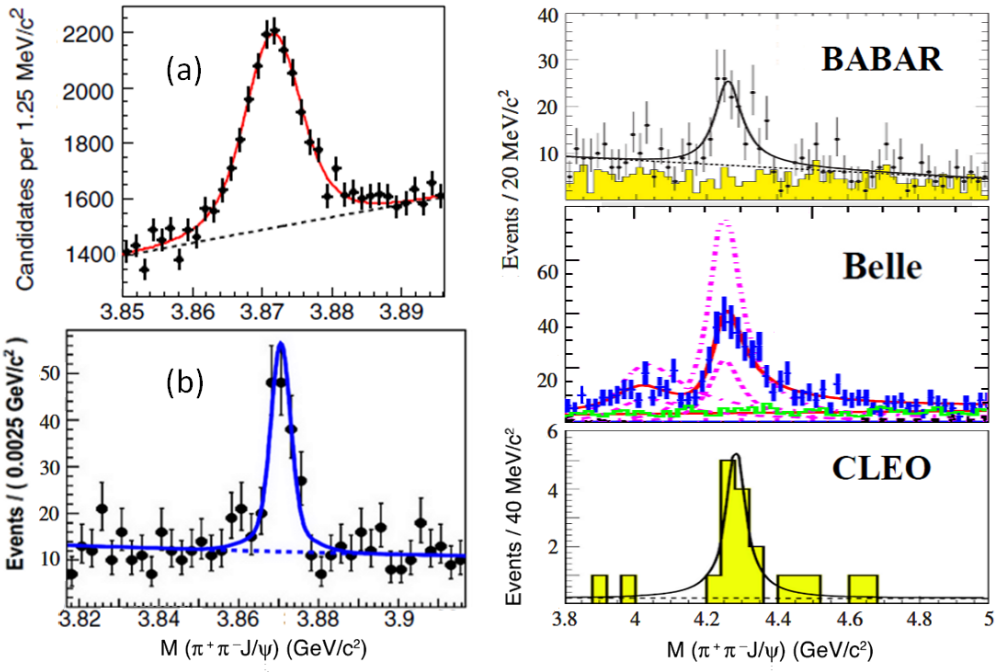

Figure 1.11: Recent measurements of both established charmonium like states above the $D\bar{D}$ threshold. Even though recent measurement at HEP facilities delivered a lot of new discoveries in the charm sector, further dedicated charm experiments are needed to improve the knowledge about these new states. *Left*: Inclusive precision measurement of the $X(3872)$ in $J/\psi\pi^+\pi^-$ decays produced in the continuum of $p\bar{p}$ annihilations [24] (a) and inclusive reconstruction in the decay $B^+ \to X(3872)K^+$ at an e^+e^- collider [25] (b). *Right*: Discovery (top [26]) and confirmation (middle [27]), bottom [28]) of the $Y(4260)$ state. Solid lines represent the best fit, dashed lines indicate the substracted background and, in case of the BELL data, contributions of two different solutions assuming a single or two states.

on experiments in the domain of high-energy particle physics (HEP). As a consequence, associated experiments are not optimized to perform a fine scan in the charm quark sector. However, a lot of discoveries and interesting observations in the charm quark sector were delivered in particular as by-product of extensive studies on B mesons. Selected results from recent measurements in the sector of charmonium-like XYZ states are shown in figure 1.11. Physics results from the B factories stimulated interest to specifically study charm encountered at lower energies. In this context two experiments, CLEO-c and BESIII, were set up. Both of them are electron-positron colliders, which intrinsically limits the possibility for high-precision spectroscopy to charmed hadrons with fixed quantum numbers of $J^{PC} = 1^{--}$. Early non-HEP measurements with antiprotons at Fermilab [29, 30], which allowed a formation of states with any quantum number, did not cover the full charm spectrum due to the limited centre-of-mass energy achievable.

As outlined in the previous reviews, experimental data still needs to be improved. There are many open questions remaining in the field of charm flavour physics. In particular

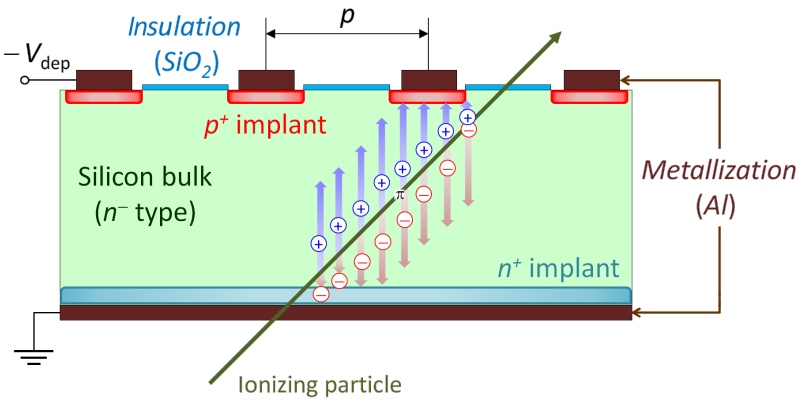

Figure 1.12: Schematic cross section through a silicon tracking detector and illustration of the detection principle. Due to the applied reverse bias voltage V_{dep} the detector bulk is fully depleted. Electron-hole pairs are created along the track of a traversing ionizing particle. Both charge carriers are drifting in opposite direction to the outer borders of the active volume where they can be collected at the metalized readout structure.

most recent results of different experiments at BELLE, BaBar and CLEO-c do not deliver a consistent picture. Currently, BESIII is the only running experiment dedicated to charm flavour physics. A significant improvement of the statistics for charmed hadrons is expected by planned upgrades of the B factories (e.g. BELLE II) and future LHC experiments. Nevertheless, they are not designed for a fine-tuned scan over the full charm spectrum but focus, respectively, again on the b-quark sector and physics topics at the TeV scale. It is obvious that a dedicated experiment for charm physics is strongly desired in order to perform high-precision spectroscopy for the entire mass region of the charm spectrum. Therefore, the PANDA experiment is planned, which is in the focus of the present work. A detailed description is given in chapter 2.

1.4 Silicon tracking detectors

The use of semiconductor materials offers many advantages for the detection of ionizing particles. Typical densities are more than three orders higher compared to gaseous detectors. They allow a very compact design and the construction of self-supporting structures. Moreover, ionizing particles produce a large number of charge carriers along their paths within the medium. As a consequence, very thin detector layers can be used without a significant degradation of the signal quality. Another advantage of semiconductor detectors is their fast timing characteristics providing a high-rate capability. The above properties are most crucial for tracking systems in high energy and hadron physics. Besides, parts of the existing process technology used in commercial microelectronic applications can be adapted for the custom made detector production. In this way, a cost-effective fabrication of large detector quantities becomes possible. More basics on semiconductors and further descriptions of their particular detector application can be found e.g. in [31], [32] or [33].

Silicon is one of the most commonly used semiconductor materials. It has a density of $2.33\,\mathrm{g/cm^3}$ and a small gap energy of 1.12 eV at room temperature. The typical energy loss per length unit, dE/dx, of minimizing ionizing particles (MIP) in a silicon bulk material is given by 3.8 MeV per centimetre. It is meaningful because in case of tracking detectors most particles are relativistic and have mean energy loss rates close to the minimum. An approximate description of the electronic energy loss by charged particles is given by the Bethe-Bloch formula (for more details see [34]). In case of silicon an average energy of 3.6 eV is needed for the creation of an electron-hole pair. Compared to the ionization energy in gases this is about one order of magnitude smaller and thus provides sufficiently large signals with much smaller sensor dimensions. Typical sensor thicknesses in tracking applications are in the order of one to a few hundreds of micrometer.

Detrimental effects for the detection of traversing particles are related to the thermal generation of electron-hole pairs, which is related to the small energy gap. The intrinsic charge carrier density of pure silicon at room temperature results in $1.45\times10^{10}\,\mathrm{cm^{-3}}$ which yields an intrinsic resistivity of approximately 230 kΩcm. The number of thermally created charge carriers is thus four orders of magnitude larger than the signal of a MIP. As a consequence, nearly all silicon detectors are based on a reversed biased junction diode. In this mode they can be operated at room temperature, which makes them superior to other semiconductor materials such as germanium. A doping of the semiconductor, i.e. the substitution of a small fraction of lattice atoms by doping atoms with additional (n-type) or missing (p-type) valence electrons, is necessary to built such detector type. The depletion zone then acts as sensitive detection volume. Therein, created electron-hole pairs can be separated by the latent intrinsic field. Due to the high mobility for both charge carriers, short collection times in the order of 10 ns can be achieved with silicon detectors. Moreover, the range of δ-electrons [2] is very small and prevents large shifts of the centre of gravity of the primary ionization from the position of the track. These particular properties allow a very precise position measurement down to a few micrometers.

A schematic cross-section through a silicon tracking detector is shown in figure 1.12. It consists of the low-doped silicon bulk material acting as sensitive volume and implanted regions of high-doped n and p type at both sensor sides, respectively. In most cases detectors are based on (1,1,1) n-type bulk materials. The highly doped regions at the surface are metalized to allow the electrical contact. By applying a sufficiently large reverse bias voltage, the width of the space-charge region associated with the $p-n$ junction extends across the entire thickness of the silicon bulk thus resulting in a fully depleted detector. Typical depletion voltages for radiation hard detectors are in the order of several tens to hundreds of volts.

When a charged particle crosses the detector volume it deposits energy by many collisions with electrons. These interactions cause the creation of electron-hole pairs within picoseconds along the track. Due to the electric field both charge carriers drift in opposite directions. While conduction electrons move towards the n-side, holes propagate towards the p-side. An electric signal can be detected due to the resulting currents until free charge carriers are fully collected at the boundaries of the active volume. Because the mobility of electrons at room temperature is roughly three times larger than for holes, the collection

[2] Higher energetic δ electrons are produced to a small fraction after the primary ionizing collision of a charged particle in the medium. They have sufficient energy to induce secondary ionizations.

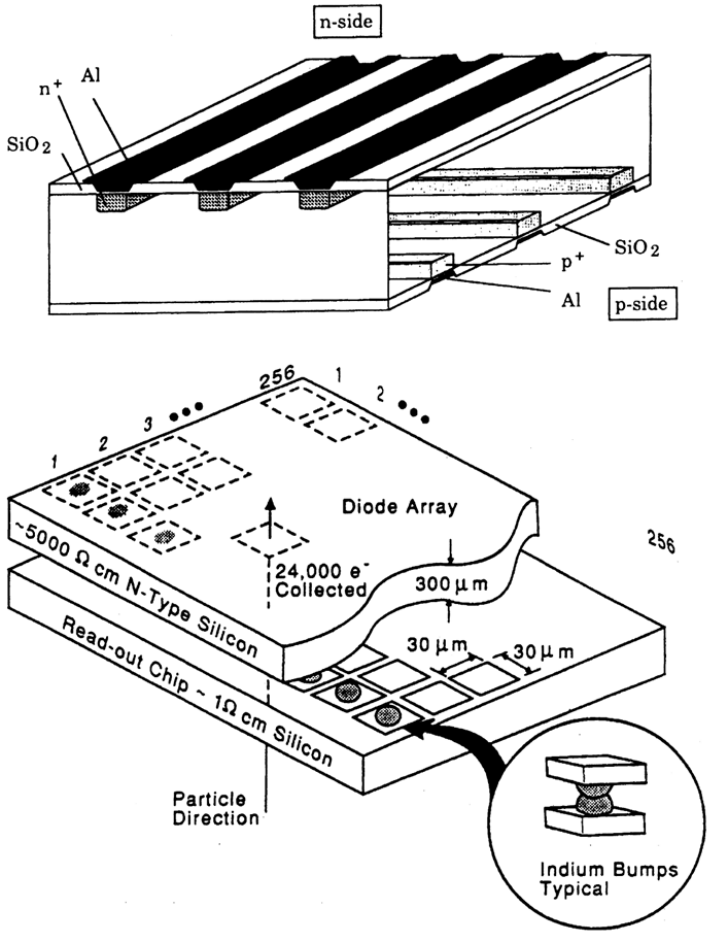

Figure 1.13: Schematic picture of a double-sided silicon strip detector (*top*) and a hybrid pixel detector consisting of separate detector and electronic chips connected through indium bump bonds (*bottom*). (Illustrations taken from [35].)

time for both is different. However, in contrast to gaseous detectors the time scale is still small enough to base analysis on the integrated currents of both charge carriers.

The charge signal created as described above is proportional to the energy loss of the incident particle. Position information is obtained by a subdivision of the electrodes into a number of independent segments with separate readouts. The necessary insulation is obtained by an interjacent oxygen layer. Different detector types differ basically in the chosen geometry. These are illustrated in figure 1.13. In case of pixel detectors the top electrode is subdivided in two dimensions thus forming a checkerboard pattern. The 2D hit coordinates are then directly related to the activated pixel cell. Only one coordinate is obtained if the readout electrode is split into individual strips. Full 2D information with strip detectors can be obtained either by using two single-sided detectors or by a subdivision on both sides of the detector. The resulting 2D pattern depends, according to

the chosen solution, on the tilt angle between two single-sided detectors or the introduced stereo angle between the strips of both detector sides.

Taking into account only the hit information (binary readout) and neglecting effects of large incident angles and charge diffusion during collection, the measurement precision for one coordinate is mainly given by the interspacing, p, between individual readout segments which is commonly denoted as pitch. In this case, the root-mean-square (RMS) deviation from the true coordinate, σ_{RMS}, is given by:

$$\sigma_{\mathsf{RMS}} = \frac{p}{\sqrt{12}} \tag{1.1}$$

This value can be substantially improved with an analogue readout once the signal charge is collected in more than one channel and the coordinate can be interpolated, e.g. by using the centre of gravity of the obtained signals. Therefore, the pixel cell size or the strip interspacing (strip pitch) must match the charge spread during the its collection, which is related to the diffusion and the track inclination. In case of strip detectors it is possible to reduce the number of channels by one dimensional charge division along a line which interconnects all strips. Thereby, only a fraction of the strips is connected to the readout amplifier while the ones in between are left floating. Applying a resistive or capacitive division the collected charge is shared among two neighbouring readout strips according to the relative position. In this way a spatial resolution of 10 µm can be reached [33]. The achievable position-measurement precision with interpolation methods based on an analogue readout is limited by the noise performance of the electronics and can be roughly estimated as:

$$\sigma_{\mathsf{RMS}} \approx (S/N)^{-1} \cdot p \tag{1.2}$$

with (S/N) corresponding to the signal-to-noise ratio. Moreover, the analogue information can be used to correlate signals from two sides. Making use of Landau fluctuations and the exact equality of positive and negative charge created by each ionizing particle traversing the detector, it is partly possible to resolve ambiguities. These occur when several particles hit the detector simultaneously.

Detector type and geometrical parameters have to be adjusted to the special requirements of the experiment. One advantage of pixel detectors is given by the low noise level due to the small size of each individual cell. Compared to similar strip detectors a reduction of more than one order of magnitude can be reached [36]. Moreover, there are no hit ambiguities as for strip detectors. Technical challenges arise from the electrical contacts to each pixel cell and the high integration density of detector and frontend electronics. Besides, the number of pixel readout channels is significantly larger than for strip detectors. This fact has to be considered carefully because it has an impact on the overall material budget and the required space needed for all associated components of the readout electronics including cables and cooling. As a consequence, most tracking detectors use strip detectors in the outer layers to cover relatively large areas.

The advantage of double-sided strip detectors over the single-sided type is given by the reduced material budget and the correlated information of the signals obtained for the two coordinates. Special problems occur for the readout on the n-side. Due to the isolating oxygen layer at the surface, a thin accumulation layer of mobile electrons is produced and

thus opens a conduction path between the electrode strips. To remedy these potential problems, additional p-implants (p-stops) are introduced in between the n-doped areas. The sensitive bulk thickness of silicon detectors used within tracking devices ranges between 100 µm up to 300 µm. Restrictions are given by technical limitations of the wafer thinning process and the created charge amount needed to obtain the specified signal-to-noise ratio. The latter depends on the desired position-measurement precision including the initial choice between binary or analogue readout. Moreover, a more accurate extraction of the deposited energy may be useful to support different particle hypotheses. Even though a silicon tracking detector is not suited for calorimetry, the analogue information of the obtained charge sum can be correlated to some extent to the typical energy loss per length unit, $\mathrm{d}E/\mathrm{d}x$, which depends on the momentum and the mass of the traversing particle.

Most of the tracking systems operate in a harsh radiation environment and thus radiation-induced damages have to be considered carefully. They are connected with non-ionizing energy transfers to the atoms, which may lead to irreversible changes of the lattice. Radiation damages are accumulated during the measurement and may change the properties of the detector. Detrimental effects are related to a degradation of the signal quality due to reduced charge collection efficiency and increased leakage currents, a type inversion of the bulk material, a worsening of the time characteristics and a significant change of the depletion voltage which, in the worst case, culminates in a destruction of the whole detector due to electrical breakdown. Extensive studies have been performed to obtain a qualitative and quantitative description of underlying mechanisms and to develop appropriate techniques allowing the fabrication of silicon detectors with sufficient radiation tolerance [37, 38]. One of the favourable results of these investigations is the self-annealing effect of silicon detectors observed after irradiation, which soccurs already at room temperature.

1.5 Tracking algorithms

The path of a particle of known mass can be parameterized by its three momentum components and the three spatial position coordinates given at selected time intervals. In general, track information is obtained from a set of space points. They are defined by the intersections of the particle with real detector planes or the projection on idealized planes, which are usually chosen perpendicular to the particle direction. In the absence of any external forces the particle track is given by a straight line which can be described by four parameters. For the helical movement of charged particles in a constant magnetic field, five track parameters are needed. In ideal cases a minimum of two and three track points are needed for a full determination of the linear and the helical trajectory, respectively.

Due to the limited detector resolution and positioning precision, measured track points only approximate the exact space points of the physical path. Moreover, material effects and inhomogeneous magnetic fields change the ideal flight path of the particle. As a consequence, fitting algorithms are needed to extrapolate particle tracks to the positions of the measured hit points in the detectors and to calculate the distance between hits and tracks, i.e. the residuals. Errors and uncertainties are described by an associated covariance matrix. Basically, the quality of the fit is improved with an increasing number of hit points. Track fitting algorithms in particle spectrometers are commonly based on the mathematical principles of the Kalman filter [40, 41]. This is given by a set of mathematical equations,

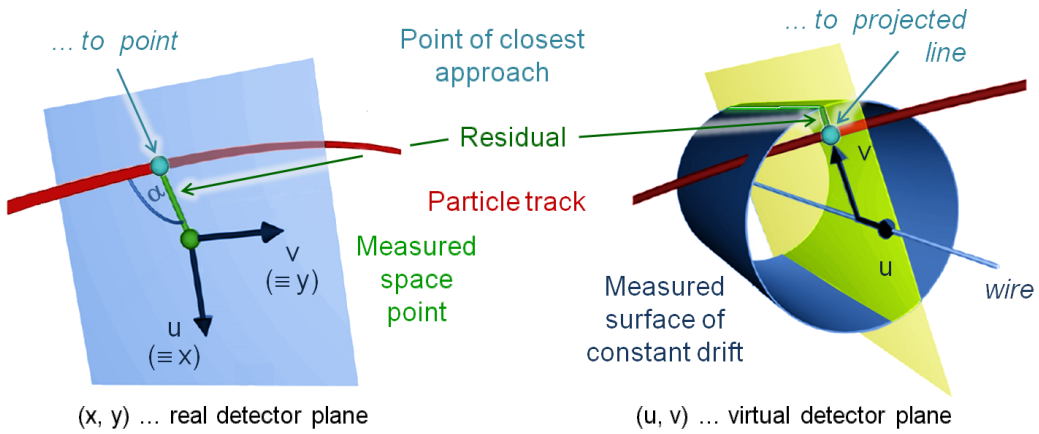

Figure 1.14: Illustration of tracking measurements with a position sensitive detector delivering 3D space points (*left*) and for a wire-based drift detector (*right*). In case of the 3D position detector the virtual detector plane can coincide with the real detector plane. Detector-based information only represents an approach to the particle track, which may be either the physical or the reconstructed one. Optimized tracking algorithms aim on a minimisation of the remaining residuals. (Picture adapted from [39])

which allows for a precise solution in a dynamical system where all latent and observed variables have a Gaussian distribution (often a multivariate Gaussian distribution).

Validated Kalman filters for particle tracking are based on true values of single hit measurements that contain random variations related to the experimental conditions, e.g. the detector resolution, material effects and inaccuracies of applied magnetic fields. With these input data, the particle path is predicted and an estimate of the uncertainty of the predicted values is deduced. Finally, a weighted average of the predicted and the measured values is computed, which gives the most weight to the value with the least uncertainty. Estimates obtained with this method tend to be closer to the true physical path than the original measurement because the weighted average has a better estimated uncertainty than either of the individual values used for its calculation.

Particular challenges in particle and nuclear physics result from the high complexity of events and the large number of hit points delivered by a combination of different detector species. In almost every event there are several particles to be tracked simultaneously. To minimize the huge combinatorics and thus to guarantee a convergence of the global fit, a fast pattern recognition is necessary with which a pre-selection of track candidates is performed. A common approach is the choice of suitable transformations in the parameter space allowing a straight-line fit and neglecting effects of energy loss and multiple scattering. Standard methods for helical trajectories are e.g. the conformal mapping [42] or the Riemann tracking algorithm [43].

For the conformal mapping the track is projected onto two planes. The first one is formed by the trajectory and the z-axis along the magnetic field, the second one is orientated perpendicular to the magnetic field. In this way the projection of the track corresponds to a straight line and a circle, respectively. The latter can be straightened by an angle-

preserving transformation. This method requires the knowledge of the first track point. If the position of the interaction point is well known, a vertex constraint can be applied which reduces the computation time appreciably. Track segments are formed from the outer to the inner layers of the detector excluding the first track point. Track candidates are then defined by track segments with a sufficient number of hit points, a minimum length and an acceptable approximation to the excluded first track point by the linear fit.

The Riemann track finder is based on a fast circle fit. Assuming the XY-plane to be perpendicular to the magnetic field, corresponding coordinates of the hit points can be projected on a paraboloid to obtain the third coordinate. Three points are necessary to calculate the Riemann plane. Obtained fit parameters deliver the radius and the origin of the defined sphere. A linear dependence is obtained in a 2D representation plotting the arc length of the hits against their z-position. Once the Riemann plane is defined, the distance of all other hit points to the plane can be calculated. Assigning only hit points with small distances, a track candidate is then defined if more than three points are obtained within one Riemann plane.

After the pre-selection of track candidates a precise reconstruction of the track parameters can be performed. Figure 1.15 schematically illustrates the conceptual approach of a track fit algorithm. In most cases a straightforward track following method is implemented for the fitting procedure. Its main tasks are the bidirectional transport of track parameters, i.e. particle momentum, position and direction, from one hit point to another and the propagation of the associated errors together with the mean values. GEANE is one of the established track following codes [44]. It takes into account Coulomb multiple scattering, energy loss and the applied magnetic field. The energy loss parameterization includes typical fluctuations in low density media described by a Landau or a Vavilov distribution. A present generic framework for the track fitting in complex detector systems is provided by the C++ based, object oriented GENFIT software toolkit [39].

Basically, the implemented tracking algorithms must be optimized according to the requests of the experiment and the individual setup of the tracking system. In more complex applications a pre-selection of appropriate candidates by means of a track finder is mandatory before the precise track reconstruction. The latter takes into account detrimen-

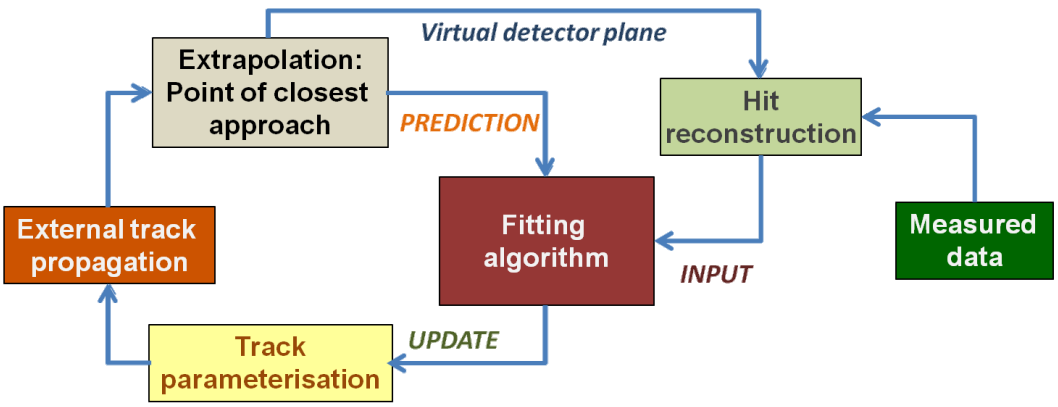

Figure 1.15: Schematic concept of track fit algorithms.

tal effects due to energy loss, multiple scattering and a non-homogeneous magnetic field. Hence, besides a good single hit resolution and the precise alignment of tracking detectors in the experimental setup, a proper description of the material budget is essential to improve the quality of the extracted track parameters. A good particle tracking is essential for the further vertex reconstruction in which several tracks must be combined. Moreover, it is prerequisite for a precise determination of the particle momentum in case of using an analyzing magnet.

2 The $\bar{\text{P}}$ANDA experiment at FAIR

The $\bar{\text{P}}$ANDA (anti**P**roton **AN**nihilation at **DA**rmstadt) experiment [45] is one of the key projects at the future **F**acility for **A**ntiproton and **I**on **R**esearch (FAIR) [46] which is currently under construction at GSI, Darmstadt. For this new facility the present GSI accelerators will be upgraded and further used as injectors. The completed accelerator facility will feature a complex structure of new accelerators and storage rings. An overview of the FAIR facility is given in figure 2.1. Further details of the accelerator complex are described in [47]. The FAIR accelerators will deliver primary proton and ion beams as well as secondary beams of antiprotons or radioactive ions, all with high energy, high intensity and high quality. Experiments to be installed at the facility will address a wide range of physics topics in the fields of nuclear and hadron physics as well as in atomic and plasma physics. An executive summary of the main FAIR projects can be found in [46] and [48].

The present chapter will focus on main aspects relevant for the $\bar{\text{P}}$ANDA experiment. An overview of the physics program of $\bar{\text{P}}$ANDA is given in section 2.1. Section 2.2 summarizes the experimental conditions, which will be met during the operation. Finally, detector setup and overall detection concept of the $\bar{\text{P}}$ANDA apparatus are presented in section 2.3.

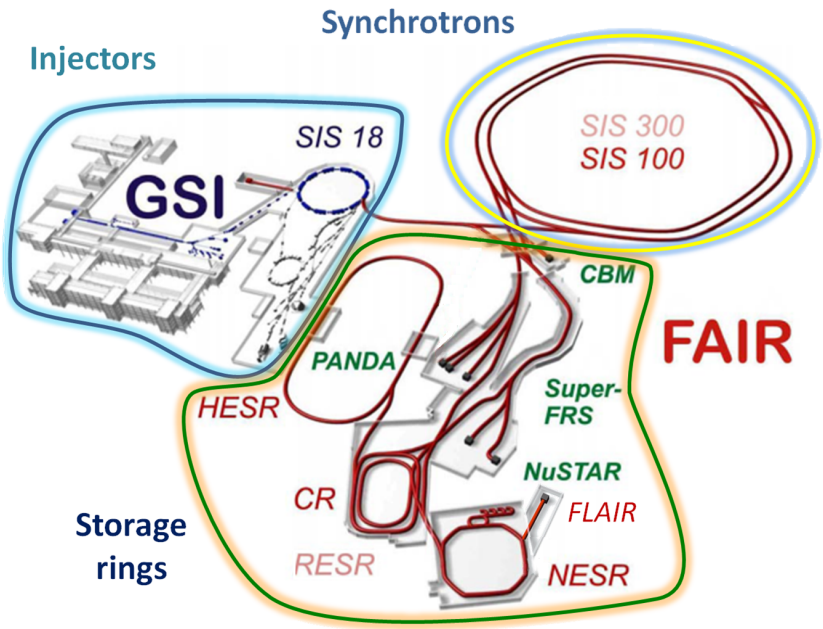

Figure 2.1: Overview of the future FAIR facility. The upgraded accelerators of the existing GSI facility will act as injectors. New accelerator and storage rings are highlighted in red, experimental sites are indicated with green letters.

2.1 $\bar{P}$ANDA physics program

The $\bar{P}$ANDA experiment will perform precise studies of antiproton-proton annihilations and reactions of antiprotons with nucleons of heavier nuclear targets. It will benefit from antiproton beams with so far unrivalled intensity and quality. The covered centre-of-mass energy between 1 GeV and 5 GeV allows for very accurate measurements especially in the charm quark sector. As outlined in section 1.3, an energy scan with high precision over the full charm spectrum is still missing and will not be delivered by future experiments currently planned as upgrade at existing facilities. Therefore, the antiproton experiment $\bar{P}$ANDA represents a unique tool to improve both statistics and precision of existing data and to further explore the physics in the charm quark sector. Associated topics refer to the strong force and the structure of multi-particle systems bound by this interaction. A short outline of these subjects was given in section 1.1.

The multi-purpose design of the $\bar{P}$ANDA detector facilitates many different experiments, which partly will be executed in parallel. As a consequence, a broad physics program can be tackled. Figure 2.2 gives an overview of possible hadron configurations in the accessible mass range. Related topics will be briefly discussed in the following subchapters. More details and dedicated simulations have been compiled in [5].

Charmonium spectroscopy

A systematic study of the charmonium spectrum is one of the key points in the core physics program of $\bar{P}$ANDA. Compared to high-energy experiments with rather large energy steps and other experiments with limitations either on the directly accessible quantum numbers or on the maximum centre-of-mass energy available, the $\bar{P}$ANDA experiment is better suited for a high precision spectroscopy in the whole mass range of charmonium systems, which also includes a detailed analysis of their decay patterns. Of particular interest are helicity or G-paritity non-conserving decays in hadronic channels, radiative decay modes, branching ratios of hadronic decay channels and rare or suppressed decay modes. Exclusive measurements of charmonium decays are an ideal tool to test QCD predictions with high accuracy. The above topics are addressed in particular in the mass region below the open-charm threshold. They will benefit from the high statistics in the $\bar{P}$ANDA experiment expected for the well established charmonia [50, 51].

Main parts of the charmonium program can be started shortly after commissioning. Examples for such early stage experiments are e.g. the direct comparison of hadronic decays between the J/ψ and the $\psi(2S)$ meson or a study of the radiative deexcitation of the spin-triplet states, $\psi(2S)$ and χ_{cJ}, which gives access to the electric dipole transition in charmonia. The study of higher multi-poles will be facilitated by the measurement of angular distributions for the χ_{J1} and the χ_{J2}. In a second step,high precision measurements of spin-singlet states can be performed in formation experiments e.g. to improve the so far rather poor experimental data on the h_c or the η_c.

Measurements above the open-charm threshold are of particular interest. First of all they are needed to improve the experimental data on the four established charmonia (see figure 1.10). To date none of these states has been studied in a dedicated formation experiment. Moreover, systematic scans of the mass region of higher lying charmonia are from utter importance to extend knowledge either by discovering a lot of the states still

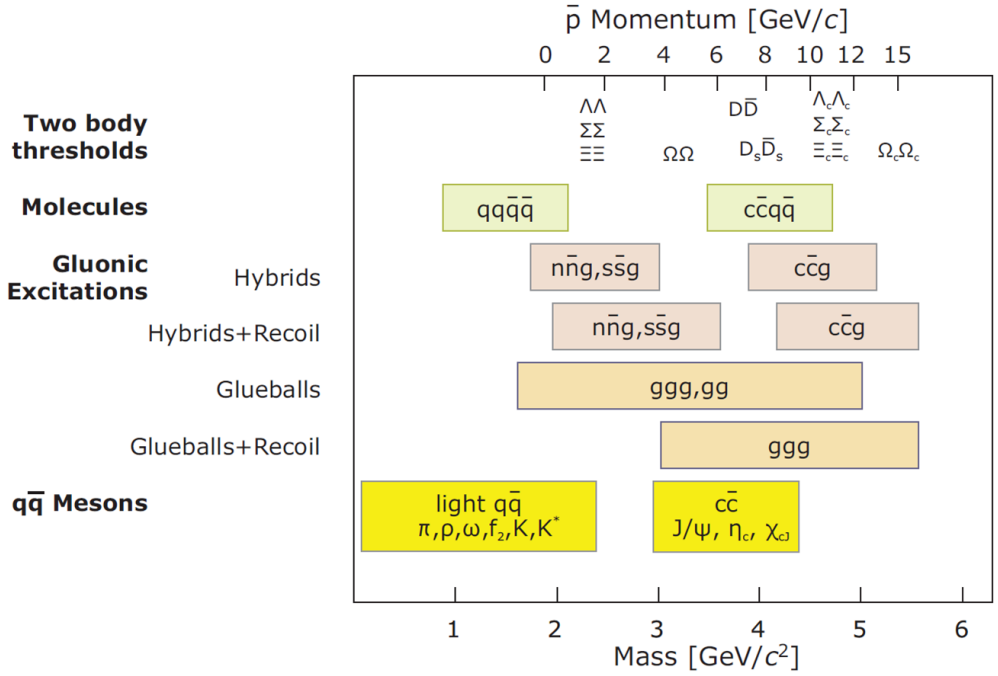

Figure 2.2: Accessible mass range of hadrons at the P̄ANDA experiment. The corresponding momentum for the available rest mass in a fixed target setup is given at the upper scale. The delivered antiproton beam ranges between a beam momentum of 1.5 GeV/c and 15 GeV/c. It covers the entire region of charmonium systems and overcomes many two-body thresholds for D mesons or hyperons. Theoretical predictions of charmed hybrids and glueballs still need experimental confirmation. (Picture taken from [49].)

missing in the spectrum or by establishing observed states as member of the $c\bar{c}$ family. In addition, the discovery and confirmation of charmonium-like states with exotic properties is likely to be the most important issue of the P̄ANDA experiment.

Open charm spectroscopy

After the commissioning of P̄ANDA, the luminosity will be increased stepwise until it reaches the maximum design value. Depending on the available centre-of mass energy, several combinations of two different D mesons are possible at higher beam momenta, thus defining discrete thresholds at various energy levels. Some of them are separated by only a few MeV due to the low mass differences in the D meson spectrum.

Generated D mesons can be associated with a decay of higher charmonia or charmonium-like states. The non-resonant $D\bar{D}$ production at threshold yields up to 100 D meson pairs per second. It delivers a better situation for high precision measurements because of the very little excess energy which significantly suppresses the generation of additional pions or other particles. If there are only two D mesons in the intermediate state after the $p\bar{p}$ annihilation, the kinematic situation is well defined and one D meson tags the other one.

As a consequence, both the mass and the width of D mesons can be measured with high accuracy taking advantage of the beam quality and the well suited detector.

The high statistics for D mesons at $\bar{P}$ANDA will also permit a detailed study of their decay patterns including the search for rare decay modes. For instance, one of the theoretically interesting channels, $D^0 \rightarrow \mu^+\mu^-$, is related to flavour changing neutral currents, which would indicate physics mechanisms beyond the standard model. Moreover, precise studies of a possible $D\bar{D}$ flavour mixing and the associated CP violation in the charm quark sector are envisaged. Improved experimental data is needed to reduce the errors on extracted numbers of recent measurements in order to confirm the observation of a nonzero value [52, 53, 54, 55].

Search for non-conventional QCD states

The confirmation of exotic QCD configurations and the search for new states is another key point of the $\bar{P}$ANDA physics program. For this purpose high statistic measurements must be combined with a sophisticated analysis of quantum numbers and a fully exclusive reconstruction. In order to exploit the discovery potential, the $\bar{P}$ANDA experiment will first run at highest beam momentum and work in a production mode for so far unknown states. Once an interesting mass region is located, precision experiments can be performed aiming at a direct formation of potentially interesting states.

Exotic states are expected by many theoretical models in the $\bar{P}$ANDA relevant mass region between $3\,\mathrm{GeV/c^2}$ and $5\,\mathrm{GeV/c^2}$. To date, several candidates for such non-conventional QCD states have been identified experimentally. However, more data is needed for a final confirmation and a proper determination of their quantum numbers, which would allow a clear theoretical interpretation.

Other physics options

Besides the spectroscopy of charm containing QCD bound states, several other physics topics will be covered within the scope of $\bar{P}$ANDA. They are briefly itemized in the following.

→ In-medium modifications

In dense nuclear matter and at high temperatures a partial restoration of the chiral symmetry is expected for the light quarks due to a change of the quark condensate [56]. As a consequence, in-medium modifications of meson properties are predicted leading to a mass shift, a changed width or reduced coupling constants. Indeed, results from proton-proton, photon-proton and heavy ion collisions indicate such effects for light mesons such as pions, ρ, ω or ϕ mesons [57]. $\bar{P}$ANDA will allow an extension of these ongoing studies to the charm quark sector. Therefore, heavier nuclear targets will be used in a later stage of the experiment to study antiproton-nucleus interactions and, in particular, the behaviour of charmed mesons in nuclear matter.

Starting point for this program will be the measurement of J/ψ dissociation cross sections in nuclear matter, which deliver important input for the description of the quark-gluon plasma. The study of a possibly modified particle width yields information on inelastic interactions inside the nuclear medium. In-medium mass shifts of lower-lying charmonium

states such as the J/ψ are expected to be rather small [58]. The measurement of similar effects with D mesons is experimentally challenging. However, model calculations predict a mass splitting bewteen the D and the $\bar{D}$ of around 50 MeV to 100 MeV and an additional downward mass shift of the averaged D-$\bar{D}$ mass in the same order of magnitude [59]..

The $\bar{P}$ANDA experiment also offers the opportunity to study in-medium properties of hadrons in the light quark sector, which have sufficient energy to penetrate into the interior of the nucleus. The nuclear potential can be probed quasi at rest by backward scattering from a nuclear proton. Considering nuclear absorption effects of the incident and the outgoing particle, the potential of e.g. antiprotons, antihyperons ($\bar{\Lambda}$) or the ϕ-mesons can be accessed with this method.

→ Electromagnetic processes

These studies focus on annihilation measurements into two photons and related exclusive processes with a scalar meson, a vector meson or a di-lepton pair. They can be executed in parallel to the charmonium and the charmed hybrid program. The comparison of differential cross sections allows a test of theoretical predictions and offers new insights into the annihilation process. Information on the hadron structure is connected to the transverse quark distribution. It can be studied in semi-inclusive lepton production or in Drell-Yan processes for di-muons ($\bar{p}p \rightarrow \mu^+\mu^- + X$). Besides, the electromagnetic form-factor of the proton can be extracted from the cross sections for the process $\bar{p}p \rightarrow e^+e^-$. Due to the high statistics, a separate measurement of the electric and the magnetic form factor becomes possible. A further approach combining both methods is given by the extraction of generalized parton distributions (GPDs).

→ Hypernuclei physics

In a later stage of the $\bar{P}$ANDA experiment, a precision γ-ray spectroscopy of single and double hypernuclei will be performed. Therefore, a secondary nuclear target made from beryllium, boron or carbon must be used. The production of hypernuclei is then a two-step process: First, a hyperon-antihyperon pair must be created. In the following, one of the hyperons must be stopped in the secondary target where it can be captured by a target nucleus to form a hypernucleus. The hypernucleus can be detected by γ-rays from bound nuclear levels within the nuclear potential. The such measured level scheme of single and double hypernuclei provides information about the hyperon-nucleon and the hyperon-hyperon interaction and give access to the spin-dependent part of the nuclear potential. More details about the program can be found e.g. in [60].

2.2 Experimental conditions

The $\bar{P}$ANDA experiment will be located at the **H**igh **E**nergy **S**torage **R**ing (HESR) [61] of the FAIR facility. The following subsection summarize the experimental conditions which $\bar{P}$ANDA will meet during operation. They are intimately connected with the delivered antiproton beams. An outline of the overall antiproton chain of the FAIR facility is given in the introductory subsection 2.2.1. Afterwards, an overview of the HESR design is given in subsection 2.2.2, which also includes a short description of the operation cycle. The beam dynamics and the associated cooling scenario of the HESR are explicitly discussed in subsection 2.2.3. In the last subsection 2.2.4 special emphasis is given to the expected luminosity for the $\bar{P}$ANDA experiment. A detailed description is very important both for the detector development and the future physics performance.

2.2.1 Antiproton chain at the FAIR facility

The FAIR facility will deliver high quality antiproton beams within a considerably large momentum range. They are produced in a sophisticated multi-stage process. It starts with the preparation of an adequate proton beam. Therefore, protons will be injected from the linear accelerator (LINAC) into the SIS18 synchrotron ring with a repetition rate of 5 Hz. After four cycles a transfer to the bigger synchrotron SIS100 will be carried out. In this way a stepwise acceleration from 70 MeV at the end of the LINAC, to 2 GeV in the SIS18, and finally 29 GeV in the SIS100 can be obtained. Furthermore, up to 2×10^{13} protons can be accumulated. They will be compressed into a single short bunch of less than 50 ns length, which then can be directed from the SIS100 onto the exterior antiproton production target. The proton acceleration cycle will be repeated every ten seconds; a further upgrade to five seconds is considered.

For the production of antiprotons a nickel target with a length of 60 mm is foreseen. The proposed working mode with proton bunches is introduced in order to minimize heating effects. A magnetic separator will be placed behind the production target. Antiprotons within the momentum acceptance will be accumulated in a collector ring (CR). The final number of antiprotons in the accepted phase space volume is expected to be in the order of 10^8 per bunch and result in an average production rate of ten to twenty million antiprotons per second. Limiting factors for the antiproton production are the proton intensity delivered by the SIS 100, the target conversion efficiency and the time needed for pre-cooling of the accumulated antiprotons in the CR, which is applied to decrease their momentum spread. After the pre-cooling, antiprotons will be distributed to the different experiments. In the final stage an additional storage ring (RESR) for high luminosity experiments will be implemented allowing the accumulation of up to 10^{11} antiprotons moderately compressed in one single bunch.

Basically there are two main applications for antiprotons at FAIR: experiments with low energetic antiprotons at FLAIR (for details see [62]) and the study of high energetic antiproton collisions at $\bar{P}$ANDA. The appropriate storage rings for these experiments are the HESR and the NESR for the high and low momentum domain, respectively. A detailed discussion of the HESR hosting the $\bar{P}$ANDA experiment can be found in the next subsection. An illustration of the main components for the antiproton program at FAIR is given in figure 2.3.

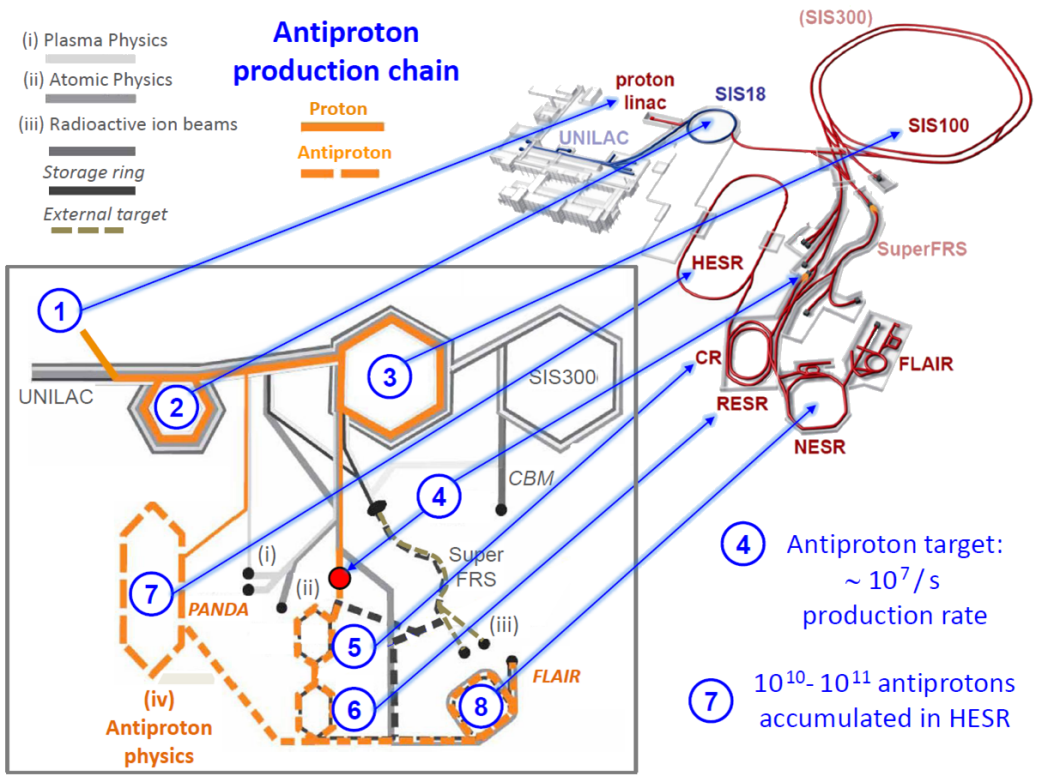

Figure 2.3: Schematics of the antiproton chain at FAIR indicated in orange (*bottom left*) and its allocation at the facility (*top right*). The physics program for antiprotons is performed by $\bar{\text{P}}$ANDA and FLAIR. (Picture adapted from [48].)

2.2.2 The High Energy Storage Ring (HESR)

The HESR is designed to supply the $\bar{\text{P}}$ANDA experiment with high quality antiproton beams in a broad momentum range from 1.5 GeV/c to 15 GeV/c. Pre-cooled antiprotons are injected with a momentum of 3.8 GeV/c. The HESR then serves as a slow synchrotron to obtain the desired beam energy and afterwards as a storage ring for internal target experiments. A special combination of phase-space cooled beams and dense targets allows an operation in two different working modes: the high-luminosity (HL) mode with beam intensities of up to 10^{11} antiprotons over the full momentum range and a momentum accuracy $\Delta p/p$ of approximately 10^{-4} and the high resolution (HR) mode with a momentum spread of a few times 10^{-5} defined in a momentum range between 1.5 GeV/c and 8.9 GeV/c at a slightly lower beam intensity.

The HESR lattice is designed as a racetrack shaped ring made out of two 180° arcs and two 155 m long straight sections with a total circumference of 575 m [63]. A schematic picture is given in figure 2.4. The magnet arrangement in the arc sections will allow a flexible beam adjustment. In the straight section opposite to the injection point, an electron cooler is foreseen. The $\bar{\text{P}}$ANDA experiment with the internal target is placed at the other side. Two dipole chicanes embed the $\bar{\text{P}}$ANDA detector in order to compensate for

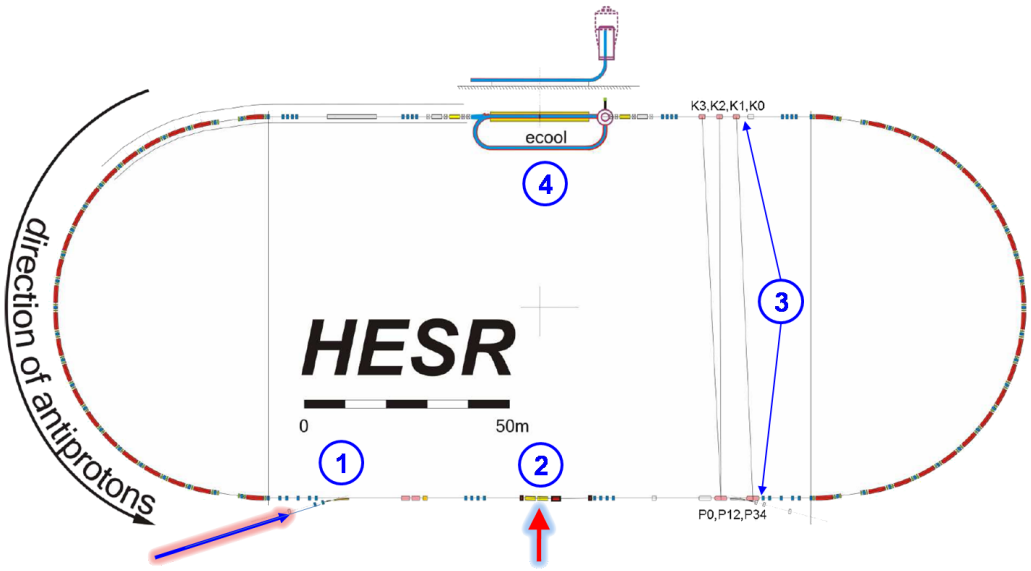

Figure 2.4: Schematic view of the HESR ring [61] with: 1 - Injection point, 2 - PANDA experiment, 3 - Stochastic cooling, 4 – Electron cooler. The antiprotons are injected from the lower left (indicated by the blue arrow). In addition the position of the internal target for the PANDA experiment is marked (red arrow). The stochastic cooling components are pickups (P0-4) and kickers (K0-3) placed at the lower and upper straight section, respectively.

the magnets used therein (for details see section 2.3). Due to the asymmetric placement of the chicanes, the beam axis in the experiment is slightly tilted with respect to the straight axis. Other components within the straight PANDA section are beam injection kickers, septa and RF cavities. They allow for a compensation of energy losses due to the beam-target interaction, a bunch rotation and the decelerating or accelerating of the beam, respectively. Stochastic cooling is implemented via four kickers and opposing pick-ups on either side of the straight sections.

The overall operation cycle of the HESR can be separated into two main sequences. They are related to the beam preparation and the data taking time, respectively. A schematic illustration of all subsequent processes is given in figure 2.5. The initial point of the operation cycle is defined by the injection phase. It must be adjusted to the previous stage of the accelerator complex. Working with the RESR, the desired number of antiprotons is already accumulated in a moderately compressed bunch. They can be then injected into the HESR with a resulting bunch length of less than 200 m. In this setup maximum beam intensities can be achieved, which are necessary to work in the high luminosity mode. However, the RESR will be installed only in the second stage of the FAIR installation and thus at the beginning the HESR will be used for accumulation instead. Therefore, bunches of up to 10^8 antiprotons are transferred subsequently from the production target to the CR and then directly to the HESR. The final number of antiprotons in the HESR is obtained in a multi-stacking process. It is limited by the needed time for a pre-cooling in the CR, which corresponds to the antiproton cycle of 10 s. Hence, a maximum number of 10^{10}

instead of 10^{11} antiprotons is achievable after a defined upper limit of 1000 s corresponding to 100 cycles.

After the injection of antiprotons, a pre-cooling is performed in order to obtain beam equilibrium. In the next step, the beam is decelerated or accelerated to the desired momentum. During this time different test measurements with the $\bar{\text{P}}$ANDA detector can be carried out, e.g. a pulser calibration or noise and signal quality analysis for individual subdetectors. The beam preparation is completed by a fine-tuned focussing in the target region as well as the section for the electron cooler. Excluding an additional accumulation inside the HESR, typical preparation times range from 120 s at 1.5 GeV/c to 290 s at 15 GeV/c beam momentum [61]. Once running at the specified momentum, an appropriate beam cooling is started and the target can be switched on. During the experimental time the beam intensity decreases due to the beam-target interaction, which is correlated with a limited beam lifetime. As a consequence, the target and the beam cooling are switched

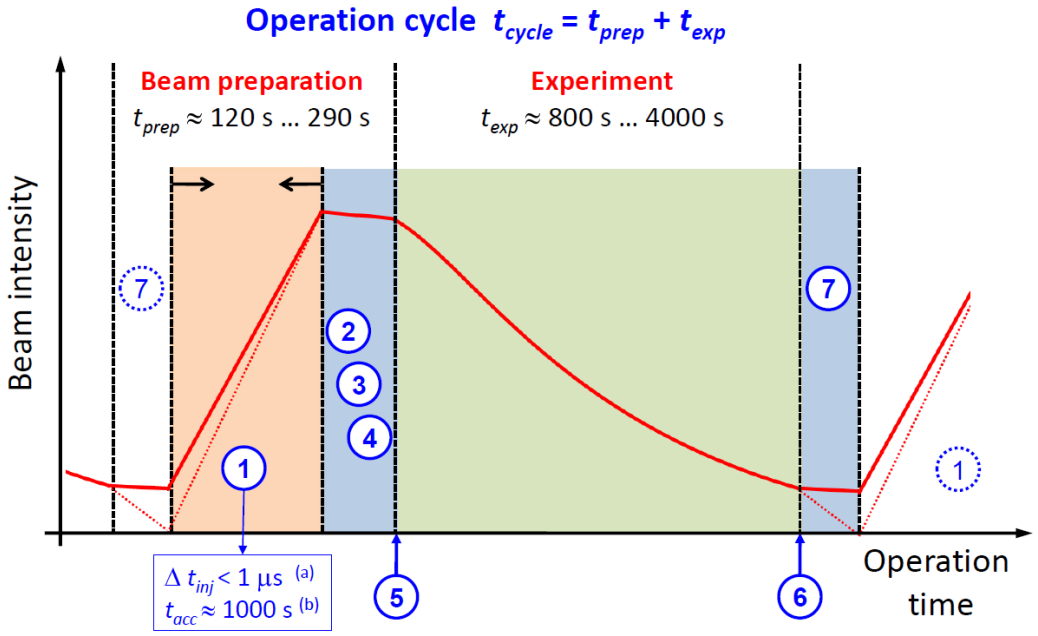

Figure 2.5: Schematic diagram of the beam intensity during operation illustrating the different steps of the operation cycle: 1 - Injection; 2 - Pre-cooling; 3 - Acceleration/Deceleration; 4 - Beam steering and squeezing; 5 and 6 - Cooling and target switch-on and switch off, respectively; 7 - Recycling or beam dumping. The accumulation time for antiprotons in the HESR, t_{acc}, is only required during the first stage of the experiment without the RESR (b). The beam injection time, t_{inj}, is small compared to the overall beam preparation time t_{prep}. Thus, working with the RESR (a) the overall cycle time, t_{cycle}, is reduced and thus increases the percentage of the experimental time t_{exp}. Given values refer to upper and lower limits of the different setups. The dotted line indicates a dumping of all remaining antiprotons after the target switch-off.

off after a certain time and the ring is refilled with new antiprotons. Working in the high luminosity mode, all remaining antiprotons will be re-used in the new cycle. This requires a dedicated concept of bunch manipulations by the RF cavities during refilling.

2.2.3 Beam dynamics and cooling scenario

An accurate adjustment of the beam parameters is essential for the physics studies of $\bar{P}$ANDA. Precise positioning of all components inside the HESR is a prerequisite. Smaller distortions can be accommodated by closed orbit corrections [65]. The quality of the experiment is driven by the beam dynamics. Therefore, associated heating effects must be counter-balanced by powerful cooling mechanisms in order to warrant a stable operation with the specified design parameters. A detailed discussion for the HESR can be found in literature [61, 64, 66, 67].

Basically, transverse and longitudinal cooling is foreseen in the HESR in order to compensate a transverse beam blow up and to achieve a low momentum spread, respectively. Two different cooling systems will be applied in the HESR, namely stochastic cooling and electron cooling. While the first system is favourable for the HR mode, the second one is intended to be used for the HL mode [68]. More details about the basic concepts and the experimental status of both cooling mechanisms can be found in the given references [69, 70, 71, 72]. Further improvements may be achieved by a combination of electron and stochastic cooling.

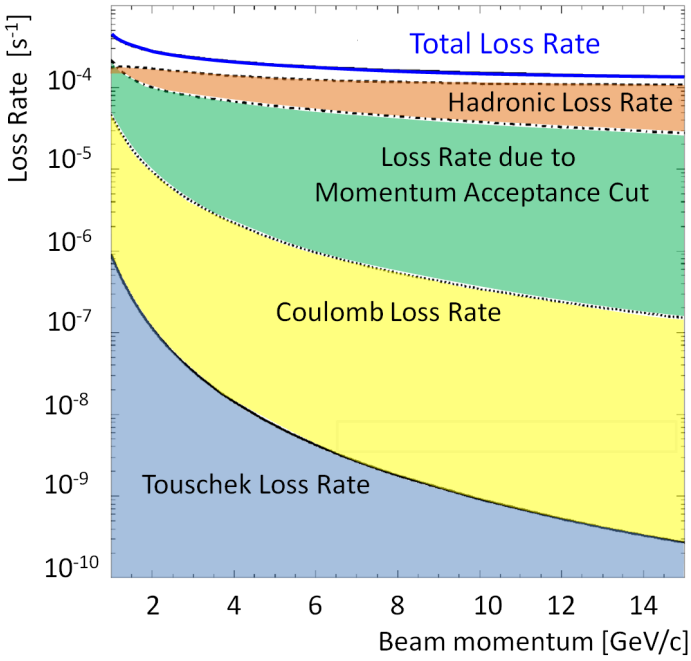

Figure 2.6: Contributions of individual loss rates to the total beam loss rate within the beam momentum range of $\bar{P}$ANDA. Results are taken from [64]. Calculations are based on a standard mode operation with a beam emmitance of 1 mm·mrad and an acceptance cut of 10^{-3}.

Main heating sources are given by intra-beam scattering and beam-target interactions. Both define the momentum spread of the circulating antiprotons. Particles with higher momentum deviations get lost if they exceed the acceptance range of 10^{-3} defined for the HESR. Beam losses are dominated by hadronic interactions between antiprotons and target protons, single large-angle Coulomb scattering in the target and energy straggling induced by Coulomb interactions of the antiprotons with target electrons. Additional contributions arise from single intra-beam scattering, which is mostly connected to large-angle scattering of two particles within the beam (Touschek effect). Main contributions of all effects to the total loss rate are illustrated in figure 2.6. Resulting beam lifetimes for the HESR range between 1540 s and 7100 s. They are defined by the time, after which the initial beam intensity is reduced by a factor of $1/e = 0.37$. Simulation results on the achievable RMS on the momentum spread for the HR mode deliver values of $\Delta p/p = 7.9 \times 10^{-6}$, $\Delta p/p = 2.7 \times 10^{-5}$ and $\Delta p/p = 1.2 \times 10^{-4}$ at a beam momentum of 1.5 GeV/c, 8.9 GeV/c and 15 GeV/c, respectively [73, 74].

2.2.4 Luminosity considerations for the $\bar{\text{P}}$ANDA experiment

The luminosity L describes the flux of beam particles convolved with the target opacity. Multiplied with the total hadronic cross section $\sigma_{p\bar{p}}$ it defines the interaction rate R, i.e. the number of antiproton-proton interactions per second at a given time interval δt. The given interaction rate determines the achievable number of events for all physics channels and allows the extraction of occupancies in different detector regions. These are needed as input for the associated hardware development.

To yield a high luminosity in the experiment, the delivery of an intense beam, a highly effective target thickness and an optimized beam-target overlap are essential. The specified design value for the maximum luminosity at $\bar{\text{P}}$ANDA is $2 \times 10^{32}\,\text{s}^{-1}\text{cm}^{-2}$, which translates into a maximum interaction rate of $2 \times 10^{7}\,\text{s}^{-1}$ corresponding to the average antiproton production rate envisaged. While these upper limits apply for the HL mode, values for the HR mode are decreased by one order of magnitude because of the reduced beam intensity.

Obviously, the luminosity is directly linked with the number of available antiprotons in the HESR. They are injected into the ring at discrete time intervals which are defined by the operation cycle (see figure 2.5). The maximum luminosity is obtained directly after the target is switched on because at this instant the number of antiprotons, $N_{\bar{p},0}$, available for the experiment has reached the maximum. During the time of data taking, t_{exp}, the luminosity decreases according to the total loss rate of the beam, which was discussed in the previous subsection 2.2.3. Therefore, the average cycle luminosity, $\bar{L}$, is defined. It takes into account both the time dependency of the luminosity during data taking as well as the beam preparation time, t_{prep}, needed to inject or accumulate $N_{\bar{p},0}$. An illustration is given in figure 2.7, left side. Assuming a dumping of the remaining antiprotons after each cycle, $\bar{L}$ reads as:

$$\bar{L} = N_{\bar{p},0} \cdot f_0 \cdot n_{\text{eff}} \cdot \frac{\tau \left[1 - e^{-\frac{t_{\text{exp}}}{\tau}}\right]}{t_{\text{exp}} + t_{\text{prep}}} \tag{2.1}$$

where f_0 is the revolution frequency of the antiprotons in the ring, n_{eff} is the effective target thickness defined as an area density given in atoms per square centimetre and τ

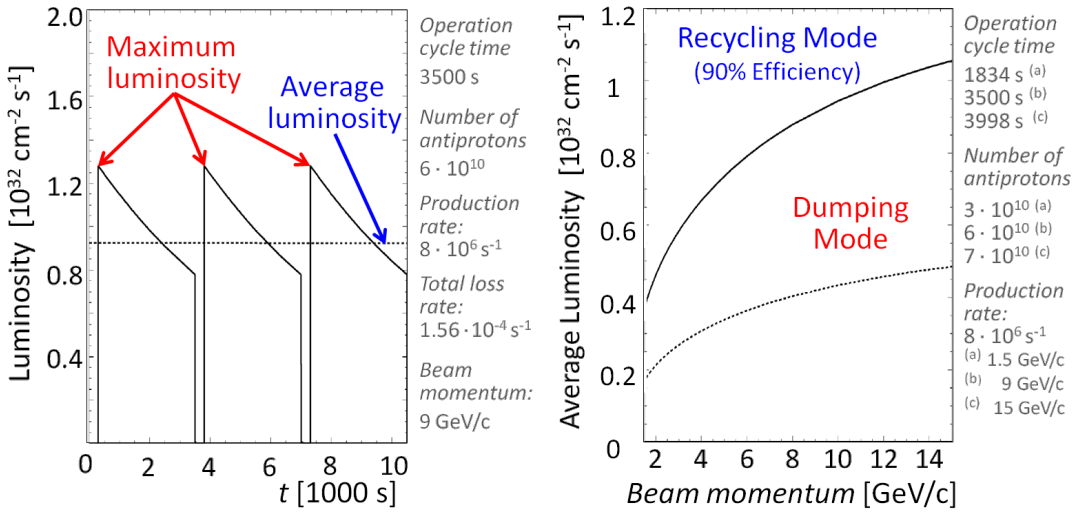

Figure 2.7: Results from luminosity studies for $\bar{P}$ANDA using a hydrogen target with an effective thickness of $4{\cdot}10^5$ atoms/cm^2 [64]. *Left*: Time dependent luminosity profile obtained with the recycling mode. *Right*: Average luminosity for the recycling (solid line) and the dumping mode (dashed line) within the momentum range of $\bar{P}$ANDA. Corresponding input parameters are given at the right of each diagram. The chosen cycle time corresponds to a stop of data taking after one half of the $1/e$ beam lifetime.

corresponds to the mean beam lifetime. Assuming 10^{11} antiprotons in the ring, a value of $n_{\text{eff}} = 4 \times 10^{15}\,\text{atoms} \cdot \text{cm}^{-2}$ is required for a hydrogen target in order to achieve the design goal of $\bar{P}$ANDA .

The average luminosity can be increased if the residual antiprotons after each cycle are transferred back to the injection momentum and then merged with the newly injected particles. The difference between the dumping and the recycling mode can be seen in figure 2.7, right side. Moreover, the cycle time, t_{cycle}, must be chosen carefully in order to achieve a preferably high average luminosity. A reasonable choice to stop data taking is given after one half of the mean beam lifetime, i.e. $t_{\text{cycle}} = t_{\text{prep}} + 0.5 \cdot \tau$. In this case the luminosity ratio between stop and start of each data taking period is equal to $1 \,/\, \sqrt{e} = 0.61$.

Figure 2.8 shows the achievable average luminosity in dependence of the cycle time according to specific parameters of the $\bar{P}$ANDA experiment. Theoretical limits, $L_{\text{max,th}}$, assuming no beam losses and a continuous source of antiprotons, are given at the top. They result from the ratio of the antiproton production rate, $\dot{N}_{\bar{p}}$, to the total hadronic cross section $\sigma_{p\bar{p}}$.

Including all beam losses and without any restrictions on the maximum numbers of antiprotons in the ring, the achievable average luminosity reaches a plateau, which levels at a value smaller than $L_{\text{max,th}}$. Further limitations are related to the restricted maximum number of 10^{11} antiprotons in the HESR. With this value, the achievable average luminosity at highest beam momentum peaks at $1.6 \times 10^{32}\,\text{s}^{-1}\text{cm}^{-2}$ and a corresponding cycle time shorter than the mean beam lifetime. At lower beam momenta, the beam lifetimes

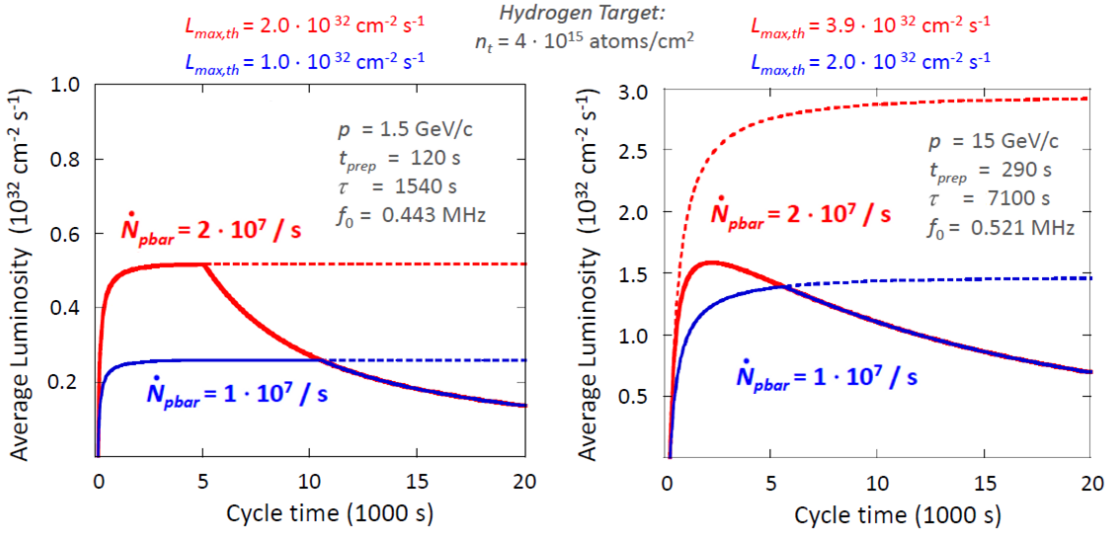

Figure 2.8: Achievable average luminosity vs. cycle time for antiproton-proton collisions at minimum (*left*) and maximum (*right*) beam momentum [61]. Results are shown for two different production rates $\dot{N}_{\text{pbar}}$ assuming a maximum number of 10^{11} antiprotons (solid lines) and an unlimited maximum number (dashed lines). Theoretical upper limits are given above each of the diagrams (details see text). Listed parameters are the effective target density, n_t, beam preparation times, t_{prep}, beam lifetimes, τ, and revolution frequencies f_0.

further decrease. If they fall short of 5000 s, the given antiproton production rates do not compensate the beam losses and thus the required number of 10^{11} antiprotons is not reached. As a consequence, the average luminosity drops below the envisaged design value at around 2.4 GeV/c to finally roughly $0.5 \times 10^{32}\,\text{s}^{-1}\text{cm}^{-2}$ at 1.5 GeV/c.

Besides the cycle-averaged luminosity an evaluation of peak values for the luminosity during the data taking is indispensable for performance studies of the $\bar{\text{P}}$ANDA detector. Both refer to the integrated data load and the maximum data rates to be handled by different subsystems, respectively. Assuming no beam losses during the beam preparation, the peak luminosity in the experiment is equivalent to the maximum cycle-averaged luminosity obtained with an unlimited maximum number of particles inside the HESR (see figure 2.8).

For an estimate of peak count rates on detector level, possible variations of the effective target thickness on a microscopic timescale have to be taken into account. Even though in all cases a constant effective target thickness is aspired, the achievable quality depends on the chosen target type. The most critical setup is given by a pellet target, which is one of the options foreseen for $\bar{\text{P}}$ANDA (details in subsection 2.3.3). In this application there are several variables, which potentially have noticeable impact on the homogeneity of the target density. Deviations from the time-averaged density are caused by variations of the pellet size, the pellet trajectory and the interspacing between consecutive pellets. The latter is of utter importance for maximum values of the peak luminosity due to the possible presence of more than one pellet in the beam at the same instant. First studies on the expected fluctuations for the pellet target for $\bar{\text{P}}$ANDA have been performed. Assuming

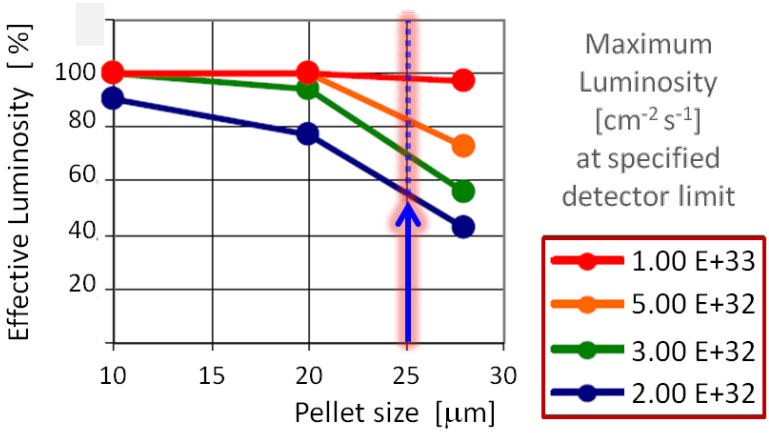

Figure 2.9: Simulation study of luminosity fluctuations with a pellet target in the HL mode of $\bar{P}$ANDA [75]. If the peak luminosity exceeds the given detector limit, the effective luminosity drops below 100%, i.e. there is a loss of data due to the defined detector limits on the maximum count rates.

a pellet size of 25 µm, the maximum peak luminosity is expected to be in the order of $10^{33}\,\mathrm{s}^{-1}\mathrm{cm}^{-2}$ thus exceeding the defined design luminosity by a factor of five [75].

So far, all results on the luminosity were explicitly given for an internal hydrogen target. Necessary modifications for nuclear targets rely on the total hadronic cross section, $\sigma_{\bar{p}A}$, for the interaction of antiprotons with target nucleons. In a first approach it can be estimated from geometric considerations taking into account the radius of a spherical nucleus, R_A,

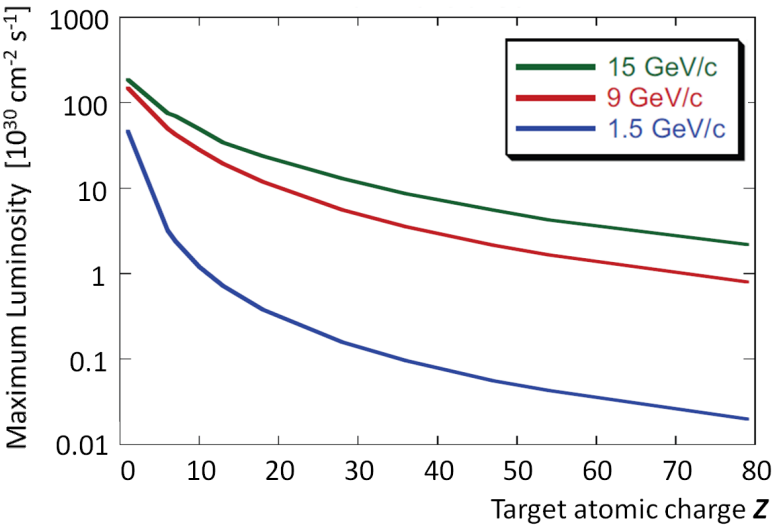

Figure 2.10: Maximum average luminosity vs. atomic charge, Z, of the target for three different beam momenta (taken from [5]).

Target material	$\bar{L}_{\text{eff}}$ (p_{beam}=1.5 GeV/c) [$\text{cm}^{-2}\text{s}^{-1}$]	$\bar{L}_{\text{eff}}$ (p_{beam}=15 GeV/c) [$\text{cm}^{-2}\text{s}^{-1}$]	n_{eff} [atoms / cm^2]
deuterium	5×10^{31}	1.9×10^{32}	3.6×10^{15}
argon	4×10^{29}	2.4×10^{31}	4.6×10^{14}
gold	4×10^{28}	2.2×10^{30}	4.1×10^{13}

Table 2.1: Expected average luminosities, $\bar{L}_{\text{eff}}$, and required effective target thickness, n_{eff}, for heavier nuclear targets at PANDA at minimum and maximum beam momentum p_{beam}. Given numbers refer to an assumed number of 10^{11} antiprotons in the HESR.

and the proton radius of $r_p = 0.9\,\text{fm}$. The radius of a spherical nucleus can be roughly approximated as $R_A = r_0 A^{1/3}$, with $r_0 = 1.2\,\text{fm}$ and the mass number A. With the given total hadronic cross section for antiproton-proton collisions, $\sigma_{\bar{p}p}$, and the assumption that $\sigma_{\bar{p}p} := \pi r_p^2$, the required total hadronic cross section, $\sigma_{\bar{p}A}$, for a nucleus of mass number A can be deduced as follows:

$$\sigma_{\bar{p}N} = \sigma_{\bar{p}p} \cdot \left(\frac{R_A}{r_p} + 1 \right)^2 = \pi (R_A + r_p)^2 \tag{2.2}$$

The total hadronic cross section, $\sigma_{\bar{p}p}$, decreases with higher beam momentum from approximately 100 mb at 1.5 GeV/c to 50 mb at 15 GeV/c. Simulation results on maximum average luminosities based on equation 2.2 are shown in figure 2.10. They include adapted beam losses in the target due to single Coulomb scattering and energy straggling. Compared to antiproton-proton experiments, the maximum average luminosity for nuclear targets decreases rapidly with both, higher atomic charge Z and lower beam momenta, by up to three orders of magnitude. Specific values for selected nuclear targets are given in table 2.1 with the effective target thickness required to reach these numbers.

2.3 Detector setup

To cover the broad physics program, the PANDA apparatus serves as a multi-purpose detector. The experiment uses a fixed target, which results in a forward boost of emitted particles in the laboratory frame after the beam-target interaction. Therefore, PANDA employs a target spectrometer surrounding the interaction point (IP) and a forward spectrometer covering small angle tracks. For the momentum analysis of charged particles a solenoid and a dipole magnet are used in the central and the forward part, respectively.

A sketch of the PANDA apparatus is shown in figure 2.11 where the main components are labelled. Individual sub-systems are implemented inside the solenoid and along the beam axis before, inside and behind the dipole magnet in order to perform tracking, particle identification and calorimetry. They will be briefly discussed in subsection 2.3.1 and 2.3.2, respectively. The different target systems intended to be used in PANDA are discussed in more detail in subsection 2.3.3. The last subsection 2.3.4 is dedicated to the overall detection concept of PANDA.

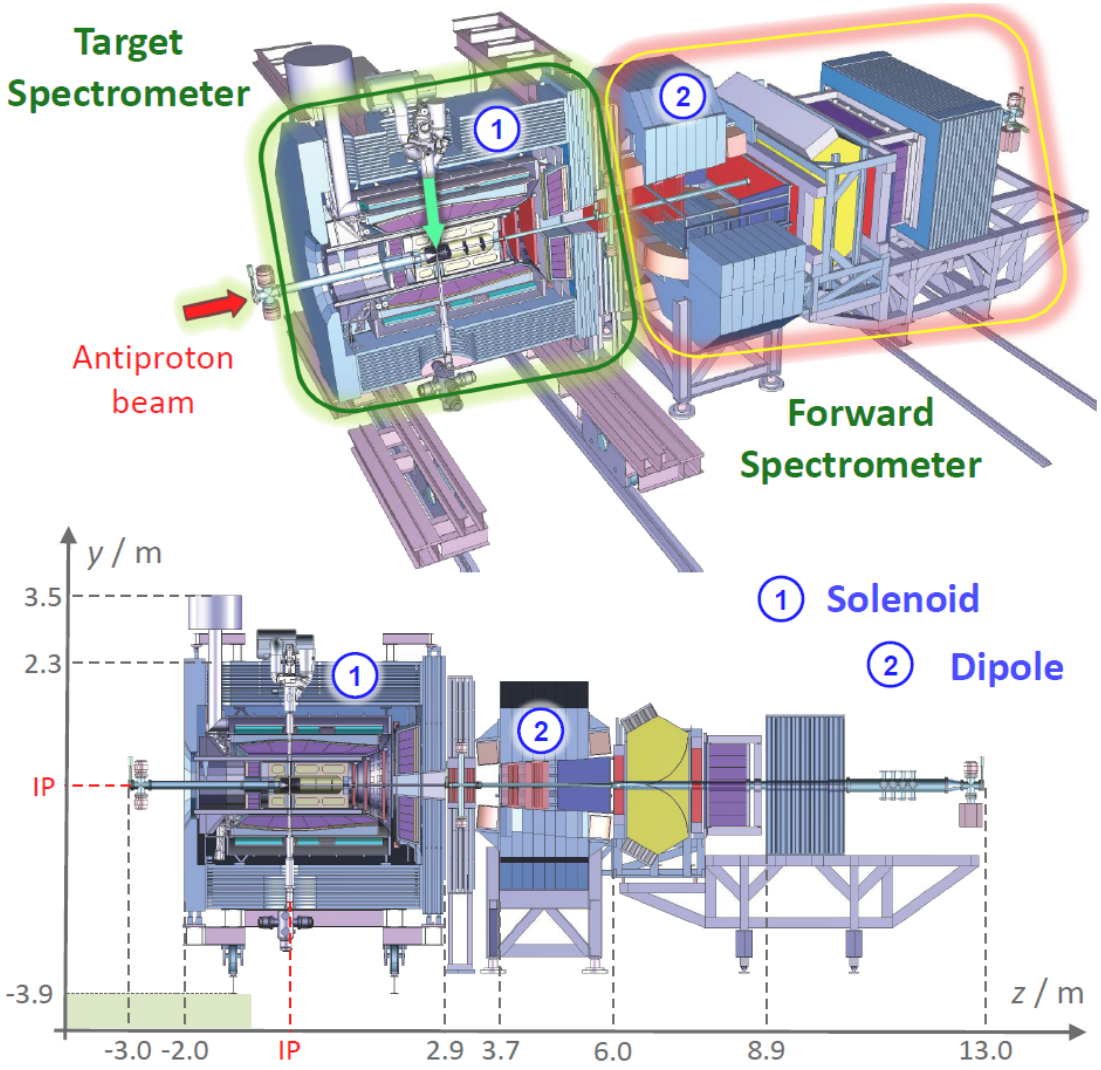

Figure 2.11: Main setup of the $\bar{P}$ANDA detector (*top*). The target material is introduced from top (indicated by a green arrow). A side view with the overall detector dimensions is shown at bottom. Given measures refer to the interaction point (IP).

2.3.1 Target spectrometer

The target spectrometer is designed in an onion-shell-like configuration around the interaction point similar to the layout of collider detectors. The beam is guided through a narrow and thin pipe, which intersects with a vertical pipe needed for the injection of the target material. The target pipe crosses the entire spectrometer from top to bottom and thus breaks rotational symmetry around the beam axis. As a consequence, the target spectrometer will be left-right separated along the middle plane.

The subdetector systems are inside the warm bore of a superconducting solenoid mag-

net. They are arranged in barrel layers which cover polar angles between 22° and 140°. In forward directions the detectors form endcap structures which extend the small-angle acceptance of the target spectrometer down to 5° and 10° in vertical and horizontal direction with respect to the beam pipe, respectively. An additionally planned calorimeter in the backward hemisphere would eventually provide information on backscattered particles at large polar angles between 145° and 170°. The main components of the target spectrometer will be briefly discussed in the following. An illustration can be found in figure 2.12 on page 52.

→ Magnet system and muon chambers

The superconducting magnet has an external iron return yoke and will provide a very homogenous solenoid field of 2 T with fluctuations of less than ±2%. The solenoid coil has a length of 2.8 m and an inner diameter of 90 cm. The load of the integrated inner subsystems can be picked up at defined fixation points. The flux return yoke is laminated and hence acts as a range system for the detection of muons and their discrimination against pions. For the absorption in the forward endcap an increased amount of material is needed. Therefore, the muon system will be extended by removable muon filters which are placed in between the solenoid and the dipole magnet. Within the absorber layers rectangular aluminium Mini Drift Tubes (MDT) are foreseen. They are similar to the ones applied in the COMPASS muon detection system [76]. Two bores of 100 mm diameter positioned above and below the interaction point allow the insertion of internal targets. A precise description of the magnet and the integrated muon system as well as detailed field strength calculations can be found in the technical design report for the magnet system [77].

→ Beam-Target system

The beam-target system consists of the apparatus for the target production and the corresponding vacuum system for the interaction region. The beam and target pipe cross sections inside the target spectrometer are decreased to an inner diameter of 20 mm close to the interaction region. A beam-target cross is currently foreseen for intersection of the target cross section with the beam pipe. The innermost parts are planned to be made of beryllium, titanium or a suited alloy which can be thinned to wall thicknesses of 200 µm. Due to the limited space and the constraints on the material budget close to the IP, vacuum pumps along the beam pipe can only be placed outside the target spectrometer. Insections are foreseen in the iron yoke which allow the integration of either a pellet or a cluster-jet target. The target material will be injected from the top. The dumping of all target residuals after beam crossing is mandatory to prevent backscattering into the interaction region, which would increase the residual gas concentration and dramatically worsen the overall performance of the experiment. The entire vacuum system is kept variable and allows an operation of both target types. Moreover, an adaptation to non-gaseous nuclear wire targets is possible. More details on the different target options are discussed in subsection 2.3.3.

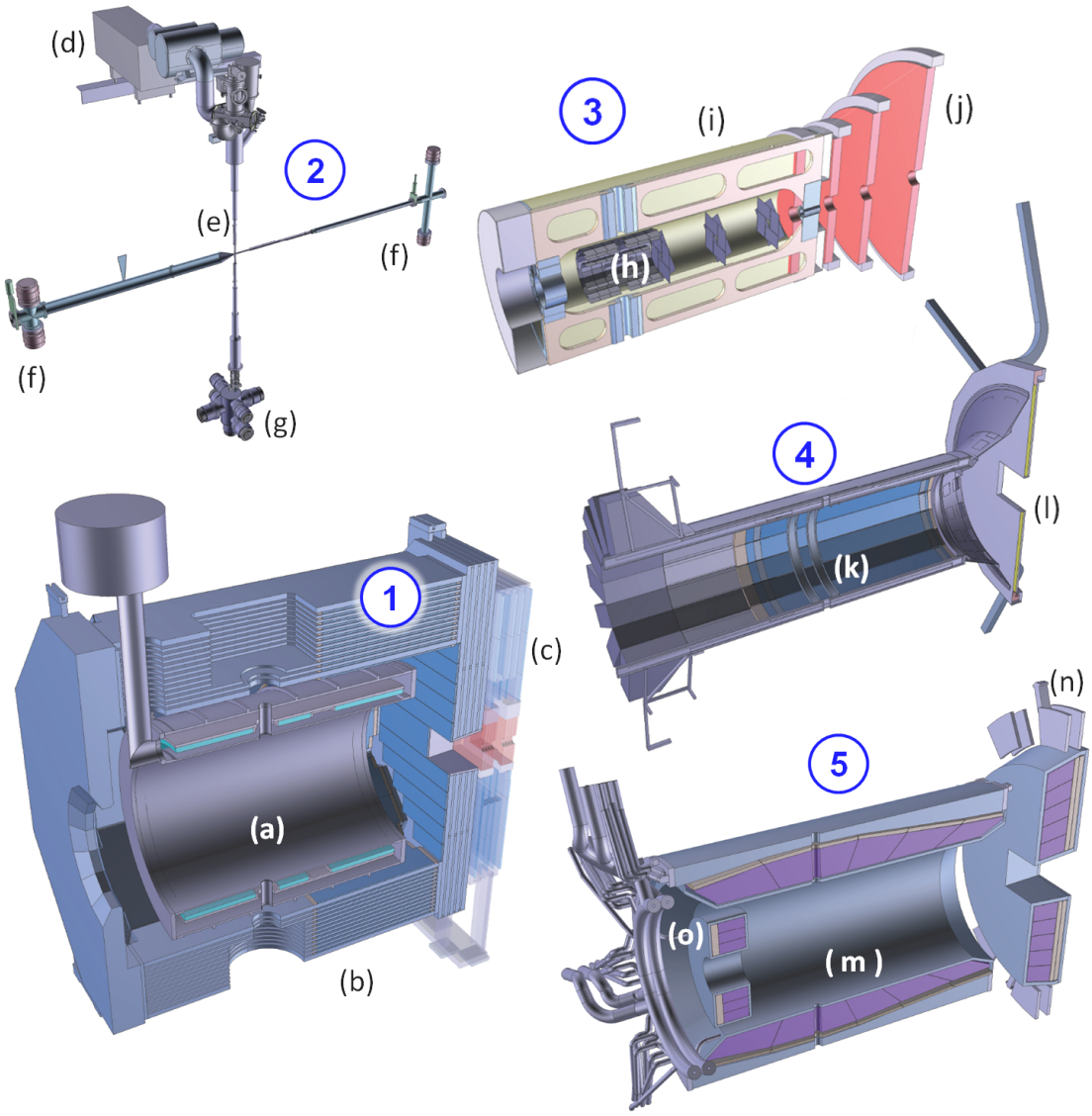

Figure 2.12: Main components of the target spectrometer: 1 - Solenoid magnet and muon system with (a) the cryostat, (b) the iron yoke instrumented with muon chambers and (c) removable muon filters in forward direction; 2 - Beam-target system with (d) target apparatus, (e) interaction point, (f) vacuum pumps along the beam pipe and (g) dumping system; 3 - Tracking system with (h) inner tracker (MVD), (i) outer tracker and (j) forward GEM stations; 4 – Cherenkov detectors and TOF system with (k) barrel DIRC and TOF system and (l) disk DIRC; 5 - Electromagnetic calorimeter with (m) barrel part, (n) forward endcap and (o) an additional backward endcap. The components 2 to 5 are integrated subsequently into the solenoid magnet from the inside to the outside. (For a better illustration, given detector parts are scaled slightly different.)

→ Tracking system

The tracking system of the target spectrometer consists of three main parts: the inner micro - vertex detector (MVD), the outer tracker following subsequently at higher radii and tracking stations in forward direction. The MVD will be equipped with fast silicon detectors and is restricted to a maximum outer radius of 150 mm. A detailed description is given in chapter 3 explicitly. The adjacent outer tracking detector will have a total length of 1.5 m and a maximum outer radius of 50 cm. An individual support frame for both trackers will allow the insertion into the target spectrometer. Currently two solutions for the outer tracker are under investigation: a straw tube tracker (STT) or a technically more challenging but advantageous time-projection chamber (TPC).

The STT will consist of self-supporting aluminium Mylar tubes. They will be filled with a gas mixture and operated at a pressure of 2 bar, i.e. a stabilizing overpressure of 1 bar. Each straw tube is constructed with a single anode wire in the centre. A limitation of the gas gain to 10^5 is foreseen to warrant long term stability. Finally, in the current design [78] there are 4636 straws, which are arranged in a hexagonal shape around the MVD. There are four stereo double-layers with a skew angle of 2.89° for 3D reconstrunction.

The planned TPC consists of two large gas-filled half-cylinders. Due to the applied electrical field, electrons created by ionizing particles drift along the beam axis. The anode is positioned at the upstream end and segmented by a pad readout plane thus delivering 2D information. The signal amplification will be based on gas electron multiplier (GEM) foils. The third coordinate of the track is extracted from the measurement of the drift time for each electron cluster.

Due to the geometry of the outer tracker, polar angles below 22° are not fully covered. Therefore, three stations equipped with gaseous micro-pattern detectors based on GEM foils as amplification stage are placed at upstream positions at 1.1 m, 1.4 m and 1.9 m with respect to the IP. These detectors have a sufficiently high rate capability to cope with the enhanced particle flux in the forward detector region. Current design studies are underway, which evaluate the option of a fourth GEM station inserted closer to the IP while shortening the outer tracker by 30 cm.

General comments on the tracking components and a comparison between different options are compiled in subsection 2.3.4 on page 58. Experimental and simulation results for the STT are given in [79] and [80], respectively. The current status of the $\bar{\text{P}}$ANDA TPC project is reviewed in [81] and [82]. More details about the performance of GEM tracking stations in similar applications at the COMPASS experiment can be found in [83] and [84].

→ Cherenkov detectors and time-of-flight system (TOF)

A TOF system and Cherenkov detectors are foreseen as subsequent detectors following the inner trackers. They cover polar angles between 22° and 140°. Due to the short flight path in the target spectrometer, all TOF detectors must have a very good time resolution between 50 ps and 100 ps. An additional start detector close to the IP is disfavoured because it would considerably deteriorate the performance of the electromagnetic calorimeter. As a consequence, only relative timing of a minimum of two particles can be used. However, the TOF information can be used as a reference for the readout of the adjacent Cherenkov detectors. Possible candidates for the TOF system are scintillator bars or pads of multi-

gap resistive plate chambers, which are cylindrically arranged around the outer tracker at radial distances between 42 cm and 45 cm with respect to the beam axis.

Cherenkov detectors are used to determine the velocity of fast particles. A short explanation of the underlying effect will be given in subsection 2.3.4. Measurements in the target spectrometer will be performed in the barrel part and in the forward end-cap based on the detection of internally reflected Cherenkov (DIRC) light. The overall concept is similar to the one used for the BaBar detector [85], which is based on fused silica as radiator material. In the barrel part, quartz slabs will be arranged at a radius of 45 cm to 54 cm. In the forward part a disk shape of the radiator is used which has an outer radius of 110 mm. More details of the barrel and disk DIRC can be found in [86, 87] and [88, 89], respectively.

→ Electromagnet calorimeter

The electromagnetic calorimeter (EMC) consists of a barrel part and a forward endcap. In addition a backward endcap is under study. Lead tungstate ($PbWO_4$) is chosen as scintillator material. It is a high density inorganic scintillator with a short radiation length, short decay times of less than 10 ns and sufficient radiation hardness. The crystals will have a length of 20 cm corresponding to approximately 22 radiation lengths and allowing a compact design. There are 11,360 crystals in the barrel part and 3600 crystals in the forward end-cap. Roughly 600 crystals are foreseen for the backward end-cap. An increase of the light yield will be achieved by cooling the EMC and the readout electronics down to −25 °C. A detailed description of the EMC can be found in the technical design report [90].

2.3.2 Instrumentation of the forward part

In the forward part of the $\bar{P}$ANDA apparatus a dipole magnet is used for the determination of the momentum of charged particles. Detectors will be arranged consecutively along the beam pipe. A schematic side view is depicted in figure 2.12. With this set-up it is possible to cover about half of the acceptance gap left in the target spectrometer and perform an explicit analysis of the extremely forward going particles. All main components are shortly described in the following.

→ Dipole magnet

The dipole magnet will be positioned about 4 m downstream of the target and has an aperture of more than 2 m. The bending power of 2 Tm causes a deflection of 2.2° for antiprotons with the maximum momentum of 15 GeV/c. The dipole will cover a rectangular solid angle of ±5° in vertical and ±10° in horizontal direction, respectively. The design of the magnet features a high dynamic range for charged particles. Slow particles can be detected due to an instrumentation of the yoke surrounding the magnet. More specifications are given in [77].

→ Forward tracking system

Three pairs of tracking detector layers are foreseen to measure the deflection of charged particles in the field of the dipole magnet. They will be positioned in front of, within and

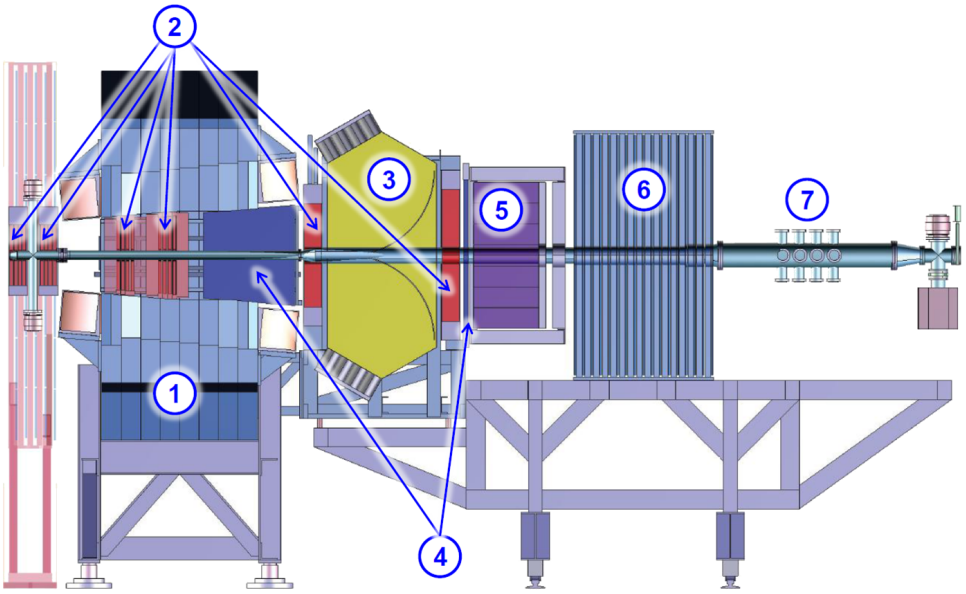

Figure 2.13: Side view of the forward spectrometer setup with its main components: 1- Dipole magnet; 2- Forward tracking system with the two foremost stations integrated inside the muon filter; 3- RICH detector; 4- TOF system; 5- Electromagnetic calorimeter; 6- Forward muon detector. In addition, a luminosity monitor (7) is located at the most upstream position in $\bar{\text{P}}$ANDA.

behind the magnet. Each of the stations is intended to be equipped with two skewed straw tube layers. In this way, a separate reconstruction of three track points can be achieved. The foremost tracking layers will be integrated into the muon filters inserted between the solenoid and the dipole magnet.

→ Cherenkov detector

A ring imaging Cherenkov detector (RICH) will be positioned behind the dipole magnet. The design is based on similar detectors used at the HERMES experiment [91]. The use of two radiator materials will yield a better separation power between different particles within the relevant momentum range of 2 GeV/c up to 15 GeV/c. The readout is foreseen to be done by photomultiplier tubes placed outside of the active volume.

→ Time-of-flight systems

The installation of a TOF wall made of plastic scintillator slabs is foreseen at about 7 m distance with respect to the IP. It will be located in between the RICH detector and the adjacent forward calorimeter. The readout at both ends of the slabs will be done by fast PMTs. For the detection of low momentum particles additional detectors of the same type are placed inside the dipole magnet opening. In this case, the readout must be probably adapted to the changed environment in the magnetic field. The achievable time resolution of the detectors is expected to be in the order of 50 ps.

→ Electromagnetic calorimeter

A Shashlyk-type calorimeter placed at a distance of 7.5 m from the IP is intended to be used as forward calorimeter. This detector type is based on lead-scintillator sandwiches read out by wavelength shifting fibres passing through the block and coupled to photomultipliers. A total number of 351 modules arranged in 13 rows and 27 columns will be needed to cover the relevant acceptance range. Experimental setups and results of similar systems at other experiments can be found e.g. in [92] or [93].

→ Muon detectors

The very forward part of the muon spectrum will be covered by a range tracking system consisting of interleaved absorber layers and rectangular aluminium drift tubes. In addition to the discrimination of hadrons, it allows the detection of pion decays and, with moderate resolution, an energy determination of outgoing nucleons. The detector system will be placed at around 9 m from the target.

→ Luminosity monitor

The luminosity monitor will be introduced at the most downstream position of the experiment to measure elastically scattered antiprotons in a range of 3 mrad to 8 mrad with respect to the beam axis. It will consist of four subsequent track planes made of silicon detectors positioned between 10 m and 12 m away from the IP. They will be placed inside a vacuum chamber in order to minimize scattering effects. The planes are separated by roughly 20 cm. A circular arrangement of four rectangular detectors around the beam axis is foreseen. An absolute precision of 3% for the luminosity determination is envisaged with the chosen detector concept.

2.3.3 Target systems

The design of the solenoid magnet allows for an implementation of different target systems. $\bar{P}$ANDA will use both gaseous and non-gaseous targets. A very precise positioning of the target is crucial for the exact definition of the primary interaction vertex. In this context, big challenges for either system result from the long distance of roughly 2 m between the target injection point and the dumping system. Hydrogen target systems will be used for the study of antiproton-proton reactions. A high target density of about 4×10^{15} hydrogen atoms per cm^2 must be achieved to fulfill the design goals of the high luminosity mode. Besides the application of hydrogen as target material, an extension to heavier gases such as deuterium, nitrogen or argon is planned for complementary studies with lighter nuclear targets.

At present, two different solutions are under development: a cluster-jet and a pellet target. Both will potentially provide sufficient target thickness but exhibit different properties concerning their effect on the beam quality and the definition of the IP. Solid targets are foreseen for hyper-nuclear studies and the study of antiproton-nucleus interaction using heavier nuclear targets. A short outline of the different target options is given in the following.

→ Cluster jet target

Cluster jet targets provide a homogeneous and adjustable target density without any time structure. Optimum beam conditions can be applied in order to achieve highest luminosity. The uncertainty of the IP in a plane perpendicular to the beam axis is defined by the optimized focus of the beam only. An inherent disadvantage of cluster-jet targets is the lateral spread of the cluster jet leading to an uncertainty in the definition of the IP along the beam axis of several millimetres.

For the target production a pressurised cooled gas is injected into vacuum through a nozzle. The ejected gas immediately condensates and forms a narrow supersonic jet of molecule clusters. The cluster size can be well adjusted by the gas pressure. In case of hydrogen, the average number of molecules per cluster varies from 10^3 to 10^6. The cluster-jets represent a highly diluted target and offer a very homogenous density profile. However, the demands of $\bar{\text{P}}$ANDA still require a density increase compared to current applications. First prototypes seem to indicate the feasibility of higher target densities reaching the specified values [94, 95]. At present a target density of 8×10^{14} hydrogen atoms per square centimetre can be achieved with a prototype using the exact $\bar{\text{P}}$ANDA geometry [96]. A further increase of the target density is part of ongoing R&D work.

→ Pellet target

Pellet targets provide a stream of frozen molecule droplets, called pellets, which drip off from a fine nozzle with fixed frequency. The use of pellet targets gives access to high effective target densities. The spatial resolution of the interaction zone can be defined with high precision. It is connected to the pellet size and can be further improved by a tracking of individual pellets. However, pellet targets suffer from a non-uniform time distribution, which results in considerable variations of the instantaneous luminosity (see also subsection 2.2.4, page 48). The maximum achievable average luminosity is very sensitive to deviations of individual pellets from the target axis. The beam must be widened in order to warrant a beam crossing of all pellets. Therefore, an optimization between the maximum pellet-beam crossing time on the one hand and the beam focusing on the other is necessary.

The design of the planned pellet target is based on the one currently used at the WASA-at-COSY experiment [97]. The specified design goals for the pellet size and the mean lateral spread of the pellet train are given by a radius of 25 µm to 40 µm and a lateral RMS deviation in the pellet train of approximately 1 mm, respectively. At present, typical variations of the interspacing of individual pellets range between 0.5 mm and 5 mm. A new test setup with an improved performance has been constructed [98]. First results have demonstrated the mono-disperse and satellite-free droplet production for cryogenic liquids of H_2, N_2 and Ar [99]. However, the prototype does not fully include the $\bar{\text{P}}$ANDA geometry. The handling of the pellet train over a long distance still has to be investigated in detail. The final vertex resolution envisaged is in the order of 50 µm. Therefore, an additional pellet tracking system is planned.

→ Other target options

In case of solid target materials the use of wire targets is planned. The hyper-nuclear program requires a separate target station in upstream position. It will comprise a primary and secondary target. The latter must be instrumented with appropriate detectors. Therefore, a re-design of the innermost part of the $\bar{P}$ANDA spectrometer becomes necessary. This also includes the replacement of the MVD. However, measurements with this modified setup are only foreseen at a later stage of the experiment.

2.3.4 Closing remarks on the overall detection concept

Fully exclusive measurements are one of the main means necessary to study many aspects of the physics program. This requires a detection capability for both charged and neutral particles over the full solid angle. Moreover, good particle identification (PID) is mandatory. High resolution tracking is needed for background suppression of rare channels and the determination of secondary vertices of shorted-lived particles. Further performance criteria for high precision spectroscopy are connected to a high momentum resolution of charged particles and high quality calorimetry. Due to the high beam intensities all detectors must withstand a large radiation dose and exhibit high rate capability. An accurate tracking of very slow particles with momenta of about 100 MeV/c to 200 MeV/c and a detection of soft photons must be included. This requires a very low material budget to reduce scattering effects and low thresholds of the detecting sub-systems resulting in a high dynamic range to be coped with.

The modular concept of the detector allows a high flexibility. A sophisticated data acquisition and trigger concept is necessary to cover the broad physics program. The overall detection concept is shown schematically in figure 2.14. The main parts are discussed in the following paragraphs. Finally, the data acquisition envisaged for the $\bar{P}$ANDA experiment is presented on page 61.

→ Global tracking

Tracking systems are positioned inside the target spectrometer and in the forward region around the dipole magnet. They deliver information on the trajectory of charged particles traversing the sensitive detection volumes. Main tasks of the global tracking system are the accurate determination of the particle momenta, a high spatial resolution of the primary interaction vertex and the detection of displaced secondary vertices.

Measurements of different subsystems must be merged in order to access the full information i.e. the precise track parameters for all charged particles in an event. The solenoid field in the central part leads to a bending with respect to a projected plane perpendicular to the beam axis. The particle momentum then can be extracted via the determination of the bending radius. However, for small angle tracks in forward directions the impact of the length-limited solenoid field on the particle track inside the target spectrometer vanishes. For this case, the particle deflection induced by the subsequent dipole magnet is used to measure the particle momentum. Due to the different analyzing magnets, track fitting algorithms distinguish among forward and central tracks. As a consequence, the global particle tracking is split into two associated parts. In overlap regions the inner tracker or

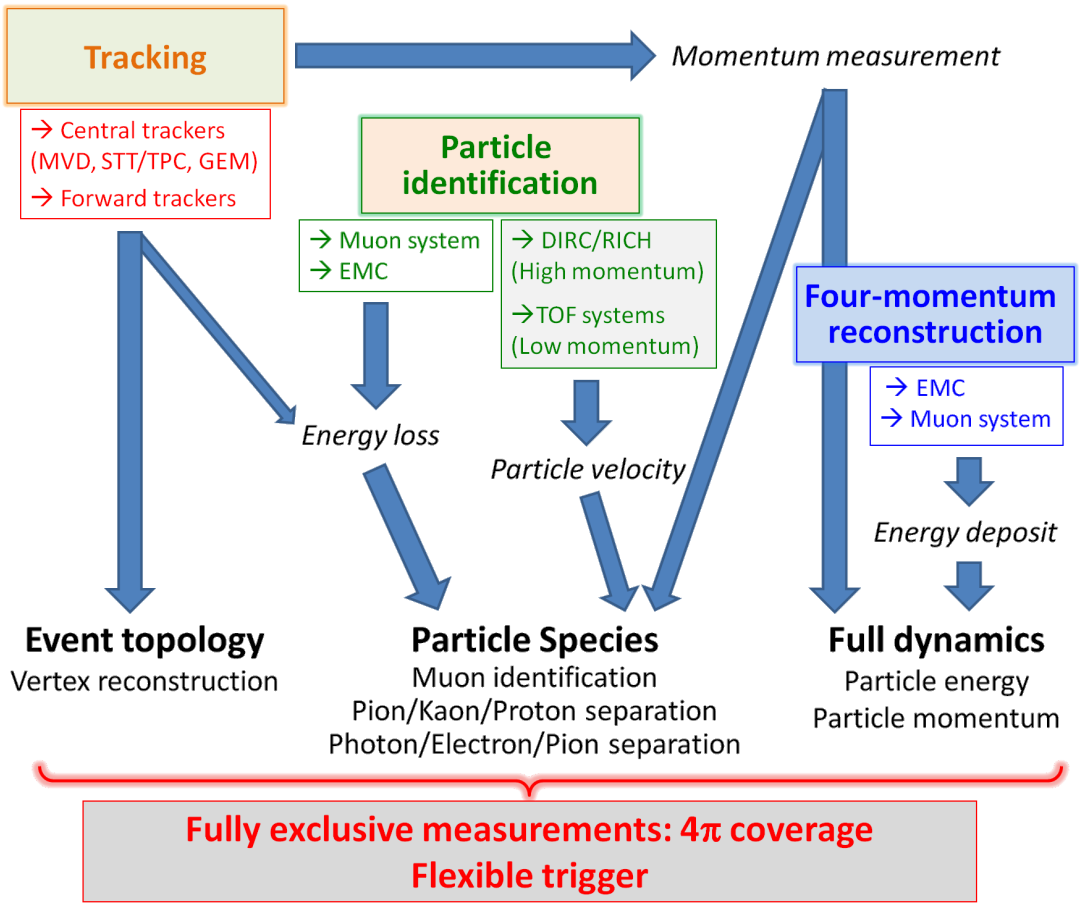

Figure 2.14: Schematics of the detection concept for the $\bar{\text{P}}$ANDA apparatus. The hermetic design allows a measurement over nearly the full solid angle (4π). The MVD as part of the central tracker contributes complementary information needed to perform exclusive measurements.

the GEM stations can contribute to the forward tracking. The availability of an additional track point closer to the IP will significantly improve the fitting results.

Initially, the central and the forward tracking are performed independently. Central tracks are reconstructed by combining hit points in the MVD layers with the tracking information of the outer tracker or the GEM stations. Obviously, the final tracking algorithms must be adapted to the involved detectors and thus depend on the solution for the outer tracker. The overall tracking performance of the STT is affected by the limited 3D resolution along the beam axis, which is associated with the relatively small skew angles introduced between different tube layers. The TPC system would provide an improved tracking resolution. Moreover, information about the deposited energy of the tracks inside TPC are superior to the achievable energy loss measurements in the STT and thus could deliver important input to the global PID. Challenges for the TPC arise from the large number of tracks accumulated in the drift volume, which are related to the slow drift times and the high occupancy. Therefore, a fast reconstruction of tracklets will be needed to

allow a matching against other detector signals or to point them towards the IP. Appropriate algorithms have to be developed requiring either high computing power and a very high bandwidth at the full interaction rate.

After the global identification of all individual tracks and the determination of the associated particle momenta an event mapping will be performed. Different tracks of the same event can be matched to a common vertex which either corresponds to the primary interaction vertex or a delayed decay of short-lived particles. In this way it is possible to obtain information about the event topology. The central tracking system is of particular importance for the reconstruction of charmed hadrons. In many instances associated charged decay modes release a high transverse momentum of up to 1.5 GeV/c, which leads to a large opening angle of the daughter particles in the laboratory reference frame. A particular task of the tracking system is the tagging of D mesons via their displaced vertex. It is crucial for many applications of the physics program.

The luminosity monitor at the downstream end is a tracking device of its own right. It was introduced to measure the time integrated luminosity, which is essential for the determination of cross sections for different physics processes. Therefore, elastically scattered antiprotons are measured under small angles corresponding to small momentum transfers. The associated differential cross sections are well known and thus provide an ideal reference channel. Additional information from the central tracker will eventually improve the measurement by taking advantage of the reconstructed slow recoil proton at polar angles of around 90°, which is associated with the highly energetic antiproton track detected in the luminosity monitor.

→ Global particle identification

The global particle identification (PID) is based on accumulated input of various detector systems. Only a suited combination of different measurements facilitates a complete assignment of all particle species over the full momentum range. A detailed description for the $\bar{P}$ANDA detector is given in [100]. In the following, basic principles will be briefly summarized.

First contributions to the global PID can be delivered by the characteristic energy loss of different particle species in the tracking detectors. However, it should be mentioned that the separation power of tracking detectors is in general limited so that a particle hypothesis can be corroborated only with a certain probability. Independent measurements, which directly contribute to the global PID, can be performed with electromagnetic calorimeters and range systems such as the muon chambers. Another common approach for PID is the complementary measurement of the velocity and the momentum of a particle, which then can be identified by its rest mass. Therefore, a tracking system in combination with Cherenkov detectors or TOF systems is needed.

Cherenkov detectors can be employed to extract the velocity of charged particles which exceed the speed of light within the detector medium. In this case, Cherenkov light is emitted at a fixed angle $\theta = \arccos(1/n\beta)$, where $\beta = v/c$ describes the measured particle velocity, v, with respect to the speed of light, c, and n corresponds to the refraction index of the medium. The chosen detector material must be transparent for the Cherenkov light.

For the Cherenkov detectors in the $\bar{P}$ANDA target spectrometer, fused silica with $n = 1.47$ is intended to be used as radiator. With this material a good pion-kaon-separation

from rather low momenta of 800 MeV/c up to 5 GeV/c can be achieved. The utilization of a mixture of two radiators, namely silica aerogel and C_4F_{10} gas, will enable a pion-koan-proton separation in a broad momentum range from 2 GeV/c up to 15 GeV/c. Below particle momenta of 800 Me/c, Cherenkov detectors do not contribute to the PID due to their detection mechanism. The identification of slow particles will be performed by TOF systems. A direct extraction of the particle velocity at $\bar{\text{P}}$ANDA is only possible in forward direction. In the barrel part an additional start signal from another sub-system, e.g. the MVD, is needed. Besides, energy loss measurements of tracking detectors will eventually provide additional input for the identification of slow particles.

The separation between pions and muons will be done by range systems at the outermost detector layers. These allow the distinction of energy loss processes for muons and pions as well as kinks from pion decays. A PID of photons, electrons and pions can be achieved due to different forms of the showers produced in the EMC. The barrel EMC will provide a sufficient electron-pion separation for particle momenta above 0.5 GeV/c.

→ Four-momentum reconstruction

To describe the full kinematics of a reaction, momentum and correlated energy of all particles must be determined. The momentum of charged particles is measured with the tracking system. Main purpose of the electromagnetic calorimeters is a measurement of the total energy of penetrating particles including photons. Further information can be delivered by the energy deposit in the muon range systems. Besides a direct measurement, the reconstructions of the decay products of e.g. neutral particles or missing mass methods allow the determination of kinematics variables.

→ Data acquisition

Due to the high data rates expected, the complexity of the experiment and the diversity of physics objectives, a sophisticated concept for the data acquisition will be needed. Moreover, the target interaction with a quasi continuous beam leads to a non-ordered time-structure of the events. Conventional hierarchic trigger systems are typically based on a layered approach in which a subset of specially instrumented detectors is used to evaluate a first level trigger condition. The accepted events are then transported to the next higher level trigger or storage. This approach is severely constrained in both complexity and flexibility because of the hard-wired detector connectivity. Therefore, an alternative concept of self-triggering subdetector systems will be applied for the $\bar{\text{P}}$ANDA experiment. It is based on autonomous signal detection and pre-processing by the subdetectors. Hit-detection, noise-suppression and clustering are requested at the readout level in order to extract the physically relevant information and to reduce the data rate significantly. The selected data must be marked with a precise time stamp and then buffered for further processing. The final trigger decision will be computed in external nodes, which have access to the buffers via a high-bandwidth network fabric. In this way, subdetectors can contribute in equal measure to the trigger decision without restrictions due to hard-wired connectivity.

Key technologies for the implementation of the proposed system are high-speed serial links (10 Gb/s per link) and high-density FPGAs with a large number of programmable gates, which include advanced embedded features. Basic building blocks for the hardware

infrastructure will be intelligent front-end modules, a highly precise time distribution system and data concentrators providing a point-to-point communication via an optical link in combination with online data manipulation and buffering. Finally, powerful compute nodes are needed. A specified bandwidth of 200 GB/s is required for the experiment assuming a flat hierarchy with a direct transfer of all data to the processing notes. The resultant data rate for the mass storage will range between 100 MB/ s and 200 MB/s. Besides data storage a continuous calibration with data for all detectors must be performed during the measurement. Therefore, the normal data taking is interleaved with special calibration runs. A small fraction of unfiltered raw data is then transmitted additionally to the mass storage in order to monitor the data quality and the calibration constants.

3 The Micro-Vertex-Detector (MVD)

The MVD is the innermost part of the central tracking system. This particular component of the $\bar{\text{P}}$ANDA apparatus is the main objective of the present work. In the following sections, key aspects of the MVD will be outlined. Main tasks and detector requirements are specified in section 3.1. The basic detector layout is depicted in section 3.2. Further details on the conceptual design are summarized in section 3.3. The position of the MVD inside the $\bar{\text{P}}$ANDA apparatus, the beam-target geometry and the boundary conditions for the MVD are shown in figure 3.1.

3.1 Main tasks and detector requirements

The MVD plays a key role for the global tracking concept of the $\bar{\text{P}}$ANDA experiment. It delivers 3D information of the track position for charged particles very close to the IP. As innermost sub-detector of the entire $\bar{\text{P}}$ANDA apparatus, the MVD defines the earliest possible point of time in the reaction channel which is experimentally accessible. Track and time information both provide important input for the further event reconstruction. Precise timing is essential for an accurate assignment of individual tracks to the appropriate event. In addition a fast detection of particles inside the MVD can be used as time reference for outer detector systems. The track information gives access to the particle momentum and the event topology. Additional input can be delivered by an energy loss measurement. However, the impact of the MVD is limited in this case and mainly results in a loose particle hypothesis.

Main task of the MVD is the measurement of both the primary interaction vertex and secondary decay vertices of short lived particles with high precision. Relevant particles with a delayed vertex are charged hadrons with charm or strange quark content. Of particular interest for the $\bar{\text{P}}$ANDA experiment is a tagging of D mesons through their charged decay products. A vertex reconstruction with a precision of better than 100 µm is required to clearly identify the groundstate D mesons via their displaced decay vertex (see table 1.4). To achieve this demanding task, a detection of first track points very close to the nominal vertex is mandatory. Moreover, a very good intrinsic detector resolution is needed thus requiring a high granularity. Further improvements can be achieved by weighting methods between neighbouring channels (see also chapter 1.4). For this purpose an analogue readout is needed which also enables energy loss measurements of crossing particles. Besides a high 2D resolution within the detector plane, a very precise alignment of all individual detector elements is necessary to achieve a good 3D resolution.

The general detection concept of $\bar{\text{P}}$ANDA requests an optimized detector coverage over nearly the full solid angle. Certainly, limitations are given by the beam-target geometry and the space to be reserved for routing purposes (see also figure 3.1). Other boundary conditions are defined by space requirements of adjacent subdetectors. A sufficient number

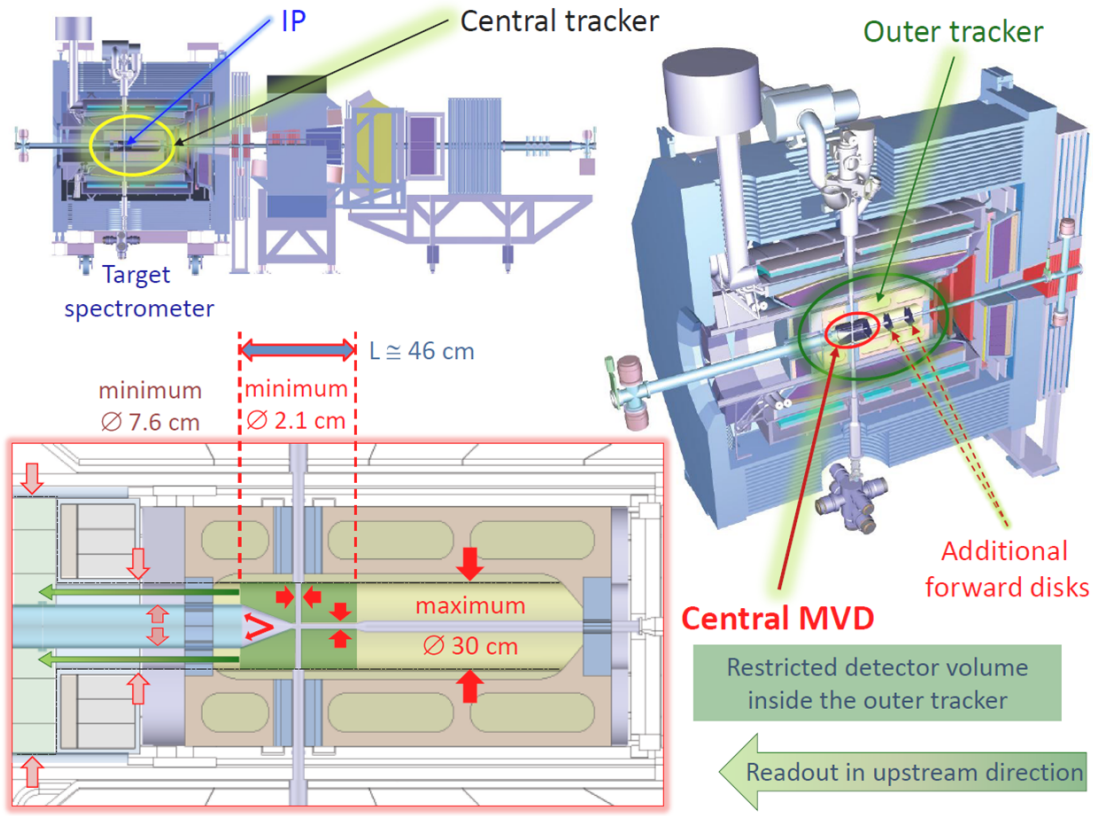

Figure 3.1: Positioning of the MVD inside the PANDA apparatus: The MVD is part of the central tracker surrounding the interaction point (IP) (*top, left*). Placed inside the bore of the outer tracker it is the innermost detector of the target spectrometer (*top, right*). Besides the central MVD there are two additional disks in forward direction. *Bottom, left:* Beam-target geometry and boundary conditions for the MVD volume. Given measures refer to the outer limits of adjacent sub-systems without any safety margin.

of MVD hit points is necessary for high tracking performance. In the best case an independent pre-fit of MVD tracklets can be performed. Therefore, a minimum of four track points is desired for central tracks at polar angles above 10° thus allowing the use of fast algorithms for the helix fit. At small polar angles any point of the MVD contributing to the straight line fit improves the resolution significantly due to the long leverarm. Moreover, an enlarged number of detector layers in forward direction must be considered to obtain hit points close to secondary decay vertices of particles with a larger displacement from the IP in downstream direction.

Further requirements result from the insertion of the MVD inside the target spectrometer. A minimization of the material budget is very crucial because a high material load of the MVD would affect all outer detector components. The experimental conditions at PANDA populate a lot of particles with relatively small momenta below 1 GeV/c (see chapter 6.1). As a consequence, scattering effects become much more significant compared

to HEP experiments and must be studied carefully in order to optimize the overall detector performance. Detrimental effects for the tracking of charged particles are introduced by spatial distortions and a momentum loss of the particle due to energy straggling inside the detector material, which increases the bending radius in the solenoid field.

Besides, conversion and attenuation of photons are the most severe material effects leading to a reduced detector performance. The development of a low mass detector with high integration density is one of the technically most challenging engineering tasks. Another consequence of the close position with respect to the IP is a harsh radiation environment. All detector components must withstand an adequate radiation dose. The requested radiation tolerance in terms of the expected total ionizing dose (TID) is in the order of $10^{14}\, n_{eq}\mathrm{cm}^{-2}$ assuming a 50% duty cycle in the 10 years lifetime of $\bar{\mathrm{P}}$ANDA [101]. These values stay below the maximum numbers required in high energy experiments such as at LHC. Nevertheless, dedicated production techniques are required in order to achieve sufficient radiation hardness.

Finally, the specific trigger and readout concept of the $\bar{\mathrm{P}}$ANDA experiment requests an autonomous readout scheme for the MVD. The readout electronics must integrate an internal trigger and a first data concentration for each channel and on frontend level, respectively. This approach exceeds common state-of-the-art solutions and requires an extended research and development program. The achievable time resolution of the MVD must cope with the maximum expected interaction rate of twenty million annihilations per second given as design parameter for the $\bar{\mathrm{P}}$ANDA experiment. Taking into account possible fluctuations for the pellet target (see subsection 2.2.4) and the requested timing precision defined by the global clock frequency of the $\bar{\mathrm{P}}$ANDA experiment [102], an absolute time resolution of better than 10 ns is required.

3.2 Basic detector layout

The MVD is split into a barrel and a forward part. Outer limits are given by the detector position inside the outer tracker. It defines a maximum radius of 15 cm and an extension of $z = \pm 23$ cm along the beam axis. As for the entire target spectrometer a half-detector system must be applied in order to accomodate to the target pipe, which crosses the entire MVD volume perpendicularly. A schematic picture of the MVD detector layers is given in figure 3.2. Silicon hybrid pixel detectors and double-sided silicon microstrip detectors are foreseen in the inner and the outer parts, respectively. A further discussion of the chosen detector technology will follow in the next section.

The barrel part of the MVD consists of four detector layers and covers polar angles between 40° and 150° (see figure 3.2, bottom). The maximum downstream extension is given by both strip layers. The two shorter pixel layers have different lengths. In this way, large crossing angles of particles originating from the IP are avoided. The upstream extension differs for all barrel layers in order to fit with the opening cone of the beam pipe. The radii of the innermost and the outermost barrel layer are set to 2.5 cm and 13.5 cm, respectively. The two intermediate barrel layers are arranged in increasing order at radii of 5.5 cm and 9.5 cm. Safety margins to adjacent subcomponents or in between different barrel layers are included in these numbers.

In forward direction there are six disk layers enabling a measurement at small polar

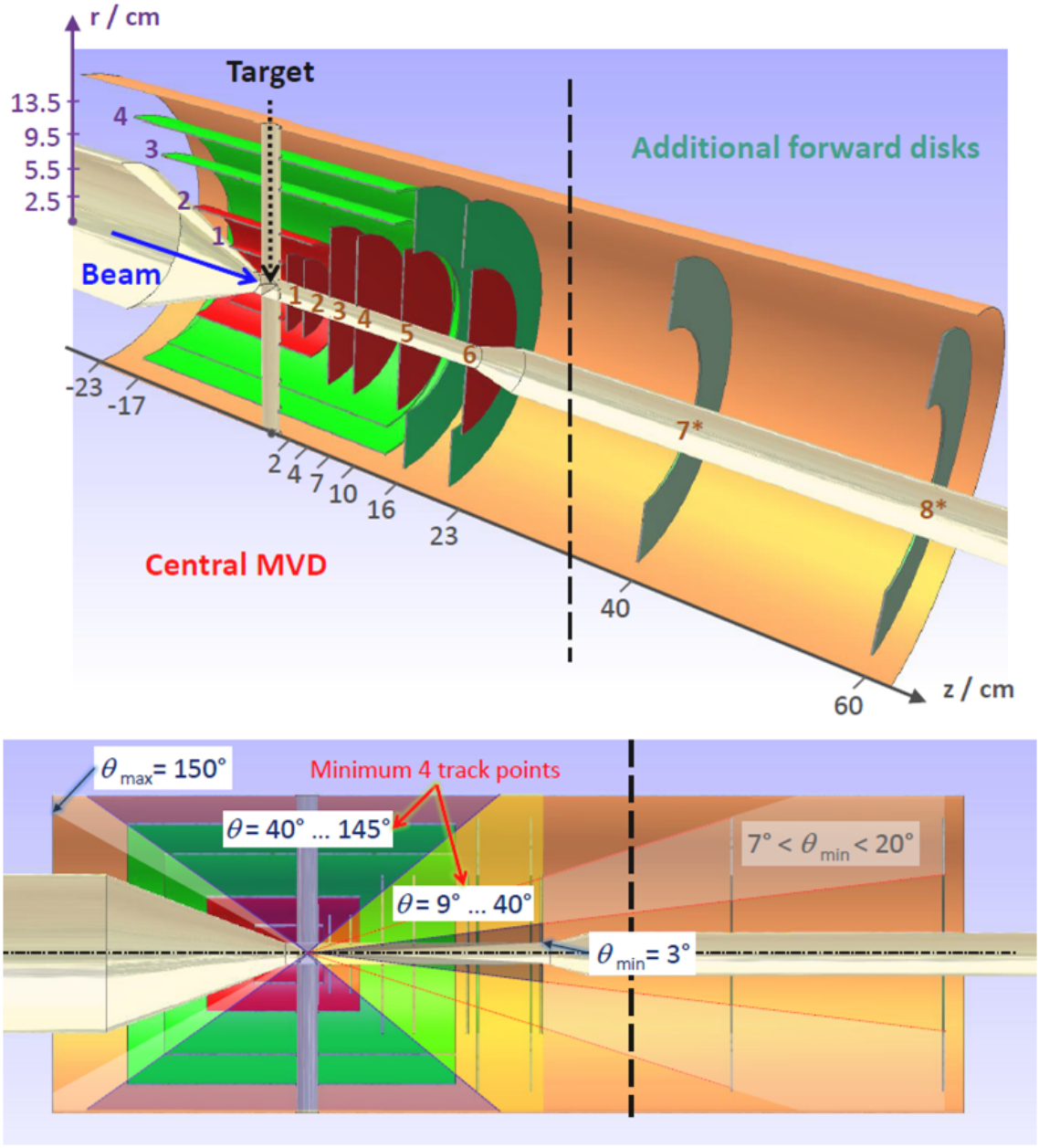

Figure 3.2: Basic layout of the MVD and the two additional disks in forward direction (*top*). The red inner parts are equipped with silicon hybrid pixel sensors. Double-sided silicon microstrip detectors utilized in the outer layers are highlighted in green. The additional forward disks (labelled 7 and 8) are based on the conceptual design of the outer strip disks. *Bottom*: Illustration of the solid angle coverage. The MVD covers polar angles (θ) from 3° up to 150°. A minimum of four detector layers contribute in a range of $9° \leq \theta \leq 145°$. The barrel and the forward part are joined at $\theta = 40°$.

angles between 3° and 40°. The first two pixel disks are inside the outer pixel barrel layer and have an interspacing of 2 cm. The innermost disk located at z =2 cm is the closest of all detector layers with respect to the nominal IP. After the two small pixel disks there are four large pixel disks following in downstream direction. While the first two of them are positioned inside the strip barrel layers, the ones further downstream are extended by additional strip disks.

Apart from the central part of the MVD there are two extra disks in forward direction filling the gap until the forward GEM tracking station. They are intended to contribute to the vertex reconstruction of hyperons, which have much longer lifetimes and consequently a larger displacement of the secondary vertex than D mesons. The conceptual design of these additional disks is similar to that of the strip disks used for the central MVD.

3.3 Conceptual design

This section contains a description of the conceptual design for the MVD, which is based on the predefined layout as described before. First of all, the chosen detector technology is justified and the use of different detector types for the MVD is motivated. Afterwards, the segmentation of generalized detector layers into individual sensors is discussed. The deduced sensor geometry is then introduced including both sensor dimensions and the geometric sensor arrangement. Finally, mechanics aspects connected with the infrastructure for the MVD and the overall detector integration are summarized.

3.3.1 Choice of detector technology

Silicon detectors excel in a fast response and a low material budget. Moreover, they allow a high degree of miniaturization and they can be produced in big quantities with a very good reproducibility. Due to these properties they meet perfectly the requirements imposed on the MVD. An introductory description of main properties, basic principles and applications for silicon detectors has been already given in chapter 1.4.

Specific requirements are defined for sensitive detector volumes placed at different regions of the MVD. A high spatial resolution is crucial for the first hit points close to the nominal IP. Moreover, a very high occupancy must be handled in the innermost detector regions. Silicon pixel detectors deliver discrete 2D information with a high granularity and allow very precise measurements. Therefore, they are used in the inner MVD layers. A drawback is the 1:1 area ratio between the active pixels and the back-to-back coupled readout chip. Moreover, the total number of channels required to cover larger surfaces increases rapidly due to the small pattern segmentation. The overall material budget including detector material, frontend chip and appropriate services scales linearly with the number of channels. It must be minimized in order to fulfil the requirement of a low-mass detector as specified for the $\bar{\text{P}}$ANDA experiment. For this reason, double-sided silicon microstrip detectors are used in the outer parts of the MVD. They allow the coverage of a much bigger detection area with significantly less channels. A negative effect is the introduction of ambiguities in case of multiple hits in the detector. As a consequence, their use very close to the primary vertex is disfavoured.

The final application of both detector types according to picture 3.2 respects all key

aspects discussed above. Detailed studies on the occupancy and connected count rates in different regions of the MVD are explicitly summarized in subsection 6.2.3. In the following, all individual silicon detectors will be denoted as either pixel or strip sensors in order to avoid misinterpretations.

3.3.2 Sensor geometry

The schematic detector layers are approximated by an appropriate arrangement of individual detector elements. Shape and size of the implemented sensors must be optimized accordingly. Besides purely geometric considerations also technical aspects have to be taken into account. Moreover, the specific size of the readout structure has direct impact on the sensor design. For the two different detector types it is given by the pixel cell size and the strip interspacing, which is commonly denoted as strip pitch. The final number of different sensor types should be kept small in order to facilitate a modular concept and to obtain a high compatibility.

In case of pixel sensors the shape is restricted to a rectangular form due to technical reasons [103]. The design for the MVD is based on a quadratic pixel cell size with a side length of 100 µm. There are four different pixel sensors, each of them have the same width but different lengths. The dimensions correspond to basic units of a pixel readout chip, which is connected to approximately 100 × 100 cells. The different pixel sensor types are shown schematically in figure 3.3, left side. Right next to it, the basic geometry for the pixel sensor arrangment is illustrated. A pixel barrel layer is made out of a double-ring arrangement in order to achieve sufficient radial overlap. The forward disk layers consist of an appropriate configuration of pixel sensors, which are aligned in different rows.

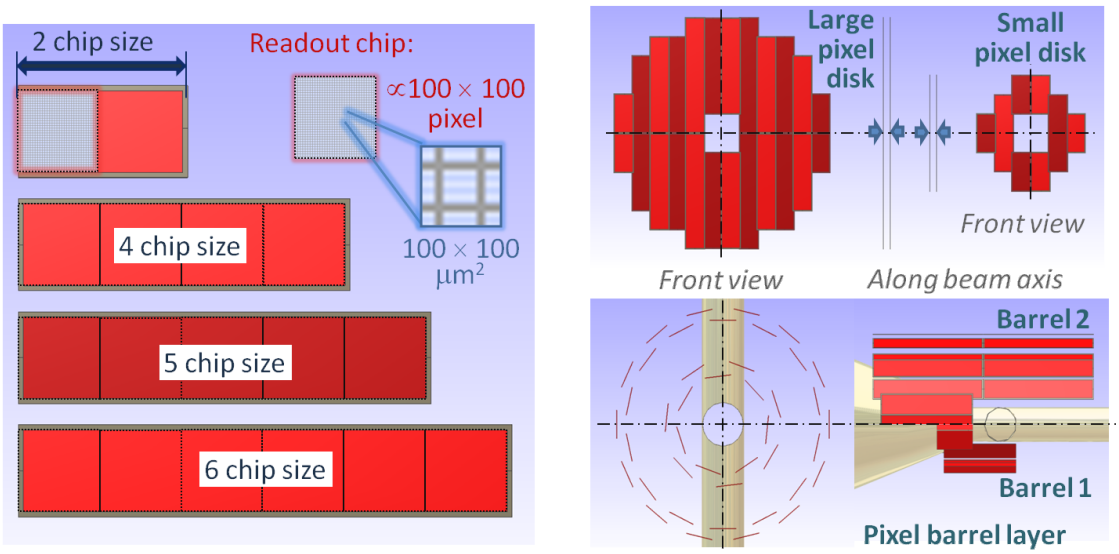

Figure 3.3: Schematics of the basic pixel sensor geometry. *Left:* Main pixel sensor types. The design is based on a quadratic pixel cell size of 100 × 100 µm² and an effective readout area of approximately 100 × 100 pixels per individual readout chip. *Right:* Pixel sensor arrangement in different detector layers.

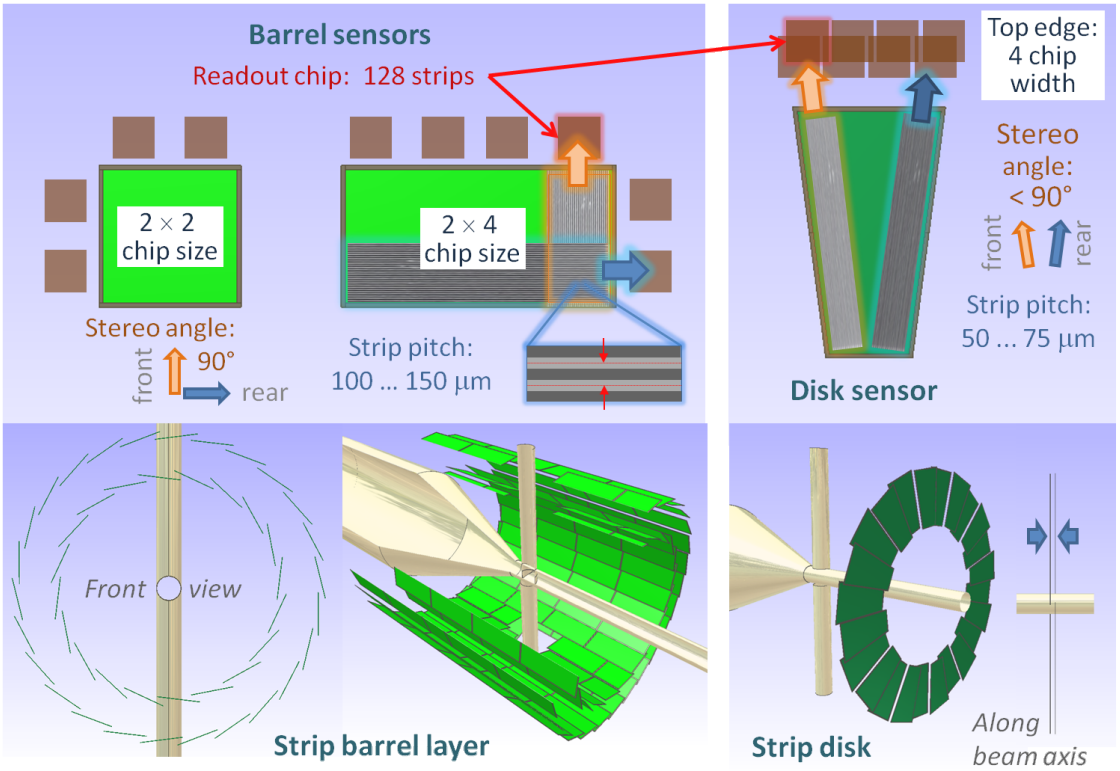

Figure 3.4: Basic sensor geometry for the MVD strip part: Sensor types (*top*) and sensor arrangement in the different detector layers (*bottom*). The underlying segmentation of the sensors is given by the stereo angle and the strip pitch assuming 128 channels per readout chip.

Alternating rows are positioned with a small interspacing along the beam axis thus allowing the compensation of the passive edge around the active area.

For the MVD strip part three different sensor shapes are implemented. Quadratic and rectangular sensors are used for the barrel part, while a trapezoidal design is chosen for the forward disks. The respective stereo angle is set to 90° in case of barrel type sensors and to a reduced angle for the trapezoids. In this way strips always run in parallel to one sensor edge. The defined size of the readout structure is driven by estimates on scattering effects in the preceding pixel layers, which define a range of 100 µm to 150 µm. Compared to the barrel sensors, the strip pitch for trapezoidal sensors is roughly a factor of two smaller in order to recover the worsened resolution induced by the smaller stereo angle. The strip barrel layers are formed by a paddle-wheel sensor arrangement. Neighbouring trapezoidal sensors of the forward disks are located at two positions slightly shifted along the beam axis in order to make up for the passive sensor edge. A schematic picture of the strip sensor geometry is given in figure 3.4.

To accomodate the target pipe crossing, a gap must be opened in the barrel part of the MVD. Therefore, quadratic strip sensors of the size of the target pipe are circularly arranged at the IP and some sensors are left out at the top and bottom. In case of the pixel barrel layers, shorter sensors are used at these positions to obtain sufficient space for the

target pipe lead-through. The precise sensor dimensions and the exact sensor positioning result from an explicit design optimization. This will be discussed in section 5.2. Finally, there are approximately 11 million pixel and roughly 200.000 strip readout channels.

3.3.3 Technical design aspects

Besides the positioning of active sensor elements inside the MVD there are many other technical aspects which have to be considered within the conceptual design. First of all, this is related to the hybridisation of detector modules combining silicon sensors with customized readout electronics. Because an active cooling is needed for these components, the dimensioning and implementation of a cooling system for the MVD has a huge impact on the overall detector design. The corresponding routing scheme for all services including cooling and cabling must be defined carefully. In addition, a support concept for the different detector layers must be developed and the final detector integration of the complete MVD inside the target spectrometer must be defined. The most important points of the above topics are briefly discussed in the following.

→ Hybridisation

The hybridisation of pixel and strip modules is considerably different. The direct connection of the pixel readout chip to the backside of the silicon pixel sensor allows a very compact design, which integrates also local cooling, cabling and support structures. A standard hybrid technology is illustrated schematically in figure 3.5. In contrast, the double-sided readout of strip sensors requires more sophisticated technical solutions. However, readout electronics can be placed independently of the sensor by introducing appropriate adapter components. The overall number of readout channels can be further decreased by connecting strips of neighbouring sensors. Figure 3.6 illustrates schematically the basic approach for the strip modules intended to be used inside the MVD.

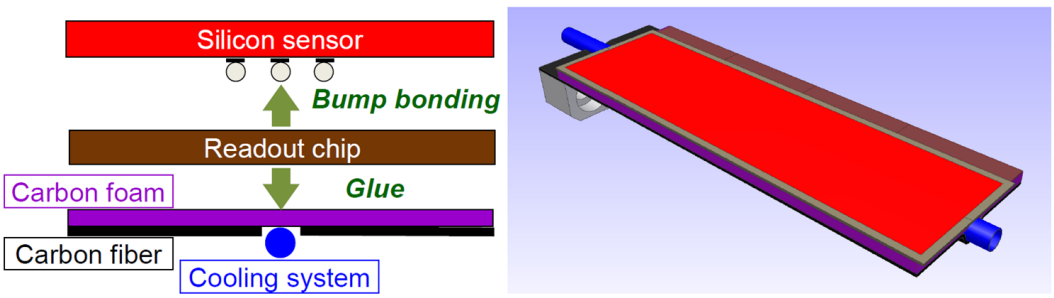

Figure 3.5: Schematics of a standard hybrid technology for silicon pixel detectors (*left*). The hybridisation features a compact design of detector modules including sensor, frontend electronics, local support and the cooling system (*right*).

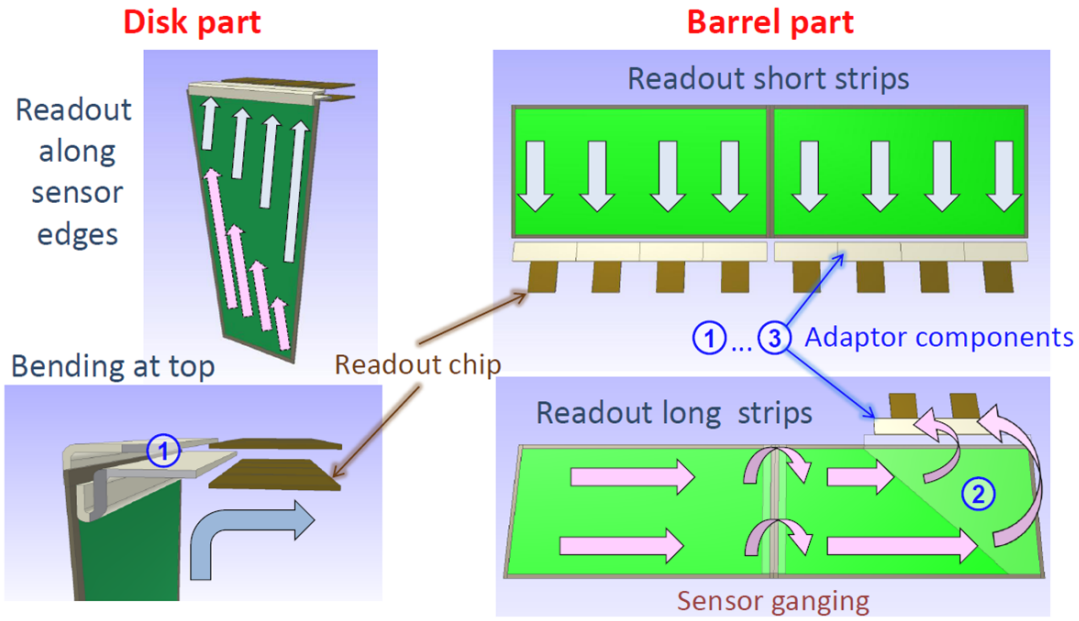

Figure 3.6: Basic concept for the hybridisation of strip modules with a double-sided readout. Introduced adaptor components allow a spatial separation of sensor and frontend electronics. The readout of the disk modules is turned by 90° to minimize the radial extension. In case of strip barrel modules all readout chips are positioned along the long sensor edge. Therefore, the readout of long strips must be folded by 90°. Long strips of subsequent sensors are ganged in order to reduce the total number of readout channels. Details on further local support structures and cooling components are given in chapter 5.3.

→ Cooling

The MVD will operate under normal pressure conditions at room temperature of approximately $+25\,^{\circ}\mathrm{C}$. Self-heating effects of the silicon sensors are counter-balanced by air conduction, which may be obtained either by free convection or a forced air flow [104]. Moreover, active cooling of both pixel and strip readout electronics is needed due to the high power dissipation of up to $1\,\mathrm{W}/\mathrm{cm}^2$ specified as an upper limit [105, 106]. It is crucial for a long term stability of the operating system. Besides the protection of all readout components a possible heat transfer to the sensor must be prevented in order to avoid a destructive thermal runaway therein [107]. This aspect is particularly important for the pixel hybrid. The cooling system is intended to be designed similar to the one of the ALICE silicon detector [108] using $18\,^{\circ}\mathrm{C}$ water as coolant and working in an underpressure mode in order to avoid any damages in case of a leakage. Therefore, the water is forced through the system by a hydrostatic pressure requiring a minimum height of approximately three metres [109].

→ Routing

The routing scheme for all MVD services comprises pipes of the cooling system, supply cables for sensors and readout electronics as well as signalling cables for data and slow control of the readout chips. A schematic picture is given in figure 3.7. More details are presented in chapter 5. Due to the restricted space and the fixed target setup, guiding to the outside of the target spectrometer is only possible in upstream direction. In this region the opening cone of the beam pipe reduces the free cross section available for routing purposes. As consequence, the services of the inner barrel layers must follow the beam pipe geometry to outer radii. The routing concept for the forward part is more complicated. At first, all services of the pixel disks must run in downstream direction before they can be brought to outer radii in parallel to all routing components of the strip disks. Further guidance in upstream direction is performed for the entire forward part in between the outermost barrel layer and the remaining space to the outer tracker and the subsequent backward endcap EMC.

A circular occupancy is envisaged for the overall routing of both, barrel and forward part, in upstream direction due to the restricted volume and the large required cross section. For the pixel disk services inside the barrel layers a bundling at the top and bottom promises a more advantageous solution. Also for the two additional disks, this solution represents a possible alternative. Finally, patch panels are foreseen further upstream, which allow a connection to peripheral systems for e.g. the cooling circuit, power supply or slow control behind the backward endcap EMC.

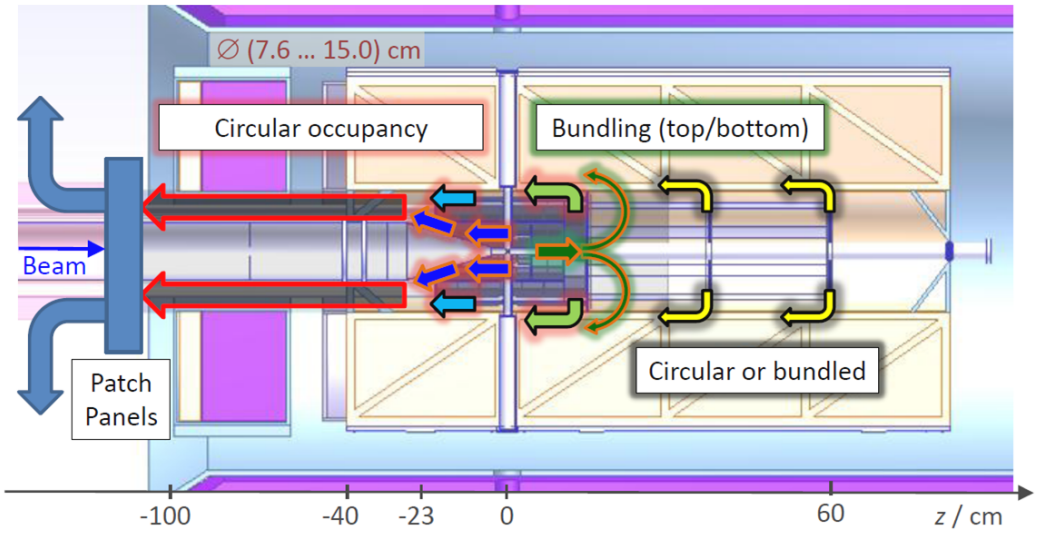

Figure 3.7: Overall routing concept for the MVD and the two additional forward disks. The lead-out of all services must be performed in upstream direction. The available cross section is limited by the outer radius of the beam pipe and the inner radius defined for the central tracker and the backward endcap EMC.

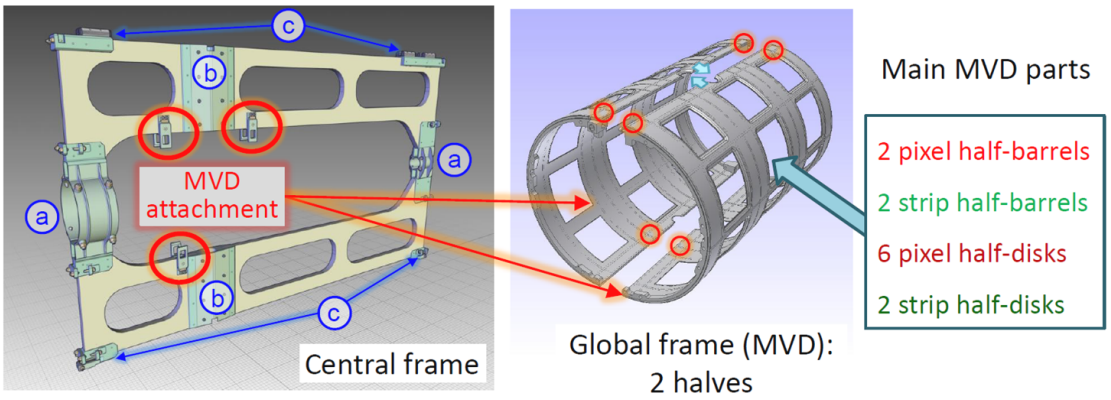

Figure 3.8: Mechanical mounting structure for the MVD. The interface to the external parts of the $\bar{\text{P}}$ANDA apparatus is defined by a three-point fixation to the central frame (*left*). This reference and support frame also provides fixation points for the beam pipe (a), the target pipe (b) and connection points to a rail system (c) allowing an installation outside of the target spectrometer and the insertion to the nominal position. The main MVD parts (*right*) are integrated in two half-frames (*middle*), which are connected separately to the central frame.

→ Support concept and detector integration

All support structures inside the MVD must be composed of light-weight materials commonly made of carbon or carbon foam. At appropriate points, stiffer materials are introduced for a load pick-up. Additional support structures are also needed for MVD services. The overall support concept ensures the integration of two half-detectors as required for the MVD and features a modular built up [110]. The mechanical interface of the MVD to external parts of the $\bar{\text{P}}$ANDA apparatus is defined by a three point fixation to the central frame. This particular component of the target spectrometer serves as reference frame and global support for the entire central tracking system. Moreover, it features a consecutive assembly of the beam-target system, the MVD and the outer tracker outside of the solenoid magnet. After completion, a safe insertion of these sub-systems to their nominal position is facilitated via a rail system.

The global support structure for the MVD is composed of two half-frames. Both halves are mechanically independent in order to avoid any introduction of stress to either half-detector. They allow the internal mounting of all detector-half-layers and the attachment to the central frame. Basic ideas of the detector integration for the MVD are depicted in figure 3.8. A detailed description is given in subsection 5.3.2.

4 Hardware development

In parallel to the conceptual work, adequate hardware development is required. The associated engineering tasks include a variety of different activities starting from the research on suitable silicon detectors in connection with appropriate frontend electronics right to e.g. the production of lightweight support structures, the dimensioning of suited cooling systems or the processing and evaluation of cables and converters for signal transmission. Hardware specifications are defined by the basic detector layout, experimental conditions and particular physics requirements.

A prototyping of individual hardware components is indispensable to prove the feasibility of the intended detector concept. It provides direct feedback and delivers important input to the further detector development. Besides the manufacturing of hardware components with the given specifications, diverse test systems must be set up. Therefore, standardized procedures have to be developed allowing a characterization and validation of the particular components under study. These routines lay the groundwork to further procedures of quality control during the final detector assembly. Finally, the iterative process of the detector optimisation aims at a reasonable compromise between technical feasibility and economical aspects on the one hand and basic guidelines motivated by physics aspects on the other.

Main hardware activities for the MVD are summarized in the present chapter. Because of the ongoing work it is only a status report. Nevertheless, important results are already included within the design optimization presented in chapter 5. Section 4.1 summarizes main hardware developments for the pixel part of the MVD, which have been performed by a collaborating group at INFN in Torino [111]. Hence, shown results in this subchapter do not represent the work of the author but they are relevant for the further detector optimization performed within the scope of this thesis. The following section 4.2 then represents own hardware activities related to the strip part of the MVD, which have been carried out at the affiliated universities in Dresden and later in Bonn. Integrative work is outlined in section 4.3. It refers mostly to the development of lightweight support structures and cooling test systems. In addition, an existing full-size mechanical mock-up for the MVD is described.

4.1 Pixel development

A complete research and development (R&D) program for the pixel part of the MVD is in progress at INFN Torino [111]. It includes the study and design of a custom pixel detector able to cope with the challenging requirements. These are e.g. the high radiation level, the trigger-less readout concept acquiring a huge amount of data and the stringent material budget. Innovative solutions are necessary to meet all technical requests. Additionally, aspects of cost-effectiveness, timelines and availability must be considered. In this context,

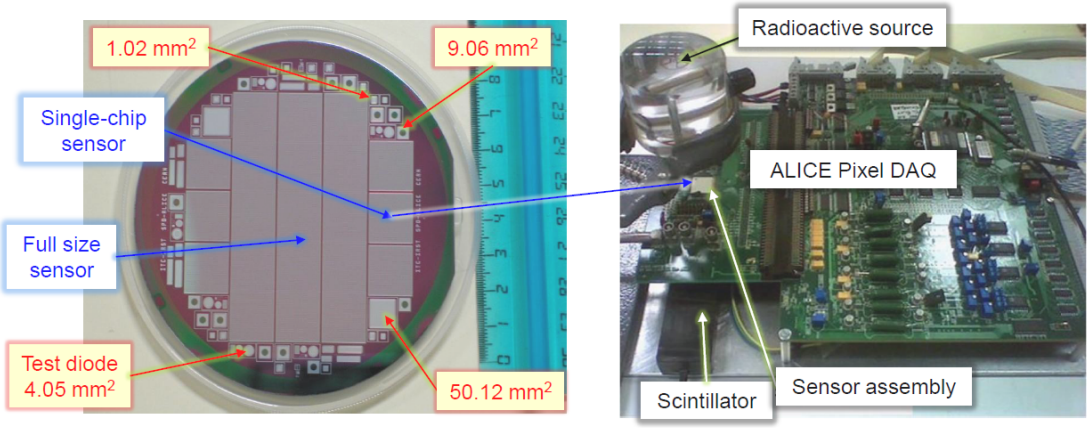

Figure 4.1: Photographs of a manufactured epitaxial sensor wafer [113] (*left*) and a test setup used for characterization of different epitaxial sensor assemblies [114] (*right*).

a hybrid technology is chosen for the MVD pixel part, which is based on thinned epitaxial silicon sensors and a custom-made readout ASIC. Main developments of both parts are summarized one after the other in subsection 4.1.1 and 4.1.2, respectively. An overview to the R&D program can also be found in [105] and [112] .

4.1.1 Epitaxial pixel sensors

Epitaxial silicon sensors excel in their intrinsic radiation resistance thus qualifying them as an adequate candidate for $\bar{\text{P}}$ANDA. They have been widely studied over the last years. No type inversion is expected even at high fluences as specified for the MVD. The overall annealing behaviour features a long-term stability due to the absence of significant differences in the bias voltages with respect to the pre-irradiation levels [112].

Up to now, three different sensor prototypes have been produced. They differ basically in the thickness of the active n-type epitaxial layer, which ranges between 50 µm and 100 µm. The active layer is deposited on a thinned Czochralski (Cz) substrate wafer thus defining a total thickness of 100 µm, 120 µm and 150 µm, respectively. The provided sensor masks include full-size and single-chip sensors together with diagnostic structures such as test diodes. A photograph of one sensor wafer is shown in figure 4.1, left side. The mask design refers to the ALICE pixel detector with a pixel cell size of 50×425 µm^2 and thus does not represent the precise $\bar{\text{P}}$ANDA geometry. However, the fabricated prototypes are well suited to evaluate main sensor characteristics such as leakage current or depletion voltage and to investigate radiation damage effects.

For the measurements, single-chip sensors were bump-bonded to ALICE pixel readout chips and a standby DAQ system was used for their characterization [115]. A photograph of the setup is shown in figure 4.1, right side. In addition, complementary tests for the overall sensor functionality including leakage current measurements were performed at a probe station [114]. A study of radiation damage was done with test diodes using neutrons from a nuclear research reactor [113].

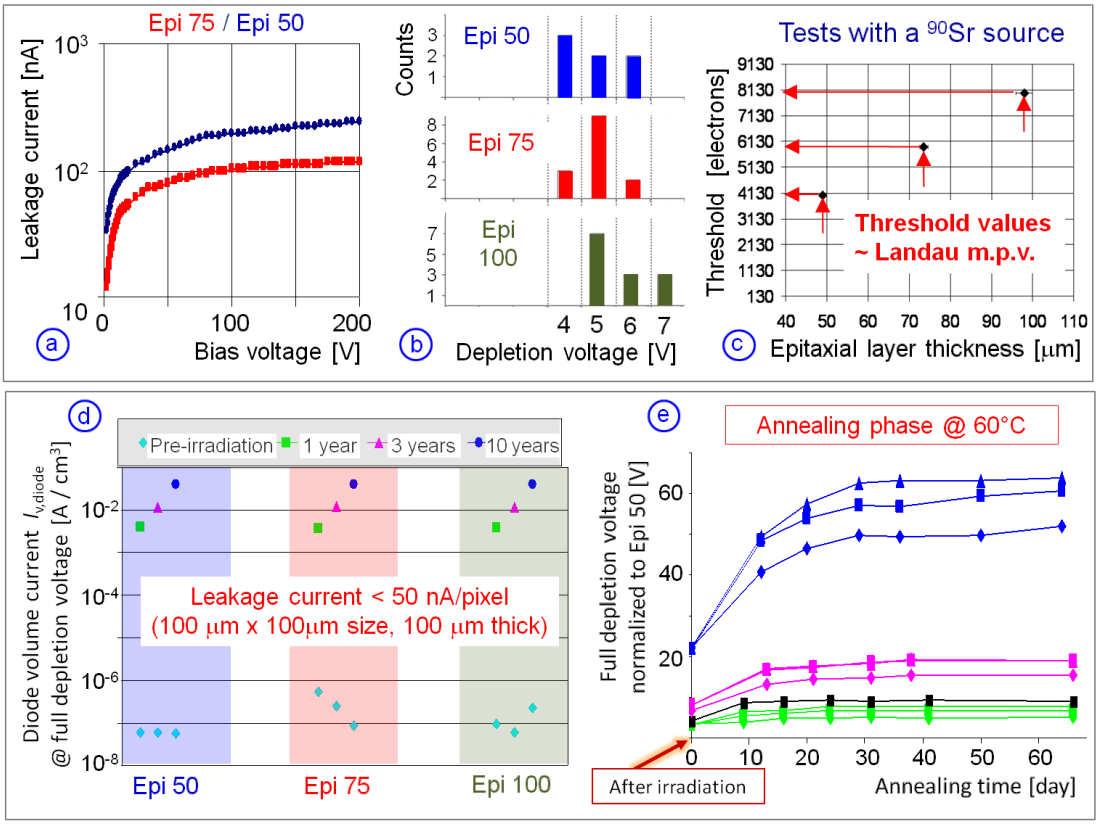

Figure 4.2: Characterization of silicon devices with different epitaxial (epi) layer thicknesses [114] (*top*) and results of radiation damage tests [112] (*bottom*) with: (a) Sensor leakage current versus applied bias voltage, (b) Distributions of the full depletion voltage for diodes of different epitaxial layer thicknesses, (c) Threshold values for minimum ionizing particles (MIP) of a ^{90}Sr source corresponding to the Landau most probable value and being in good agreement with theoretical predictions, (d) Resulting diode volume current at full depletion voltage measured for different epitaxial layer thickness at three different neutron fluxes corresponding to 1 year, 3 years and the full 10 years lifetime of the $\bar{\text{P}}$ANDA experiment, (e) Study of annealing effects for the same irradiated diodes obtained at a temperate of 60°.

Main sensor characteristics and the behaviour of test diodes during and after irradiation are summarized in figure 4.2. Results indicate overall functionality and an acceptable radiation tolerance benefiting from positive annealing effects. Further investigations will concentrate on a tuning of the epitaxial layer resistivity taking into account short and long term annealing components.

4.1.2 Custom made pixel readout chip

The ASIC development for the pixel readout is implemented in CMOS 0.13 µm technology. Basic geometric parameters are given by a quadratic pixel cell size of $100 \times 100\,\mu\text{m}^2$ and

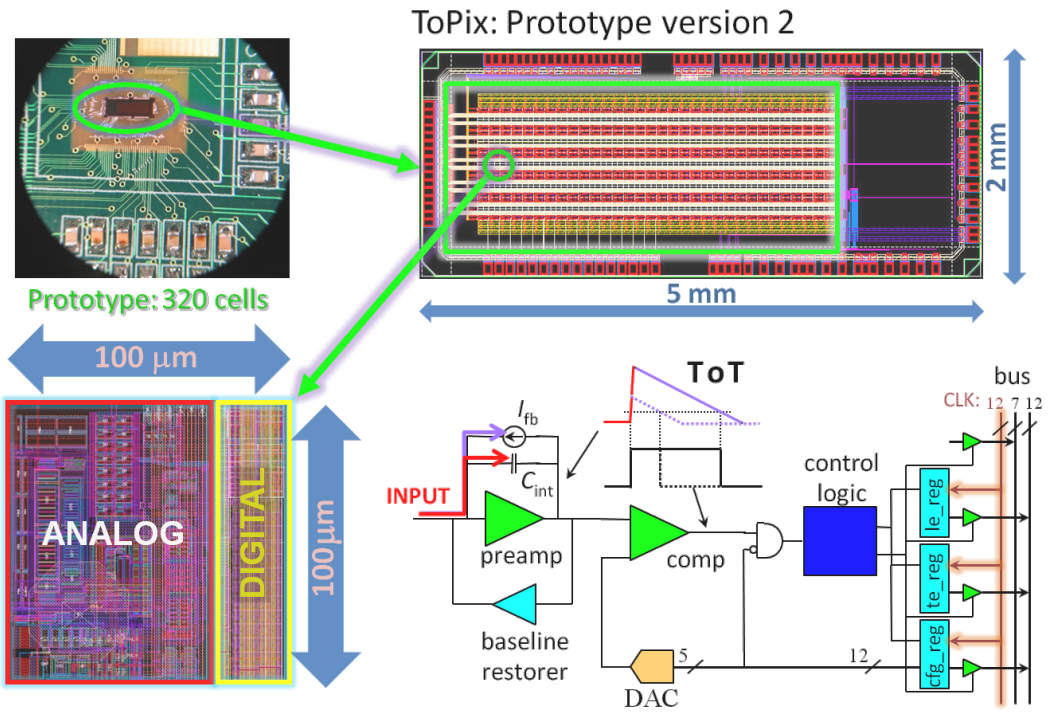

Figure 4.3: *Top*: Photograph of the ToPix chip connected to a testing board (*left*) and schematics of the floor plan for the prototype (*right*) [116]. *Bottom*: Floor plan (*left*) and schematics (*right*) of a single pixel cell [116]. The amplified input signal is discharged with a current feedback source (I_{fb}). A baseline restorer is set in parallel. The output signal of the preamplifier (`preamp`) is analyzed by a comparator (`comp`) externally configurable by a digital-to-analogue converter (`DAC`). Thus, a time-over-treshold (`ToT`) technique can be applied. A 12 bit global clock (`CLK`) distributed on the bus lines delivers the required time stamps. The stored value in the leading edge register (`le_reg`) delivers timing information, while the difference between leading and trailing edge (`te_reg`) time stamps contain the signal amplitude. Configuration data, e.g. the DAC value for the comparator or parameters for the signal shaping, are stored in an individual register (`cfg_reg`). For this purpose 7 bits are reserved on the bus. The output data is transmitted in a 12 bit format.

a total area, which is in the order of $1\,\mathrm{cm}^2$ (see figure 3.3). Experimental conditions and physics requirements demand a high linear input range in combination with a good signal resolution for both time and amplitude. Moreover, hit detection must be performed in a self-triggering mode and a timestamp has to be associated with each hit. The overall cooling system is dimensioned for a maximum power dissipation of $1\,\mathrm{W/cm}^2$. Based on these specifications a dedicated frontend chip named ToPix has been designed and two reduced prototypes were fabricated [118, 119]. They contain 32 single pixel cells and two columns with 128 cells, respectively. The final version will consist of a matrix of 114 pixel rows and 110 pixel columns. A picture of the second prototype is shown in figure 4.3 at the top left.

Each pixel readout cell has an analogue chain to amplify and digitize the charge signal and a digital logic unit to process all hit information. A schematic picture is given in figure 4.3 at bottom. The readout architecture of the pixel is based on an adapted time-over-threshold technique (ToT) [120, 121] allowing a low-power charge digitization without an external trigger signal. Therefore, a comparator threshold is set and the time of a signal above the configured value is evaluated by counting up the increment of global clock cycles. Besides the time difference also an absolute time for the event can be defined by the time stamp of the first clock cycle corresponding to the leading edge of the signal. The ToT technique provides a good linearity and an excellent resolution even in a saturation mode of the preamplifier [117].

The overall ToPix architecture consists of three main functional parts: the pixel column, the end of column logic and the data transmission unit. The latter two must be added to the effective readout area thus extending the dimensions of the readout chip compared to the sensor area. All pixel column cells share the same buses and control lines. Pixel cells with a detected hit are tagged by a busy signal. If at least one of the pixels in a column is active the corresponding data of all pixels containing hit information is sent with fixed priority to the output bus and then stored in a buffer at the end of column logic. Parts of these tasks as well as further data concentration and transmission are carried out by external module controller ASICs driving a number of individual readout chips. In between, appropriate bus cables are needed.

So far, various measurements with the ToPix prototypes were performed in parallel to substantial simulations implementing the whole infrastructure and input data coming from physics simulations. Selected results are shown in figure 4.4. Measurements and simulations are in good agreement and indicate a satisfactory electrical performance. In addition, radiation tests show a good resistance in total dose effects. Further optimization

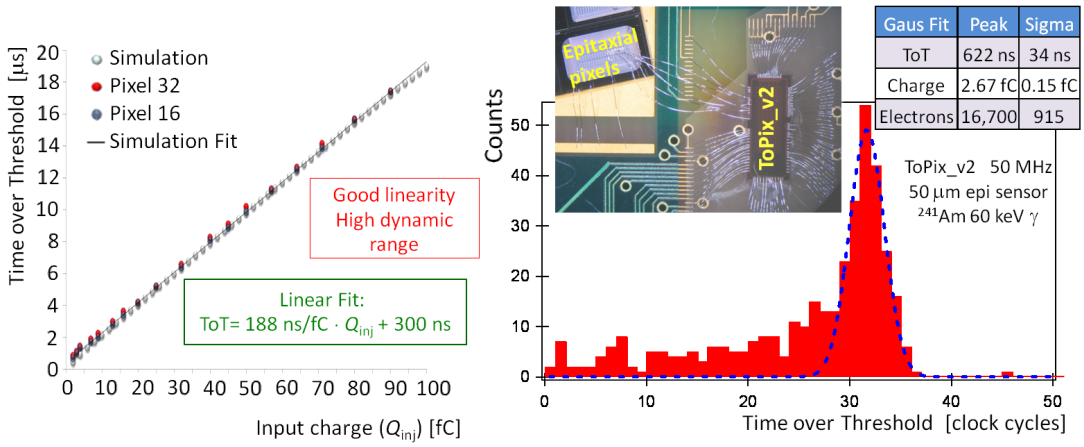

Figure 4.4: Selected results obtained with the ToPix prototype [117] indicating good linearity of the gain over a high dynamic range (*left*) and the successfull calibration measurement performed with an ^{241}Am source (*right*). Some pads were wire-bonded to epitaxial pixel cells. A photograph of the setup is shown in the left inset in the diagram.

is needed for the analogue part of the pixel cell in order to improve somewhat larger variations of noise and signal gain during irradiation. Moreover, work is underway to limit the effects of single-event upsets (SEU). SEU corresponds to a radiation induced flipping of stored values inside an internal latch memory. Finally, an assembly of epitaxial pixels and a ToPix prototype was accomplished using wire bonding connections. A calibration was performed succesfully with a ^{241}Am source.

4.2 Hardware activities for the MVD strip part

The use of double-sided silicon microstrip detectors (DSSD) in the outer layers of the MVD requires a separate R&D program [106]. The readout at both sensor sides requires specific packaging, assembly and interconnection technologies. The overall concept for the MVD is based on a standard process for radiation hard sensors with a target thickness of 200 µm. The proposed technology follows approved solutions of other tracking systems already installed at HEP facilities. Some applications are described e.g. in [122], [123] or [124]. A general description on basic principles is given in [32]. A wafer run of first sensor prototypes for the PANDA MVD is scheduled [125]. As for the entire apparatus the trigger-less readout concept represents one of the major technical challenges and requests the implementation of new technologies. Currently two solutions are under investigation. They refer to ASIC developments at GSI Darmstadt based on the NXYTER front-end chip [126] and an adaptation of the ToPix readout chip to the specific requirements of microstrip sensors [117], respectively.

Initial steps of the hardware development served the purpose of setting up all prerequisites and the infrastructure needed for a proper handling and testing of microstrip sensors.

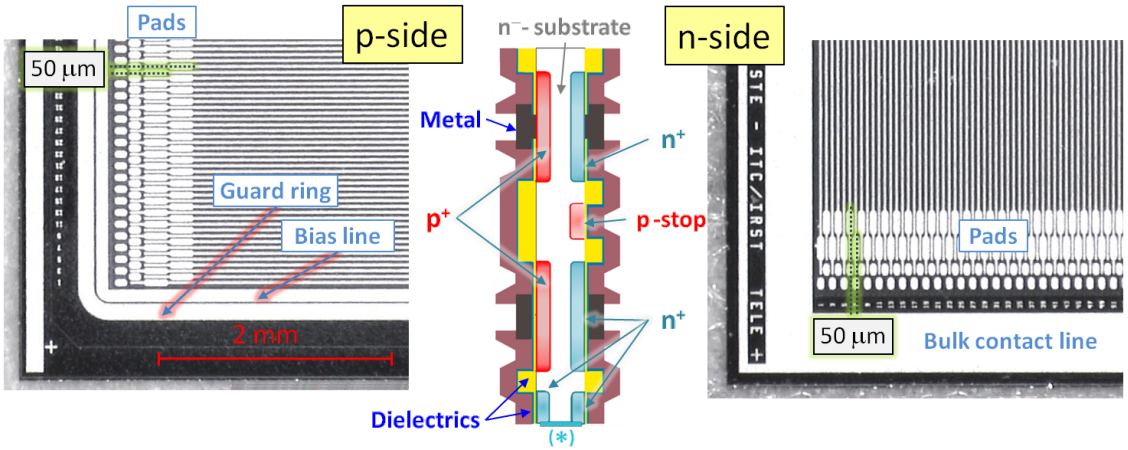

Figure 4.5: Photographs of the metallization on both sides of a double-sided silicon test sensor with a strip pitch of 50 µm and a stereo angle of 90°. It is used in the laboraty setup and the tracking station presented in subsection 4.2.1 and 4.2.2. A schematic cross section through the sensor is illustrated in the middle.

These activities lead to a laboratory setup allowing the characterization of microstrip sensors and connected frontend electronics as well as the performance of first measurements with radioactive sources. Basic concept, assembly and main results of this test setup are outlined in subsection 4.2.1. More details can be found in [127]. Further developments resulted in the set-up of a tracking station which is presented in subsection 4.2.2. One of the main goals for this setup is the development and validation of suited tracking algorithms and the measurement of scattering effects induced by different materials.

4.2.1 Laboratory test setup

The laboratory setup described here provides a fast and flexible way of different testing procedures to evaluate main characteristics of both DSSD and connected frontend electronics. It features a modular concept thus facilitating an adaptation to different sensor and frontend prototypes under study. In a first run, square sensors with a side length of 2 cm and a thickness of 300 µm [129] were used in combination with the APV25-S1 readout chip [128]. Specifications of both components still differ partly from $\bar{\text{P}}$ANDA requirements such as a lower radiation hardness of the test sensor and the request of an external trigger for the front-end ASIC. However, the setup suffices for a proof of basic concepts, the setup of an adequate data acquisition and the development of analysis tools needed in future $\bar{\text{P}}$ANDA applications.

Shape and dimensions of the implemented test sensor are similar to the one defined for the MVD barrel sensors. Moreover, the stereo angle of 90° between the strips of both sensor sides is compliant. The strip pitch is 50 µm and thus corresponds to the lower limit as specified in figure 3.4 on page 69. Therefore, the hybridization of appropriate detector modules provides important input on technical details such as mounting procedures and feasible techniques for the electrical connection at very small dimensions.

A photograph of the test sensor is shown in figure 4.5. It is glued to L-shaped circuit boards thus allowing a double-sided readout with one common design. Electric connections

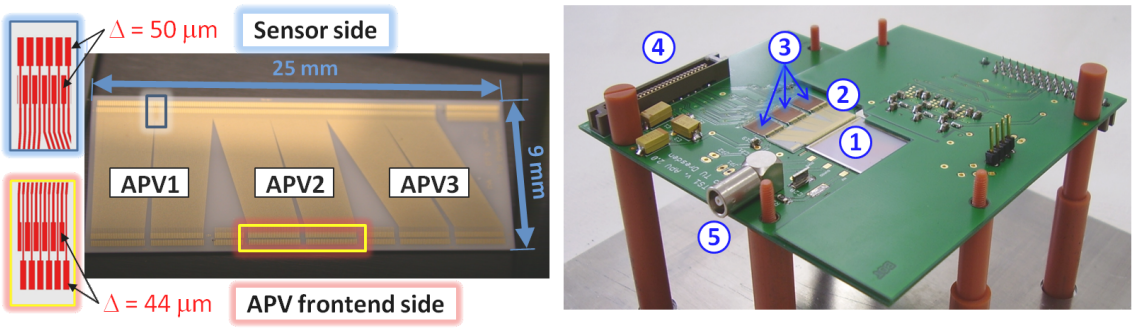

Figure 4.6: Photographs of the fabricated pitch adapter (*left*), leading from the readout pitch of the sensor to the needed structure of the APV frontend chip [128], and a complete sensor module (*right*) using two identical L-shaped PCB boards for the double-sided readout. Main components are: (1) Sensor; (2) Pitch-adapter; (3) Frontend chips; (4) High-density connector for power supply, slow control, data output; (5) HV connection for sensor supply.

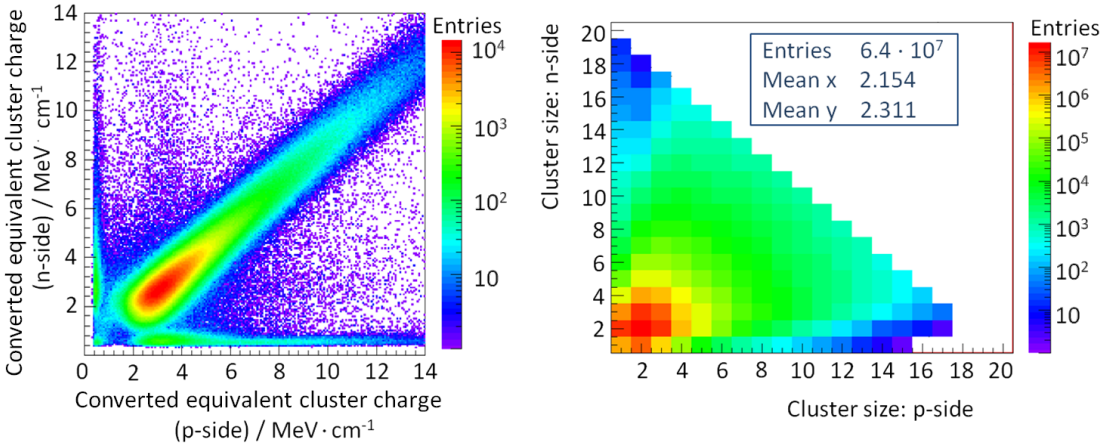

Figure 4.7: Results of long-term measurements with a ^{90}Sr source: Correlation of deposited energy (*left*) and cluster size (*right*) for both sensor sides (p-side and n^+-side).

are done by wire-bonding. A ceramic pitch adaptor is introduced in between sensor and readout chip. It allows parallel straight-line connections between corresponding pads. This specific requirement is given by technical limitations of the applied wire-bonding process due to the small dimensions. A similar solution for both, adapter component and electrical connection, is defined as default solution for the MVD. Photographs of the pitch adapter and a complete detector module are given in picture 4.6. A detailed description of the software and data acquisition implemented for the laboratory setup can be found in [127] and [130].

An extended characterization of both sensor and connected frontend chip has been carried out proving the full functionality of the setup [131, 132]. In the following, measurements with a β-emitter (^{90}Sr) were performed. Selected results are shown in figure 4.7. On the left, the charge collection of both sensor sides is plotted. It exhibits a linear correlation thus indicating a proper operation of the sensor. The slope is slightly smaller than unity due to the higher charge collection efficiency for electrons on the n^+-side compared to the one for holes at the p-side.

The extracted hit coordinates represent the most important data. In order to visualize the spatial resolution capability of the detector, an SMD device was placed on top of the sensor acting as an absorber for the β-electrons emitted by the ^{90}Sr source. The resulting image is shown in figure 4.8 on the left. On the right, the fitting procedure used to obtain the image resolution is shown exemplarily for one selected 1D profile. The same has been performed for 22 different profiles within the selected area indicated on the left side of figure 4.8. The image resolution is determined to 49($\pm$7) µm (FWHM), which is the average value of all 22 analyzed edges. The given error is equal to the standard deviation of the average of all measurements and dominated by scattering of the electrons of the ^{90}Sr source, which have rather low momenta. An extraction of the intrinsic spatial resolution for single hit points in the sensor requests advanced methods to be performed with a more complex experimental setup such as e.g. the tracking station described in the next subchapter.

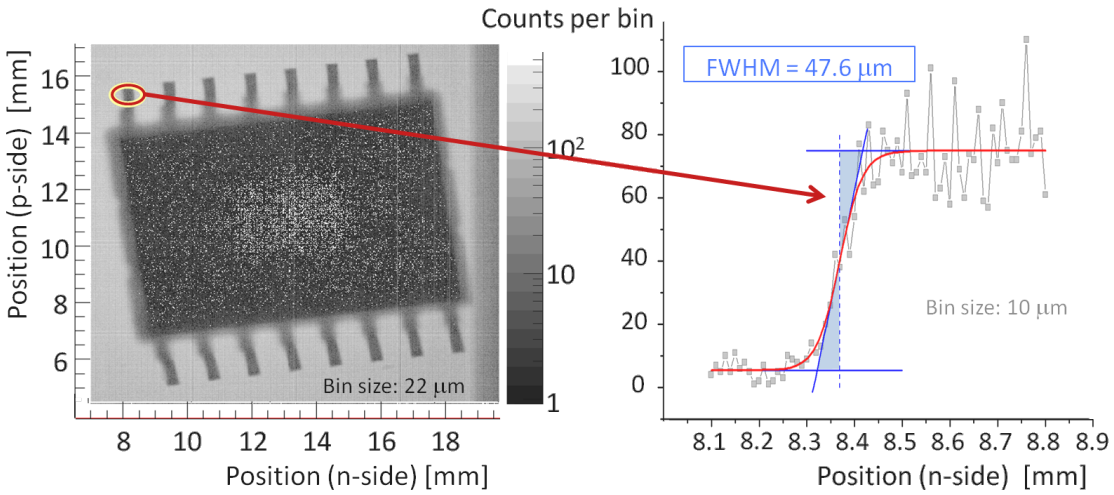

Figure 4.8: 2D imaging of a SMD device placed on top of the sensor and acting as an absorber for the β-electrons of a ^{90}Sr source (*left*). *Right:* Example of an extracted 1D profile at the edge of one of the legs. The image resolution of $\approx$ 50 µm obtained by a fitted S-curve is driven by scattering effects of the electrons and thus it does not not represent the intrinsic detector resolution.

4.2.2 Tracking station

The installed laboratory test setup delivers basic input to an advanced system of double-sided silicon strip detectors [133]. It consists of four sensor boxes hosting four of the same detector modules as illustrated in figure 4.6. Optionally, a fifth sensor box or an additional scattering body can be placed in the middle of the overall setup. In this way, it is possible to track fast charged particles and to study the scattering effects of different materials. For a suitable application, highly energetic particles are necessary to obtain a track point in each sensor. Hence, measurements must be performed at appropriate accelerator facilities where the tracking station operates as a beam telescope. Besides sole mechanics extensions, a sophisticated FPGA based readout and data acquisition concept is implemented for the tracking station [134, 135]. Both the evaluation of powerful FPGA algorithms for particle tracking and the investigation of scattering properties of different materials are crucial for the MVD development.

Experiment	Particle species	Particle momentum	Stored data
COSY	protons	0.8 GeV/ 2.95 GeV	71 million events
B1	photons	$\leq$ 2 GeV	14 million events
DESY	electrons	1 ... 5.4 GeV	146 million events

Table 4.1: Beam time measurements with the tracking station.

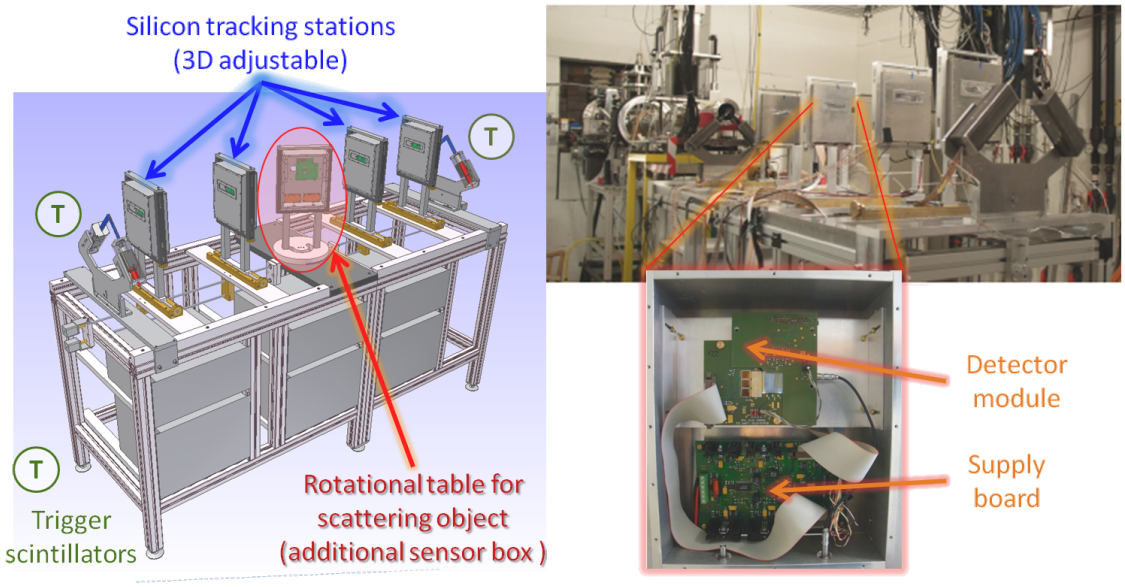

Figure 4.9: CAD drawing of the silicon tracking station (*left*) and photograph of its experimental setup at the COSY accelerator (*right, top*). *Right, bottom*: View inside an opened sensor box. The used detector modules are the same than the ones for the laboratory setup (see figure 4.6, on the right side).

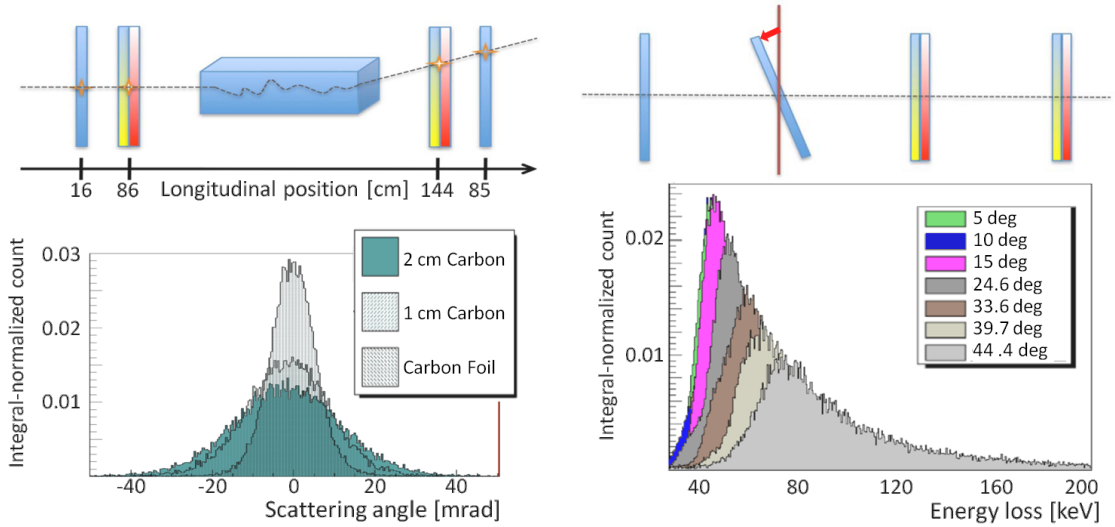

Figure 4.10: Results obtained with the tracking station: Distributions of the projected scattering angles obtained with 2.95 GeV/c protons crossing different scattering materials (*left*) and the energy loss of 4 GeV electrons in a double-sided detector rotated with respect to the beam direction (*right*). Measurements were performed at COSY and DESY, respectively.

A schematic picture of the tracking station is shown in figure 4.9, left side. The four sensor boxes for particle tracking can be moved in all three dimensions thus allowing an alignment with respect to the beam axis. The experimental table in the centre of the station is rotatable. In this way, different effective path lengths of crossing particles in scattering objects can be studied with the same experimental settings. First measurements have been performed during beam times at different facilities thus allowing a study with protons, electrons and photons at different energy regimes. They are summarized in table 4.1. The analysis of the large data samples collected has started. So far, the software alignment of the sensors needed for a precise reconstruction of particle tracks is accomplished. Simplified tracking algorithms are developed and tested [136]. First results based on a simple two-line approach are given exemplarily in figure 4.10. Further studies will facilitate a comparison with simulation results [137].

4.3 Integration work

Besides specific R&D programs focussed on the two different detector technologies, other parts of the hardware development overlap for both parts benefiting from synergy effects for the work on cooling and support structures, cables and elements for the signal transmission. Engineering solutions for the overall detector assembly and installation sequence can be tested using a full-scale mechanical mock-up. Main activities related to these aspects are briefly summarized in the following.

→ Lightweight support structures

The material load introduced by mechanical support structures must be minimized. Therefore, the use of lightweight carbon support structures is foreseen. They are based on carbon fibre layers with a thickness of 200 µm up to 400 µm and lighter foam materials with sufficient thermal conductivity. The latter allow a manufacturing of larger components with higher stiffness and represent a low mass solution compared to solid structures. Moreover, local support structures for detector modules can act as a heat bridge between frontend electronics and cooling pipe. For most parts of the MVD support a combined sandwich structure will be used to reduce the overall radiation length. Therefore, carbon foam or another light foam material will be used on the inner part, which is embedded in carbon fibre layers.

First prototypes of various components have been manufactured. Their design is based on a detailed CAD model that exists for the MVD (for more details see chapter 5) and dedicated FEM simulations. Examples of first produced support components are compiled in figure 4.11. One of the biggest challenges in terms of stability and reproducibility is given by the requirement for half-cylindrical support structures for the different detector layers and the global MVD frame. Further optimization will be accomplished imposing experimental results of e.g. stress tests and the measured thermal behaviour. Besides, feasibility studies of more complex carbon structures are underway, which will deliver important feedback to the overall detector design.

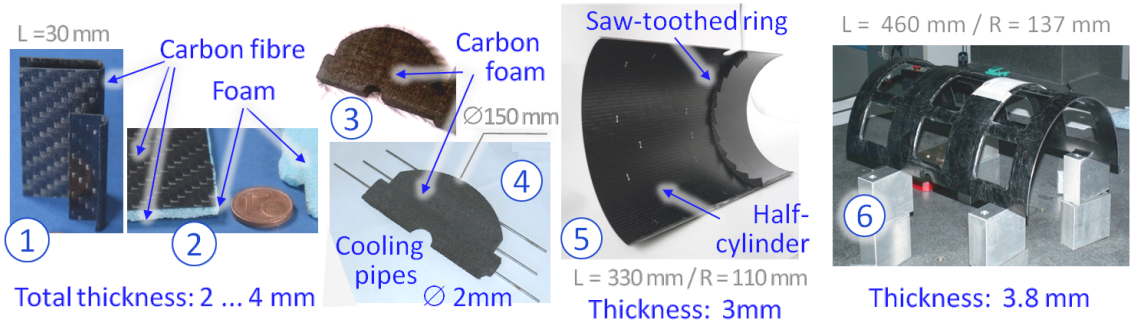

Figure 4.11: Photographs of manufactured carbon support prototypes. (1) Bend carbon fibre layers (thickness 400 µm) utilized for the local support of barrel supermodules, (2) Sandwiched structure made of carbon fibres embedding a light foam material [138], (3) Cut-out slice of carbon foam for the pixel disk support. Water cooling is applied during cutting, (4) Final support structure with cooling pipes between two glued half-disks. Cut foam slices are baked out and drilled to integrate the pipes, (5) Strip barrel support made of a sandwiched carbon structure. Water cutting was used to obtain the saw-toothed ring stick onto the half-cylinder, (6) First full-scale prototype of the global MVD half-frame using a sandwiched carbon structure.

→ Low-mass cables

The material load introduced by cables is significant. The research on appropriate low-mass cables for the MVD has started. First prototypes of thinned bus cables with a total thickness of about 50 µm to 70 µm have been produced [139]. Basically they consist of an aluminium structure with a thickness between 7 µm and 15 µm which is deposited or laminated on both sides of a kapton layer. Both cable samples thus deliver a differential pair in a folded layout. So far, the prototypes could be produced with a total length of 1 m. First tests indicate overall functionality for a transmission rate up to 2 Gb/s. In addition to further studies on the developed prototypes, the search on customized solutions commercially available is ongoing.

→ Cooling systems

The work on cooling systems for the MVD comprises measurements at appropriate test setups in combination with thermal simulations. First prototypes for the inner cooling systems have been developed. In accordance with the default solution for the MVD cooled water is used as cooling fluid. The coolant is distributed in thin pipes with a wall thickness of 80 µm and an outer diameter of 2 mm. They are made of a special nickel-cobalt alloy and embedded in carbon foam acting as local support and heat exchanger.

A photograph of the test setup developed for barrel detector modules is shown in figure 4.12, at the top left. Next to it, first test measurements are compared to simulation results. Both are in good agreement. An effective cooling of all elements in the barrel part below 30°C can be achieved by an improved contact area of the cooling pipe with the heat bridge. Another test setup representing a reduced prototype for the pixel disks

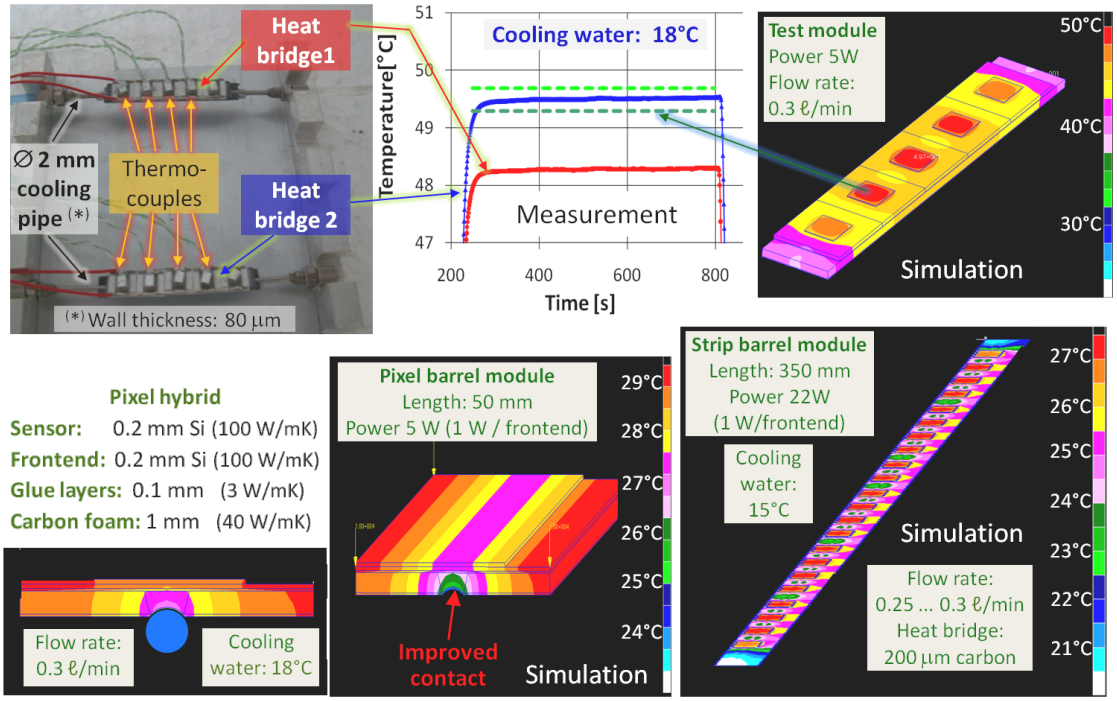

Figure 4.12: *Top*: Photograph of a test setup of a cooling system for the barrel part (*left*). Obtained measurement results (*middle*) are in good agreement with thermal simulations (*right*). *Bottom*: Simulations with an improved contact surface between cooling pipe and carbon foam. Results indicate achievable temperatures below 30°C for both pixel and strip modules.

delivers similar results. It is shown in figure 4.13. Moreover, the small dimensions of the cooling pipes and the restricted space inside the MVD require a miniaturization of appropriate cooling connectors. First prototypes made of thermoplastic resin have been manufactured [140].

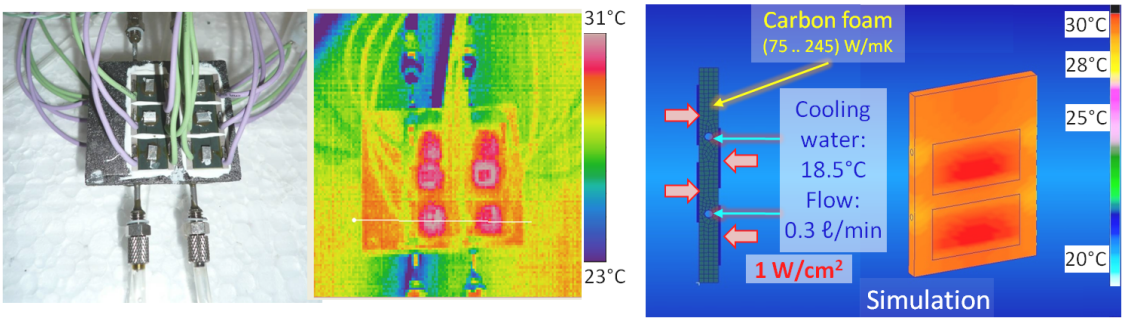

Figure 4.13: Photograph of a reduced cooling test system for the pixel disks (*left*). The picture taken by an infrared camera (*middle*) indicates a good agreement of measured values with thermal simulations (*right*).

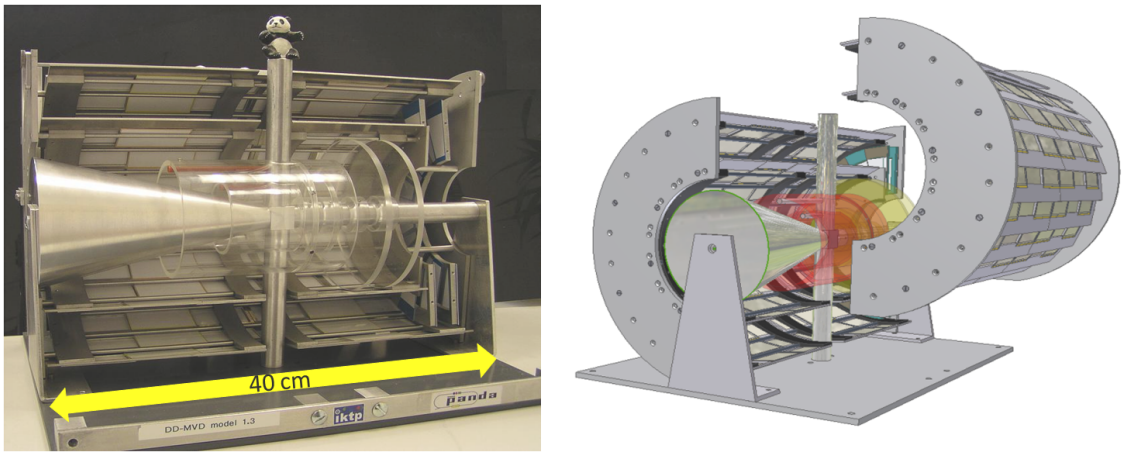

Figure 4.14: Photograph (*left*) and associated CAD model of the full-scale mechanical mock-up of the MVD (*right*).

→ Full-scale mechanical mock-up

A full scale mock-up made of aluminium has been built [141] to extract a feasible mechanical concept for the MVD. It focused in detail on the microstrip part of the MVD. Besides the setup of basic conventions for the CAD development [142], main ideas of this work, e.g. concerning the individual layer support, were adopted for the actual MVD design presented in chapter 5. The mock-up also serves as a test object for the routing procedure inside the MVD, the installation sequence and the overall handling of the MVD half-detectors. A sketch of the underlying CAD model and a photograph of a fully assembled half-detector are shown in figure 4.14.

5 Development of a detailed MVD model

The introduction of a realistic detector description for the MVD is an essential part of the present thesis. Within the scope of this objective a comprehensive detector model has been developed. It follows the conceptual design as presented in chapter 3 and is based on the input of the engineering developments summarized in chapter 4. The evolved design represents an optimization between physics requirements and technical feasibility. A 3D-CAD software [143] was used for its implementation. The complete model was successfully integrated into the simulation software of PANDA [144]. In this way it is possible to perform dedicated simulations allowing a survey of main detector properties as well as the analysis of selected benchmark channels for a test of physics performance. Outcomes of these simulations will be presented later, cf. chapter 6.

Introductory remarks on the general approach are given in section 5.1. The optimization of sensor dimensions and their geometric arrangement in the different detector layers is outlined in section 5.2. Section 5.3 contains the input of engineering models. The finalized detector version Mvd-2.1 is described in the last section 5.4. It also explains the integration of the developed model into the simulation software. A sketch of the MVD-2.1 version is presented in figure 5.1.

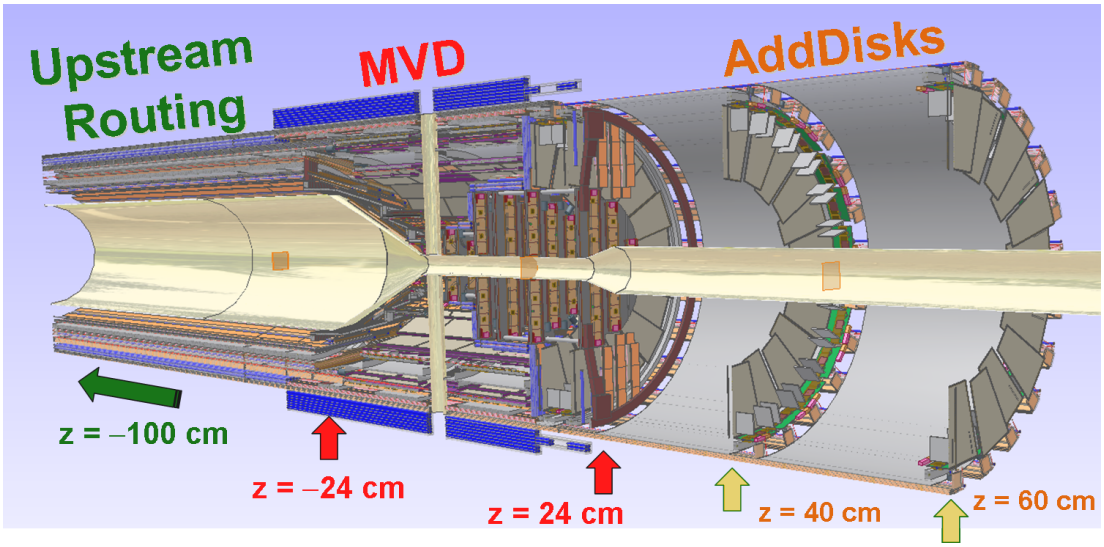

Figure 5.1: CAD drawing of the developed model MVD-2.1 consisting of the additional forward disks (AddDisks), the central MVD and the associated upstream routing. For illustration the model is cut at the YZ-plane along the beam pipe. Corresponding axial positions are given below.

5.1 General approach

The main goal of the CAD development for the MVD is to obtain a realistic model that respects technical requirements and contains feasible solutions for the final detector assembly. Initial point for this work is the configuration of active sensor elements inside the MVD. It defines the number of associated passive elements such as readout chips, cooling pipes, cables or support structures and must ensure sufficient space for their integration. Therefore, an optimization is needed.

The design of further components is based on engineering input. Simulations and, if existent, measurements with available prototypes warrant the abidance by required technical specifications. The resulting model contains a very comprehensive detector description. In terms of physics relevance there are two categories: Active elements delivering hit points for the measurement and passive elements, which basically affect the behaviour of crossing particles without contributing any information.

Associated physics studies on the overall detector performance refer to the hit information extracted from induced signals in the sensors and the impact of the introduced material budget on the entire measurement. Consequently, the given engineering model must be adapted to the needs of physics simulations. Basic conventions and a proper definition of the hierarchy are indispensable to handle accurately the complex structure of the model and, in particular, to merge properly different standards defined for mechanical engineering and physics analysis [142].

Geometric conventions for the CAD modelling are given by the definition of the global coordinate system in the PANDA simulation software. It corresponds to a Cartesian system in which the z-axis coincides with the beam axis. The y-axis running from bottom to top is in opposite direction to the motion of the target particles. The origin is equal to the nominal interaction point. All basic definitions are depicted in figure 5.2, on the left side.

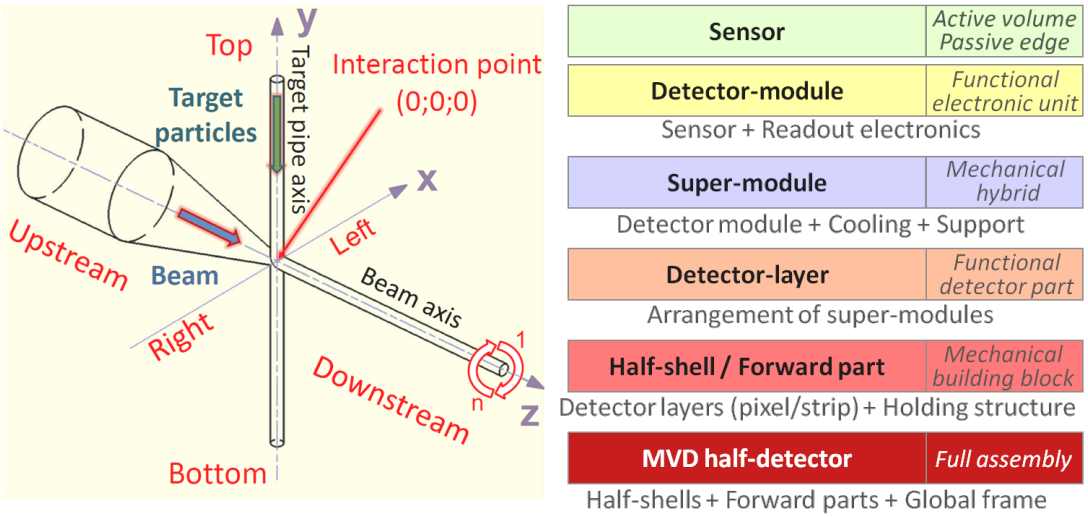

Figure 5.2: Definition of the global coordinate system (*left*) and the hierarchical structure of the MVD models (*right*).

The hierarchical structure of the CAD models is based on a modular concept following the future test and installation sequence of the detector. The silicon sensors represent the lowest level therein. A detector module is defined as the smallest functional unit which is electronically independent. It is formed by all hard-wired connections between individual sensors and assigned components of the readout electronics. The finalized hybrid is formed by a super-module including several detector modules and the associated cooling and support structure. It corresponds to the smallest mechanically independent unit for the detector assembly. Different detector layers are then composed of super-modules which are attached to the respective mechanical holding structure. In this way four main building blocks are created. They are given by the individual pixel and strip layers forming two half-shells in the barrel part and two half-disk structures in the forward part. The half-detector concept is required due to the target pipe which crosses the entire MVD volume. A schematic picture of the hierarchy is given in figure 5.2, on the right side.

5.2 Design optimization

Mechanical detector models are derived from the sensor configuration inside the MVD. Hence, a precise definition of both sensor dimensions and positioning is an important prerequisite needed for a profound detector concept. Main guidelines are given by the conceptual design and the defaults for the sensor geometry outlined in subsection 3.3.2. Furthermore, boundary conditions result from integration aspects. They are related to the space requirement of supplementary components needed for cooling, readout electronics and support structures. Moreover, additional safety margins must be included. They are important for the overall detector assembly including the routing and installation sequence.

The performed design optimization results in a fixation of sensor sizes and basic parameters for the layer composition that permits for an optimum coverage and a problem-free mechanical integration. Due to the different approaches a separate discussion is given for the pixel and strip part in subsection 5.2.1 and 5.2.2, respectively.

5.2.1 Pixel part

The main approach for an optimization of the pixel geometry is schematically shown in figure 5.3. Basic input for the sensor dimensions is given by the specified matrix size of the ToPix readout-chip (see subsection 4.1.2). The extracted sensor layout is based on a coverage optimization for the forward disks [145]. The main free parameter is the number of associated readout-chips. They are aligned in one row thus defining one common sensor width. Fine tuning is possible by a slight enlargement of pixel cells at the edges of each readout matrix. In this way the 200 µm rim of the ToPix readout chip can be accommodated.

Precise measures of the implemented pixel sensors are given in figure 5.4. The active area of the sensor is surrounded by a passive edge. It contains a protective guard ring and defines along with the specified sensor thickness of 200 µm the maximum volume of sensor elements with respect to their mechanical integration. It should be noted that for a proper functional description of the sensor the effective sensitive detection volume must be taken into account. As a consequence, smaller signal amplitudes results from the envisaged

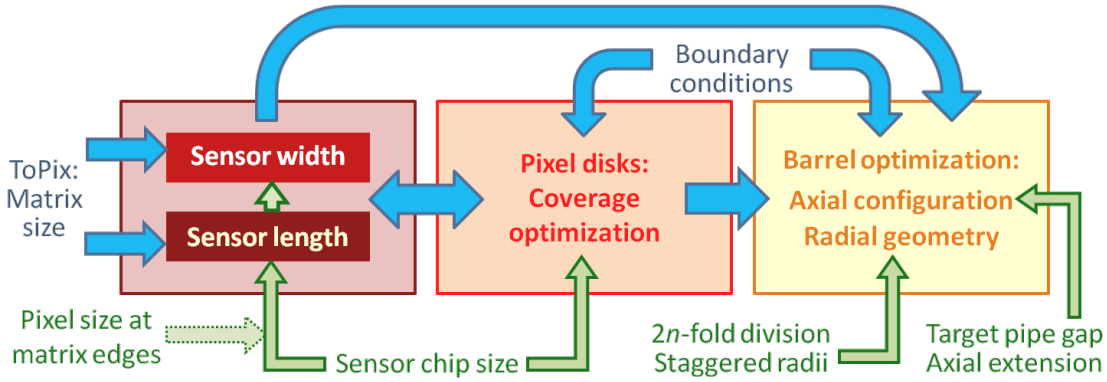

Figure 5.3: Schematics of the design optimization for the pixel part. Constraints are indicated in blue, free parameters for optimization in green. Boundary conditions refer to space requirements of additional components including the dimensions of the ToPix readout-chip, given constraints from the conceptual design and safety margins needed for the overall integration.

thickness of 50 µm to 100 µm for the active epitaxial layer. The physical dimensions of the ToPix readout chip must be considered for the sensor arrangement due to the hybrid design of the pixel detector. In particular, the extended width of 14.8 mm needed for the end-of-column logic results in an asymmetric extension of the detector-modules.

The optimized sensor configuration for the pixel disks is shown in figure 5.5. It is driven by the outer dimension of the beam pipe, which limits the inner diameter to 22 mm. The

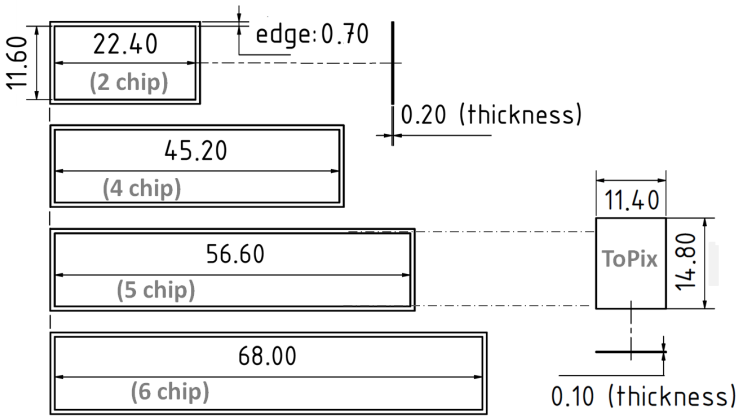

Figure 5.4: Final pixel sensor sizes (*left*) and dimensions of the ToPix readout chip (*right*) as introduced into the MVD model. Assuming a matrix of 114 × 110 for the readout chip, enlarged pixel cells at the edges are needed to accomodate the rim of 200 µm (in length) and to cover the full width of the active area. The latter can be avoided by an updated design of the readout chip with 116 instead of 114 pixel rows. The total ToPix width of 14.8 mm includes additional space needed for the end-of-column logic. Measures given in mm.

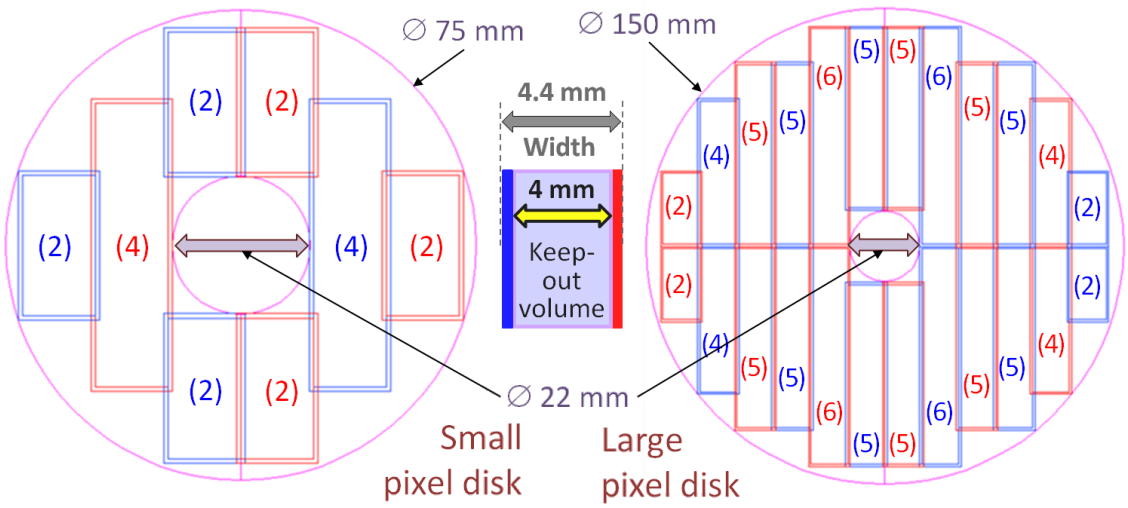

Figure 5.5: Optimized sensor configuration for the pixel disks. Bracketed numbers correspond to the sensor chip size as defined in figure 5.4. Different colours indicate the sensors positioned on the front and rear side. The intermediate keep-out volume is reserved for readout electronics, cooling and support.

specified outer diameters for the small (75 mm) and the large pixel disk (150 mm) include appropriate safety margins for the disk insertion inside the barrel layers. Alternating arrangement on the front and rear side of the disk support structure is needed to achieve sufficient radial coverage. The presented solution delivers a total coverage of 65% and 82% for the small and the large disk, respectively. The axial extension of the pixel disks is defined by the sensor thickness and an additional volume with a width of 4 mm reserved for the cooling and support structure inserted in between the sensors at the front and rear side of one half-disk.

The barrel layers are formed by a staggered double-ring arrangement using the same sensor types as were introduced for the pixel disks. The radial geometry is adjusted based on the common sensor width. The optimum number of circularly arranged elements for each barrel layer can be easily extracted from the sensor width and the circumference at the predefined radius given in the conceptual design (see table 5.1). An even number is required to facilitate the half-detector concept. Free parameters for further layer optimization are the two staggered radii for adjacently arranged sensors. A picture of the final barrel

Radius (chapter 3.2)	Circumference c	Active sensor width d_{act}	c/d_{act}	Number of elements	Residual overlap
25 mm	157 mm	11.6 mm	13.47	14	0.38 mm
(Barrel 1)				16	1.8 mm
50 mm	314 mm	11.6 mm	27.08	28	0.39 mm
(Barrel 2)				30	1.1 mm

Table 5.1: Extraction of the optimum number of elements for the pixel barrel layers.

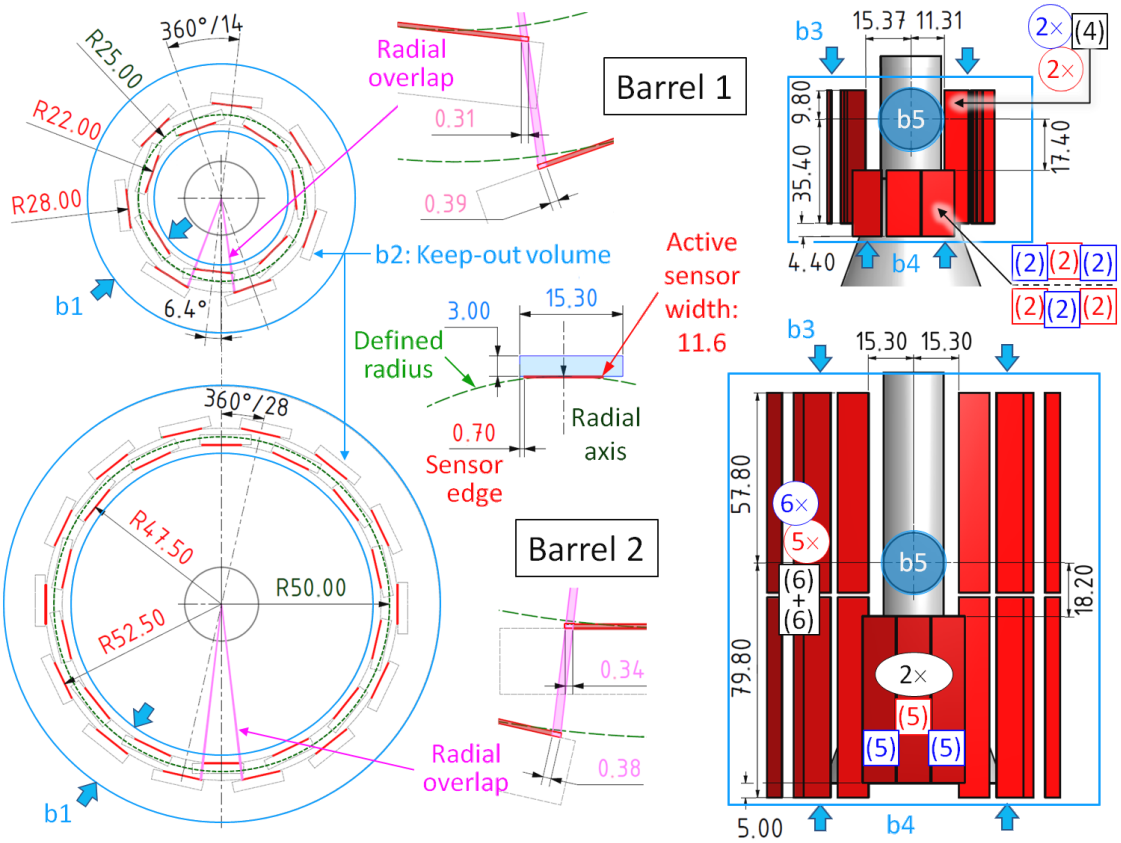

Figure 5.6: Optimization for the pixel barrel layer: Radial geometry (XY front view, *left*) and axial configuration (*right*). Boundary conditions are given by constraints on the radial layer extension (b1), the keep-out volume defined for individual super-modules (b2), the subsequent forward pixel disks placed in front of the pixel barrels (b3), the opening cone of the beam pipe in upstream direction (b4) and the crossing target pipe (b5). The final circular arrangement ensures a minimum radial overlap of more than 300 µm. The staggered radii and the average design radius are written in red and green, respectively. The introduced keep-out volume accounts for readout-electronics, cooling, local support and an additional safety margin for assembly. Bracketed numbers in the axial configuration correspond to the sensor chip size (see figure 5.4). Blue and red colours indicate the position at the inner and outer radii within the layer, respectively. All measures are given in mm.

geometries is shown in figure 5.6, left side. The fixed configuration delivers sufficient radial overlap while respecting all boundary conditions including an appropriate keep-out volume for the individual super-modules. Additionally, a rotation of the overall barrel geometry is used for the first barrel layer in order to warrant sufficient space of all passive elements to the target pipe.

Besides the radial arrangement, an additional adjustment is necessary for the axial sensor configuration. Constraints are given by the first pixel disk and the beam pipe opening in

downstream and upstream direction, respectively. Moreover, a passageway for the target pipe must be introduced. Therefore, different sensor types are utilized within one layer. The target pipe gap is left open in downstream direction due to technical reasons related with the feasiblity of the barrel integration. Details are shown on the right side of figure 5.6.

5.2.2 Strip part

The optimization for the barrel and the forward strip layers can be performed separately due to the different sensor types. Associated concepts are shown schematically in figure 5.7. In contrast to the pixel part there are no direct predefinitions for the sensor segmentation due to the readout chip. As a consequence, the strip pitch is one of the main optimization parameters. An approximate range is given by the average track deviation related to scattering effects in the previous pixel layers. Calculated values for the mean scattering angle and the associated deflection of tracks are shown in figure 5.8, on the left side. They are obtained with an empirical formula for the multiple scattering in a Gaussian approximation given by Lynch and Dahl [146]. Plotted results for a silicon thickness of 0.6 mm and 1.2 mm represent the minimum effective path lengths of particles crossing two and four pixel layers, respectively. Assuming a minimum free flight path of roughly 10 cm between the pixel and the barrel layers the resulting scale of the lateral track resolution is in the order of a few hundred micrometers. A lower bound results from technical limitations due to the bonding process. It is set to 50 µm thus corresponding to the strip pitch of the test sensors presented in subsection 4.2.1.

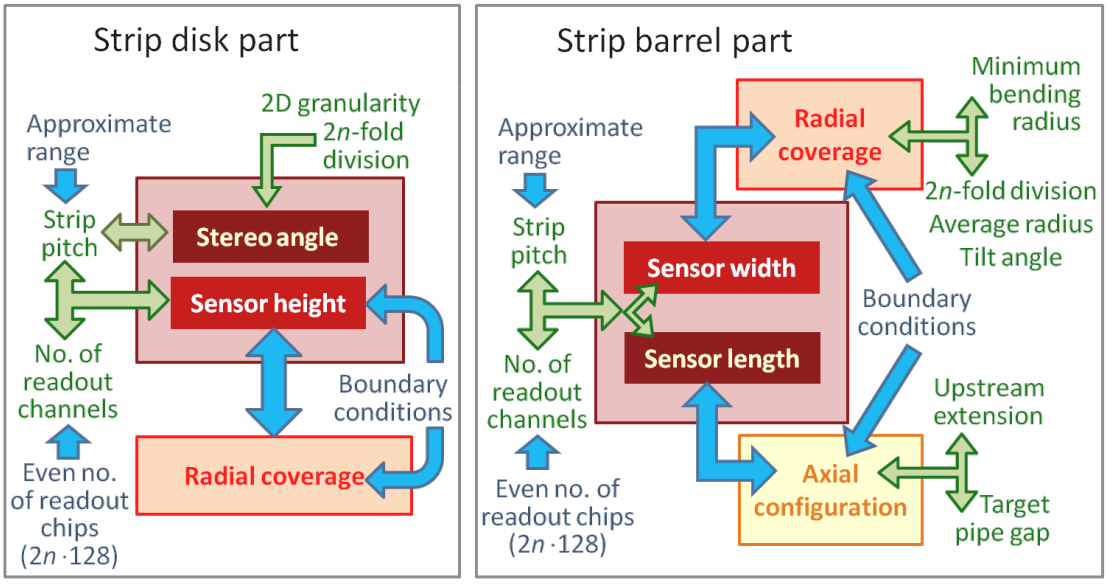

Figure 5.7: Schematics of the design optimization for the strip disk (*left*) and the strip barrel part (*right*). Constraints are indicated in blue, free parameters for optimization in green. Boundary conditions refer to space requirements of additional components, given constraints from the conceptual design and safety margins needed for the overall integration.

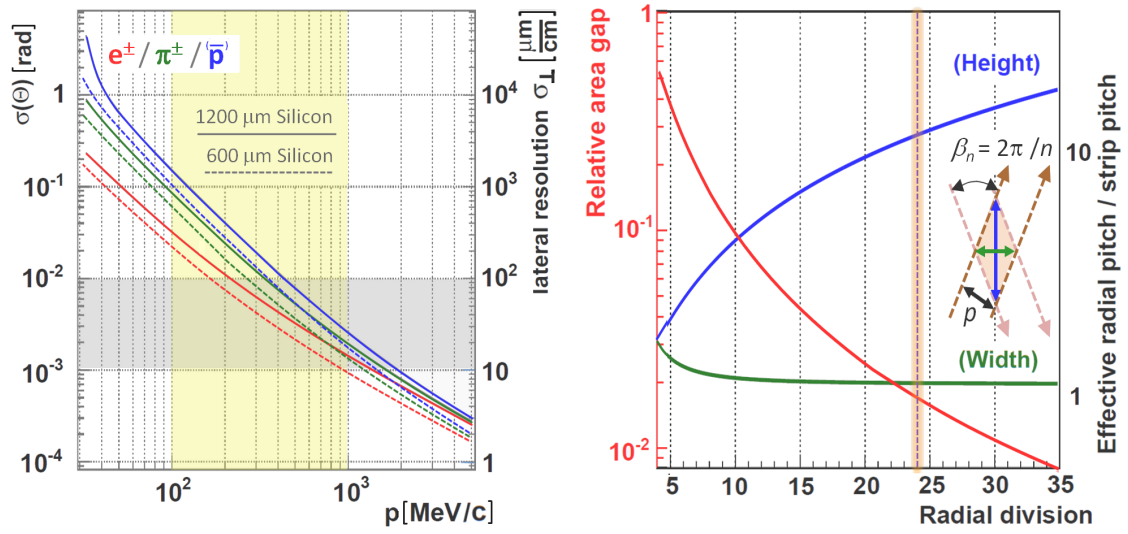

Figure 5.8: *Left*: Mean scattering angle, $\sigma(\Theta)$, and the associated particle deflection, $\sigma_\perp$, as a function of the particle momentum, p, for two effective silicon layer thicknesses. Values for electrons, pions and protons were calculated with a Gaussian approximation [146]. The relevant momentum range is highlighted in yellow. *Right*: Optimization of the stereo angle for the trapazoidal sensors. Relative area gap (red) and effective segmentation are plotted against the radial division of the disk layer assuming a ratio of two between the outer and the inner radii. The gap results from the approximation of the annular ring with trapezoids. The effective segmentation given by the short (width) and the long diagonal (height) of the resulting diamond is shown as inlet.

The spatial resolution of the sensor results from the strip pitch and the stereo angle between the strips on both sensor sides. The stereo angle for the barrel sensors is fixed to 90° thus delivering a maximum granularity. In case of trapezoidal sensors the pitch corresponds to the radial division of the disk layer which is required to be even to allow the introduction of two identical half-disks. A diamond-shaped area results as smallest segmentation unit due to the reduced stereo angle. The effective radial pitch enlarges concomitantly. Consequently, both radial division and strip pitch must be optimized with respect to the resulting 2D segmentation (see figure 5.8, right side). The chosen stereo angle of 15° associated with a 12-fold geometry represents a good compromise between high radial coverage (98.3%) and small segmentation. The latter results in a ratio of 7.66 for effective pitch of the long diagonal with respect to the nominal strip pitch. Therefore the strip pitch for the trapazoidal sensors must stay well below 100 µm to deliver an effective segmentation in the approximate range as defined in figure 5.8 on the left.

The total number of strips has to match the connected readout chips with 2^n input channels. A typical value of 128 channels is currently specified for the MVD readout chip [147]. The final strip number on one sensor side is required to be consistent with an even number of connected readout chips thus taking into account further frontend developments with eventually 256 input channels. In all cases, a passive edge of 1 mm

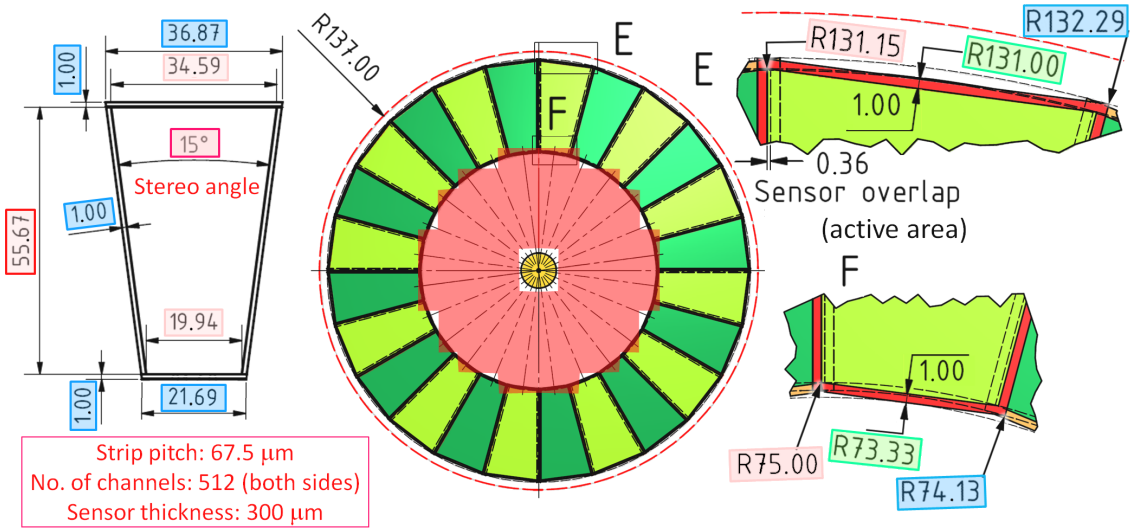

Figure 5.9: Dimensions of the trapezoidal strip sensor (*left*) and front view (XY) of the composited strip disk layer (*middle*). The associated pixel disk area is highlighted in red. Maximum radial extensions of the strip disk layers are shown on the right. All values are given in mm.

around the active area must be considered. It is needed for the guard ring in a standard radiation-hard design. The defined thickness of 300 µm for all strip sensors represents an upper limit with respect to the physical dimensions. The envisaged target thickness of about 200 µm will fall short of this value. Associated effects must be considered properly in the simulations e.g. for the induced charge quantity and its distribution to adjacent readout strips. Final considerations are related to the overall senser size. The total area must allow for an effective exploitation of the silicon wafers used for the sensor production. Moreover, the unnecessary introduction of large hit multiplicities in the final application due to an oversized sensor must be prevented.

With the fixed radial division of the strip disks final measures of the trapezoidal sensors result from the definition of the circular ring to be covered. The minimum radius must accommodate a full overlap with the corresponding area of the inner pixel disk while the outer radius is restricted by boundary conditions needed for the introduction of associated passive elements and the overall mechanical integration of the strip disks. Moreover, a small radial overlap of adjacent sensors is required. In this way it is possible to adjust the side length at the top of the sensor with the strip pitch to obtain a total number of $2n \times 128$ readout channels. The final layout of both, trapezoidal sensor and disk layer, is shown in figure 5.9.

The optimization of sensor dimensions for the barrel part is connected to the radial geometry for the width and the axial configuration for the length, respectively. Particular considerations have to be taken into account due to the fan-like sensor arrangement. It introduces a tilt angle of individual elements as additional free parameter and results in an asymmetric radial coverage and an enlarged radial extension with an unequal distance of the minimum and maximum radius to the nominal one. An illustration is given in

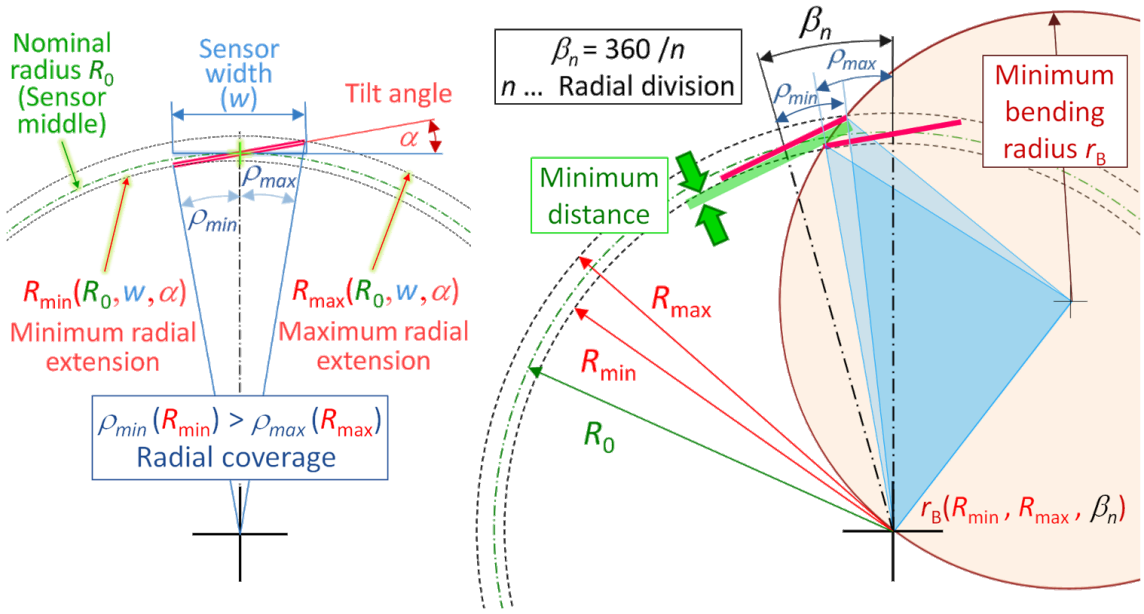

Figure 5.10: Illustration of all relevant parameters for a single barrel segment (*left*) and its radial arrangement within the barrel layer (*right*).

figure 5.10, left side. The radial division must ensure sufficient radial overlap while keeping a minimum distance between adjacent elements. In addition, the minimum bending radius related to the remaining gap must be considered (see figure 5.10, right side). The different curvature of particles and antiparticles is counterbalanced by a reversed tilt angle in the two different layers.

There are four interdependent parameters for the optimization of the radial barrel geometry: the sensor width, the tilt angle, the radial division and the nominal radius. A crucial precondition is settled by the request of a common sensor width for both barrel layers. Furthermore, the introduced tilt angle should stay below 15° to avoid a strong reduction of the effective sensor width available for the radial coverage. As for the disk layer, an even radial division is requested for the half-detector concept. An approximate range for the senor width can be set by fixing upper limits for the radial division and the radial extension defined by the difference between the minimum and maximum radius. They are related to a minimization of the material budget and the additional space needed for passive elements next to the sensors, respectively. A minimum radial division for the such enclosed sensor width is then given by the request of a minimum bending radius, which corresponds to a particle momentum of 100 MeV/c. Slower particles are not relevant for the experiment because they are stuck already in the beam pipe [148]. Finally, the obtained minimum distance between adjacent sensor elements delivers constraints on the maximum radial division and the tilt angle. Figure 5.11 gives an overview of the associated optimization process. Presented results lead to a default sensor width between 30 mm and 35 mm, a tilt angle between 10° and 15° and a number of 20 and 26 elements arranged in inner and outer barrel layer, respectively.

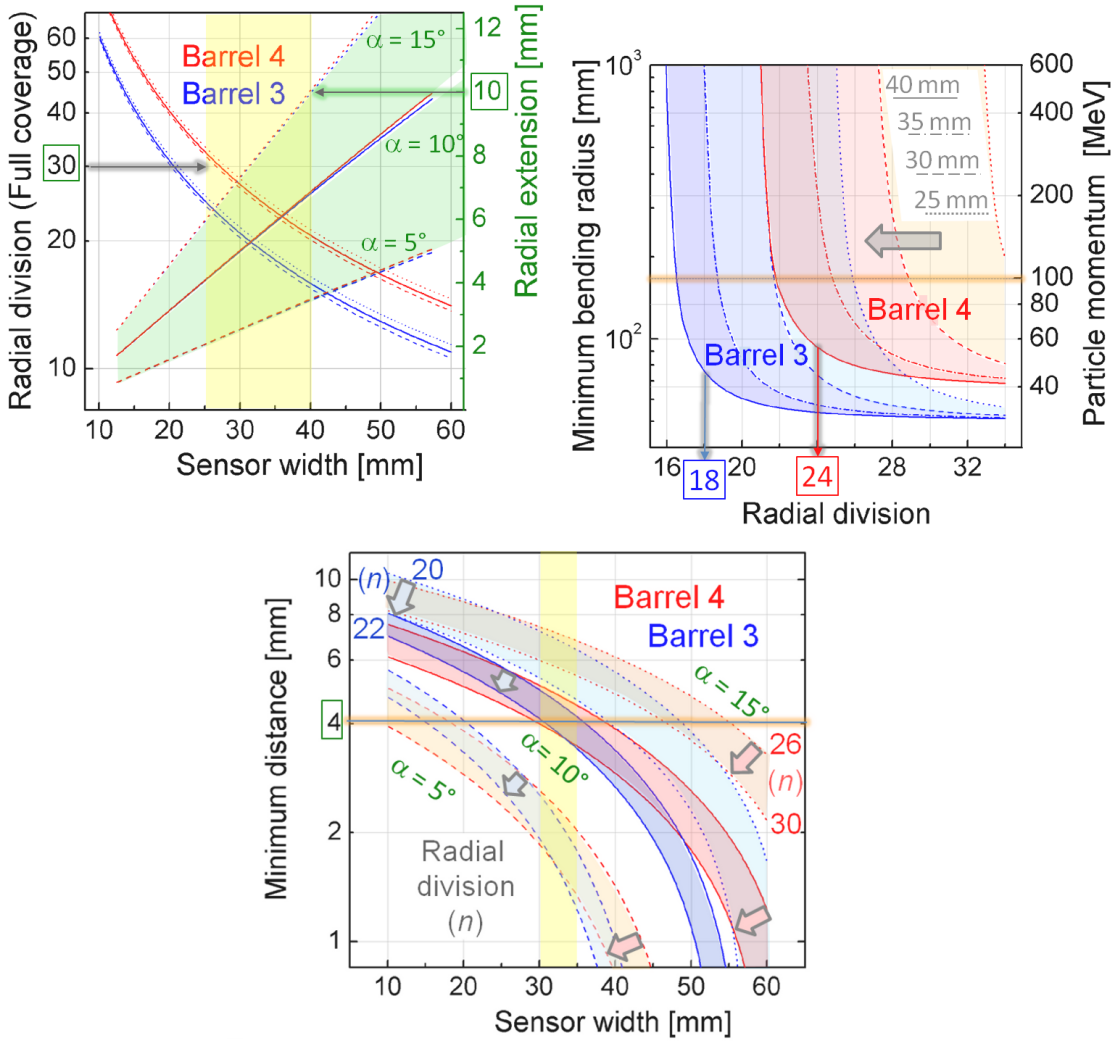

Figure 5.11: Basic results of the strip barrel optimization ($R_0 = 95\,\text{mm}/125\,\text{mm}$ for barrel 3/4). *Top, left*: Containment of the sensor width by setting maximum values for both radial division and extension. Plotted values for the radial division, $n = \pi/\rho_{\text{max}}$, do not include any overlap. The restricted region is highlighted in yellow. It is defined by the radial division of the outer barrel layer and the tilting angle α, which results in similar radial extensions, $\Delta R = R_{\text{max}} - R_{\text{min}}$, for both layers. *Top, right*: Minimum bending radius for different sensor widths between 25 mm and 40 mm obtained with a tilt angle of 10°. The corresponding particle momentum is plotted at the right axis. The minimum required bending radius corresponds to a particle momentum of 100 MeV/c. The resulting minimum radial devision is indicated by arrows. *Bottom*: Minimum distance between adjacent sensors *vs.* sensor width. Results are shown for different tilt angles, α, and radial divisions. The requested minimum interspace sets upper limits on the radial division. It is optimized within an interval of 5 mm, which is highlighted in yellow.

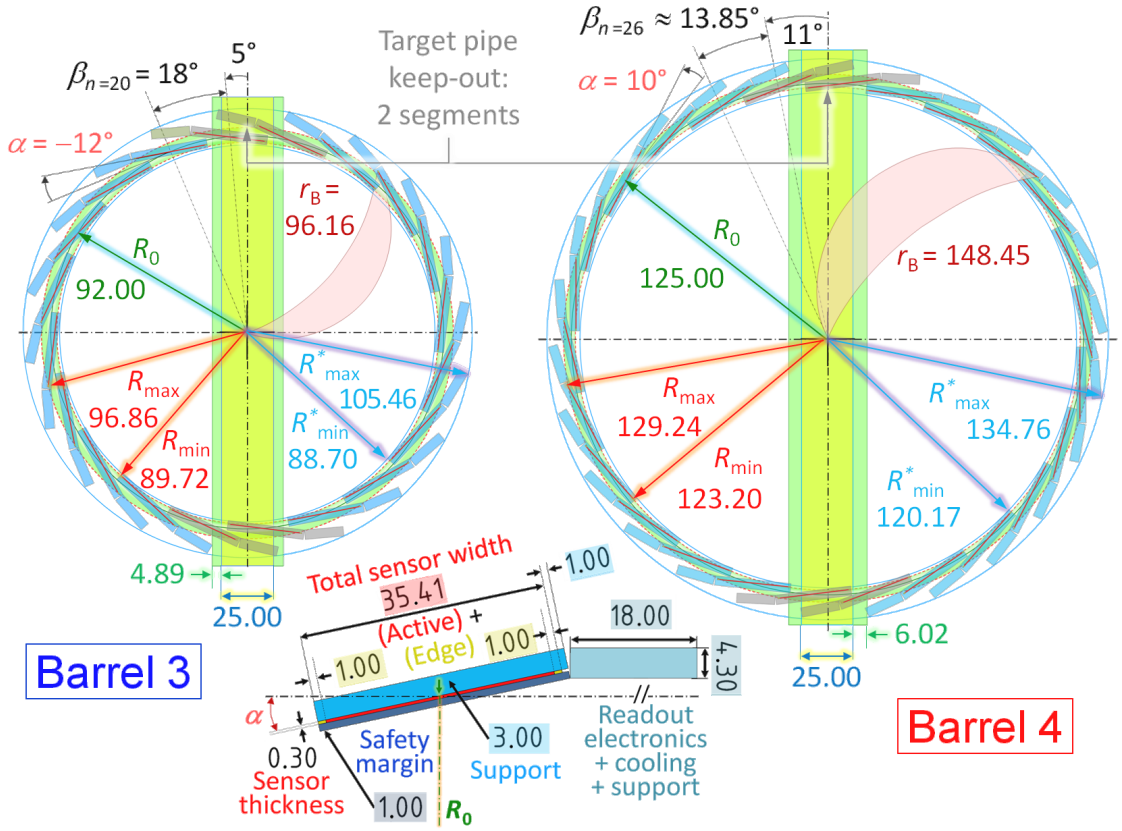

Figure 5.12: Radial geometry (XY front view) for both strip barrel layers. An adequate keep-out volume for the individual super-modules is considered. The final layout is optimized accordingly. All measures are given in mm.

The final radial layout of the barrel layers is shown in figure 5.12. Besides the sensor elements an adequate keep-out volume is considered for associated passive components. It is inclined with respect to the sensor and compensates the tilt angle to reduce the radial occupancy. An additional safety margin is left around the sensor. The total sensor width and the strip pitch are chosen accordingly. The whole geometry is rotated to obtain sufficient space for the target pipe crossing with a minimum number of elements to be left out.

The maximum length of the barrel layers downstream of the IP is limited to 140 mm. The optimization of the two different sensor lengths is driven by the required keep-out for the target pipe and the maximum extension of both barrel layers in upstream direction. Stringent conditions are defined by the use of the same two sensor types for both barrel layers and the fixation of the same strip pitch for each of them. The final solution for the axial barrel arrangement is shown in figure 5.13. It utilizes the same strip pitch on both sensor sides thus resulting in a rectangular and a squared barrel sensor type. A halved strip pitch size for the barrels sensors is still possible. In case of proven necessity it could be applied as an upgrade in sensitive regions close to the IP.

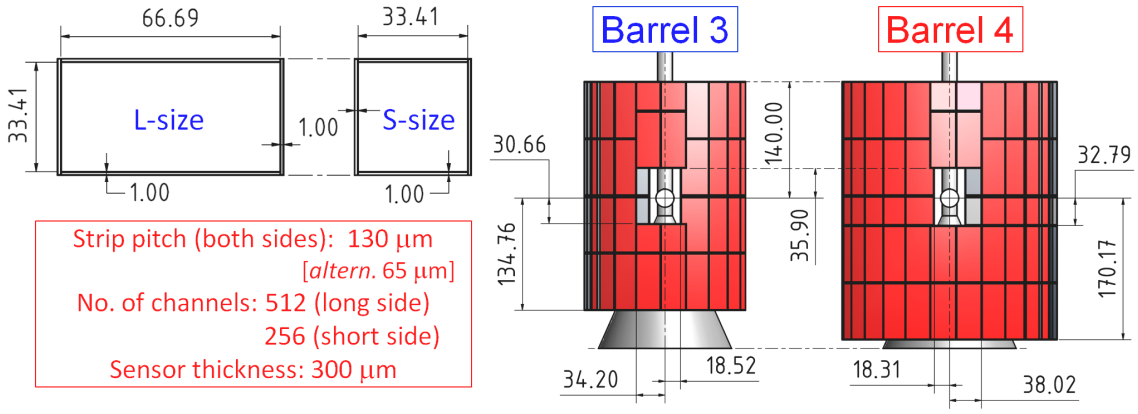

Figure 5.13: Final sensor dimensions for the strip barrel layers (*left*) resulting in a rectangular and a squared sensor type. *Right*: Axial sensor configuration for both barrel layers. All measures are given in mm.

5.3 Input from engineering models

Engineering solutions are based on the fixed boundary conditions within the design optimization. Associated models as shown in figure 5.14, on the right, deliver a realistic description of all passive detector materials. Basic input is given by technical specifications of the readout electronics and main concepts for the detector assembly. They are related to the insertion of electronics components along with a cooling system and appropriate support structures. Super-modules are introduced as smallest mechanical component for the

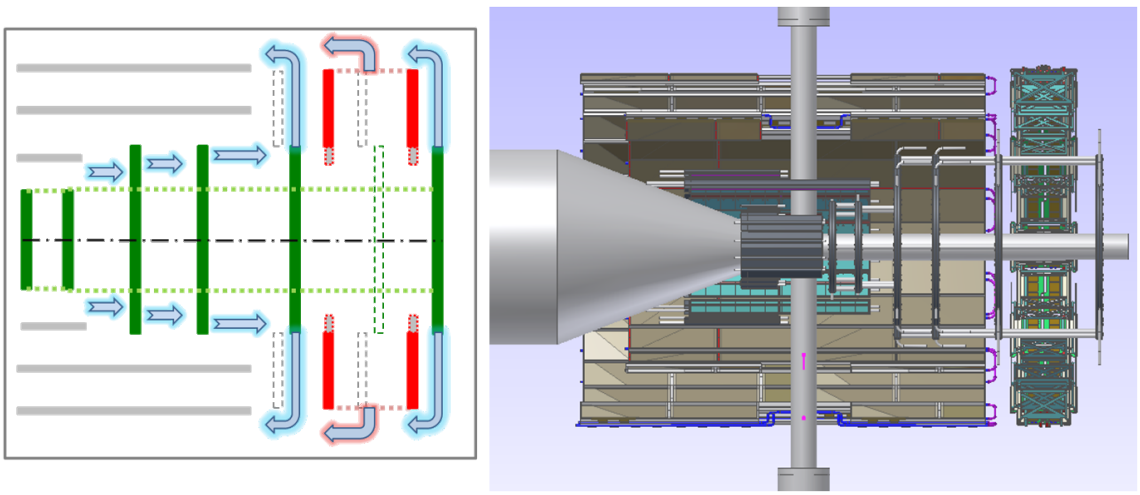

Figure 5.14: Schematic concept (*left*) and side view of the engineering CAD model (*right*). The forward strip part is located in between the last two pixel disks thus allowing a collision-free insertion during the detector assembly. The arrows in the schematics indicate the main routing scheme.

detector assembly. Their structure is described in subsection 5.3.1. The underlying support concepts for the composition of all individual MVD parts are depicted in subsection 5.3.2. Finally, main aspects of the cooling system are summarized in subsection 5.3.3.

5.3.1 Hybridization of super-modules

The hybridization of super-modules incorporates detector modules with a local support structure and an embedded cooling pipe. Additional SMD components apart from the readout chip have to be considered for the detector modules. In case of strip modules a pitch-adapter is inserted in between the sensor and the readout chip in analogy to the presented concept in subsection 4.2.1. Another electronic component is given by the module controller chip operating several readout chips. To allow a separate assembly, the super-modules must be mechanically decoupled from the overall cooling and cabling system. Hence, appropriate connectors are needed.

The different strip and pixel super-modules are shown in figure 5.15 and 5.16, respectively. They basically differ for the barrel and the forward part. An omega-shaped carbon support is utilized for the super-modules of the pixel barrels. A supplementary carbon foam layer is used to obtain sufficient stiffness and to achieve better thermal conductivity. Cooling pipes will be embedded in both carbon structures. The detector modules are placed on top of the carbon foam. A pixel disk super-module consists of two half-disks made of carbon foam which are glued together thus embedding the cooling pipes. First prototypes of this kind were presented in subsection 4.3. The detector modules are then

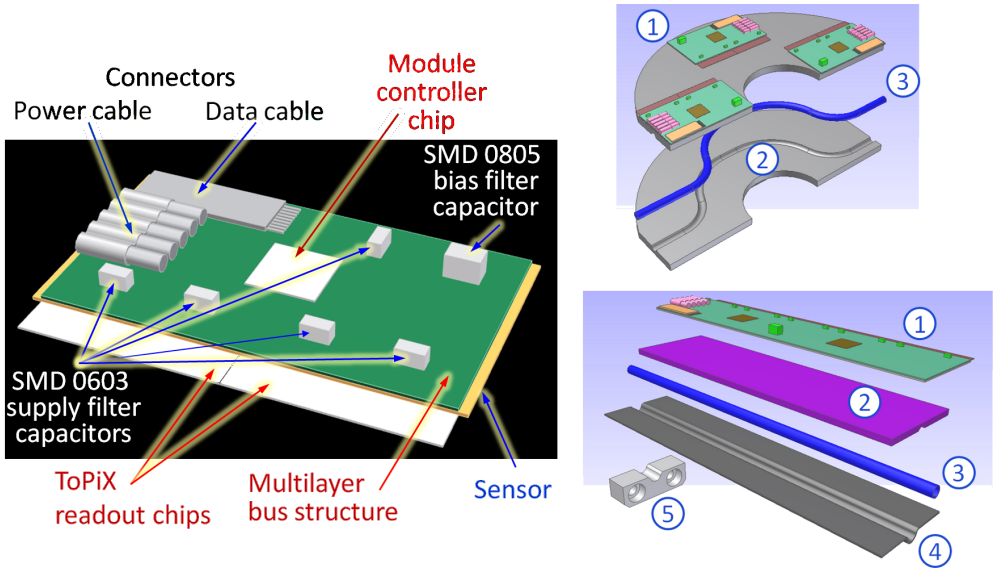

Figure 5.15: *Left*: Layout of a pixel detector module with additional electronic components and a multilayer bus structure. *Right*: Assembly of a super-module for the disk (*top*) and the barrel part (*bottom*) with (1) Detector module, (2) Carbon foam, (3) Cooling pipe, (4) Omega-shaped carbon support and (5) Reference block for the fixation of the super-module to the barrel support.

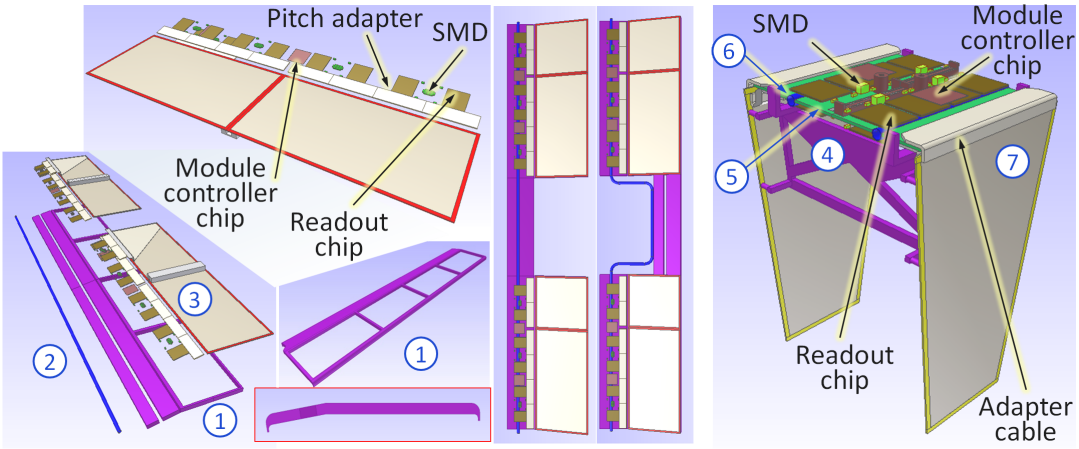

Figure 5.16: Super-module concept for the strip barrel layer (*left*) and the forward disks (*right*). A detector module consists of the sensor, readout chips, a module controller chip and additional SMD components. A stave support (1) is introduced for the barrel super-modules. Further components are the embedded cooling pipe (2) and the detector modules (3). Modified super-modules (*middle*) are required to achieve the target pipe passageway. A sophisticated carbon support structure is required for the disk super-module (4). All electronics placed in between the sensors is put on a PCB (5), which also stiffens the whole structure. Cooling pipes (6) are placed below the readout chips. An adapter cable (7) allows the connection to the sensor.

placed on the front and rear side. The local support of barrel super-modules utilized in the strip layers is formed by a stave structure made of carbon and carbon foam. Notches are foreseen for the active area of the sensors. The readout electronics and the cooling pipe are hosted on the inclined outer part of the support structure. There is one common super-module for each barrel layer. In addition, modified super-modules have to be used at the top and bottom for the passageway of the target pipe. A disk super-module combines successive sensors of the two strip disk layers. All associated passive components are then placed in between at the top side. In this way, a minimum radial occupancy is achieved.

5.3.2 Support concept

Adequate support structures are required to compose the different detector layers with precise relative positioning. Besides load pick-up and alignment of associated super-modules, attachment points to the global MVD frame must be provided. Barrel and disk layers of the pixel and the strip part are combined separately. They are split into two halves thus forming eight individual parts for the detector assembly.

The pixel barrel support is designed as a truncated cone placed in upstream direction. Each of the half-cones provides three fixation points at the upstream end of the global MVD frame. Super-modules of both layers are attached to two appropriate surfaces at the small end face. The fixation is achieved by a custom-made screw connection of the reference block to the support cone. In this way, a very precise positioning of the super-modules is

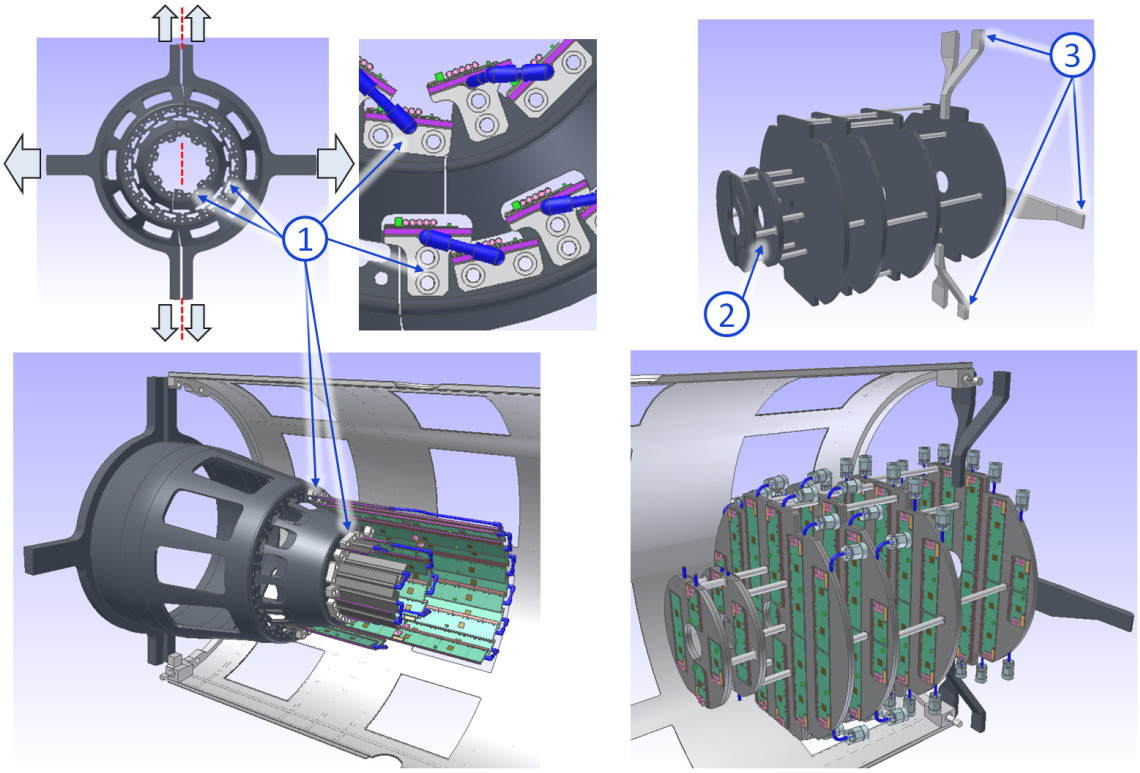

Figure 5.17: CAD drawings of an engineering model illustrating the integration of the pixel barrel layers (*left*) and the forward part (*right*). The super-modules in the barrel part have screw connections to the support cone (1). The fixation points to the global frame are indicated with arrows. The support concept of the forward part is based on spacers (2) between the individual disks and suspenders (3) for an attachment to the global frame.

obtained. Appropriate notches at the support cones allow the lead-out of all services. The pixel disks are connected to each other by three spacers per half-disk. Three suspenders are fixed at the last pixel disks thus allowing the attachment to the global frame at the downstream end. The integration of the MVD pixel part is illustrated in figure 5.17.

In contrast to the pixel part, the barrel support for the strip layers extends in downstream region over the full length. It is made from two half-cylinders in between the inner and the outer layer. Saw-tooth-shaped structures on the inside and the outside form a support surface for the super-modules. The fixation is done by a clip connection at both ends. The overall concept is based on the ALICE ladder repositioning system with a precision of better than 6 µm [149]. The attachment of each equipped half-shell to the global MVD frame is implemented by a three point fixation at the upstream end. The strip disk super-modules in the forward part are plugged to a common half ring support. The corresponding attachment points to the global MVD frame are defined around the last keep-out sections at the downstream end. The overall concept of the strip disk layers follows the basic idea presented in [150]. A sketch of the associated support components is shown in figure 5.18.

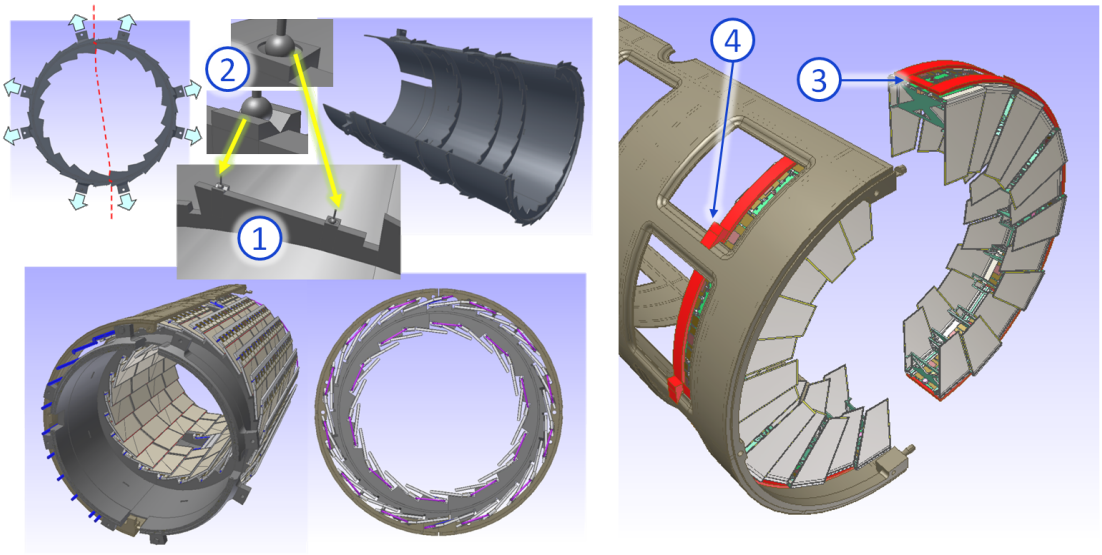

Figure 5.18: Support concept for the barrel (*left*) and the forward strip part (*right*) of the MVD. The fixation points of the barrel support to the global frame are indicated with arrows. A saw-tooth-shaped structure (1) provides a support surface for the barrel super-modules, which are fixed with a clip connection (2). The disk super-modules are plugged onto a half ring support (3), which is then connected at the keep-out sections of the global frame (4).

5.3.3 Cooling structures

Local cooling structures are defined by the embedded cooling pipes in the super-modules. They represent the active part of the cooling system which is needed for the readout electronics. The outer diameter of these pipes is fixed to 2 mm (see also figure 4.12, page 87). Due to technical and practical reasons a transition to flexible pipes is required in the subsequent stage of the cooling system. Therefore, appropriate connectors are used which allow a junction between the rigid steel pipes and plastic pipes with an outer diameter of 4 mm. Custom-made micro-fittings are needed for the interconnection of different cooling pipes.

Basically, each barrel super-module is equipped with a single cooling pipe. A cooling circuit is defined by the interconnection of two adjacent super-modules at the downstream end. Modifications are needed for the outer strip barrel layer due to the division into 13 super-modules per half-barrel. Here, the cooling circuit of the last super-module is closed by a second cooling pipe running back along the same super-module. A much higher thermal load is expected in the forward pixel disks. Therefore, individual cooling pipes are used for each pixel sensor row. There are no interconnections between cooling pipes within the super-module in order to achieve maximum cooling power. In case of the strip disks individual cooling pipes can be connected or bended to the outside. Therefore, sophisticated micro-fittings are required and currently under investigation. Further thermal simulations are also needed to fix the final number of readout chips connected to one individual cooling circuit. An illustration of the local cooling structures is given in figure 5.19.

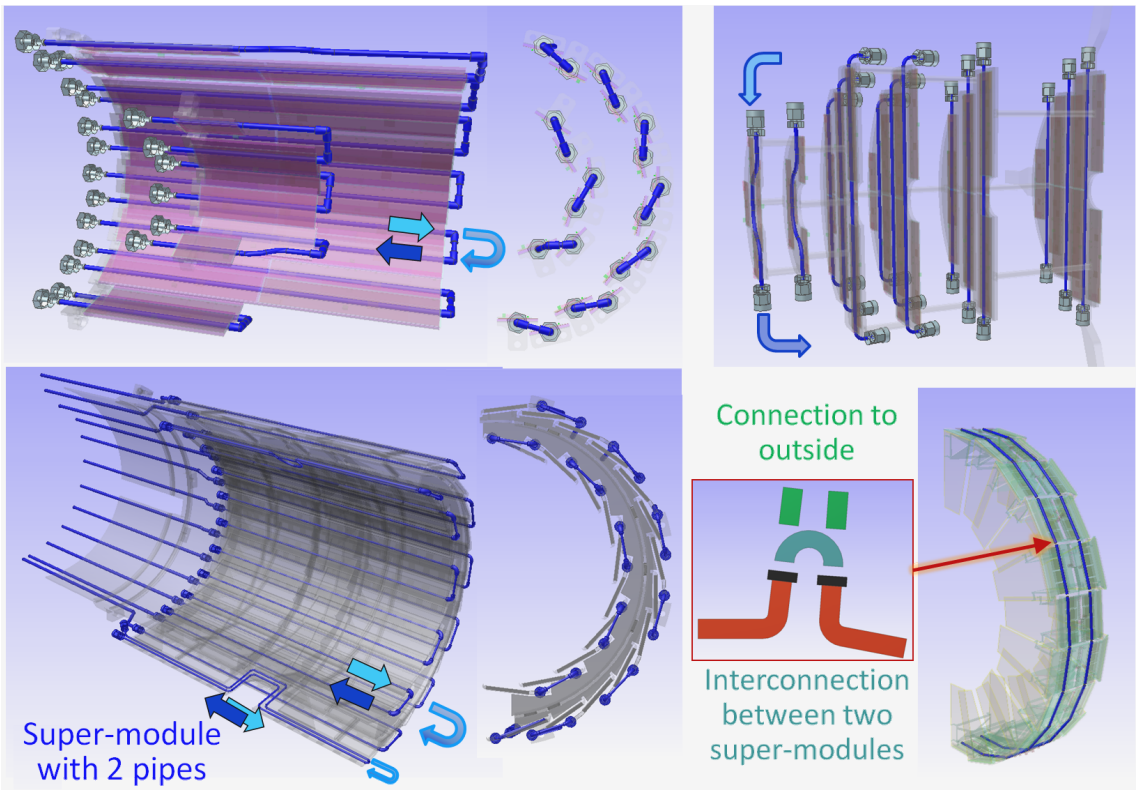

Figure 5.19: Schematic illustration of the local cooling structure of the barrel (*left*) and the forward part (*right*).

5.4 Mvd-2.1: A detailed detector model for physics simulations

This section is devoted to a detailed description of the detector model Mvd-2.1, which is finally implemented into the physics simulation. It is based on the design optimization and inputs from engineering models both presented in the previous sections 5.2 and 5.3. The integration of such a complex CAD model into the detector simulation software requires suitable tools to define and properly convert all associated volumes. Therefore, adaptations to the particular requests of the developed conversion tools and the needs of physics simulations become necessary. Concept, tools and modifications of the CAD model that has been developed are summarized in the first subsection 5.4.1. Basic features and main structure of the finalized model Mvd-2.1 are presented in subsection 5.4.2. More details on its main components are given in the last subsection 5.4.3.

5.4.1 Migration of the CAD model to the simulation software

The simulation framework for the $\bar{\text{P}}$ANDA experiment [144] is a ROOT [151] based, object oriented software. It provides its own geometry package which allows the interfacing to external Monte-Carlo simulations for tracking or reconstruction and other applications such as the visualisation of reactions in an event display. However, the direct creation of a root geometry describing a complex object such as the presented model for the MVD is strained to the limit because it requests the manual creation and 3D positioning of each single element.

CAD software provides a lot of advantages including the extraction of objects based on 2D sketches, the extraction of 2D sketches from 3D arranged objects, the definition of dependencies and a dynamic creation of cloned objects and 3D arrangements. Moreover, all work is based on graphical programming thus delivering a direct visualisation. Consequently, the development of the Mvd-2.1 geometry was done in a CAD environment [143].

Once the CAD model has been created, it must be transformed into a root geometry

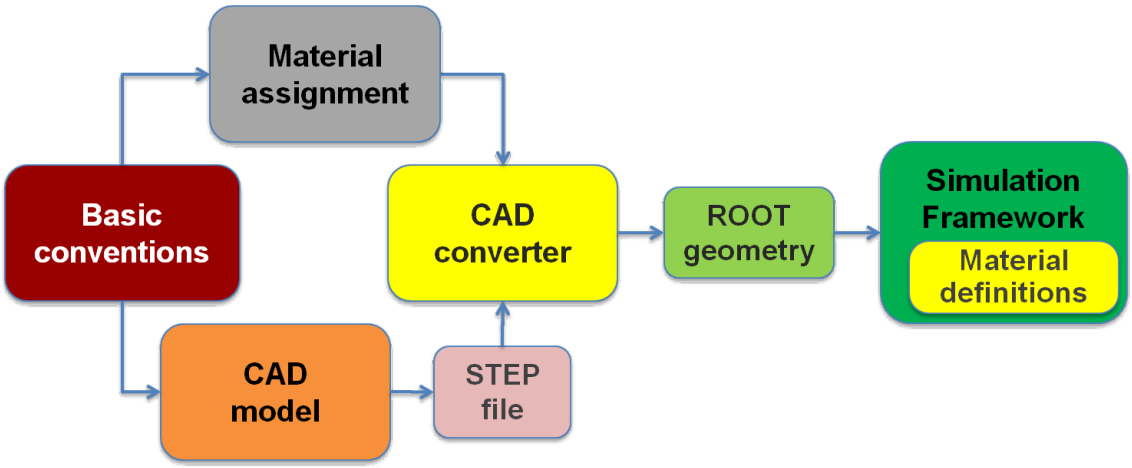

Figure 5.20: Schematics of the migration of the CAD model into physics simulation.

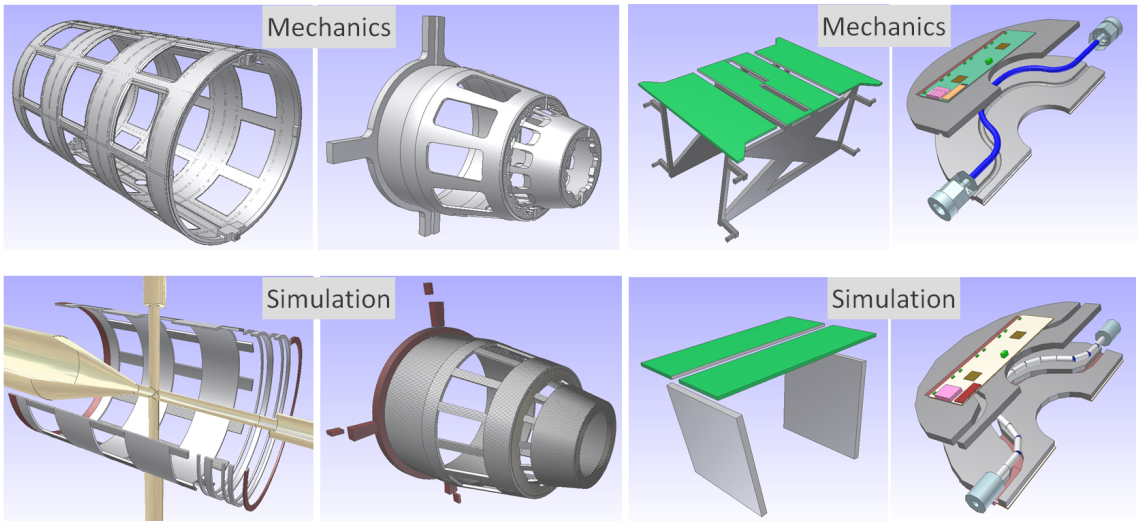

Figure 5.21: Adaptation of different components from engineering models (*top*) according to the needs of physics simulation (*bottom*). From left to right: global MVD frame, pixel barrel support, strip disk super-module, pixel disk super-module.

suited for simulations within the PandaRoot framework [144]. A CAD converter has been developed especially for this purpose [152]. This application uses step-files as input data. The step-file format is a common standard for CAD software. Besides the sole conversion of the geometry, a material definition is required in order to obtain a complete description of all detector volumes. A schematic of the migration of the CAD model to the physics simulation is given in figure 5.20.

Basic conventions and a proper definition of the model hierarchy are a prerequisite to merge different standards defined for the CAD development in mechanical engineering and physics analysis. A rigorous naming convention is needed for an unambiguous assignment of each component and a comfortable definition of the associated material. Moreover, it allows a fast localization of individual volumes within the model. The hierarchical structure is based on the modular concept as presented in figure 5.2. However, the implementation of the full detector model must be adapted to the needs of physics simulations. Therefore, the internal structure remains the same but the mechanical volumes are split into different functional groups. In this way an easy selection of different detector components becomes possible, which allows a study of their impact in physics simulations. A proper definition of the volume centre for each element is important for a correct conversion. In some cases a simplification of complex volumes is necessary due to limitations of the CAD converter. It is reached by a composition of the main volume out of simple basic volumes. Moreover, for selected components the substitution of very detailed structures by basic forms suffices for physics purposes and thus eventually speeds up the simulations. Some examples are shown in figure 5.21.

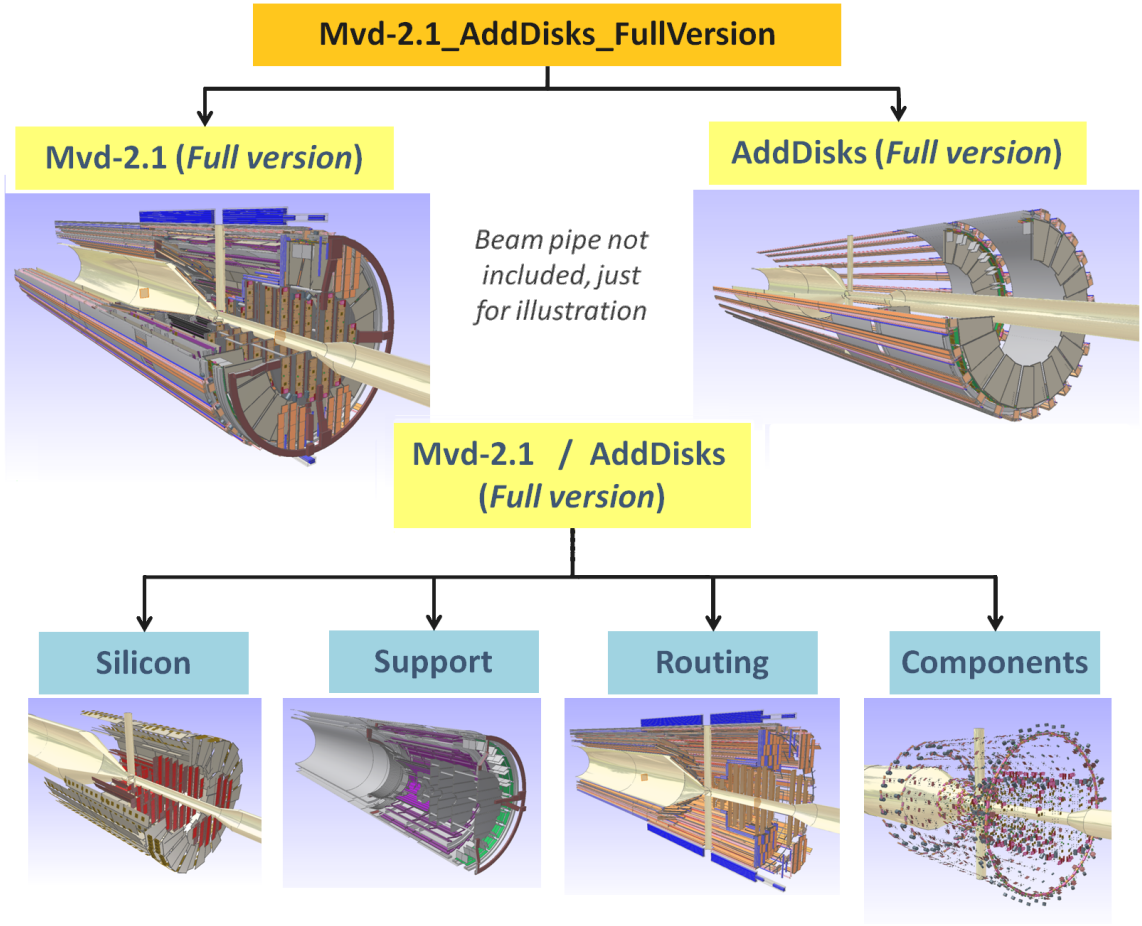

Figure 5.22: Main structure of the Mvd-2.1 model (full version).

5.4.2 Basic description and main structure

The detector model Mvd-2.1 contains all mechanics input from engineering models. Moreover, it includes a detailed routing concept within the MVD volume and in further upstream regions. The main scaling factor for the cooling and cabling system is given by the number of readout channels resulting from the amount of introduced pixel and strip sensors in combination with their defined 2D segmentation. The routing concept is based on specifications of the actual electronics and detector development. Besides the central MVD, the two additional forward disks are also inserted. While the central MVD is already optimized (see section 5.2), the design of the forward disks represents only a conceptual layout. Basically it is adapted from the design of the strip disks of the central MVD.

In parallel to the main detector geometry a complete material list of all components is defined. Besides the basic elements, common materials and substances such as steel or water are predefined in the ROOT material files. Other compounds are considered by the definition of density weighted materials. Their charge number Z and the atomic number A refer to the main element of the compound. The effective density is then obtained by

Name	Description
Mvd-2.1_AddDisks_FullVersion	Full version: Central MVD + additional disks (AddDiks)
Mvd-2.1_AddDisks_Sensitive	Reduced version: Only sensitive volumes, MVD + AddDisks
Mvd-2.1_FullVersion	Full version: Central MVD
Mvd-2.1_Sensitive	Reduced version: Only sensitive volumes, Central MVD

Table 5.2: Main version of the Mvd-2.1 model available for physics simultaion. They are accessible under [154].

adding a second material and weighting between both. In this way a realistic description in terms of the resulting radiation length can be achieved in a very simple way.

Extensive collision checks were performed before and after the CAD conversion with special tools available in the CAD software as well as in ROOT [153]. Moreover, the proper conversion of all specific geometric arrangements was carefully checked. Finally, four versions of the MVD model are available for simulations [154]. They are listed in table 5.2. The reduced model containing only active elements is inserted as reference to study material effects. The complete version contains 70,458 individual volumes and 597 different volume types. The two main parts are the central MVD and the additional disks. Both are introduced independently and split into four main components. These are the silicon part, the support structure, the routing system and a part containing additional components. More details on the substructure are given in the next subsection. Relevant numbers associated with the implemented model are compiled in table 5.3. An illustration of the main structure is shown in figure 5.22.

Basic parameter	**Pixel part**	**Strip part**
Number of super-modules	66	70
Number of detector modules	176	140
Number of sensors	34 (2 chips size) 28 (4 chips size) 54 (5 chips size) 60 (6 chips size)	172 (rectangular) 34 (squared) 48 (trapazoidal)
Total:	176	254
Active silicon area / [m^2]	0.106	0.494
Number of frontend chips	338 (barrels) 472 (disks)	940 (barrels) 384 (disks)
Total:	810	1324
Number of readout channels	$\approx 10.3 \times 10^6$	$\approx 1.7 \times 10^5$

Table 5.3: Compilation of cornerstone data for the MVD extracted from the developed Mvd-2.1 model.

5.4.3 Description of major subparts

The four main parts of the Mvd-2.1 model are further subdivided into different functional groups. The silicon part includes all sensors and the associated readout chips thus representing the sensitive elements for the measurement and the close-to-detector electronics. Its substructure follows the implemented hierarchy shown in figure 5.2. The sensor consists of an active volume and a passive edge. The positions of the active detector volumes in the different detector layers are summarized in table 5.4.

Main layer	Sub-layer	(r_{def}) [mm]	$\langle r_{\mathrm{opt}} \rangle$ [mm]	r_{min} [mm]	r_{max} [mm]	(z_{def}) [mm]	$\langle z_{\mathrm{opt}} \rangle$ [mm]	z_{min} [mm]	z_{max} [mm]
Barrel layer 1	Inner ring	25	22	21.80	22.75	-	-	−39.8	9.8
	Outer ring		28	27.80	28.58				
Barrel layer 2	Inner ring	50	47.5	47.30	47.85	-	-	−79.8	57.8
	Outer ring		52.5	52.30	52.82				
Barrel layer 3		95	92	89.72	96.86	-	-	−133.8	139.0
Barrel layer 4		135	125	123.20	129.24	-	-	−169.2	139.0
Disk layer 1	Sdk 1, front	<50	-	11.70	36.56	20	22	19.7	19.9
	Sdk 1, rear							24.1	24.3
Disk layer 2	Sdk 1, front	<50	-	11.70	36.56	40	42	39.7	39.9
	Sdk 2, rear							44.1	44.3
Disk layer 3	Ldk 1, front	<95	-	11.70	73.96	70	72	69.7	69.9
	Ldk 1, rear							74.1	74.3
Disk layer 4	Ldk 2, front	<95	-	11.70	73.96	100	102	99.7	99.9
	Ldk 2, rear							104.1	104.3
Disk layer 5	Ldk 3, front	-	-	11.70	73.96	160	150	147.7	147.9
	Ldk 3, rear							152.1	152.3
	StripDk 1, L	-	-	74.33	131.15		162.5	160.0	160.3
	StripDk 1, S							165.0	165.3
Disk layer 6	Ldk 4, front	-	-	11.70	73.96	230	220	217.7	217.9
	Ldk 4, rear							222.1	222.3
	StripDk 2, S	-	-	74.33	131.15		207.5	204.7	205.0
	StripDk 2, L							209.7	210.0

Sdk ... small pixel disk, Ldk ... large pixel disk, StripDk ... strip disk

Table 5.4: Positions of the active volumes within the different detector layers. r_{def} and z_{def} are the predefined values for the radius and the axial extension as given in figure 3.2 on page 66, $\langle r_{\mathrm{opt}} \rangle$ and $\langle z_{\mathrm{opt}} \rangle$ are the corresponding mean values in the sub-layers after optimization. $r_{\mathrm{min/max}}$ and $z_{\mathrm{min/max}}$ refer to the outer limits of the radial and axial extension of active volumes in the respective layers.

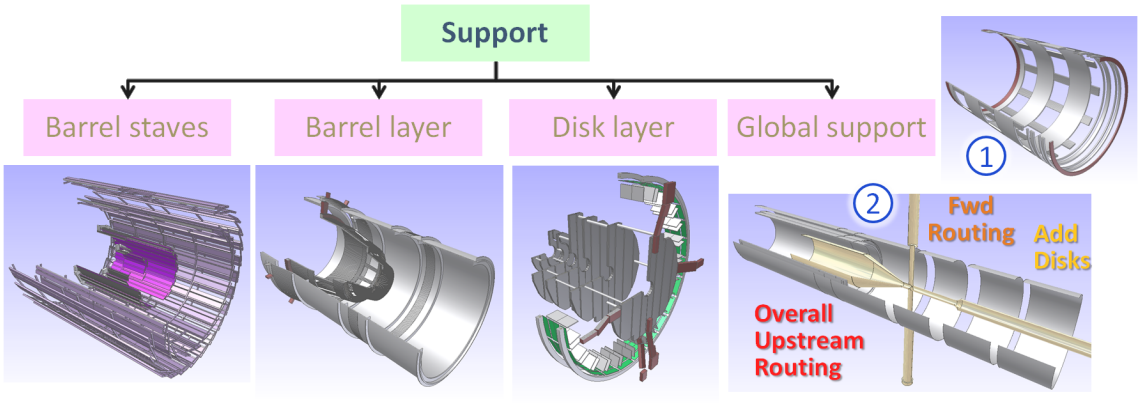

Figure 5.23: Main structure of the support part. The global support consists of the global MVD frame (1) and the routing support (2).

The support part includes the barrel staves, the barrel layer support, the super-module and layer support structures of the forward disks and the global support. The latter contains the global MVD frame for the central detector and additional support structures for the routing of the additional forward disks as well as the overall system further upstream. The routing support is inserted schematically as a structure made of thin cylindrical layers. The lightweight carbon support structures are defined as carbon or carbon foam with different ratios of carbon and air. In spite of the global support, the substructure of the support part is in agreement with the predefined hierarchy. An illustration is shown in figure 5.23.

The structure of the routing part as shown in figure 5.24 refers to the cabling and cooling system. Different cable types are introduced for the high voltage supply of the sensors, the power supply of the readout electronics and the bus cable for the data transmission and slow control of the readout electronics. All cables are spit into a metallic core and PVC insulation. The cable cross sections are in accordance with the given electronic specifications. The cooling lines consist of a water core and a casing material which is defined either as steel or PVC. The routing scheme is locally connected to the predefined

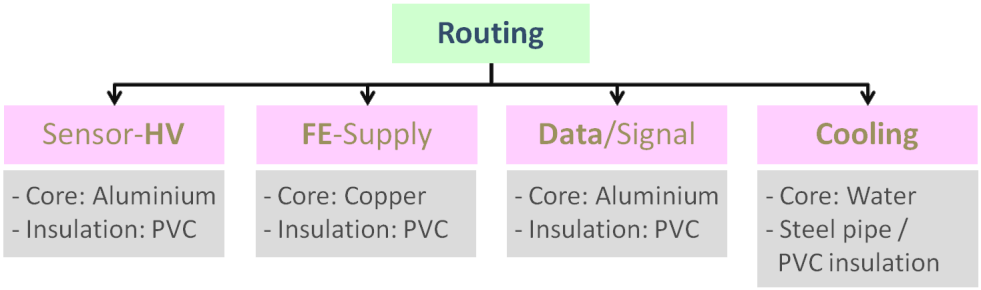

Figure 5.24: Main schematics of the routing part. (Abbreviations: HV - high voltage, FE - frontend readout chip).

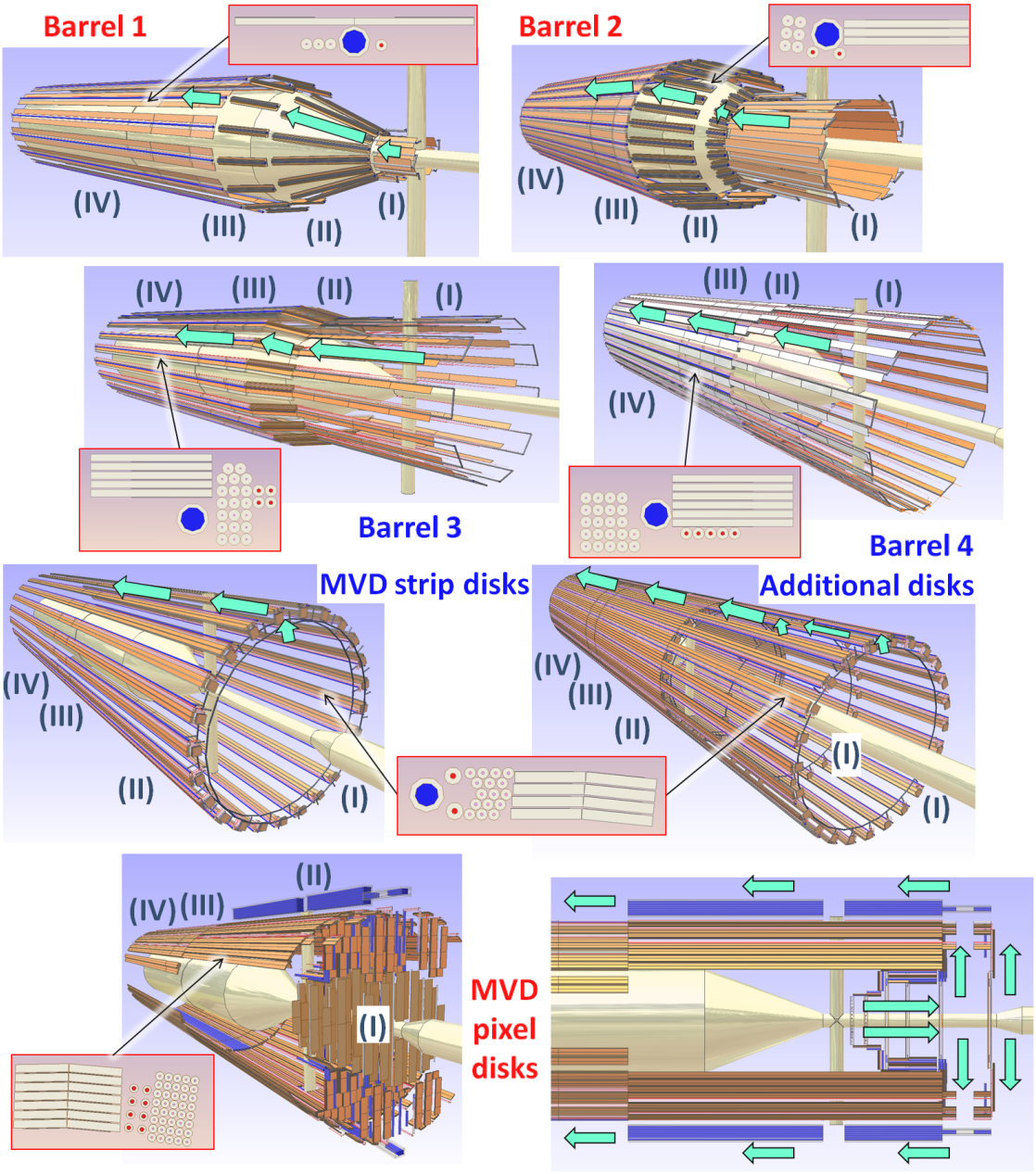

Figure 5.25: Different routing schemes for the individual detector layers. The individual packages formed for each super-module are indicated in the red-framed inlets. The barrel layer services are guided straightforward in upstream direction. They follow the shape of the target pipe. The strip disk services are lead out to the top from where they are further extended in upstream direction. The pixel disk routing requires a more complex scheme and includes a regrouping and further bundling of the initially defined packages. The different regions are defined as (I) active detector part, (II) MVD volume, (III) the region until $z = -30\,\text{cm}$ (end of central frame) and (IV) until $z = -1\,\text{m}$ (end of backward EMC end-cap).

Routing part	Type	Number of lines	Core		Insulation		Region
			Size [mm]	Material	Size [mm]	Material	
Sensor supply	Cable (HV)	1 per sensor [a]	⌀ 0.5	Al	◎ (0.5-1.0) ◎ (0.5-1.5)	PVC	I-II III-IV
Frontend supply	Cable (LV)	1 per chip [a],[b]	⌀ 0.25	Cu	◎ (0.25-0.75) ◎ (0.25-1.0)	PVC	I-II III-IV
Data/ Slow control	Bus cable	1 per 2 chip (pixel) 4 chip (strip)	10×0.025	Al	13×0.15 15×0.45 15×0.9	PVC	I^{pixel} I-II III-IV
Cooling	Pipe Tube	1 per chip raw [c]	⌀ 1.8 ⌀ 3.0	Water	◎ (1.8-2.0) ◎ (3.0-4.0)	Steel PVC	I II-IV

[a]...accounting for 2 physical lines (V_{dd},GND), [b]...cross section according to voltage drop in V_{dd} line,
[c]...Barrel part: 1/stave; Pixel disks: 1 row = 2...12 chips; Srip disks: 1 row= (4+4) chips

Table 5.5: Summary of the implemented routing scheme. Assigned regions correspond to the convention given in figure 5.25. The density of PVC set as default for most of the insulation is close to other material options such as e.g. kapton.

hierarchy. Moreover, most of the parts are superimposed at a higher level because they are situated outside the core volume of the MVD components. The overall routing is divided into four different regions corresponding to the active detector region, the MVD volume and two areas in upstream direction. Outside the active region individual packages for each super-module are defined, which bundle all associated services. An illustration of the routing scheme for all individual detector parts is given in figure 5.25. Details of the defined cross sections and materials are listed in table 5.5.

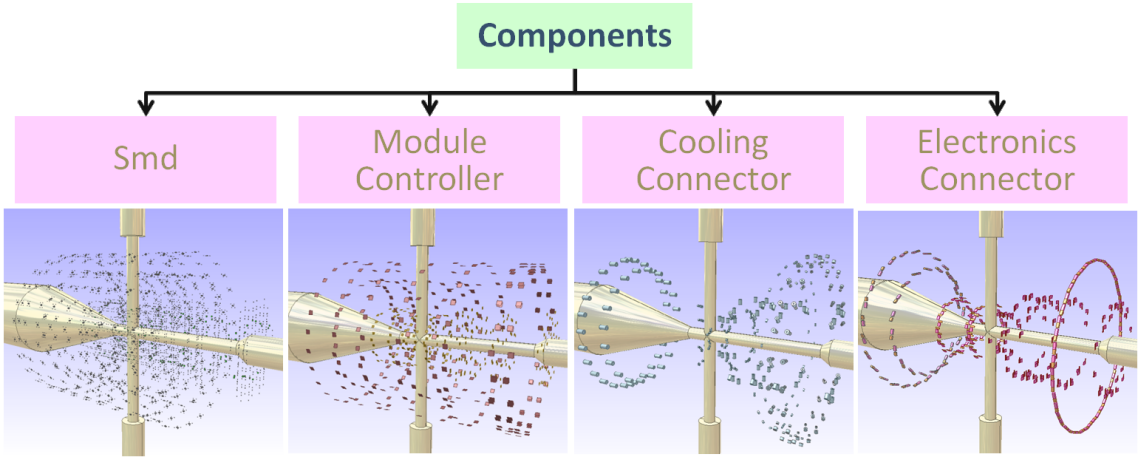

Figure 5.26: Illustration of the substructure for the additional components.

Finally, remaining additional components are compiled in a separate part. They contain all implemented SMD elements, the module controller chips and connectors for the cabling and the cooling system. PVC and silicon are defined as standard materials for the cooling connectors and the module controller chips, respectively. A heavier PVC material is used for the electronic connectors while a light aluminium material is used for the SMD elements. An overview of all components is given in figure 5.26. All additional components are extracted from mechanical models thus following the predefined hierarchy.

6 Simulation

The simulation of basic conditions within the experiment and the performance of the MVD under these circumstances are necessary to validate the previously introduced detector model Mvd-2.1. Main results are summarized in this chapter. The first section 6.1 is dedicated to a detailed study of the hadronic environment. It delivers important input to further detector simulations presented in the following section 6.2. There, basic parameters such as the detector coverage and the overall material budget of the full model are examined. Moreover, count rates studies are performed. They allow the extraction of averaged and maximum event rates in different detector regions. Based on these numbers important hardware specifications can be deduced. The last section 6.3 contains physics simulations of selected benchmark channels performed with a complete description of the $\bar{\text{P}}$ANDA apparatus including all adjacent sub-detectors.

6.1 Main hadronic reaction channels

An accurate treatment of the dominating processes in antiproton-proton reactions is essential to describe the experimental conditions for the MVD. Initially, they are defined by the available phase space distribution of all created particles. Due to the reaction type there are dominantly hadrons in the output channels. A reasonable approach for hadronic reactions in antiproton-proton interactions is given by the DPM model [155]. It is in the focus of the following analyses. Moreover, the UrQMD model allows an extension to antiproton reactions with heavier nuclei [156, 157].

The first part of DPM based simulations is summarized in subsection 6.1.1. It deals with the elastic process of antiproton-proton reactions. This particular part is relevant for the MVD due to its large total cross section in the beam momentum range of the $\bar{\text{P}}$ANDA experiment. A parameterization of the required cut-off parameter for the Coulomb elastic part is deduced. The overall particle distribution obtained with both generators is then shown in the subsequent subsection 6.1.2. The last subsection 6.1.3 contains an additional study on the topology of reaction products. To validate the used particle generator, main results of the performed simulations are compared with experimental data.

6.1.1 Elastic scattering process

Elastic scattering is one of the main processes contributing to the total antiproton-proton reaction cross section. As illustrated in figure 6.1 it ranges between 40 mb and 10 mb within the relevant momentum range of $\bar{\text{P}}$ANDA thus contributing 40% to 20% of the total cross section, respectively. Consequently, a good description of the differential cross section for the $p\bar{p}$ elastic scattering is required in order to quantitatively assess its impact on the MVD detector parts.

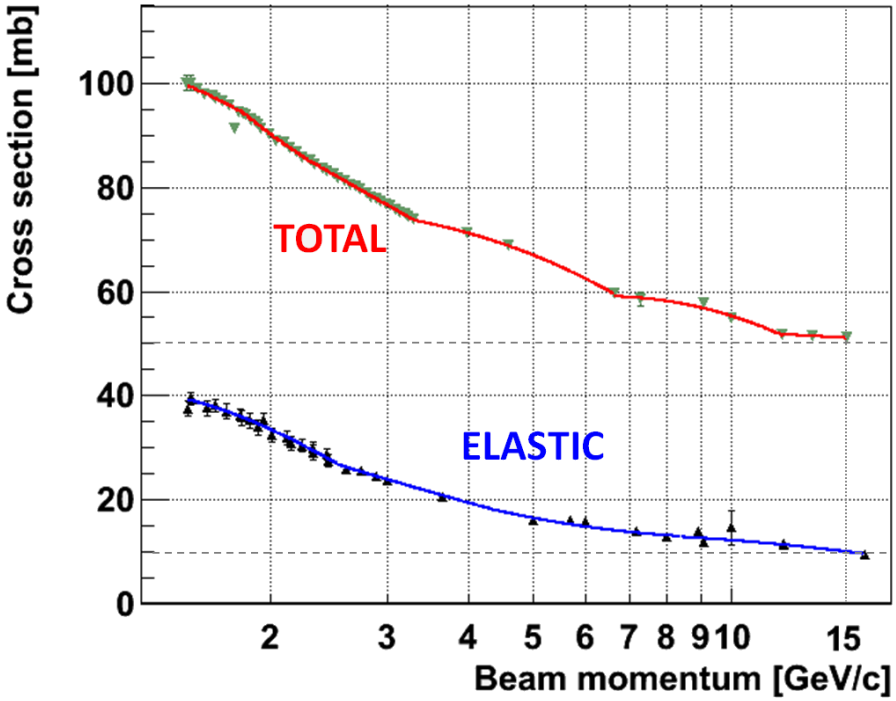

Figure 6.1: Total cross section for antiproton-proton collisions in the relevant momentum range of $\bar{\text{P}}$ANDA and contributions of the total elastic cross section. Symbols represent measurements including the given errors. Compiled data was taken from [158]. Fitted lines are for guiding the eye.

Generally there is no theory, which completely describes the elastic scattering of hadrons, but there are several phenomenological models for different regions of incident momentum transfer. In the relevant momentum range of $\bar{\text{P}}$ANDA antiproton-proton elastic scattering can be described by Coulomb and nuclear amplitudes [160]. The nuclear amplitudes are related to the total cross section by the optical theorem. Consequently, they converge if the momentum transfer tends to zero. The squared four-momentum transfer, t, is related to the laboratory kinetic energy, T_p, of the recoil protons and the corresponding recoil angle, α, defined as $90° - \theta$ with the polar angle θ:

$$-t = 2m_p T_p = \frac{4m_p^2 c^2 \sin\alpha}{(1/\beta_{\text{CM}}^2 - \sin^2\alpha)} \tag{6.1}$$

where $m_p = 938$ MeV/c^2 is the proton mass and $1/\beta_{\text{CM}}^2 = (E_{\text{beam}} + m_p c^2)/(E_{\text{beam}} - m_p c^2)$ with the beam energy $E_{\text{beam}} = \sqrt{(m_p c)^2 + (p_{\text{beam}} c)^2}$ given by the beam momentum p_{beam}.

In the region of $|t| \approx 10^{-3}\,(\text{GeV/c})^2$ the Coulomb term becomes relevant and interferes with the nuclear part. It strongly increases for smaller t thus defining 95% of the total elastic cross section at around $|t| = 5{\times}10^{-4}\,(\text{GeV/c})^2$ [160]. Due to the divergence at a momentum transfer close to zero, a cut-off is needed. It is physically motivated by the finite extension of the hadrons and can be scaled with the total cross section. A picture

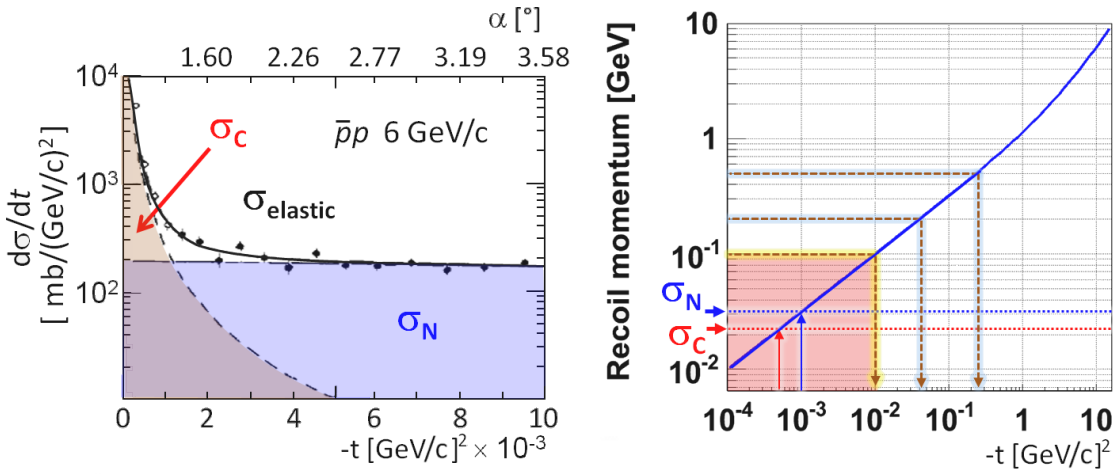

Figure 6.2: *Left*: Example of the measured differential elastic cross section in the region of a small squared four-momentum transfer, $-t$, at a beam momentum of 6 GeV/c [159]. The Coulomb (σ_C) and the nuclear part (σ_N) of the total elastic cross section, $\sigma_{elastic}$, are highlighted in red and blue, respectively. The scattering angle, α, of the recoiling proton is given at the top axis. *Right*: Resulting momentum of the recoiled antiproton vs. four momentum transfer. Lines are introduced to mark the Coulomb and nuclear dominated regions and the respective t value for a recoil momentum of 100 MeV/c, 200 MeV/c and 500 MeV/c. The domain below 100 MeV/c, in which particles do not reach the MVD layers, is highlighted in red.

of the partial and total elastic cross section is given in figure 6.2, on the left side. The correlation between the four momentum value t and the resulting kinetic energy of the recoil proton T_p is plotted on the right side.

A suited parameterization describing both terms of the elastic scattering is implemented in the DPM model [161]. It is adapted to experimental data and requests a cut-off parameter for the minimum scattering angle of the forward scattered antiproton. Simulations with a large statistical sample of 10 million events were performed at beam momenta of 1.5 GeV/c, 2.5 GeV/c, 3.5 GeV/c, 5 GeV/c, 8 GeV/c, 10 GeV/c and 15 GeV/c in order to validate the description of the antiproton-proton scattering process delivered by the DPM generator and to obtain a parameterization for the required cut-off parameter. Therefore, the DPM generator was used with the option to promote only elastic events.

The impact of the cut-off parameter, θ_{cut}, on the corresponding distributions of the recoil protons is illustrated in figure 6.3. As it can be seen on the left side, a large value of θ_{cut} leads to a rejection of slow protons in a momentum range above 100 MeV/c, which have sufficient energy to get through the beam pipe and reach the MVD layers. On the other hand, for very small values of θ_{cut} nearly all of the generated protons stay below 100 MeV/c. Corresponding recoil protons of this momentum range are not relevant for the MVD because they cannot penetrate the beam pipe [148].

To study the possible impact of elastically scattered protons on the MVD detector layers, the best description is given in case of rejecting very slow recoil protons thus obtaining

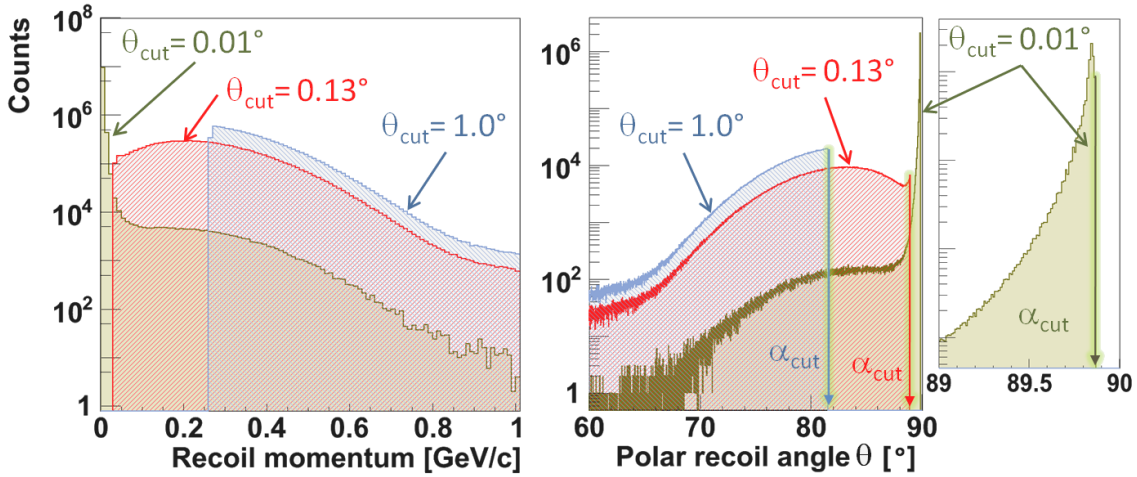

Figure 6.3: Impact of the cut-off parameter, θ_{cut}, on the momentum distribution (*left*) and the polar angle (*right*) of the recoil proton at a beam momentum of 15 GeV/c for 10 million generated elastic DPM events.

a maximum of the distribution above 100 MeV/c. The selection of the cut-off parameter also involves a cut-off angle α for the recoiling proton defining a maximum polar angle $\theta_{\text{max}} = 90° - \alpha$ as shown shown at the right side of figure 6.3. It is directly linked to the four momentum transfer t by equation 6.1. In this way it is possible to localize the cut-off parameter within the physical region of the scattering process.

An extensive study was performed to quantitatively describe the connection between the cut-off parameter given as input to the DPM generator and the corresponding four-momentum cut-off. Therefore, the cut-off recoil angle, α_{cut}, was determined for 17 different cut-off parameters θ_{cut} between 0.001° and 10° and the corresponding t values were calculated according to equation 6.1. The obtained t values in dependence of θ_{cut} are plotted in figure 6.4, left side, for all seven beam momenta. A linear behaviour in the logarithmic plot is obvious until deep into the Coulomb domain. There, a crossover is visible at, which corresponding t values flatten out and reach a minimum. The crossover point, θ_{cross}, and the minimum value t_{min} both depend on the initial beam momentum. They range from $\theta_{\text{cross}} \approx 0.5°$ to $\theta_{\text{cross}} \approx 0.01°$ and $|t|_{\text{min}} \approx 1 \times 10^{-4}\,(\text{GeV/c})^2$ to $|t|_{\text{min}} \approx 2 \times 10^{-5}\,(\text{GeV/c})^2$ for a beam momentum of p_{beam} of 1.5 GeV/c and 15 GeV/c, respectively.

Performing a linear interpolation in the logarithmic plot, a momentum dependent parameterization of the cut-off parameter for the region of the Coulomb-nuclear interference, $\theta^{\text{NC}}_{\text{cut}}$, at $|t| = 1 \times 10^{-3}\,(\text{GeV/c})^2$ and the Coulomb domain, $\theta^{\text{C}}_{\text{cut}}$, at $|t| = 5 \times 10^{-4}\,(\text{GeV/c})^2$ can be deduced. The corresponding cut-off parameters are plotted in figure 6.4, on the right side. Again, a linear behaviour is obtained in a logarithmic representation. Results of the regression are:

$$\lg(\theta^{\text{NC}}_{\text{cut}}/[°]) = 0.2489(\pm 0.034) - 0.996(\pm 0.059) \cdot \lg(p_{\text{beam}}/[\text{GeV/c}]) \tag{6.2}$$

$$\lg(\theta^{\text{C}}_{\text{cut}}/[°]) = 0.0777(\pm 0.034) - 0.976(\pm 0.059) \cdot \lg(p_{\text{beam}}/[\text{GeV/c}]) \tag{6.3}$$

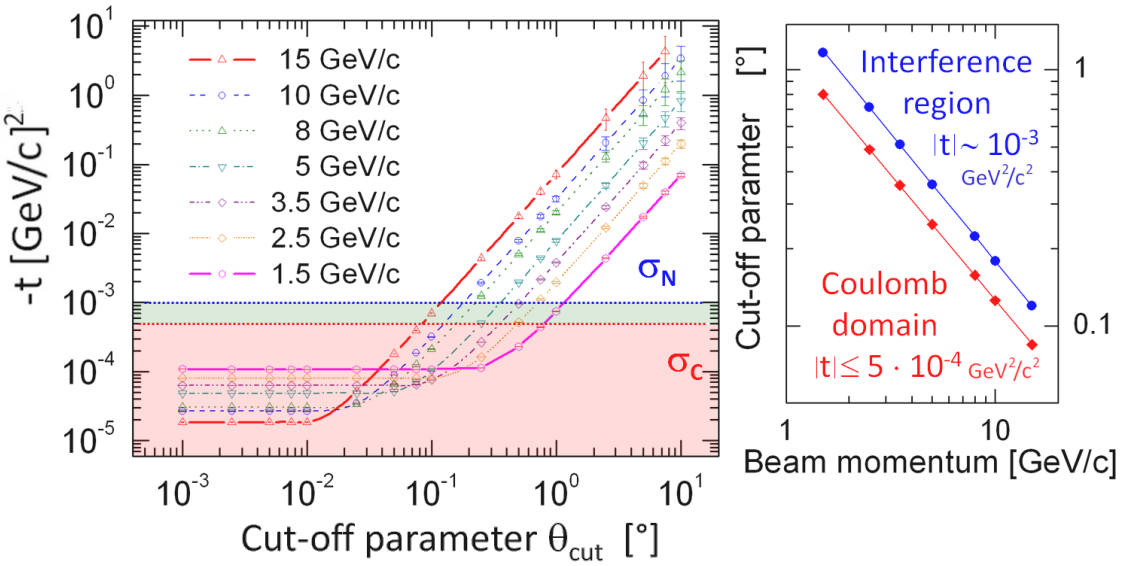

Figure 6.4: *Left*: Correlaton of the cut-off parameter required for the elastic part of the DPM generator and the corresponding squared four momentum transfer, $-t$, for seven different beam momenta between 15 GeV/c and 1.5 GeV/c. The regions of the Coulomb dominated part, σ_C, and the interference with the nuclear part, σ_N, are given in red and green, respectively. Lines represent a linear interpolation. *Right*: Resulting cut-off parameter at the interference region and the Coulomb domain within the beam momentum range of $\bar{\text{P}}$ANDA. The parameterization of the fits is given in equations 6.2 and 6.3, respectively.

For the ongoing studies the cut-off at the Coulomb-nuclear intersection point, $\theta_{\text{cut}}^{\text{NC}}$, is chosen. The resulting distribution of the four-momentum transfer is shown in figure 6.5 in comparison with experimental data. It indicates that the DPM generator describes the elastic scattering reasonably well in a four momentum range up to $|t| = 1.5\,(\text{GeV/c})^2$. The slope at small momentum transfer is matched with the data [161]. Moreover, the position of the crossing point between $0.4\,(\text{GeV/c})^2$ and $0.6\,(\text{GeV/c})^2$ and the subsequent dip becoming more pronounced with lower beam momentum are well reproduced. At higher values above $1.5\,(\text{GeV/c})^2$ a further structure is visible in the measurered data. It is not considered within the DPM model, which delivers a continuous decrease within this region. However, due to very low cross-sections these effects can be neglected when simulating the full antiproton-proton reaction chain.

Finally, the resulting distributions of the complete elastic process involving proton and antiproton are shown in figure 6.6. At high beam momentum, most of the scattered antiprotons appear at a very small polar angle below 3° and do not affect the MVD. However, the peak is shifted to higher values with decreasing beam momentum. As a consequence, an increasing number of antiprotons reach the inner rims of the pixel disks covering polar angles between 3° and 10°. These particles carry nearly all the initial beam momentum thus occupying the momentum range above 1.5 GeV/c.

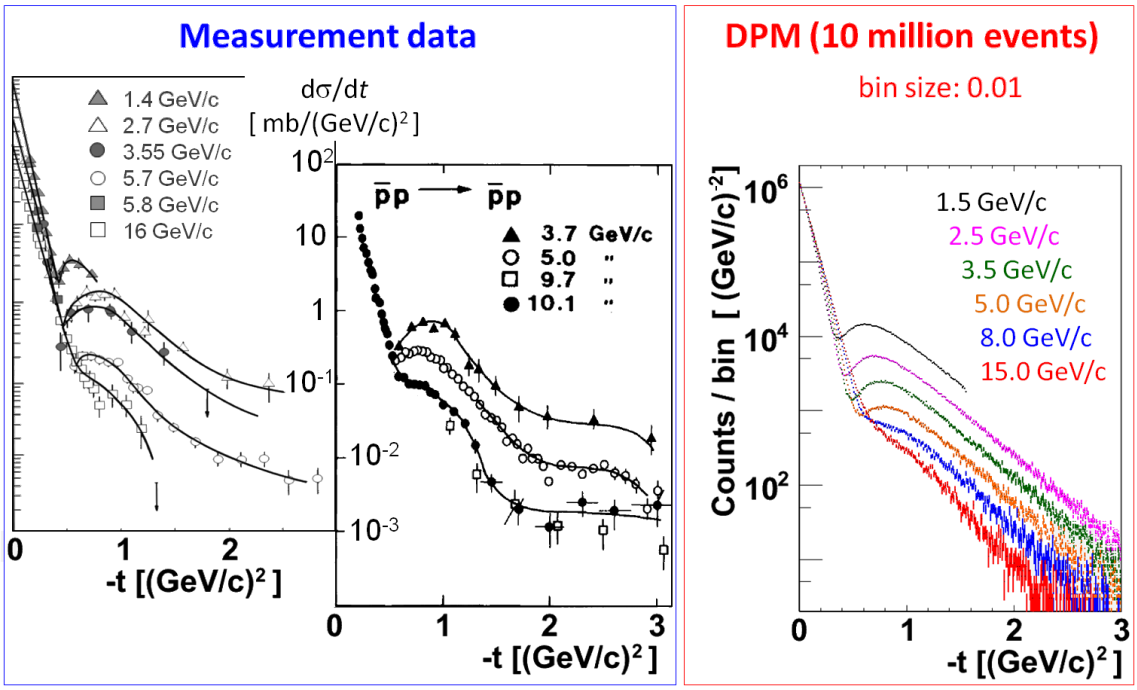

Figure 6.5: Comparison of the four-momentum distribution between simulated DPM events (*right*) and experimental data (*left*). The cut-off parameter in the simulations was set according to equation 6.2. Compiled measurement data is taken from [162] (*left*) and [163] (*middle*).

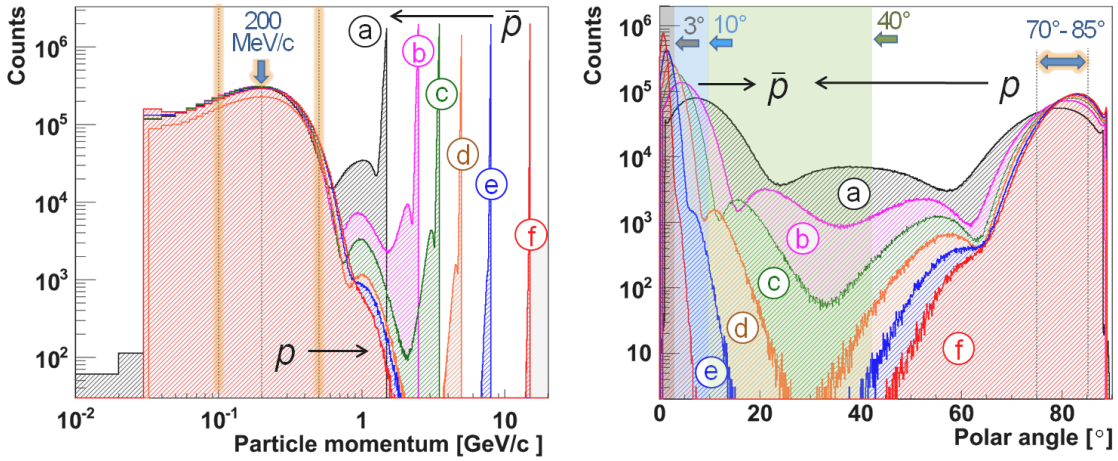

Figure 6.6: Momentum (*left*) and angular distribution (*right*) for the elastic DPM channel applying the cut-off parameter as defined in equation 6.2. Simulations were performed for 10 million events at a beam momentum of 1.5 GeV/c (a), 2.5 GeV/c (b), 3.5 GeV/c (c), 5 GeV/c (d), 8 GeV/c (e) and 15 GeV/c (f). The relevant regions of scattered antiprotons, $\bar{p}$, and the recoil proton, p, are indicated. In the right figure, polar angles below 3° (no impact on the MVD layers), between 3° and 10° (inner rims of the pixel disks) and below 40° (remaining MVD forward part) are highlighted and grey, blue and green, respectively.

The low momentum part of the spectrum is populated by recoil protons. Besides the tail at higher momenta, the slope of the recoil spectrum is nearly independent of the initial beam momentum. The maximum of the momentum distribution in this region is around 200 MeV/c. Most of the slow recoil protons are emitted at polar angles between 75° and 90°. This region is covered by the MVD barrel part. Due to the higher cross sections for an enlarged four momentum transfer at smaller beam momenta, the emission of higher energetic recoil protons in forward direction increases. A small part can thus reach the forward part of the MVD if the beam momentum drops below 8 GeV/c.

The chosen cut-off parameter limits the lowest beam momentum of the recoil protons to several tens of MeV/c. In this way a sufficient suppresion of the Coulomb part of the elastic process is obtained without a significant rejection of the nuclear part. As a consequence, the simulation of a too large number of elastic events outside the acceptance of the MVD is avoided. Moreover, the obtained spectra still deliver a realistic description of the amount of slow resoil protons reaching the MVD layers. With the applied parameterization of the cut-off parameter it is thus possible to use the full DPM generator, i.e. the elastic and the inelastic part, to perform count rate studies, which deliver a realistic estimate of the expected occupancy in different detector layers. Results are summarized in subsection 6.2.3.

6.1.2 Generated particle distributions in antiproton collisions

The gluon rich environment in antiproton-nucleon reactions results in large total cross sections. The spatial distribution and the corresponding kinetic energy of all particles emitted from the primary interaction vertex define the maximum count rates and the radiation load to be expected for different detector parts, respectively. Hence, a study of the overall particle distribution in antiproton collisions at different beam momenta is mandatory to deduce important detector requirements.

In case of antiproton-proton annihilations the DPM generator was used for the simulations taking into account the parameterization for the cut-off parameter as introduced in the previous chapter. The study was performed at beam momenta of 1.5 GeV/c, 2.5 GeV/c and subsequently in steps of 2.5 GeV/c to 15 GeV/c with a high statistics sample of 10 million generated events. Figure 6.7 illustrates the distribution of all particles emitted from the primary vertex obtained at different beam momenta. The particle abundance is plotted in a 2D histogram versus the polar angle and the particle momentum. The fixed-target setup is reflected by a forward boost of particles in the laboratory frame, which is more pronounced at higher beam momentum. Most of these particles carry away a significant part of the initial beam momentum. As a consequence, the momentum range of particles reaching the forward part of the MVD detector at polar angles between 3° and 50° spans nearly two orders of magnitude at highest beam momentum. Slower particles within a range of 100 MeV/c up to 500 MeV/c are emitted more or less isotropic over nearly the full solid angle. They are most relevant for the barrel part covering angles between 40° and 150°. The impact of the elastic scattering process is evident. The kinematics of the two body process defines a unique solution. The low momentum part can be seen clearly as a red line in all 2D histograms of figure 6.7.

A projection of the 2D histogram onto both axes is shown in figure 6.8. The elastic process significantly modifies the integrated 1D profile on either axis. Scattered recoil protons deliver a main contribution to the maximum track density around a polar angle of

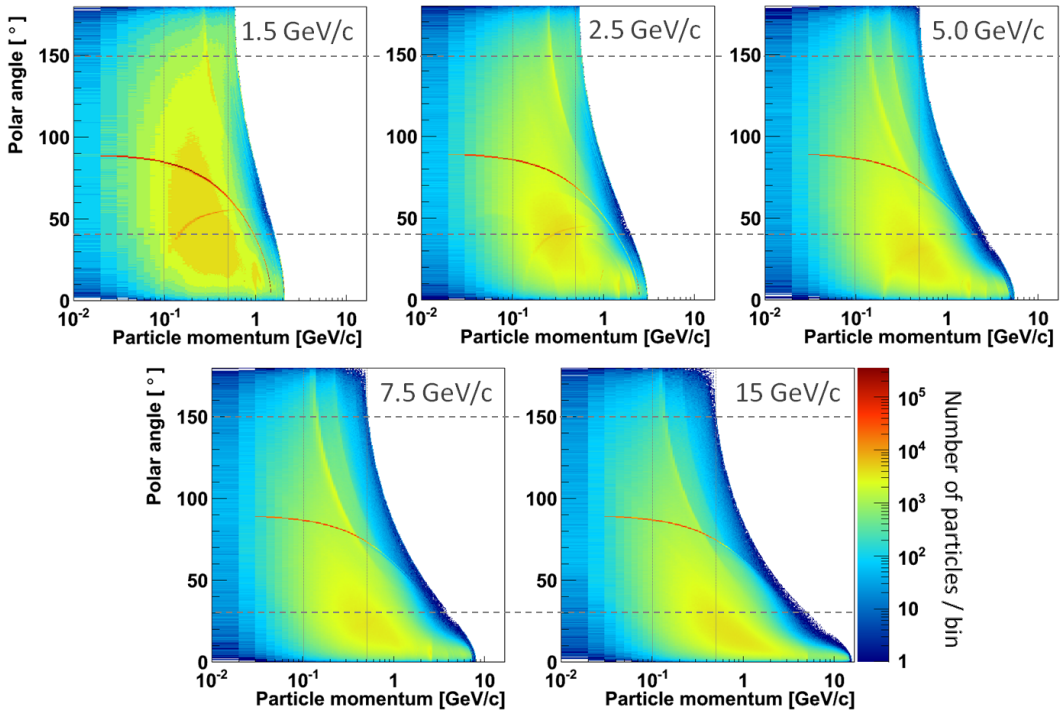

Figure 6.7: Particle abundance, obtained with 10 million generated DPM events, as a function of particle momentum and polar angle at five different beam momenta. Dashed lines at 40° and 150° indicate the crossing point from the forward to the barrel part and the maximum polar angle covered by the MVD, respectively. The red line in all plots results from the elastic process.

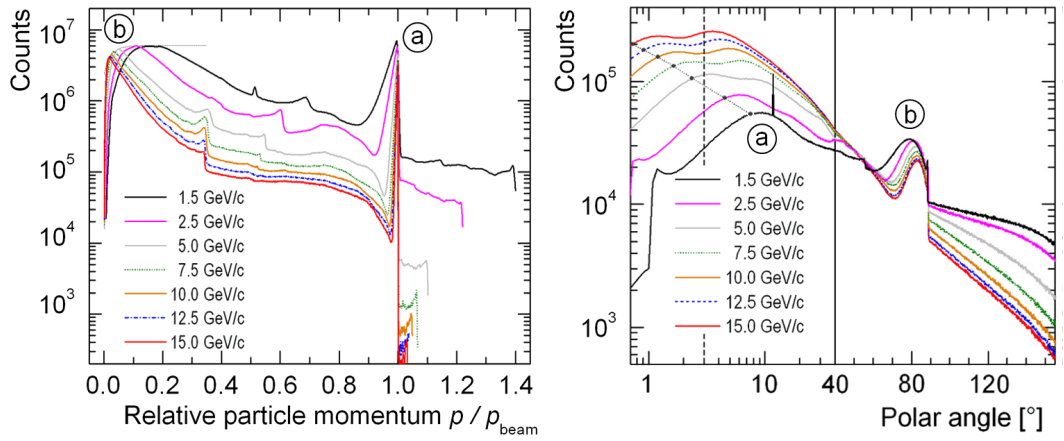

Figure 6.8: Distribution of the relative particle momentum normalized to the initial beam momentum (*left*) and the polar angle (*right*) of emitted primary particles in 10 million DPM events. Main modulations are given by the peak of the elastically scattered antiproton (a) and the corresponding recoil proton (b). The diagram on the right is separated into the forward (logarithmic scale) and the barrel part. The dashed line indicates the minimum polar angle covered by the MVD. Interpolated dots represent the position of the elastic peak in forward direction.

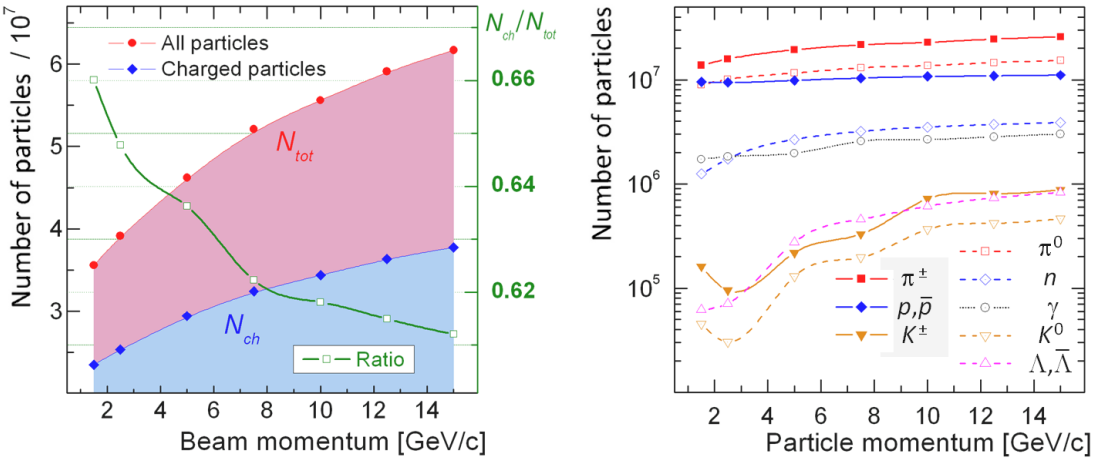

Figure 6.9: *Left*: Total particle number, N_{tot}, and number of charged particles, N_{ch}, produced in 10 million DPM events. On the right axis the ratio between both is plotted in green. *Right*: Composition of produced particle species for all DPM events.

90°. In forward direction the particle boost delivers highest track densities for the overall MVD. Maximum particle momenta are reached for high energetic pions emitted at very small polar angles. They exceed the initial value of the beam momentum (see figure 6.8, left side). With higher initial beam momentum their abundance decreases by roughly one order of magnitude (6.8, right side). A crucial point for the MVD is related to the small angle peak of elastically scattered antiprotons. With decreasing beam momentum it is shifted into forward regions covered by the inner rims of the pixel disks and thus additionally contributes to the particle flux at this detector part. At beam momenta below 7.5 GeV/c the maximum track density at polar angles between 3° and 10° is given by a summing effect of the elastic peak and the particle boost.

The composition of the hadrons in the reaction channel is shown in figure 6.9. Most of the emitted particles are pions, protons and antiprotons. The abundance of neutrons, antineutrons and photons is one order of magnitude lower. Particles with strange quark content are in the order of a few percent. Threshold effects with increasing beam momentum are clearly visible. The percentage of charged particles is mainly defined by the dominating pion emission and thus in the order of 66%. It drops down to lower values of around 61% due to the increased number of neutral nucleons and the increased production of neutral Λ pairs.

In the following, simulation results for antiproton collisions with heavier nuclear targets at the maximum beam momentum of 15 GeV/c shall be emphasized. They were performed with a small sample of 10,000 events but still suit the purpose of a qualitative description. Results for different targets are shown in figure 6.10. Most of the particles carry a momentum between 200 MeV/c and 500 MeV/c. In comparison with antiproton-proton reactions, the forward boost of particles is less distinct and vanishes with heavier nuclear targets. In case of antiproton-gold collisions the maximum track density is reached at a polar angle of around 90°. Besides the reduced forward boost, the momentum distribution of emitted

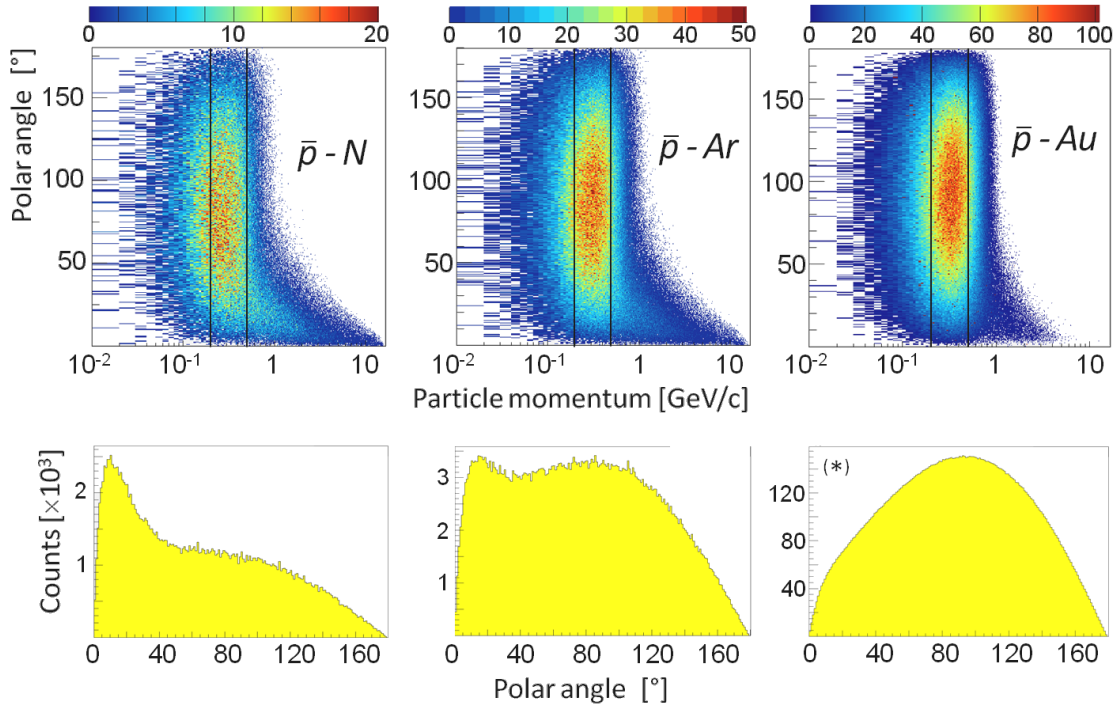

Figure 6.10: *Top*: Particle abundance, obtained with 10,000 generated UrQMD events, as a function of particle momentum and polar angle for three different target nuclei. Black lines indicate the main range between 200 MeV/c and 500 MeV/c . *Bottom*: Resulting 1D profile along the polar angle. The right diagram represents a simulation with ten times higher statistics (*).

particles differs significantly from the one in antiproton-proton collisions. In particular, there are no visible modification due to the elastic scattering process.

Finally, the event multiplicities for both reaction types are summarized in figure 6.11. Results for the $\bar{p}p$ and $\bar{p}N$ where obtained with the DPM and the UrQMD generator, respectively. The event multiplicity describes the number of generated particles per event in the reaction channel. Hence, it delivers some information about the inherent dynamic of the different reactions. In combination with the spatial distributions of emitted particles it also defines the minimum particle flux to be expected in different detector regions. In this ideal case the deadtime of the detector is assumed to be shorter than the smallest time interval between two reactions. As it can be seen in figure 6.11, bottom, the multiplicity per event increases linearly with higher atomic number A of the target nucleus. At the highest beam momentum, the mean multiplicity rises from 6.2 for antiproton-proton reactions to 188.6 obtained in antiproton-gold collisions. The multiplicity also depends on the beam momentum. In case of antiproton-proton collisions, the mean value of the particle multiplicity is roughly doubled when changing the beam momentum from 1.5 GeV/c to 15 GeV/c. Besides, the overall distribution is asymmetric due to the impact of the elastic scattering. This is shown exemplarily for three different beam momenta in figure 6.11, upper frames. In all cases the most probable multiplicity is two. The percentage of larger

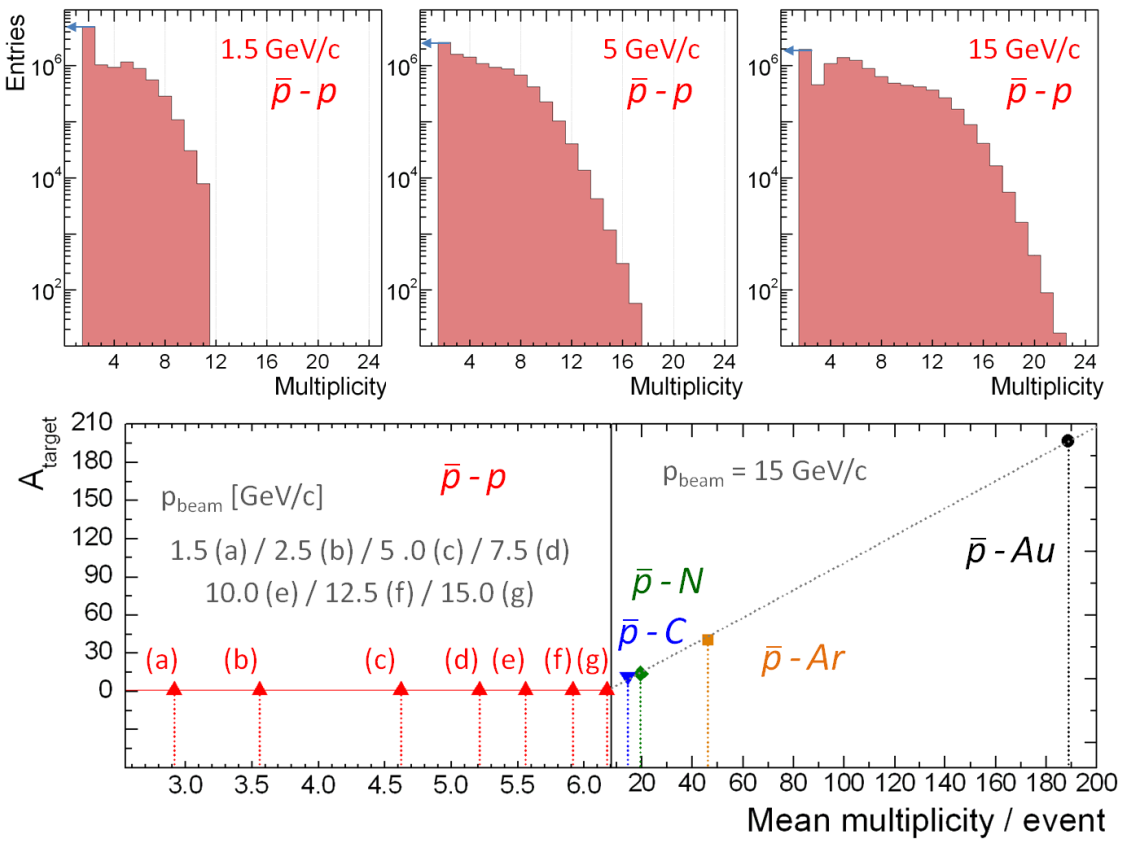

Figure 6.11: *Top*: Multiplicity distribution for antiproton-proton collision obtained with 10 million DPM events at three different beam momenta. *Bottom*: Mean value of the multiplicity at different beam momenta (*left*) and for different targets (*right*) in antiproton-proton and antiproton-nucleon reactions studied with the DPM and the UrQMD generator, respectively.

hit multiplicities increases from 50% at 1.5 GeV/c to 80% at 15 GeV/c. The maximum multiplicity per event obtained in 10 million simulated collisions accounts for 11 and 24, respectively.

6.1.3 Event topology in antiproton-proton reactions

Elastic scattering processes have the largest impact on the overall event topology. Due to the two-body system the kinematics of involved particles is fully deterministic. The resulting solutions within the PANDA beam momentum range are shown in figure 6.12 using two different representations. The relative abundance of elastic events delivered by the DPM model is plotted in figure 6.13, at the top. At the bottom, obtained results are normalized with the interpolation fits to experimental data of the total and the elastic cross section as shown in figure 6.1. The errors result mainly from the applied fit and thus are related to uncertainties of the measurements and missing data points within certain momentum intervals. The statistical error of the determined DPM values is very small due

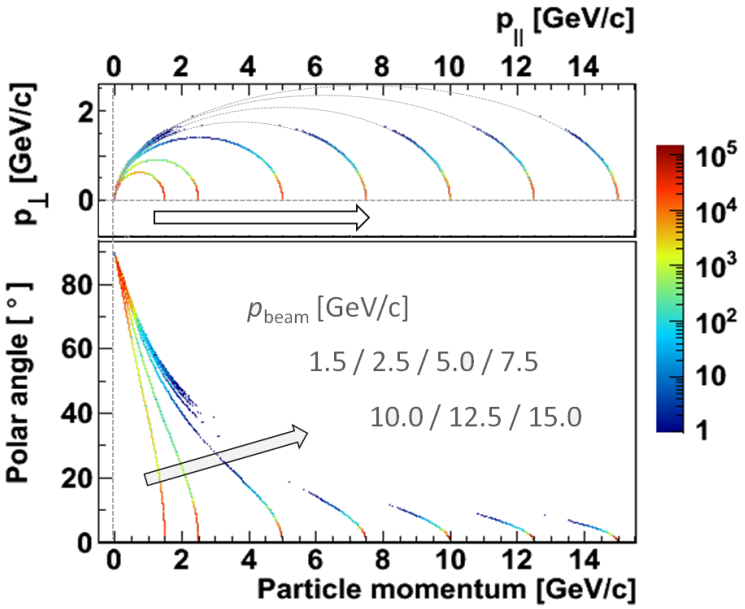

Figure 6.12: Illustration of the elastic solution for scattered antiprotons and corresponding recoil protons within the $\bar{\text{P}}$ANDA beam momentum range. *Top*: Transverse, $p_\perp$, vs. longitudinal particle momentum $p_{||}$. The grey lines represent the kinematics solution in regions with a highly suppressed occupancy. *Bottom*: Total particle momentum vs. polar angle. The relative abundance along the theoretical solution is plotted colour-coded and represents the distribution of all elastic events obtained in 10 million generated DPM events.

to the large sample of 10 million simulated events. In comparison, a reasonable agreement between the DPM generator and measurements can be observed. However, at lower beam momenta the DPM model delivers a systematic overestimation of up to 10% at 1.5 GeV/c. These deviations exceed the given errors.

Alongside the elastic process any annihilation into two particles follows a similar pattern. Kinematic limits are defined in case of pions due to the lighter particle mass. At small forward angles close to zero degrees, the resulting particle momentum exceeds the initial beam momentum by roughly 500 MeV/c. The relative abundance of two particle final states is shown in figure 6.14. At lower beam momentum, these values are in the order of per mille up to a few percent. A comparison of the DPM generator with experimental data indicates an overestimation of the two-charged-pion final state and deviations in case of the annihilation into neutral nucleons due to a too strong decrease of the abundance with increasing beam momentum. There are no available experimental data at higher beam momentum above 7.5 GeV/c.

The majority of antiproton-proton reactions result in final states with a multiplicity bigger than two. In this case the available phase space for outgoing particles is defined inside the borders of the two particle solution. Most relevant for the MVD are the emitted charged particles. Figure 6.15 summarizes the relative abundance of events with multiple pairs of charged particles generally called “prongs”. The $\bar{\text{P}}$ANDA momentum range is

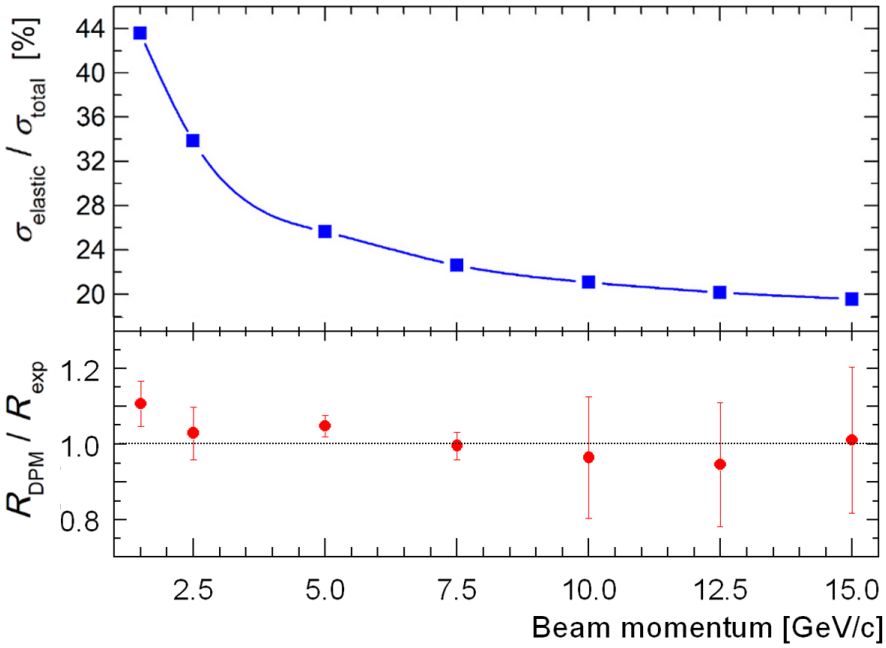

Figure 6.13: *Top*: Relative abundance of elastic events, σ_{elastic}, vs. the total cross section, σ_{total}, obtained in 10 million DPM events. *Bottom*: Comparison of the ratio, $R = \sigma_{\text{elastic}}/\sigma_{\text{total}}$, between the DPM model and experimental data [158].

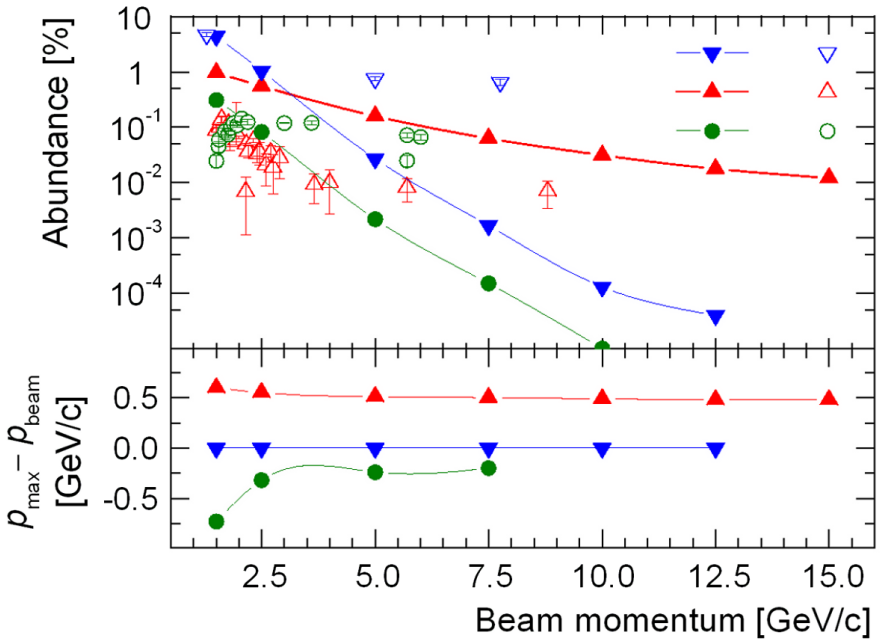

Figure 6.14: *Top*: Relative abundance of two-body annihilation within the DPM model (closed symbols) in comparison with experimental data [158] (open symbols). *Bottom*: Difference between the maximum momentum, p_{max}, of the boosted particle in forward direction with respect to the beam momentum, p_{beam}, of the incoming antiproton.

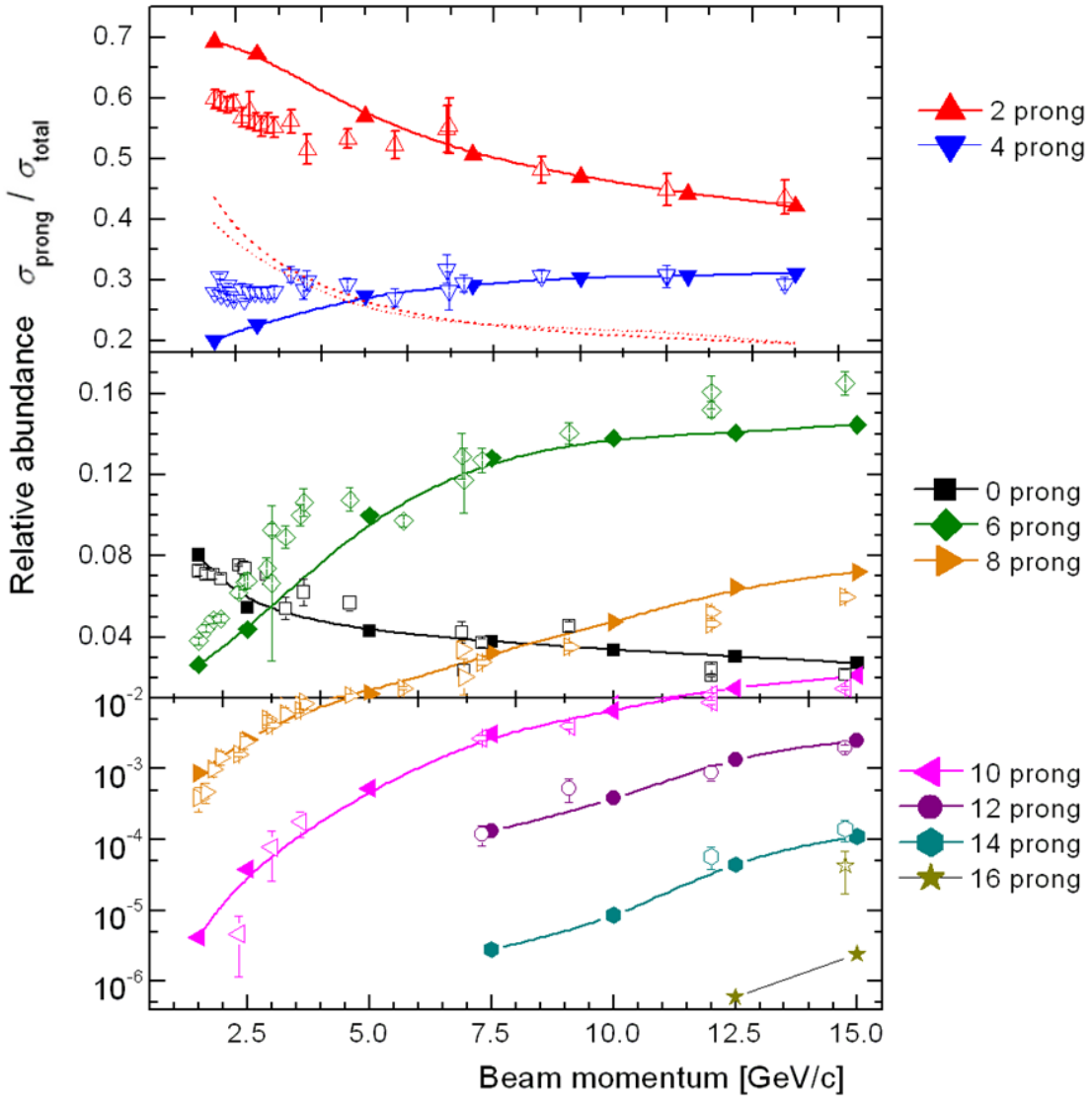

Figure 6.15: Relative abundance of different n-prong events obtained in 10 million generated DPM events (closed symbols) in comparison with experimental data compiled in [158](open symbols).

dominated by two-prong and four-prong events. The relative abundance of events with two charged particles accompanied by additional neutral particles is in the order of 20% to 25%. Again, deviations of the DPM model from experimental data become visible at beam momenta below 5 GeV/c. The overestimation of two-prong events, which also appears in the implemented elastic process is counter-balanced by an underestimation of four-prong events. The overall decrease of two-prong events from 60% to approximately 43% is correlated with an increase of six-prong events from 4% to 16% at a beam momentum of 1.5 GeV/c and 15 GeV/c, respectively. Moreover, the impact of eight-prong and ten-prong events exceeds the percent level with increasing beam momentum. They reach a maximum

of 8% and 2% at a beam momentum of 15 GeV/c. Events with more charged particles are suppressed by orders of magnitude and thus do not have a huge impact on a macroscopic scale.

In special cases a stringent kinematics is also defined by a two-particle production involving light mesons and baryon resonances with a subsequent two-body decay. Corresponding particles in the final state thus have a well-defined kinematics. Within the covered mass region of $\bar{\text{P}}$ANDA total cross sections for these reaction channels are relatively large, in particular at smaller beam momentum. They are considered within the DPM model. As a consequence, correlated modifications of the phase space become visible (see e.g. picture 6.7, top left). Main contributions can be found in multi-pion final states and in characteristic reaction channels associated with the decay of light mesons, e.g. ρ or f_0, and Δ resonances. These are more significant at the lower bound of the $\bar{\text{P}}$ANDA momentum range.

6.2 Detector simulations

Basic input for the detector simulations is given by the converted detector model Mvd-2.1 presented in chapter 5 and the studies of the hadronic background performed with the DPM generator. Main purpose is an evaluation of basic parameters such as the detector coverage and the extraction of count rates,, which deliver important input for the development of associated detector electronics. The geometric coverage of the MVD model is analyzed in subsection 6.2.1. Afterwards, a study of the material budget introduced by the realistic detector is performed in subsection 6.2.2. Count rates for different detector parts are deduced in subsection 6.2.3. These comprise averaged and maximum values on individual readout channels as well as integrated numbers for connected frontend electronics and detector layers.

6.2.1 Detector coverage

The geometrical detector coverage is connected to the optimization of the sensor arrangement. Therefore, the reduced model of the central MVD (MVD-2.1_Sensitive, see chapter 5.4.2, page 109) was used for the studies. It includes only active sensor elements and no further passive material. Pipes of the beam-target system were not introduced. Scattering effects of passive materials are thus excluded. For the purpose of this study this effect is wanted because it allows a clean mapping of the detector coverage focused on mere geometrical aspects, which are the starting point for a systematic evaluation of basic detector properties. Material effects are discussed in the next subsection 6.2.2.

The studies were performed for charged pions, protons and anti-protons in a momentum range between 150 MeV/c and 1.5 GeV/c. This interval was chosen in order to check a possible influence of the bending radius on the effective detector coverage. Particles with fixed momentum were propagated through the detector from the nominal interaction point (0;0;0) including the magnetic field of the 2 T solenoid. The $\bar{\text{P}}$ANDA root framework [144] was used as an interface to the GEANT4 transport code [164, 165]. In all individual setups two million events were simulated with a uniform distribution over the full solid angle.

During the process of the particle propagation, all important track information was buffered. In the further analysis the number of hit points within the MVD was extracted

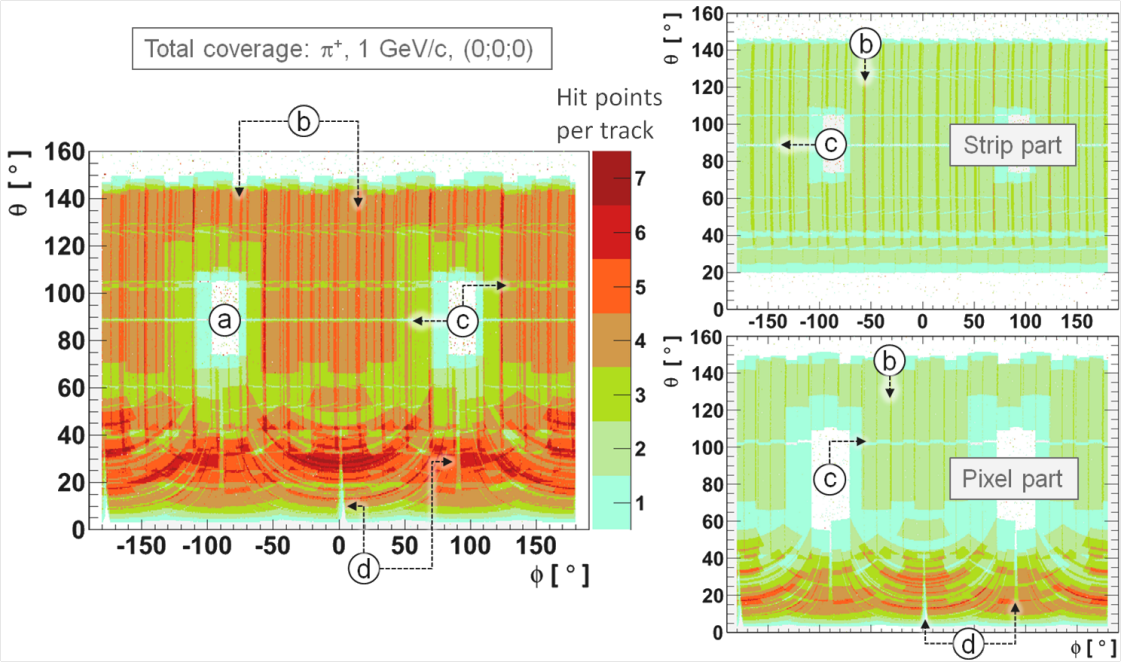

Figure 6.16: *Left*: Detector coverage for pions with a momentum of 1 GeV/c emitted from the nominal IP. The obtained number of hit points per track is plotted colour-coded against the initial polar (θ) and the azimuthal (ϕ) angle. Indicated patterns refer to the target pipe gap (a), the radial overlap of adjacent elements in the barrel part (b) and gaps in the barrel (c) and the pixel disk layers (d) due to passive edges of back-to-back arranged sensors. *Right*: Respective contributions of the pixel and the barrel part.

for each track and stored with the initial emission angles θ (polar) and ϕ (azimuthal). The corresponding 2D diagram for one selected configuration can be found in figure 6.16, on the left side. Respective contributions of the pixel and the strip part are shown on the right side. The maximum coverage of the active part of the MVD spans a polar angle from 3° to 150° (see also figure 3.2 on page 66). Bigger gaps are related to the keep-outs needed for the target pipe.

Polar angles between $\theta = 70°$ and $\theta = 140°$ are covered by all four barrel layers. They deliver a rather homogeneous coverage of four hit points. A reduced number results from the adjustment to the crossing target pipe in the different layers and gaps introduced by the passive sensor edges due to the back-to-back arrangement along the beam axis. An increased number of mostly five hit points is related to the radial overlap of adjacent elements within one barrel layer. A significant difference between the pixel and the strip part occurs in the forward region ($\theta < 60°$). Due to the approximation of the pixel disk layers with rectangular-shaped sensors, the covered solid angle corresponds to a circle-segment-shaped area in the θ-ϕ diagram. As a consequence, the six double-sided pixel disks deliver a more complex pattern compared to the homogeneous coverage of the two strip disks. Besides, the projected gap between the barrel and the forward part is larger in case of the pixel disks. It reflects safety margins needed for the detector assembly. Again,

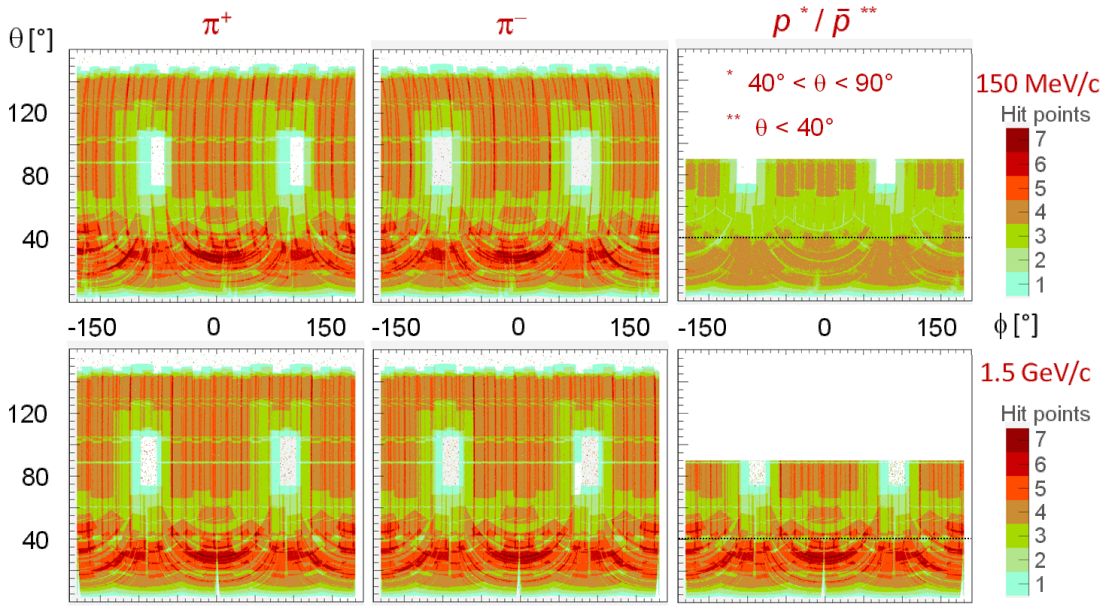

Figure 6.17: Detector coverage for charged pions (*left* and *middle*) and nucleons (*right*) at two different particle momenta. For protons and antiprotons only the relevant physical region is plotted (see subsection 6.1.1). At low momentum, the opposite bending radius is reflected by the different curvature in the barrel part. Moreover, strong attenuation effects occur for slow nucleons.

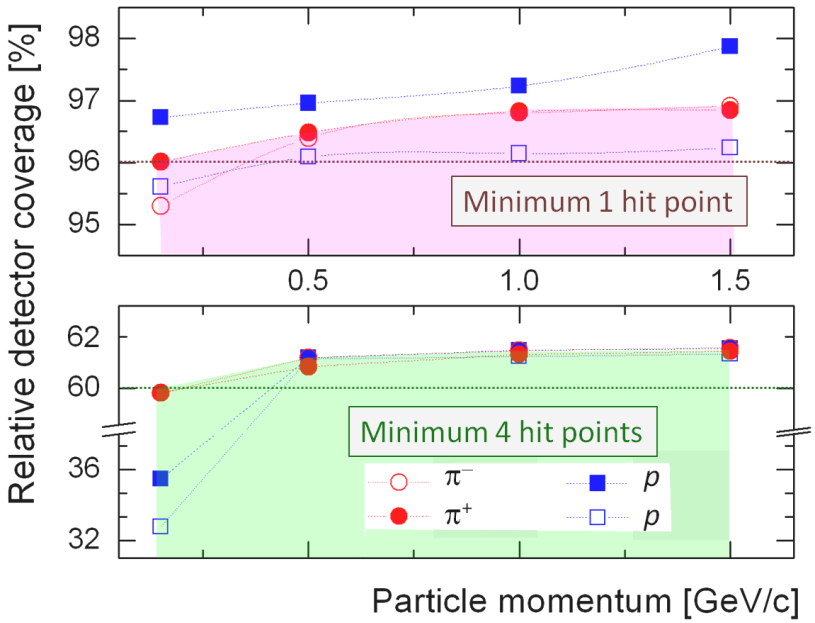

Figure 6.18: Effective detector coverage for polar angles between 3° and 150° for a minimum of one (*top*) and four (*bottom*) MVD hit points. Differences between the different particle species are related to interactions in the silicon layers.

Particle momentum	Relative coverage within $3° < \theta < 150°$ / [%] Number of hit counts 1	2	3	4	5	6	Total
Proton / *Anti-proton*							
0.15 GeV/c	5.1 *6.3*	12.5 *10.1*	45.3 *44.8*	32.2 *34.9*	0.5 *0.6*	< 0.1 *< 0.1*	95.6 *95.6*
0.5 GeV/c	5.4 *6.2*	7.1 *6.3*	22.2 *22.9*	40.7 *39.9*	16.4 *17.1*	3.6 *3.9*	96.1 *97.0*
1.0 GeV/c	5.5 *6.2*	6.8 *6.4*	22.3 *22.7*	40.6 *40.2*	16.5 *17.3*	3.8 *3.7*	96.1 *97.2*
1.5 GeV/c	5.6 *6.4*	6.7 *6.7*	22.3 *22.7*	40.6 *40.3*	16.5 *17.2*	3.9 *3.8*	96.2 *97.9*
Pions: π^+ / π^-							
0.15 GeV/c	6.3 *4.5*	7.6 *9.0*	22.3 *21.0*	38.5 *38.4*	16.9 *17.1*	3.6 *3.4*	95.0 *93.2*
0.5 GeV/c	6.1 *5.4*	6.4 *7.1*	23.0 *22.4*	39.7 *40.9*	16.9 *16.6*	3.8 *3.6*	94.9 *94.5*
1.0 GeV/c	6.0 *5.6*	6.4 *6.9*	22.7 *22.4*	40.0 *40.8*	17.1 *16.6*	3.7 *3.8*	95.2 *95.0*
1.5 GeV/c	6.0 *5.7*	6.4 *6.8*	22.6 *22.4*	40.2 *40.8*	17.1 *16.6*	3.8 *3.9*	95.2 *95.2*

Table 6.1: Results on the total detector coverage obtained with different setups.

passive edges of the sensors arranged back-to-back can be identified.

A comparison between different configurations is shown in figure 6.17. The opposed bending radius of charge conjugated particles with low momentum (150 MeV/c) is reflected by the different curvatures of the overlaps in the barrel part. Besides, there are no major distinctions proving the hermetic design of the MVD. In case of low momentum nucleons strong attenuation effects can be observed. They are caused by interactions with the active silicon material during the particle propagation. Taking into account all the pipes of the beam target system and a full material budget for the MVD, it can be concluded that slow nucleons get stuck already in one of the MVD layers. In particular, this fact becomes relevant for elastically scattered recoil protons. At higher particle momentum there are no differences in the coverage pattern between the different particle species. Further results of the corresponding studies are summarized in table 6.1.

Besides a sole visualization, the detector coverage can be characterized quantitatively. Results on the relative coverage within the maximum range between $\theta = 3°$ and $\theta = 150°$ are plotted in figure 6.18. Obtained values are in the order of 96% and 60% for a minimum of one and four hit points, respectively.

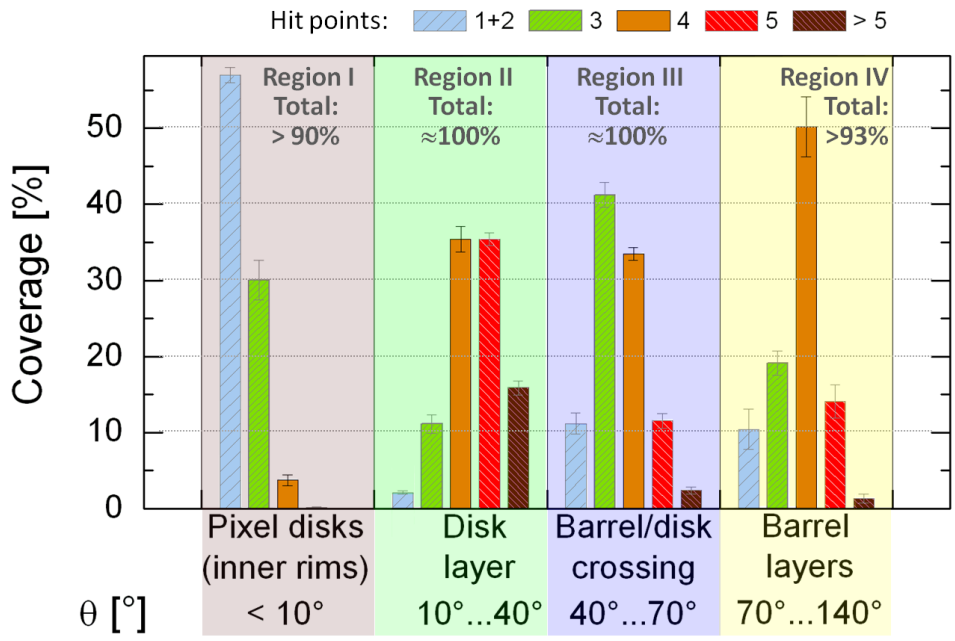

Figure 6.19: Yield of different hit counts in four different detector regions. The error bars include maximum deviations obtained with different input parameters, i.e. particle species and momentum, and statistical fluctuations.

For the following analysis the covered solid angle was split into four regions:

Region I: Polar angles between 3° and 10° representing the solid angle covered by the inner rims of the pixel disks which contribute to the forward tracking systems,

Region II: Polar angles between 10° and 40° representing the solid angle covered by the forward disk layers,

Region III: Polar angles between 40° and 70° representing the solid angle covered by the strip barrel part, the outer pixel barrel layer and the innermost pixel disk delivering the fourth hit point,

Region IV: Polar angles between 70° and 140° representing the area covered by all four barrel layers.

Figure 6.19 illustrates the yield of different hit counts for charged pions emitted into the different polar angle intervals defined above. The plotted values include information of all performed simulations, i.e. all setups with different particle species and different particle momenta as discussed in the previous paragraph. Combining all contributions, a full coverage of 100% is reached for the disk layers in region 2, the crossover between the barrel and the forward part (region 3) and down to a minimum polar angle of $\theta = 4.5°$ within region 1. This means that for forward boosted particles between 4.5° and 40° at least one hit point is generated inside the MVD. In the main barrel part (region 4) this value drops to 93.3% due to the keep-out for the target pipe.

The impact of individual hit counts differ in all four regions. In region 1, inner rims of the second, third and fourth pixel disk contribute additional hit points at polar angles above 4.5°, 6.5° and 8°, respectively. In total, the relative coverage with one and two hit points (56.5%) dominates over a higher hit count of three (30%) and four (3.3%). The highest average hit count is achieved in region 2 due to the increased number of disk layers. Four and five hit points contribute with roughly one third each. The impact of higher hit counts is in the order of 15%. It also includes the maximum number of 14 hit points for a single track inside the MVD. Events with three and less hit points level out at 10% and 1%, respectively. Based on these results it can be concluded that the physics-wise most interesting region between 10° and 40° is covered with a sufficient number of hit points thus allowing a precise reconstruction of decay vertices. Compromises have been made in region 3 to obtain a feasible solution for the detector assembly. As consequence, mostly three hit points (41%) are obtained within the covered area. However, four hit points are still delivered for roughly one third of the corresponding solid angle. Contributions in the order of 10% are given by hit counts of five and less than three. Higher hit counts occur with an abundance of 2.6%. They are further decreased in the main barrel part (region 4). There, four hit points clearly dominate (50%). Radial sensor overlaps leading to five hit points cover roughly 15% of the area. The coverage with a reduced number of hit points is mainly related to the target pipe keep-out. It is in the order of 19% and 10% for three and less hit counts, respectively.

Besides a sufficient number of hit points along each particle track, a minimized distance of the first hit point with respect to the nominal IP is crucial for the physics performance of the detector. Therefore, a similar simulation as described previously was performed for positively charged pions with a momentum of 1.5 GeV/c. This time the positions of all hit points were buffered and the distance of the first hit point to the origin was extracted in the further analysis. The corresponding 2D diagram is shown in on the left side of figure 6.20.

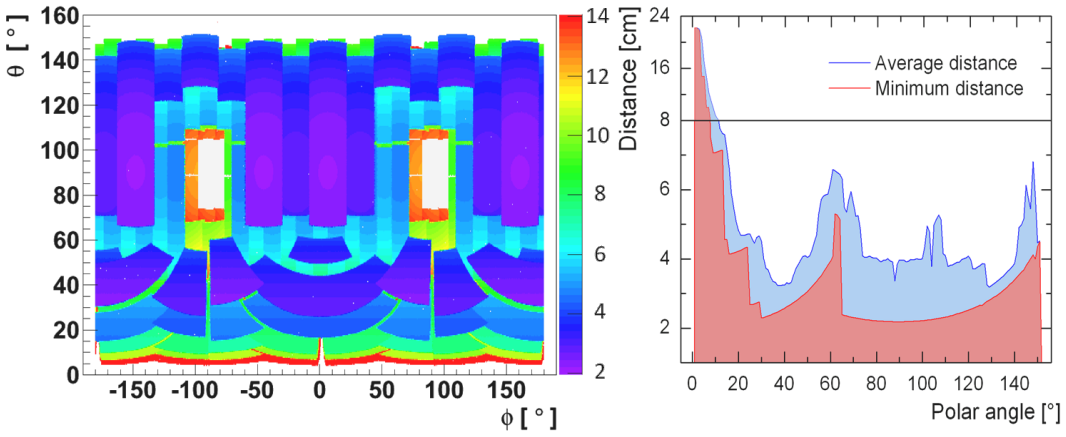

Figure 6.20: Distances of the first hit point to the nominal IP obtained for slow pions (p = 150 MeV/c). *Left*: Colour-coded plot against the polar (θ) and the azimuthal angle (ϕ). *Right*: 1D profile along the polar angle showing the minimum and the averaged value obtained within the full azimuthal angle.

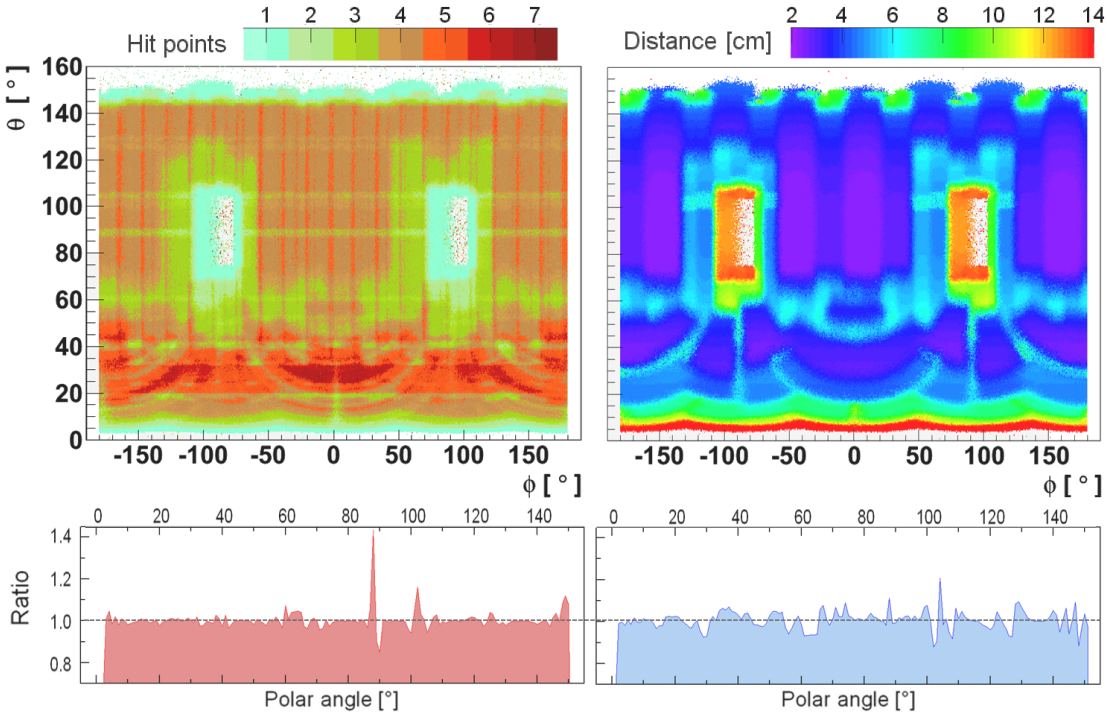

Figure 6.21: Studies with a non point-like primary vertex. Obtained results for positively charged pions with 150 MeV/c $\leq p \leq$ 1.5 GeV/c. *Top*: 2D hit count distribution (*left*) and distance of the first hit point with respect to the nominal IP (*right*). *Bottom*: Comparison with results of the previous study using a fixed vertex and a particle momentum of 1.5 GeV/c. The 1D profile along the polar angle represents the ratio between both configurations.

It indicates that a large part of the solid angle is covered by the innermost pixel layers thus resulting in a distance between 2 cm and 4 cm. Particles passing through the gaps are detected in subsequent layers, most of them in the second pixel layer having a distance of roughly 2 cm to the previous one. Besides the target pipe keep-out, a wider band between $\theta = 55°$ and $\theta = 70°$ occurs, which reflects the safety margins needed for the insertion of the innermost disk layers inside the outer pixel barrel layer. However, in a polar angle region between 35% and 55% most of the propagated particles are detected within the first pixel disk. As it can be seen on the right hand side of figure 6.20, a minimum distance of less than 4 cm can be reached within a wide range.

Finally, the study was repeated for a more realistic description taking into account a non point-like interaction region. For this, 5 million positively charged pions with a momentum between 150 MeV/c and 1.5 GeV/c were simulated with a smeared vertex. The vertex extension was approximated by a Gaussian distribution with a width of $\sigma = 2$ mm in x and y and a flat distribution of $\pm$ 3 mm along the beam axis. These values represent an upper limit according to given specifications of the beam-target system presently available [166]. Results are shown in figure 6.21. Besides the expected blurring of the pattern in the 2D diagrams there are no significant changes.

Material	Element					Compound			
	Cu	*In*	Al	C*	Si	Steel[1]	*Fibre*[2]	PVC[3]	Water
ρ / [g·cm^{-3}]	8.96	*7.31*	2.70	2.265	2.33	8.02	2.23	1.30	0.92
$X_{0,\mathsf{calc}}$ / [g·cm^{-2}]	13.16	-	24.26	43.01	21.08	14.28	-	25.84	36.32
$X_{0,\mathsf{PDG}}$ / [g·cm^{-2}]	12.86	*8.85*	24.01	42.70	12.86	-	*28.17*	25.51	36.08

Density weighted materials	Carbon foam[4]	Carbon support structures	"SMD"	"Heavy" PVC
Component A : (B)	C*	C* : Carbon foam	Al	PVC : Al
Weight(s) $\frac{w_\mathrm{A}}{(w_\mathrm{B})}$	0.1	$\frac{0.10}{0.90}$/ $\frac{0.75}{0.25}$/ $\frac{0.33}{0.67}$/ $\frac{0.50}{0.50}$/ $\frac{0.67}{0.33}$/ $\frac{0.75}{0.25}$/ 1.5	0.52	$\frac{9}{1}$
ρ / [g·cm^{-3}]	0.2265	0.43/ 0.74/ 0.90/ 1.25/ 1.59/ 1.76/ 3.40	1.41	1.44
X_0 / [g·cm^{-2}]	$X_{0,\mathsf{calc}}^{(\mathsf{C*})}$	$X_{0,\mathsf{calc}}^{(\mathsf{C*})}$	$X_{0,\mathsf{calc}}^{(\mathsf{Al})}$	28.65

* Configuration: compact, [1] Composition: 1% Si; 2% Mn; 10% Fe; 19% Cr; 68% Ni , [2] Borosilicate glass, [3] Composition: 4.8% H; 38.4% C; 56.7% Cl, [4] Low thermal conductivity, see [167]

Table 6.2: Density ρ and radiation length X_0 of different materials and compounds as taken for the presented studies with the Mvd-2.1 model. $X_{0,\mathsf{calc}}$ and $X_{0,\mathsf{PDG}}$ refer, respectively, to equation 6.4 and 6.5 defined as input to the simulations and measured values listed by the PDG [168]. Italic columns were used as reference for table 6.5. Concerning the definition of carbon foam consider the remarks given in [167].

6.2.2 Radiation length studies

Due to the comprehensive detector model described in chapter 5 it is possible to perform a detailed study of the introduced material budget and to extract a realistic estimate on the effective radiation length of the MVD. The latter gives quantitative access to the expected electromagnetic interaction of high energetic particles in the detector material. particles in the detector material. One full radiation length X_0 is equivalent to the mean path length required to either reduce the energy of relativistic charged particles by the factor $1/e$, or $7/9$ of the mean free path for a pair production by a high-energy photon. It is a specific property of each material and thus linked to the atomic number Z and the atomic mass A. A commonly used parameterization to calculate X_0 is based on a compact phenomenological fit to experimental data [169]:

$$X_0 = \frac{716.4 \cdot A}{Z(Z+1)\ln\left(\frac{287}{Z}\right)} \; [\mathrm{g \cdot cm^{-2}}] \tag{6.4}$$

Except for helium, results using this formula agree with input data to better than 2.5%. In case of a mixture or a compound made of i different elements the radiation length can be approximated by

$$1/X_0 = \sum_i \frac{w_i}{X_{0_i}} \tag{6.5}$$

where w_i and X_{0_i} are the fraction by weight and the radiation length for the i-th element. Specific values for the density and the radiation length of different materials are listed in table 6.2. Finally, the resulting attenuation coefficient X along the particle track within a specified medium depends on the density ρ and the traversed path length L.

$$X = \rho \cdot L \tag{6.6}$$

The impact of the introduced material can be then described by a fractional radiation length, X/X_0, which is accumulated in all traversed volumes j:

$$X/X_0 = \sum_j \frac{\rho_j \cdot L_j}{X_{0_j}} \tag{6.7}$$

In the following, the corresponding value of the material budget will be given in percent ($X/X_0 < 1$) or in multiples ($X/X_0 \geq 1$) of X_0.

For the presented studies, the full version of the central MVD (Mvd-2.1_FullVersion) and the one including the two additional forward disks (Mvd-2.1_AddDisks_FullVersion) were used. Simulations were performed within the simulation framework of $\bar{\text{P}}$ANDA by propagating a virtual particle ("geantino") within the GEANT4 transport code. The fictitious "geantino "particle undergoes no physical interactions but flags boundary crossings along its straight trajectory. Two million events were propagated starting from the nominal IP $(x;y;z) = (0;0;0)$ with a uniform distribution over the polar angle, θ, and the azimuthal angle ϕ. For each geantino the effective path lengths in all crossed components (L_j) were identified. The fractional radiation length (X/X_0) was then calculated based on the given material definition of the volumes. The final results of each event were stored along with the initial emission angles (θ_0; ϕ_0).

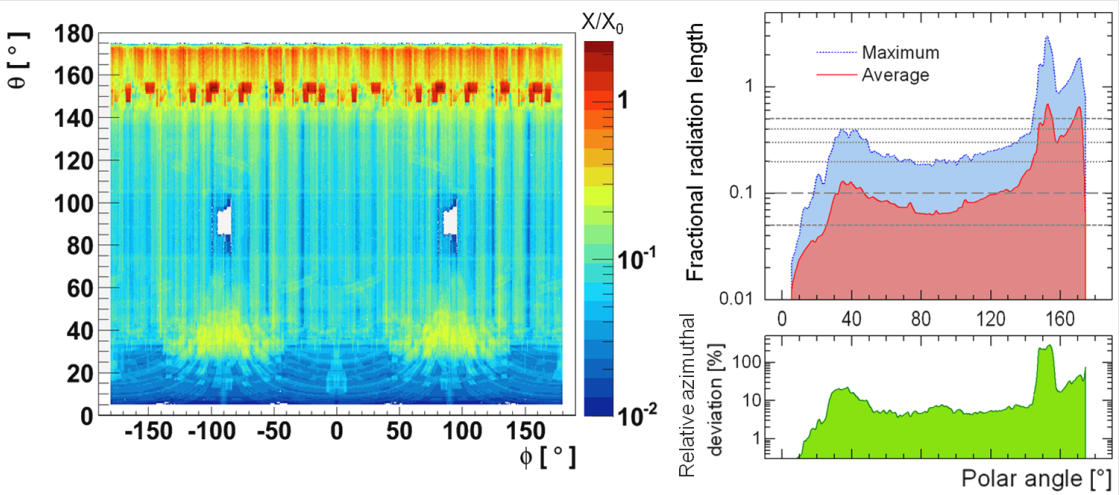

Figure 6.22: *Left:* 2D distribution of the fractional radiation length X/X_0 obtained for the central MVD. *Right:* 1D profiles along the polar angle showing the averaged and maximum values (*top*) and the associated relative azimuthal deviation (*bottom*) within defined intervals of $\Delta\theta = 1°$.

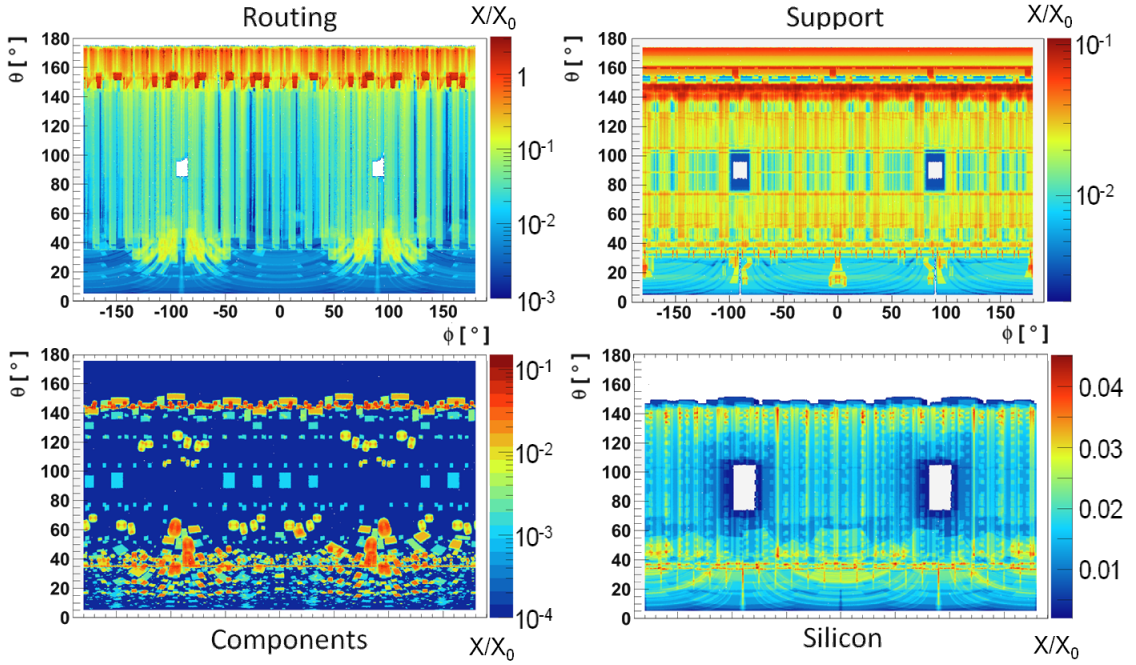

Figure 6.23: Contributions of the four main parts of the Mvd-2.1 model (see section 5.4). The fractional radiation length X/X_0 is plotted colour-coded against the polar θ and the azimuthal angle ϕ . (Note the different scales for X/X_0.)

In figure 6.22, on the left, the 2D distribution of the material budget in terms of X/X_0 is plotted colour-coded against both initial emission angles. The resulting diagram was obtained for the central MVD without the additional disks. Corresponding profiles along the polar angle are shown to the right. The average and the maximum fractional radiation length for tracks within a bin size of $\Delta\theta = 1°$ are shown at the top. The standard deviation of all values of within the θ interval, normalized with the corresponding mean value, is plotted below. It is a measure of the isotropy of the material load along the integrated azimuthal angle. Basically, all distributions indicate a low material budget in the physically most important region of interest below a polar angle of 140°. The overall material budget therein stays mostly well below $10\%X_0$ and shows a rather isotropic occupancy with relative fluctuations of not more than 10%. Larger deviations are located between $\theta = 30°$ and $\theta = 50°$. Moreover, a significant difference occurs in the very backward region manifesting itself in a much higher radiation load with hot spots of up to several radiation lengths.

For a more detailed discussion on the distribution of the material load it is useful to perform a separate analysis with different detector parts. Therefore, only the individual components of interest were switched on during the simulation. Taking advantage of the basic conventions defined for the Mvd-2.1 model (see sections 5.1 and 5.4), this procedure can be accomplished in a fast and efficient way thus allowing a whole set of different studies. As a first result, contributions of all four main substructures are disentangled in figure 6.23. The highest impact on the full material map comes from the cabling part thus delivering main modulations of the overall distribution (see figure 6.22). Average values of

individual packages level around $5\%X_0$ in the main barrel region ($40° < \theta < 140°$). The bundling of the pixel disk services at the top and bottom is clearly visible. Moreover, the unavoidable routing to outer radii leads to an additional increase of the effective radiation length in the forward region ($30° < \theta < 50°$). It results in a partial increase above $10\%X_0$ thus defining the maximum material load in the sensitive detector region. The obvious jump to a relatively high material load, including hot spots of several radiation lengths occurring at large polar angles above 140°, can be clearly assigned to the cabling part. These enhancements are related to the fixed routing scheme of the inner barrel layers along the opening beam pipe in upstream direction and the generally increased incident angle of tracks traversing the circularly arranged cables and pipes.

Compared to hot spots in the 2D map of the cabling part, maximum values for all other sub-structures fall short by more than one order of magnitude. Support structures contribute with one to three percent of a full radiation length in the active detector region. Cut-outs of large support components can be clearly identified. Moreover, higher values reflect the load pick-up of the main building blocks, which is concentrated in upstream direction at polar angles above 140°. A maximum of approximately $5\%X_0$ and $10\%X_0$ is given below (forward part) and above (barrel part), respectively. The resulting pattern of the introduced components defines a very anisotropic distribution. While the averaged number is relatively small, maximum values of roughly $10\%X_0$ are reached at singular points. Apart from a band around $\theta = 145°$, they are concentrated in forward direction ($10° < \theta < 60°$). A significant pattern originates from the cooling connectors of the innermost pixel disks. Finally, the most homogeneous material occupancy is given by the silicon part. It levels between one and two percent of X_0 and shows a typical cosine modulation reflecting the incident angle of straight lines originating from the nominal IP. A further increase at smaller polar angles is related to the enlarged number of individual detector layers in forward direction.

Taking into account the 2D distributions as shown in figure 6.23, it is obvious that an evaluation of local hot spots in the material map is crucial for a proper detector description, which includes eventual effects of an anisotropic material occupancy. Figure 6.24 illustrates the distribution of such points with an enhanced fractional radiation length along the polar angle. In principle the curves reflect again the obtained profile for the overall radiation length (see figure 6.22, top left). The given relative abundance is defined as the ratio of counted tracks, N_{spot}, with a stored value of X/X_0 above a defined maximum divided by the overall number of tracks, N_{all}, to be expected within an interval of $\Delta\theta = 5°$. The latter, N_{all}, is derived directly from the total number of simulated events which are distributed uniformly in θ and ϕ. Different intervals for the obtained fractional radiation length are chosen to classify the hot spots according to the variation from the integrated average within the sensitive detector region ($\theta < 140°$). Therefore, mean values of the fractional radiation length, $\langle X/X_0 \rangle$, and the doubled standard deviation within the $\Delta\theta$-intervals, $2 \cdot \langle \sigma_{\theta_i} \rangle$, were extracted from the 1D profiles of the full material map (see figure 6.22). Both values can be used to estimate a lower limit for the definition of a hot spot given by $\langle X/X_0 \rangle + 2 \cdot \langle \sigma_{\theta_i} \rangle = 9.1\%$.

Based on this result hot spots are divided in four categories. The first category (I) defined within an interval of $10\% < X/X_0 < 25\%$ rather describes larger fluctuations to the averaged value. Moderate hot spots of category II are in the order of $25\%X_0$ and

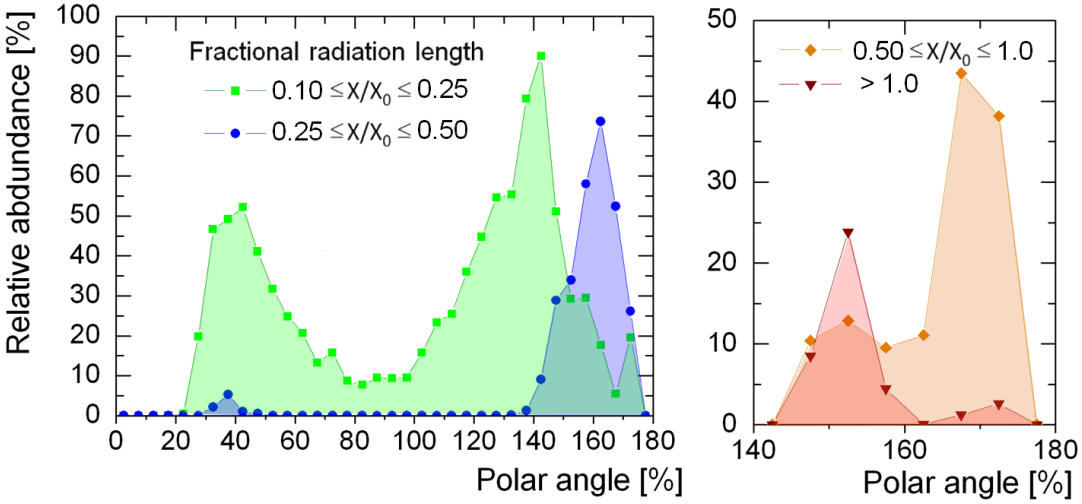

Figure 6.24: Relative abundance, $N_{\text{spot}}/N_{\text{all}}$, of hot spots in the material map along the polar angle. Specified threshold values are given inside the diagrams.

$50\%X_0$. The last two categories III and IV account for hot spots with a very large value below and above one full radiation length X_0, respectively.

Compiled results in figure 6.24 indicate that hot spots of category II to IV are basically shifted outside the sensitive detector region. An exceptional contribution of moderate hot spots (category II) in the order of 5% can be located between $\theta = 35°$ and $\theta = 40°$. It is correlated to the lead out of the pixel services to outer radii. In the upstream region between $\theta = 150°$ and $\theta = 170°$ hot spots of the second, third and fourth category occur with a maximum abundance of up to 70%, 40% and 25%, respectively. Enlarged fluctuations of the material map included in category I are spread over the entire polar angle. They occur with an abundance of up to 50% in the forward region ($30° < \theta < 50°$) and decrease to a minimum of 10% between $\theta = 70°$ and $\theta = 100°$. A second peak of the distribution with a maximum abundance of 90% shows up at $\theta = 145°$ short behind the upstream end of the sensitive detector region.

In order to evaluate the influence of different hardware developments, studies with a re-ordered setup according to table 6.3 were performed. The new definitions are based on functional groups. Corresponding results are shown in figure 6.25. On the left, a stacked diagram presents the individual contributions for each of the functional detector parts along the polar angle. Plotted values represent the azimuthally averaged radiation lengths X/X_0 within an interval of $\Delta\theta = 1°$. Peaking structures with a notable influence on the overall distribution are related to stiffening support structures along the beam axis. One remarkable result is the fact that, besides some accumulation effects in the very forward direction, the proportions of the material budget between sensors, electronics, cooling, cabling and support components remain relatively constant within the active detector region below $\theta = 140°$. Therefore, the individual contributions can be integrated to evaluate their impact on the overall material budget. The obtained pie chart is presented in figure 6.25, on the right. It indicates that the biggest amount of material is contributed by the detector

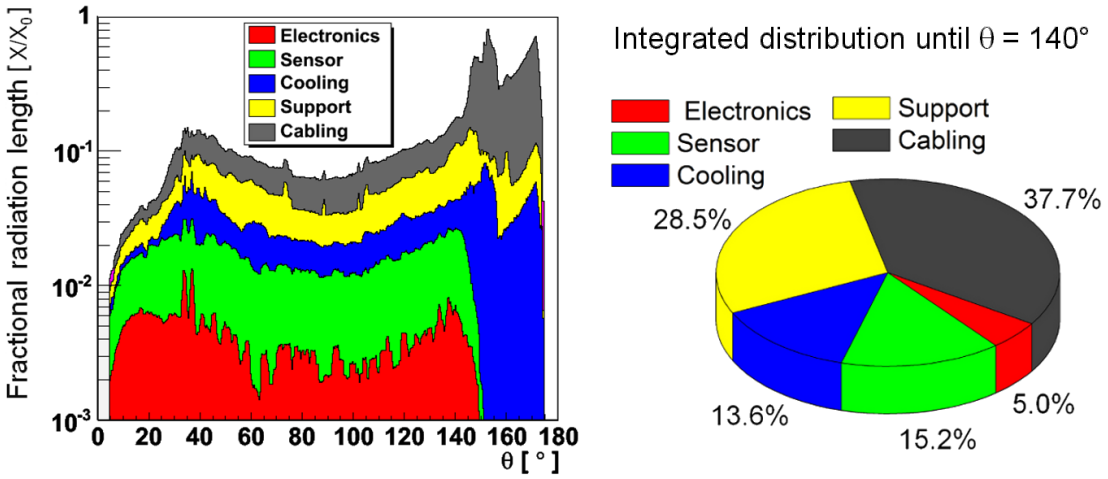

Figure 6.25: Contributions of different functional parts of the MVD to the overall material budget. *Left*: 1D profile along the polar angle. *Right*: Percentage of the different parts within the sensitive detector region ($\theta < 140°$).

cables and the support structures, which account for approximately 38% and 29%, respectively. A further breakdown of the different cable types contributing to the dominating material budget of the cabling part is given in table 6.4. The introduced sensor material accounts for only 15% while the cooling system adds another 14% to the overall material load. The total impact of the electronics stays with 5% rather small. However, in any case it should be recalled that the discussion on integrated distributions does not supersede a careful evaluation of the 2D map as done before e.g. for the hot spots.

As outlined in subsection 5.4.1 the developed software concept also features fast testing procedures obviously needed during the detector development. One of these methods is

Functional group	Components	*Previous definition*
Electronics	Frontend chip (FE) SMD Electrical connectors	*Silicon* *Components*
Sensor	Active volume Passive edge	*Silicon*
Support	Local and global support structures	*Support*
Cabling	Cable (core + insulation): Sensor-HV, FE-supply, Data	*Routing*
Cooling	Filled cooling pipes and tubes Cooling connectors	*Routing* *Components*

Table 6.3: Re-ordered components for the radiation length studies.

Cable type	Data bus cable	Sensor supply (HV)	Frontend supply
Percentage	22%	8%	70%
Ratio: Core/Insulation	0.42	0.74	2.77

Table 6.4: Composition of the material budget of the cabling part.

based on a modification of the overall material definition. In this way it is possible to evaluate the impact of different engineering solutions and to consider updated information on composites or basic materials intended to be used for specific components. Two of such studies are shown exemplarily in figure 6.26. On the left side, the density of local pixel support structures is increased thus introducing a heavier carbon foam with higher thermal conductivity (HTC POCO [170]). Its use emerged as absolutely necessary in order to fulfil the cooling requirements. As a consequence, the average material budget of the six pixel support half-disks in the forward part (see figure 5.17, page 104) is increased by approximately $1\%X_0$. Due to the reduced number of pixel layers and a lower thickness of associated local support components, the insertion of heavier carbon foam in the barrel part results in a much smaller addition below $2‰X_0$.

The second diagram on the right of figure 6.26 illustrates 1D profiles of the cabling part obtained with different assumptions on the bus cables. In the first case an increased cable thickness with respect to the default setup was chosen. Therefore, the density of the bus cables was scaled accordingly for both core and insulation without changing the defined

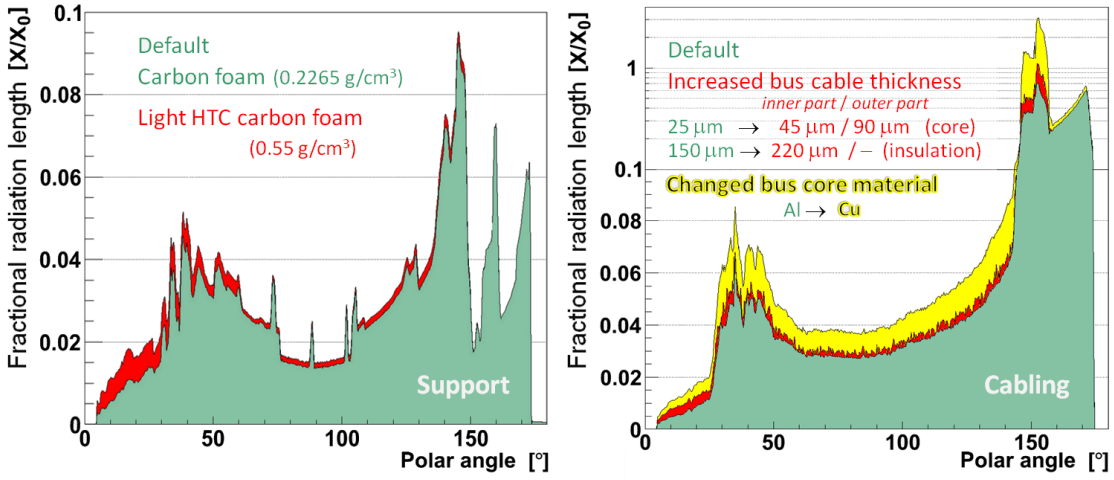

Figure 6.26: Results of radiation length studies with modified setups for the support structure (*left*) and the bus cables (*right*). All modifications have been achieved either by replacing the basic material or by changing the effective density of the appropriate volumes inside the Mvd-2.1, thus adjusting the material definition to the requested values in terms of their radiation length.

geometry of associated volumes. This approximation offers the opportunity to obtain fast results preventing a time-consuming redefinition of all volumes in the CAD model. In a second study the core material of the bus cables was exchanged, using copper instead of aluminium. In this case both relevant parameters, density ρ and radiation length X_0, were substituted. As it can be seen on the right side of figure 6.26, the resulting fractional radiation length is relatively robust against slight modification of the bus cable thickness. In contrast, the choice of the conducting material is crucial for a minimized material budget. Efforts of R&D programs thus must concentrate on the evaluation of suited aluminium cables. Taking into account only the bus cables, an average reduction of $1\%X_0$ over the full sensitive detector area and even by a factor of three for the hot spots at $\theta = 150°$ can be achieved.

The performance of simulations with modified setups as described in the previous paragraph requires a very precise definition of all specific changes. However, in some cases such detailed specification is not available or information is relatively limited at the present status of the detector development. Most of these uncertainties are related to remote parts of the detector, the extrapolation of results from ongoing R&D programs to final applications and achievable optimization scenarios at a later stage of the project. A reasonable approach to estimate the impact of future developments is given by a quantitative comparison of relative changes with respect to the integrated material budget of the default setup (see figure 6.25, on the right). In the following, all important aspects will be briefly discussed according to the listed topics shown in table 6.5.

The sensor thicknesses in the Mvd-2.1 model represent an upper limit for the maximum value to be considered for the mechanical integration. Taking into account the design goals, 100 µm to 150 µm instead of 200 µm for the pixel sensors and approximately 200 µm instead of 300 µm for the strip sensors, a further decrease of the overall material load in the order of 5% is achievable. Assuming the crossing of four detector layers under 45° this corresponds to an effective reduction of roughly $6\,‰X_0$ per track. However, the application of such ultra-thin sensors has to be studied carefully. Besides technical issues of sensor production and handling, one of the major concerns is related to the lowered charge creation in the sensitive layer, which deteriorates the signal quality. In particular, effective path lengths in the active pixel cell fall short of 100 µm. In this context it must be evaluated if the specified signal-to-noise ratio and the charge sharing between neighbouring cells both needed for the required analogue readout set lower limits on the total thickness of the sensitive layer.

The electric connection of sensors has not been considered within the the Mvd-2.1 model. Its impact can be estimated based on the area ratio of the sensor surface to the overall contact area. Even including a minimum length for the wire connection in case of strip detectors resulting material effects can be neglected for the present studies. For pixel sensors the area ratio is significantly larger due to the 1:1 coupling of pixel and readout cell. In current state-of-the-art detectors used in HEP experiments the connection is performed by bump bonds made of a high-Z material (Indium or Pn-Sn) with a typical diameter of the bumps between 15 µm and 25 µm [171]. With the specified pixel cell size of $(100\times100)\,\mu m^2$ the resulting area ratio is in the order of 4%. Although the overall impact on the material budget remains very small, a significant contribution of roughly $2‰X_0$ results if the bump is hit. In the worst case, an additional material load in the order of $1\%X_0$ can be accumulated for singular tracks. The material effects of the bump bonds are of particular interest for a

Detector part	Modification	Within model*	Impact on overall material budget	Comment
Sensor	Reduced thickness [1] Pixel: 200→ 100 µm Strip: 300→ 200 µm	no	$\langle -1.3\% \rangle$ $\langle -4.2\% \rangle$	Lower charge creation → worsened S/N: Check of detector performance
	Electric connection Bump bond (Pixel) Wire bond (Strip)	no	$\langle +0.5‰ \rangle$ Peak[2]: $\lesssim 1\% X_0$ $\langle$ negligible $\rangle$	Area ratio $(\frac{\text{bump}}{\text{cell}}) \sim 4\%$ Singular effects ($1.6‰ X_0$/bond)
Supply cables	50% core cross section[3]	yes	$\langle -30\% \rangle$	Higher voltage drop along line → Allowance to be checked
	Serial powering (less insulation)	no	$\langle -4\% \rangle$	Feasibility of powering scheme to be evaluated
	Core material HV supply Frontend supply	yes no	$\langle -1\% \rangle$ $\langle -17\% \rangle$	Al instead of Copper
Bus cables	Doubled data concentration	no	$\langle -4\% \rangle$	Limits due to high count rates → Feasibility to be checked
	Core material	yes	$\langle -13\% \rangle$	Al instead of Copper
Support	HTC foam [170]	no	$\langle +3.5\% \rangle$	Adequate cooling of pixel modules
	Optimized shape	yes[4]	-50%/piece	Cut-outs for large surfaces
	Filling material C→Light foam [138]	partly[5]	$-98\% f_L$/piece	f_L: Fraction of intermediate (sandwiched) layer
	Screws (Ti)	no	Peak[6]: $14\% X_0$	Very singular effects
Further routing	Cooling splitters (PVC)	no	Peak[6]: $25\% X_0$ $\langle -4\%]_{\theta>\theta_1}$	Placed at different z-positions Full upstream reduction[7]
	Opto-boards[8] / voltage regulators	no	$\langle +6.5\%]_{\theta>\theta_2}^{\theta<\theta_3}$ $\lesssim \langle -8\%]_{\theta>\theta_3}$	PCBs, electric components and connectors along z (upstream) Optical data transmission[9]
Cooling	Opto-boards / voltage regulators	no	$\langle +5.5\%]_{\theta>\theta_3}$	Additional cooling needed for electronic components
	Pixel disks	no	$\langle +2.3\% \rangle$	Higher cooling power required
	Strip disks	no	$\langle -1.0\% \rangle$	Less circuits (to be checked)

[1]Minimum total target thickness, [2]Assuming six bumps traversed in forward direction, [3]See table 5.5, [4]Approximation for main parts (see page 108), [5]Sandwich structure described by density weighted carbon material with heavier foam compared to [138] (see table 6.2) resulting in $-90\% f_L$/piece, [6]Assumed path length of 5 mm, [7]Less insulation, assumed ratio IN/OUT 4:1, [8]Electrical to optical conversion of data signals, [9]Maximum reduction assuming 20 bus cables/1 fibre

Table 6.5: Impact of various modifications on the overall material budget. Given numbers in $\langle ... \rangle$ and $\langle ...]$ refer to the integrated numbers obtained for the Mvd-2.1 model$^{(*)}$ in the presented studies (see figure 6.25).

proper description of the sensor behaviour.

A dominating fraction of the material load is delivered by the cabling part. Consequently, modifications therein have the largest impact on the final numbers. For the following discussion it is useful to consider the total contribution of different cable types in order to focus on the most relevant parts. As shown in table 6.4, the biggest impact originates from the supply cables of the frontend chips. The final layout of all cables strongly depends on external input parameters such as the expected peak luminosity or the global clock frequency of the experiment. Some of them still need to be specified in more detail.

The entire model of the cable part (see subsection 5.4.3) scales with the number of readout channels and is based on assumed low-mass cables as currently used in HEP experiments [172] or prototypes explicitly developed for the MVD [139]. Obtained numbers thus represent a rather realistic picture. In this context it should be recalled that several considerations towards a minimized material budget are already included in the default setup. The most significant change is related to the 50% core cross sections of the supply cables (see table 5.5) and results in a reduction of 30% of the overall material budget. It is associated with a less firm restriction on the accepted voltage drop along the line which is one of the crucial aspects for the operation of the frontend chips. Therefore, the allowance of such profound modifications with respect to the specification of the frontend electronics must be checked carefully. A conclusive evaluation still has to be performed. The overall cable cross section can also be reduced by a higher data concentration. Assuming a doubled number of frontend chips (4 pixel and 8 strip frontends) to be read out by one bus cable, the total material budget could be reduced by up to 4%. The most limiting factor for the data concentration is given by the high count rates (details see subsection 6.2.3).

Another potential saving of the cabling part by using a lighter core material, i.e. aluminium instead of copper, was already shown in figure 6.26, on the left side. Within the Mvd-2.1 model it is initially implemented for the bus and the HV cable and results in a total reduction of 14%. A further significant decrease of up to 17% could be achieved by a similar replacement of the core material for the supply cables of the frontend chips. Therefore, cables with a cross section of 90% aluminium surrounded by only 10% of copper are under study. Due to the lower conductivity, a check of the total cross section is necessary and may eventually require slightly thicker cables, which would partly counter-balance the reduction factor. Finally, the choice of a serial powering scheme instead of an individual supply for all sensors and frontends would require less insulation material. The achievable reduction potential on the overall budget is in the order of 4%. However, the feasibility of such a scheme still needs to be evaluated.

The second important part of the material budget is the detector support. As presented in figure 6.26, on the right, the required carbon foam with a higher thermal conductivity leads to a total increase of 3.5% for the integrated radiation lengths within the sensitive detector region. Besides this unavoidable deterioration, huge benefits concerning a lightweight support structure result from sandwiched carbon structures using a very light foam [138]. Moreover, a significant minimization can be achieved by the tailored design of components with large surfaces allowing the introduction of cut-outs without any or even positive effects on the stability of the structure. It should be mentioned that screws are not explicitly introduced in the presented model because of the rather small quantity, which is foreseen in the final assembly. There are indeed larger but very singular effects with peak

values of around 15%X_0 related to e.g. the custom made titanium screws foreseen for the fixation of main detector parts to the global MVD frame.

One missing point of the introduced Mvd-2.1 model is the consideration of remote parts in the routing scheme. They require additional components and thus increase the material budget at least partially. Most of them will be placed as far as possible in upstream direction in order to avoid unnecessary deteriorations of the detector performance. However, due to technical limitations and stringent restrictions of the available cross section, a positioning outside the defined MVD core volume corresponding to polar angles well above 150° is not possible in all cases. For this reason some key aspects will be discussed in the following.

The cooling system implies at some point cooling splitters distributing the coolant from a main pipe to the individual lines running through the detector modules. While on the one hand it leads to a local material increase of approximately 25%X_0, on the other hand a total reduction of 4% on the overall budget in further upstream direction results from the downsized insulation needed for the main pipes. An important task of the power system is given by a suited control and regulation of all required voltages relatively close to the supplied elements. Approximately in the same region, an additional step of the data transmission must be implemented. It is related to the degradation of electrical signals with increasing cable length, which requires an optical conversion after a maximum transmission path of roughly one meter with respect to the frontend electronics. Both discussed routing parts, the voltage regulators and the opto-boards, lead to a local increase of the overall material budget, which is in the order of 6%. A final conclusion about the overall concept

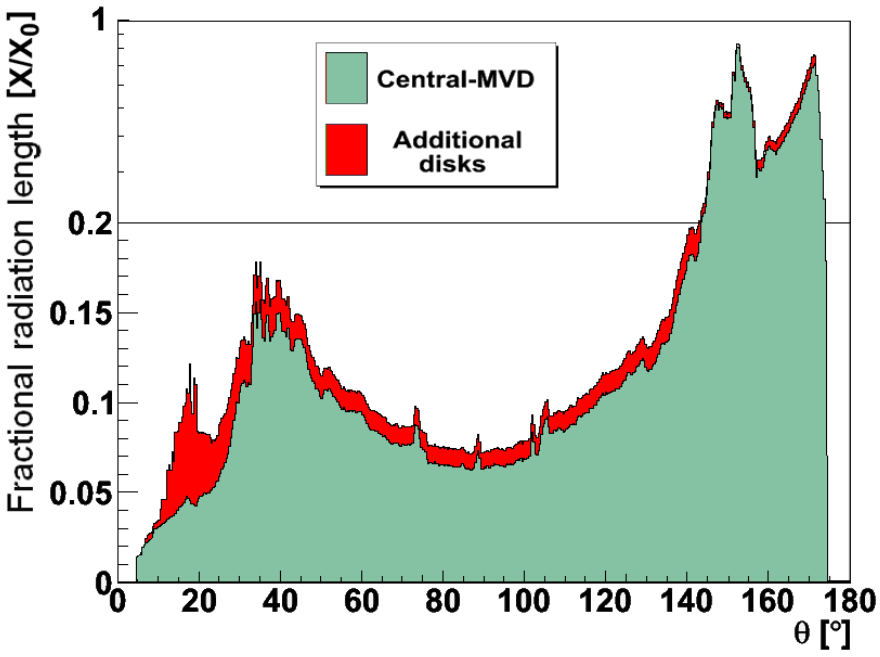

Figure 6.27: Stacked polar profile of the radiation length for the central MVD and the additional disks.

still needs to be evaluated in detail. In any case, it involves the need for additional cooling lines in upstream direction. The associated increase of roughly 5.5% is counter-balanced by a reduced material budget in the order of 8% due to the optical data transmission. Another impact on the cooling system is given by the increased cooling power needed for the pixel disks and the total number of cooling cycles for the strip disks. They result in an increase of the material budget around 2.3% and an eventual decrease in the order of 1%, respectively. For the latter case, the feasibility still has to be checked in thermal simulations.

The final point of this subsection is dedicated to simulation studies with the additional disks. Corresponding results for the 1D profile are shown in figure 6.27 in comparison to the one obtained for the central MVD. The requested upstream routing adds a constant value of approximately $1\%X_0$ to the average radiation length along the polar angle. Moreover, significant contributions arise at smaller polar angles. In particular at polar angles between 10° and 20°, the average radiation length reaches a level of $10\%X_0$. Taking into account the additional contributions of the central MVD at higher polar angles, maximum values of 12% and 16% are obtained in the forward part at $\theta = 30^\circ$ and $\theta = 40^\circ$, respectively. Therefore, pros and cons of the introduced additional disks in terms of their impact on relevant physics aspects must be studied carefully. In this context it should be mentioned that even the mere mechanical integration of these disks represents serious complications of the overall installation sequence. Furthermore, the required cross section for the additional routing fills the very tight remaining space to the given limits. As a consequence, the possibility of alternative scenarios for the routing concept of the additional disks should be taken into account.

6.2.3 Count rate studies

The evaluation of expected count rates in different detector regions is crucial for the development of all readout electronics. Based on the results of these studies important parameters for the specification of associated hardware components such as the frontend chip can be defined. Relevant information is derived from the maximum and the average count rate occurring on single readout channels and on frontend chip level. Moreover, integrated numbers obtained in different detector parts allow the estimation of the overall data load to be handled by the MVD.

The DPM generator was chosen to describe the hadronic environment of antiproton-proton collisions at three different beam momenta. The minimum (1.5 GeV/c) and the maximum (15 GeV/c) beam momentum of the $\bar{\text{P}}$ANDA experiment were included. A third study was performed at an intermediate beam momentum of 5 GeV/c. Generated particles were propagated within the $\bar{\text{P}}$ANDA root framework by the GEANT4 transport code. For all studies the full version of the central MVD was used. In addition, the beam-target pipes were included. The Monte-Carlo information of each particle track was further processed taking into account the digitization in the MVD. At this stage, particular detector properties are introduced. They contain the sensor segmentation, the created charge quantity along the pathway of crossing ionizing particles and threshold values defined individually for readout channels of different sensor types. The crossing path is calculated by a linear interpolation between the points of intersection on both sensor sides. The created charge quantity is projected on the readout plane and the resulting

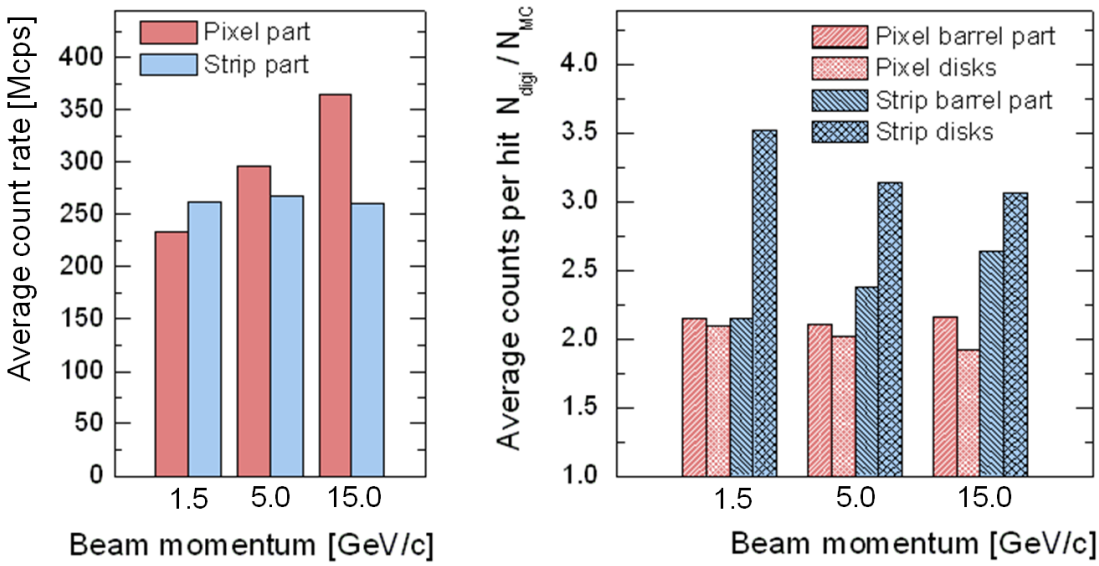

Figure 6.28: Simulation results of the average count rate (*left*) and the average number of counts per hit (*right*) for different detector parts of the MVD.

charge quantity of affected channels is compared with the threshold values. Hence, the final data output is similar to the one to be expected from a real detector. The simulations were performed without an additional noise generator. However, possible effects are negligible within the scope of this study and, in any way, would be sufficiently suppressed by the set threshold values.

To obtain a large statistical sample, two million DPM events were generated for each of the three setups. Only the binary information i.e. the hit count was used in the analysis. Therefore, the corresponding ID's of the sensor, the readout chip and the channel number of each digitized hit above threshold were stored. In this way, unambiguous results for selected readout channels, frontend chips, sensors or detector parts can be obtained by combining all three value quantities. The summed hit counts can be translated into count rates taking into account the interaction rate of subsequent events. For the extraction of average values the nominal interaction rate defined for the $\bar{\mathrm{P}}$ANDA experiment was chosen. It is given by 2×10^7 events per second. The generated data sample thus corresponds to a measurement within a time interval of 0.1 s.

The average count rates of the integrated pixel and strip part are shown on the left side of figure 6.28. While for the strip part the value at stays nearly constant at around 250 million counts per second (Mcps), an increase with higher beam momentum is observed for the pixel part. At maximum beam momentum, the corresponding value exceeds the one of the strip part by 100 Mcps. At the right hand side of figure 6.28 the ratio between the number of hit points before, N_{MC}, and after the digitization, N_{digi}, is plotted. The average number of digitized counts per hit on pixel sensors levels around two. Higher values are obtained for the strip sensors. However, it must be taken into account that the extracted numbers result from digitized hit points delivered on both sensor sides. Hence, the average

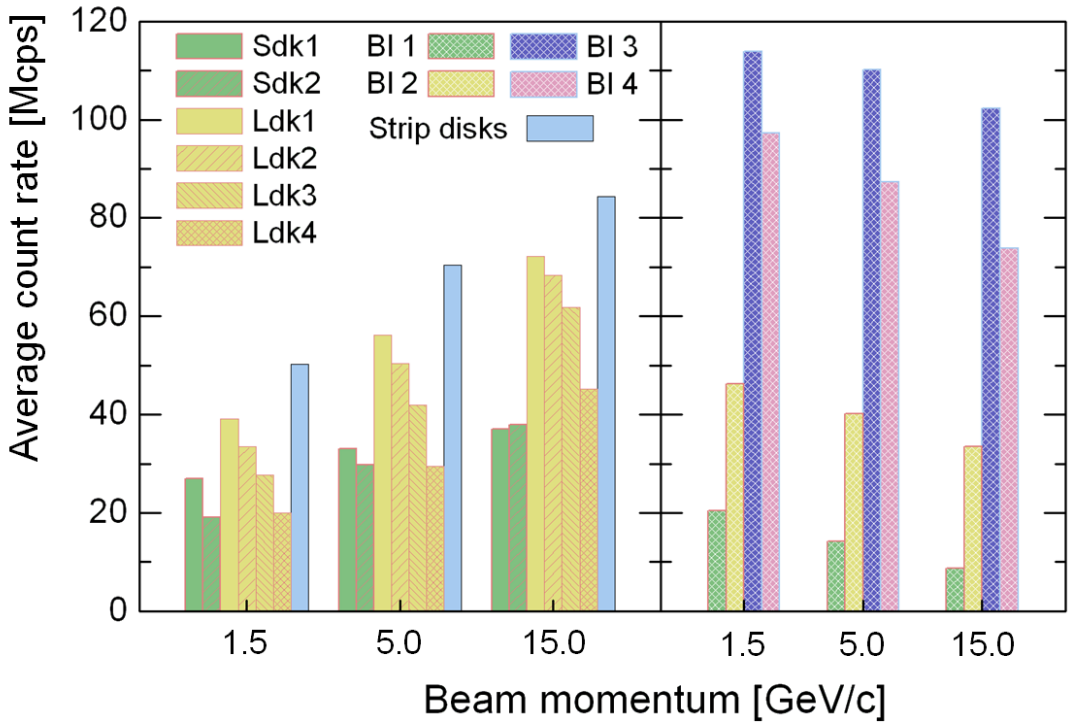

Figure 6.29: Simulation results of the average count rate for all individual MVD layers.

cluster size per hit for one sensor side of the strip sensors is smaller than the one for pixel sensors. It ranges from only 1.0 up to 1.75 and exhibits a larger dependency on the initial beam momentum.

The average count rates for all individual MVD layers are summarized in figure 6.29. They reflect the overall particle distribution (details see subsection 6.1.2), which results in an increased count rate for the disk layers with higher beam momentum. Moreover, it can be seen that the impact of the barrel and the disk layer on the overall contribution is different for the strip and the pixel part. While the latter is determined mostly by the pixel disks, main contributions in the strip part stem from the barrel layers. There, the count rate is increasing with lower beam momentum due to the changed particle distribution. As a consequence, the decreased count rate of the forward disks is counter-balanced in case of the strip part thus explaining the relatively constant integrated number obtained in 6.28. The maximum count rate of an individual MVD layer is given by the third barrel layer with 114 Mcps at a beam momentum of 1.5 GeV/c. The minimum value delivered by the first barrel layer is more than one order of magnitude lower (9 Mcps).

The highest count rates on frontend level inside the MVD occur at the innermost parts of the small pixel disks at highest beam momentum. The count rate distribution for individual frontend chips in the forward part of the MVD at 15 GeV/c is shown in figure 6.30. Maximum values within the small pixel disks reach 3 Mcps. Moreover, nearly all the frontends of the two innermost disk layers have to cope with a high count rate of more than 1 Mcps. This fact indicates the very special conditions in this detector region. They require

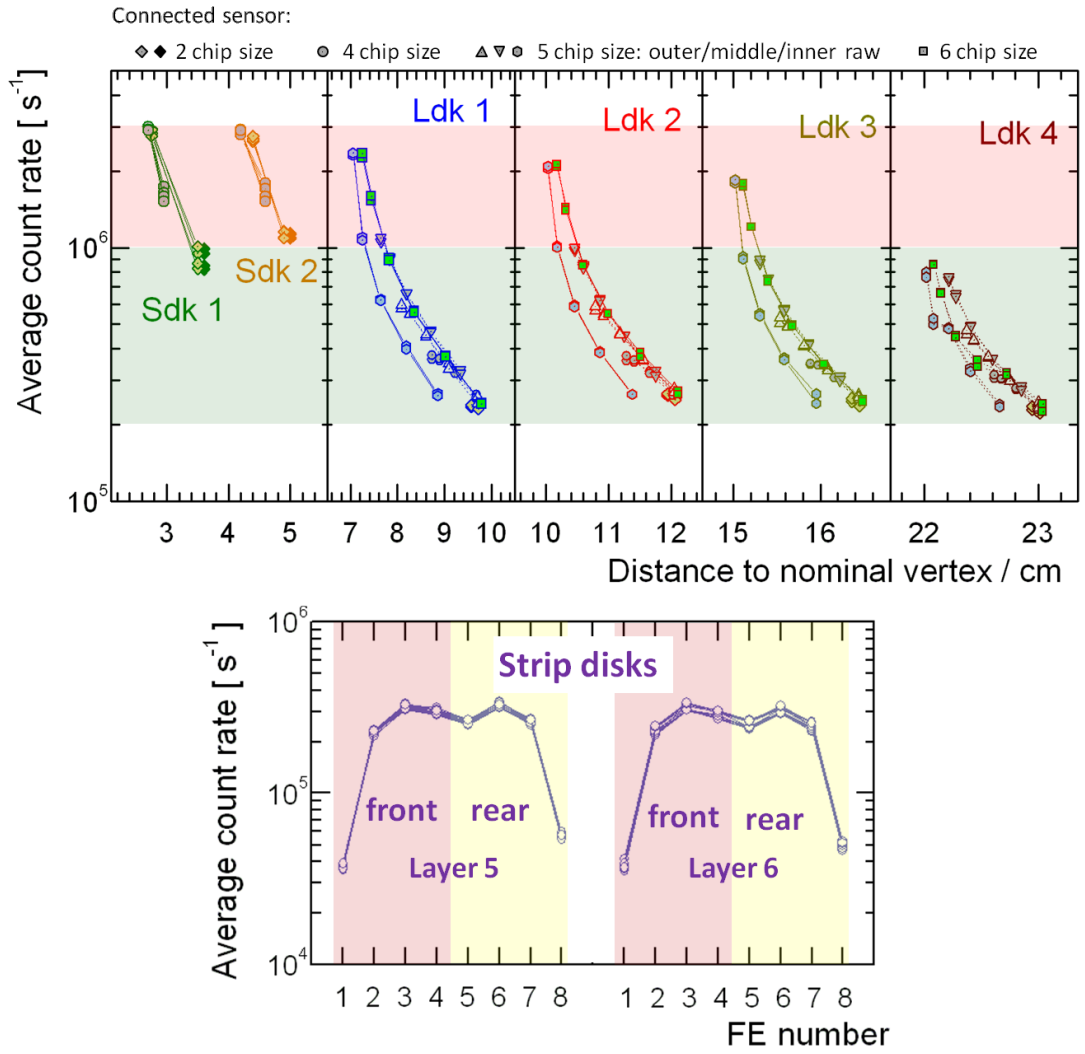

Figure 6.30: Simulation results of the average count rate on frontend level for the forward part of the MVD. Distribution within the pixel disks (*top*) and the strip disks (*bottom*) are plotted for all individual frontend chips. Values are obtained at a beam momentum of 15 GeV/c.

a sophisticated cooling concept for the frontend electronics, which is crucial for a stable operation. Also at the inner rims of the subsequent large pixel disks, high count rates between 2.5 Mcps and 1.9 Mcps are obtained for individual frontend chips. At outer radii values drop below 1 Mcps. Within the last pixel disk the average count rate on all frontend chips stay well below 1 Mcps. Maximum count rates for frontend chips of the strip disks are in the order of 0.3 Mcps. A special consequence of the trapezoidal layout is given by the lowered count rate for the frontend at the outermost position due to the shorter strips at one sensor edge. This effect is mirrored at the opposite sensor side and can be nicely seen in figure 6.30, at the bottom.

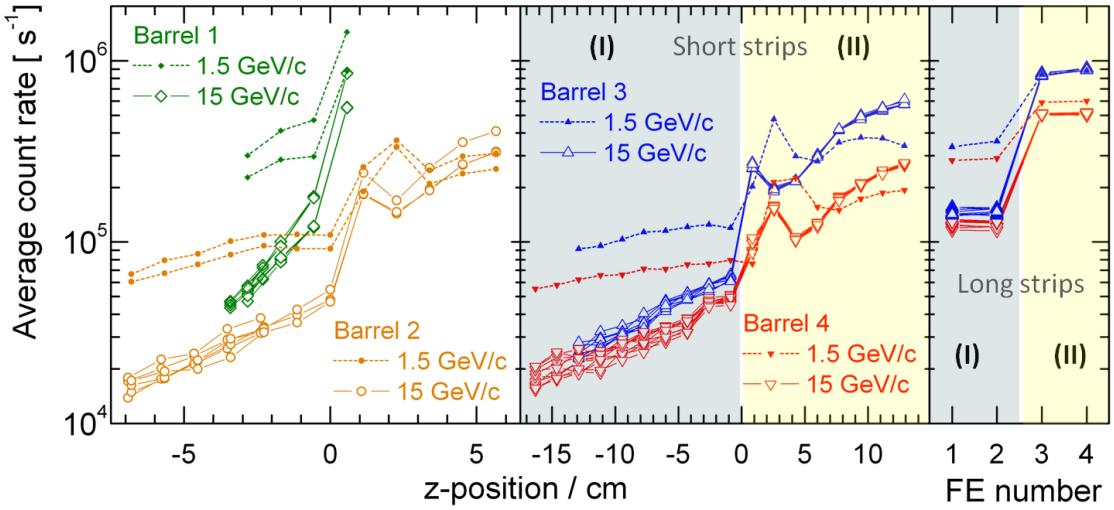

Figure 6.31: Simulation results of the average count rate on frontend level for the barrel part of the MVD. In case of 15 GeV/c, results of all individual staves are plotted to illustrate the statistical deviations. At lowest beam momentum only the distribution of the stave with the maximum count rate is shown.

In contrast to the forward part, the count rates in the barrel part increase with lower beam momentum due to the increased number of particles emitted at larger polar angles. Therefore, it is necessary to consider the full beam momentum range. The count rate distributions within the different barrel layers are shown in figure 6.31. In all cases the impact of the slow elastic recoil protons is clearly visible. It results in a local maximum for frontends close to a position of $z = 0$ and is more spread in forward direction at lower beam momentum. These observations are in agreement with the evaluated particle distributions shown previously in figure 6.8 at page 124. The count rates for frontends at the outer pixel barrel layer stay below 0.5 Mcps. Highest values for all barrel layers are obtained in the foremost frontends of the first pixel layer. At lowest beam momentum they exceed 1 Mcps. In case of the strip barrel part it must be considered that the overall design foresees a ganging of long sensor strips of subsequent sensors. As a consequence, highest count rates on individual strip frontend chips occur for the readout of connected strips of the two foremost sensors in the third barrel layer. Maximum values level short below 1 Mcps at minimum beam momentum. Due to the fixed-target setup, the count rates in the upstream barrel part do not exceed a level of 0.1 Mcps.

The extracted count rates on frontend level result from an integration over all associated readout channels. Besides this number, a careful study of the distribution on individual readout channels is unavoidable to obtain a full characterization, which is needed for the design of the readout chip. Figure 6.32 shows results for the pixel and strip frontend chip with the respective maximum count rate. It can be seen that the highest numbers for individual channels are obtained for the connected long strips in the third barrel layer. They range between 7000 counts per second (cps) and 8000 cps. The occupation on the

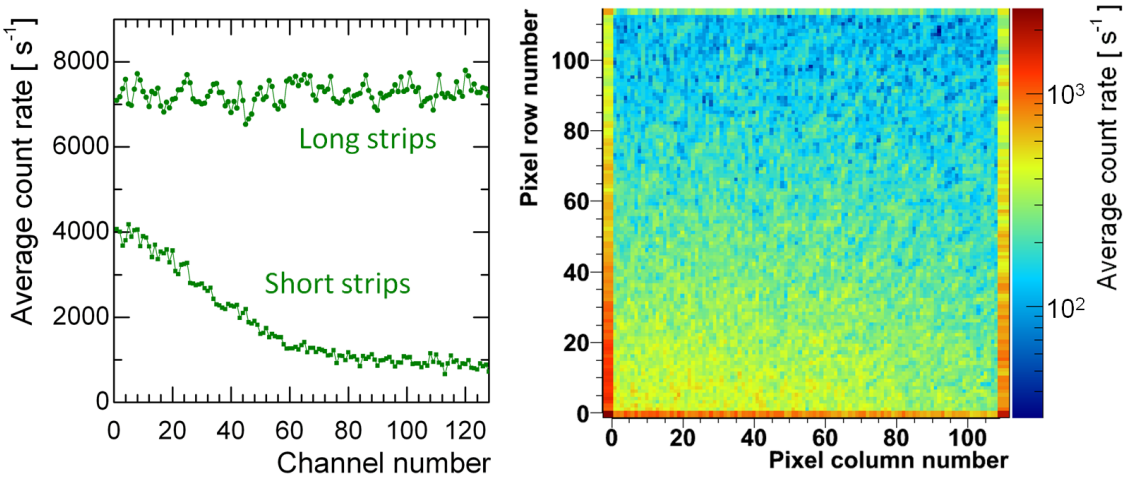

Figure 6.32: Simulation results of the occupancy for all readout channels of the strip (*left*) and the pixel frontend chip (*right*) with the highest obtained count rate. They correspond to the readout of the ganged long strips of the two foremost sensors in the third barrel layer at 1.5 GeV/c and the innermost sensor area of the first small disk at 15 GeV/c, respectively. Additionally, the distribution for the short strips of a frontend chip in forward position close to $z = 0$ is shown in the same diagram on the left. It indicates the impact of elastically scattered protons, which introduce the largest deviations within one individual strip frontend. Increased count rates at the rim of the pixel matrix correspond to the enlarged pixel cells (200 µm at the top and bottom and 300 µm at the left and right).

pixel frontend chip is much more anisotropic and reflects the forward boost of particles, which reach the inner rim of the first pixel disk. Values differ by roughly one order of magnitude. An increased count rate can be observed at the rim of the pixel matrix. It stems from the enlarged pixel cells, which are implemented to counter-balance the passive edge of the readout chip. The maximum of 2300 cps is obtained at the corner with an effective pixel cell size of 200 µm × 300 µm. However, it should be noted that an update on the pixel design has been performed, which removes the enlargement of cells at top and bottom. As a result the maximum number given above is reduced by a factor of two.

So far, all presented results were discussed in terms of an average count rate, which is directly linked to the number of digitized hits, N_{dig}, delivered after the complete analysis of the simulations. Given values for the average count rate, $\langle \dot{N}_{\text{dig}} \rangle$, were obtained with the nominal interaction rate of the $\bar{\text{P}}$ANDA experiment of $2 \times 10^7\,\text{s}^{-1}$. A factor of ten must be thus included to transfer N_{dig} resulting from two million simulated DPM events into $\langle \dot{N}_{\text{dig}} \rangle$. However, for a detailed discussion of all relevant aspects associated with the hit occupancy, additional considerations have to be taken into account.

First of all, the number of digitized hits is based on a description of the charge creation inside the sensor and does not take into account any modifications introduced by the chosen readout technique. In case of strip detectors, the envisaged design foresees an induced charge sharing between neighbouring channels to improve the spatial resolution.

It is based on a smaller substructure with interstitial floating strips to ensure a minimum number of two activated strips allowing the application of weighting methods. Basics on these techniques were discussed in section 1.4. The average number of activated channels at both detector sides in the simulation falls short of the required value of four (see figure 6.28). To estimate maximum count rates in the MVD strip part obtained results of the simulations have to be adjusted accordingly. Therefore, a factor $f_{\mathrm{r/o}} = 1.6$ is introduced.

Including the assumption that eventual fluctuations at a small time scale are compensated on frontend level, average count rates are suited to extract associated data rates of the detector. Taking into account a size of 40 bit to 50 bit for the output format of the hit data, obtained numbers given in Mcps can be scaled by a factor f_{byte} between 5 to 6 in order to obtain the average data load in megabytes per second (MB/s). However, for the development of the frontend electronics a careful evaluation of the time structure is crucial. As a first step this includes the estimation of peak rates, $\dot{N}^{\mathrm{max}}_{\Delta t \rightarrow \epsilon}$, which are introduced by macroscopic and microscopic structures of the luminosity profile and result in fluctuations of the total number of registered hits within a short time interval Δt of a fixed length ϵ. A detailed discussion on this topic was carried out explicitly in subsection 2.2.4. Macroscopic effects are related to the intrinsic change of the instantaneous luminosity profile during the operation cycle as shown in figure 2.7 on page 46. It is correlated with a minimum factor of $f_{\mathrm{peak}} \approx 1.38$ to be multiplied with the time averaged numbers. Additional fluctuations on a microscopic scale are introduced by possible time dependent changes of the effective target thickness. They become notably in the particular case of using a pellet target and thus define an upper limit of $f_{\mathrm{peak}} \approx 5$ (see figure 2.9, page 48).

Final numbers of the presented count rate studies are summarized in table 6.6. They are important to properly define specifications of the frontend electronics and to design a suited concept for the overall data acquisition. Besides the maximum values extracted from elements with the highest occupancy, mean values for all frontends and readout channels are given as comparison. The estimation of peak rates on frontend level and single channel level strongly depends on a precise description of the expected beam-target interaction, which is not fully available at present. Therefore, only upper and lower limits can be given defining a range from 4 Mcps to 14.5 Mcps and 2 Mcps to 5.5 Mcps for the peak rates of individual pixel and strip frontend chips, respectively. Peak rates of involved readout channels are in the order of 10 thousand counts per second (kcps) for pixel cells and level between 20 kcps and 70 kcps for single strips. Corresponding average numbers are in the order of 3 Mcps for pixel frontend chips, 1.5 Mcps for strip frontend chips, 2 kcps for pixel cells and 13 kcps for single strips. The total data rate of the MVD depends on the initial beam momentum due to the larger amount of data produced by the pixel part at higher beam energy. In contrast, the data rate of the strip part stays relatively constant. At highest beam momentum the maximum data load for the pixel and the strip part are in the same order of magnitude. Together they add up to a maximum data rate of roughly 4.5 GB/s at an initial beam momentum of 15 GeV/c.

	Barrel part	Forward part	Sensor level	Frontend level	Readout channel
Pixel part					
Digitized hits N_{dig} / $[10^6]$	$6.7 \mapsto 4.2$	$16.6 \mapsto 32.2$	$0.67 \mapsto 0.89$ $\langle\, 0.13 \mapsto 0.21 \,\rangle$	$0.21 \mapsto 0.29$ $\langle \lesssim 0.04 \rangle$	$2 \cdot 10^{-4}$ $\langle 3.5 \cdot 10^{-6} \rangle$
Average count rate $\langle \dot{N}_{\mathsf{dig}} \rangle$ / [Mcps]	$233 \mapsto 364$		≤ 8.9 $\langle \leq 2.1 \rangle$	≤ 2.9 $\langle 0.4 \rangle$	$\lesssim 0.002$
Estimated peak rate $\dot{N}^{\mathsf{max}}_{\Delta t \to \epsilon}$/ [Mcps]	–		–	> 4.0 < 14.5	$\lesssim 0.01$
Expected data rate $\langle \dot{N}_{\mathsf{DAQ}} \rangle$ / [MB/s]	$\sim$ 2200		45 $\langle 12 \rangle$	17 $\langle 2 \rangle$	–
Strip part					
Digitized hits N_{dig} / $[10^6]$	$21.1 \mapsto 17.6$	$5.0 \mapsto 8.4$	0.30 $\langle 0.10 \rangle$	0.09 $\langle 0.02 \rangle$	$8 \cdot 10^{-4}$ $\langle 1.5 \cdot 10^{-4} \rangle$
Average count rate $\langle \dot{N}_{\mathsf{dig}} \rangle^{(*)}$ / [Mcps]	253 / 405*		3.0 / 4.8* $\langle \leq 1.6 \rangle^*$	0.9 / 1.5* $\langle \leq 0.3 \rangle^*$	$\lesssim 0.013^*$
Estimated peak rate $\dot{N}^{\mathsf{max}}_{\Delta t \to \epsilon}$/ [Mcps]	–		–	$> 2.0^*$ $< 5.5^*$	$> 0.02^*$ $< 0.07^*$
Expected data rate $\langle \dot{N}_{\mathsf{DAQ}} \rangle$ / [MB/s]	$\sim$ 1500 / 2400*		29* $\langle 10 \rangle^*$	9* $\langle 2 \rangle^*$	–

with: $(1.5\,\mathrm{GeV/c}) \mapsto (15\,\mathrm{GeV/c})$; $\langle \dot{N}_{\mathsf{dig}} \rangle = 10 \cdot N_{\mathsf{dig}} \cdot [s]^{-1}$; $\langle \dot{N}_{\mathsf{dig}} \rangle^* = f_{\mathsf{r/o}} \cdot \langle \dot{N}_{\mathsf{dig}} \rangle$;
$\dot{N}^{\mathsf{max}}_{\Delta t \to \epsilon} = f_{\mathsf{peak}} \cdot \langle \dot{N}_{\mathsf{dig}} \rangle$; $\langle \dot{N}_{\mathsf{DAQ}} \rangle = f_{\mathsf{byte}} \cdot \langle \dot{N}_{\mathsf{dig}} \rangle^{(*)}$

Table 6.6: Main results of the count rate studies performed with 2 million DPM events for different initial beam momenta. The number of digitized hits corresponds to the raw data delivered after the complete analysis. The average count rate as used in all plots is obtained with the nominal interaction rate of $2 \times 10^7\,\mathrm{s}^{-1}$. Corrections due to the assumed readout for the strip part are indicated with *. The upper and lower limit for the peak rate is related to the profile of the instantaneous luminosity (see figure 2.7) and estimated fluctuations of the pellet target (see figure 2.9), respectively. For the extracted data rate, a 6 byte output format for each hit is assumed. Given numbers at sensor, frontend and channel level represent the element of highest occupancy. Averaged values are indicated with $\langle ... \rangle$.

6.3 Physics simulations

This section contains a collection of physics simulations performed with the full $\bar{\text{P}}$ANDA apparatus. Most of these have been accomplished in the current simulation framework of $\bar{\text{P}}$ANDA [144], which includes the MVD-2.1 model presented in section 5.4. In all cases, physics benchmark channels with only charged particles in the final state have been chosen. Such modes are intimately connected to the hit information of the MVD. In particular it accounts for the tagging of particles with open charm in the final state, which is crucial for the $\bar{\text{P}}$ANDA experiment. It is only possible with a precise determination of the decay vertices of associated ground state D mesons. In this context, the MVD is indispensable [173]. In the following, the most important results of relevant studies on D mesons and the charmonium-like system $X(3872)$ will be briefly summarized.

→ Secondary vertex resolution

A precise determination of the displaced decay vertex of D mesons is essential for main parts of the physics program at $\bar{\text{P}}$ANDA . It is one of the most important tasks directly addressed through the MVD. The observed flight length of the D meson is correlated with its lifetime, τ, and a relativistic factor $\beta\gamma = \left[\beta^{-2} - 1\right]^{-1/2}$, which depends on the ratio β of the particle velocity in the laboratory frame, v, to the speed of light, c. Hence, the mean decay length in the detector, l_{lab}, reads as:

$$l_{\text{lab}} = \beta\gamma \cdot c\tau \tag{6.8}$$

For all of the $p\bar{p} \rightarrow D\bar{D}$ reaction channels accessible at $\bar{\text{P}}$ANDA , the $\beta\gamma$-factor is bigger than one and thus leads to an elongation of the flight length due to the Lorentz

Reaction chain	Fit algorithm	Particle	p_{beam} [GeV/c]	Vertex resolution [µm] σ_x	σ_y	σ_z
$p\bar{p} \rightarrow D^+D^-$ ↱ $K^+\pi^-\pi^-$ ↳ $K^-\pi^+\pi^+$	(a)	$D^\pm$	6.57 8.50	35 37	35 36	77 92
$p\bar{p} \rightarrow D^*(2400)^0\overline{D^0}$ ↱ $K^+\pi^-$ ↳ $D^+\pi^-$ ↳ $K^-\pi^+\pi^+$	(b)	$\overline{D^0}$ D^+	13.3	86 69	86 68	100 69
$p\bar{p} \rightarrow D^*(2010)^+D^-$ ↱ $K^+\pi^-\pi^-$ ↳ $D^0\pi^+$ ↳ $K^-\pi^+$	(b)	D^- D^0	13.3	93 120	90 119	114 161

Table 6.7: Spatial resolution in three dimensions, $\sigma_{x,y,z}$, of the reconstructed secondary decay vertices of ground state D mesons in different reaction channels. Simulations were performed at different beam momenta, p_{beam}, and with different fit algorithms in the old (a) [174] and the new simulation framework (b) [175]. Results are taken from [173] and [176], respectively.

boost. Because of the fixed-target setup, the incident beam momentum is transferred to the reaction particles in the outgoing channel. As a consequence, both D mesons are emitted in forward direction. The spatial resolution in z direction is thus crucial to distinguish between the displaced decay vertices of both D mesons along their flight paths. If the $D\bar{D}$ pair is produced at rest, the opening angle, ω, between both D mesons vanishes. In this case, l_{lab} is equal to the reconstructed z component of the decay vertex, r_z, and results in a value of approximately $1.7 \cdot c\tau$. At higher centre-of-mass energy, r_z is given by the projection of l_{lab} onto the z axis, i.e. $r_z = l_{\text{lab}} \cdot \cos\omega$. However, within the momentum range of PANDA the opening angles between produced D mesons stay relatively small.

A list of the secondary vertex resolutions for ground state D mesons reconstructed in different $D\bar{D}$ reaction channels is compiled in table 6.7. Results of these complementary simulations indicate that the required precision of 100 µm is achievable [173, 176]. Maximum opening angles of roughly 30° are obtained between the charged and neutral D meson in the second study [176]. The corresponding $\beta\gamma$-factors increase by a factor of two to three. As a consequence, resulting values for r_z are still considerably larger than the obtained resolution, σ_z, for the z component of the reconstructed vertex.

→ Exclusive reconstruction of the $\bar{p}p \to \psi(3770) \to D^+D^-$ reaction channel

Initial studies focused on the reconstruction capability for light D mesons [177, 178, 173], which is one of the key tasks assigned to the MVD. They were performed with a predecessor

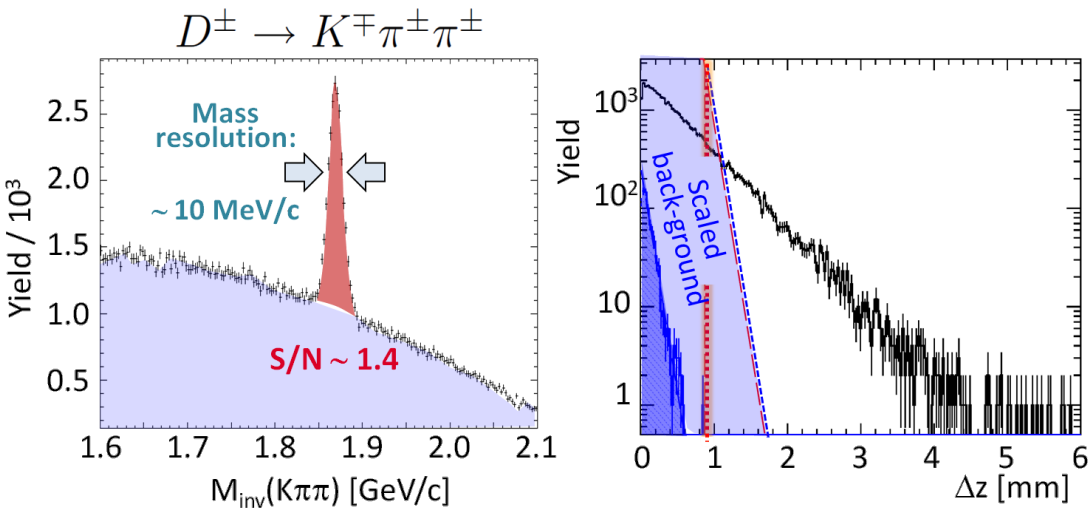

Figure 6.33: Analysis of charged decays in the $\bar{p}p \to \psi(3770) \to D^+D^-$ reaction channel [173]. *Left*: Invariant mass spectrum with an expected signal to background ratio (S/R) of 1.4. The distribution corresponds roughly to one year of data taking. *Right*: Distribution of the position difference of both reconstructed D meson decay vertices projected onto the beam axis. Black curve for signal, filled blue one for the remaining background events. The red line indicates the point with a signal to background ratio of one.

of the MVD-2.1 model. This version did not include a detailed description of all passive materials but introduced instead generalized cylinders defined as carbon. The sensor arrangement was slightly different than for the Mvd-2.1 model. However, the basic layout gave initial input for the conceptual design described in section 3.3. The size of the readout structure of strip and pixel sensors was nearly identical. For the reason of completeness it should be noted that the simulations were performed within the predecessor simulation software based on the BaBar framework [174].

Selected results of an exclusive reconstruction of correlated charged D mesons decaying into six particles in the final state are shown in figure 6.33 [173]. They are based on a conservative estimate for the production cross section of the benchmark channel $\bar{p}p \rightarrow \psi(3770) \rightarrow D^+D^-$, which results in a branching ratio of 10^{-10} for its final decay into one charged kaon and two pions ($D^+D^- \rightarrow K^+K^-\pi^+\pi^-\pi^+\pi^-$). Main background contributions, which are included in the simulation, exceed this value by up to six orders of magnitude. In the analysis three candidates for a D meson decay were combined to a common vertex and loose mass windows were set. The two momenta of the D candidates were then merged and fitted to a common vertex. Finally, a kinematic refit was performed for the whole decay tree to meet the beam four-momentum. Obtained results prove that D meson signals can be extracted efficiently from the huge hadronic background. Similar results were obtained for the exclusive reconstruction of charged D^* mesons [178].

→ Inclusive reconstruction of the $D^*_{s0}(2317)$

The $D^*_{s0}(2317)$ is one of the very interesting states in the D_s spectrum (for details see subsectionr 1.2.2). It is a very narrow state close to the $K\pi$ threshold, which makes it a possible candidate for a non-conventional QCD configuration such as a K-π molecule. A high precision measurement of the $D^*_{s0}(2317)$ width is important to distinguish between various theories about the nature of this state. Due to the very small cross section in the studied reaction channel $\bar{p}p \rightarrow D_s^{\mp}D^*_{s0}(2317)^{\pm}$, an exclusive reconstruction with sufficient statistics is not accessible in $\bar{\text{P}}$ANDA [179]. However, an inclusive reconstruction yields up to 40 events per day and thus offers a realistic option [179].

For the performed analysis [180], only the recoiling $D_s^{\pm}$ was reconstructed by its decay into three charged particles in the final state, i.e. in the decay channel $D_s^{\pm} \rightarrow \phi\,\pi^{\pm}$ with $\phi \rightarrow K^+K^-$. The particle width of the missing $D^*_{s0}(2317)^{\pm}$ was then extracted from the excitation function obtained in an energy scan around the $D^*_{s0}(2317)$ threshold. Taking into account the specified values for the beam quality, results promise a mass resolution of $100\,\text{keV/c}^2$ [180]. This value is one order of magnitude better than the current world average. However, it should be noted that a detailed study on the background contributions still needs to be performed.

→ High precision measurement of the $X(3872)$

Another focus of current simulations is the study of the $X(3872)$. Even though it is one of the best-established states above the open-charm threshold there is still a controversial debate on the nature of this charmonium-like state, which does not seem to fit into conventional quark models (see also subsection 1.2.1). In particular its very narrow width and

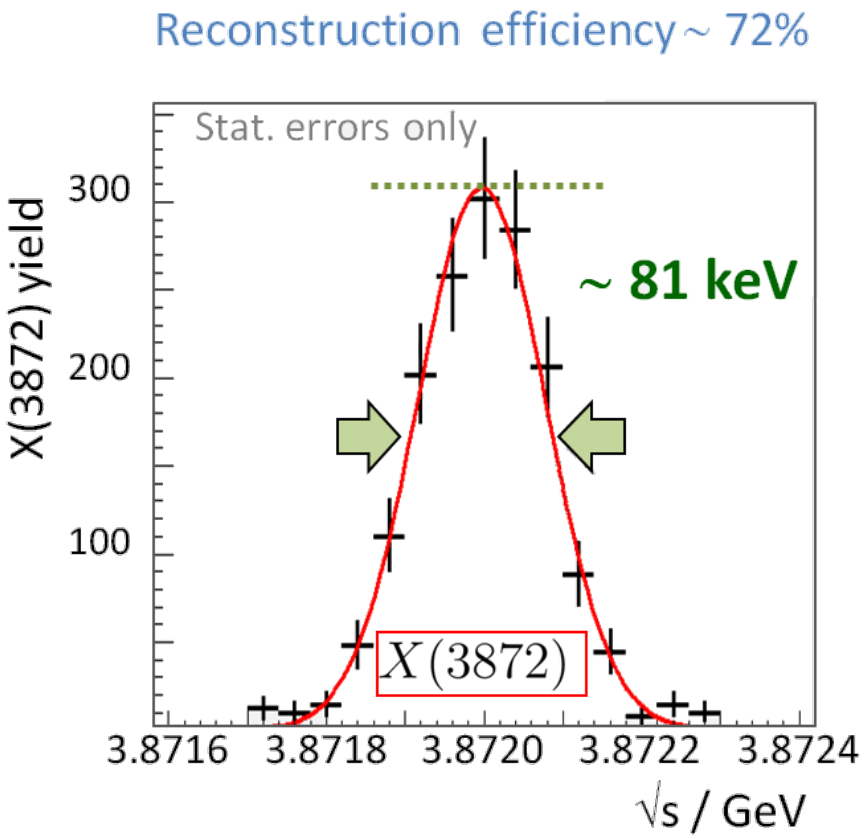

Figure 6.34: Simulation results of a resonance scan with a fixed input mass of 3872 MeV/c. Each data point corresponds to two days of data taking at the high-resolution mode of $\bar{\text{P}}$ANDA ($\Delta p/p \propto 10^{-5}$). The fit results in a systematic error on the width, which is smaller than 100 keV/c. Figure adapted from [181].

the near coincidence of its mass with the $D^0\bar{D}^{0*}$ threshold make it very interesting and stimulate a lot of theoretical work.

One advantage of the $X(3872)$ is the relatively large cross section, which is also rather unexpected from theoretical predictions. Due to this special property a large data sample is expected in a formation experiment at $\bar{\text{P}}$ANDA [182]. Moreover, the main decay mode $X(3872) \rightarrow J/\psi\,\pi^+\pi^-$ with $J/\psi \rightarrow e^+e^-/\mu^+\mu^-$ delivers a very clear signature of four charged particles with one common vertex in the final state. They can be sorted into two slow pions and the two fast leptons of an associated J/ψ decay. The latter allows a very precise reconstruction of the J/ψ, which can then be combined with the pions into a common invariant mass to extract the $X(3872)$ signal. Most promising for the research on the $X(3872)$ is the performance of a resonance scan profitting from the well-defined beam parameters at $\bar{\text{P}}$ANDA . They allow a formation experiment with very small energy steps. Preliminary Monte-Carlo results are shown in figure 6.34. With an assumed resolution $\Delta p/p$ in the order of 10^{-5}, the mass resolution achieved is better than 100 keV [183].

→ Dalitz plot analysis for higher excited D mesons

The most recent simulations [176] focus on the reconstruction capability for excited D mesons. Therefore, one charged and one neutral $D\bar{D}$ reaction channel was chosen to be investigated. They are listed in table 6.7 along with the complete decay pattern in the final state used for the reconstruction. Both channels include one excited D meson, which can be tagged with a ground state D meson. The excited D meson then decays into another ground state D meson and one charged pion. The two ground state D mesons are reconstructed via their decay into charged kaons and pions. In this way, there are two charged kaons and four charged pions in the final state.

In the following, results of a Dalitz plot analysis for the simulated reaction channel $p\bar{p} \to D^*(2400)^0\overline{D^0} \to D^+\overline{D^0}\pi^-$ will be summarized. The simulation has been performed with the full geometry of the $\bar{\text{P}}$ANDA apparatus at an initial beam momentum of 13.3 GeV/c. This value corresponds to a centre-of-mass energy of 5 GeV, which is 900 MeV above the $D^*(2400)^0\overline{D^0}$ threshold. The ground state D mesons have been reconstructed via the invariant mass of their decay particles in the final state, i.e. in the decay channels $D^+ \to K^-\pi^+\pi^+$ and $\overline{D^0} \to K^+\pi^-$, respectively. While the reconstruction of the particle tracks for the central part has been performed with a complete fitting procedure as described in section 1.5, a simplified algorithm has been used for small angle tracks in forward direction. The reconstruction efficiency of D candidates with the implemented tracking model results in 72% for the $\overline{D^0}$, 40% for the D^+ and 38% for the $D^*(2400)^0$, respectively. These numbers still include a small contribution of the combinatorial background.

Finally, a kinematic refit on the four-momentum of the $p\bar{p}$ system has been applied. The resulting Dalitz plot of the three particle final state $D^+\overline{D^0}\pi^-$ obtained with the implemented $\bar{\text{P}}$ANDA geometry is shown on the left of figure 6.35. It is in good agreement with

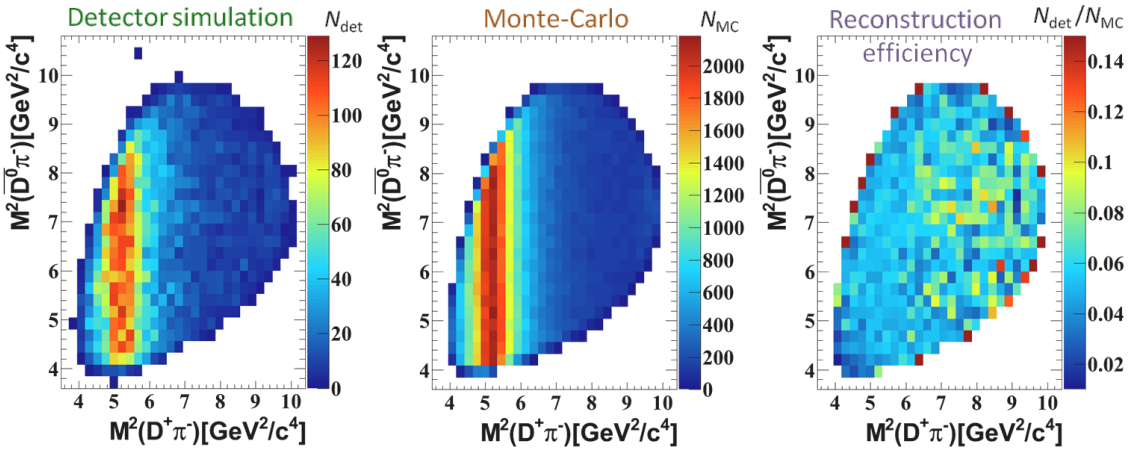

Figure 6.35: Dalitz plot coverage for the reaction channel $p\bar{p} \to D^*(2400)^0\overline{D^0} \to D^+\overline{D^0}\pi^-$. Results of detector simulations with the $\bar{\text{P}}$ANDA apparatus (*left*) are shwon in comparison with the Monte-Carlo truth *middle*. The reconstruction efficiency results from the ratio of the number of entries, N_{det} and N_{MC}, obtained in both cases. Figures adapted from [176].

the Monte-Carlo truth of the initially generated particles, which is shown as comparison right next to it. The resonant structure of the $D^*(2400)^0$ at $M^2(D^+\pi^-) \approx 5.3\,(\mathrm{GeV/c^2})^2$ corresponding to the squared mass of $m_{D^*(2400)^0} = 2.138\,\mathrm{GeV/c^2}$ is clearly visible. Also the particle width is recovered with a similar precision than the given input values taken for the Monte-Carlo truth. In order to check the impact of possible effects related to the detector acceptance, the reconstruction efficiency of the coverage in the Dalitz plot is shown on the right side of figure 6.35. It indicates a relatively homogeneous distribution with values between 5% and 10%.

For reason of completeness it should be mentioned that the second part of the study contains the reconstrucion of decay vertices, which is compiled in table 6.7, and a further discussion of main contributiong background channels. In analogy to the previously presented results of the $\bar{p}p \to \psi(3770) \to D^+D^-$ channel, a sufficiently high suppresion of the dominating hadronic background is achievable by combining kinematical constraints with an appropriate vertex cut [176].

Concluding remarks

The $\bar{\text{P}}$ANDA experiment is devoted to studies of the strong interaction in the charm quark sector. In the first part of this work, its relevance is underlined by a brief introduction of main physics aspects that can be addressed with a high precision spectroscopy in this energy domain. Moreover, a complete review of the current experimental status is given. For that, a customized scheme has been developed that allows a better classification of established states according to the quality of their accumulated experimental data.

The central part of this work contains a detailed description of the detector optimization performed for the $\bar{\text{P}}$ANDA Micro-Vertex-Detector (MVD). Starting point is the conceptual design developed in previous studies, which proved the importance of the MVD for key aspects of the physics program at $\bar{\text{P}}$ANDA. Besides the positive impact on the momentum resolution for charged particles, these account in particular for the required high precision of the vertex resolution, which is mandatory for the identification of D mesons.

Based on the conceptual design, a wide range of hardware developments for the MVD has started. They delivered central input for the development of a realistic and comprehensive detector model. Contributions to the hardware development concern the setup of a tracking station using silicon microstrip detectors. This setup provides a test facility for the commissioned sensor prototypes and customized frontend chips, which are still under development. Moreover, measurements feature the development and test of different tracking algorithms as well as the quantification of scattering effects in various materials. For instance, this will help to improve the very limited experimental data on lightweight carbon materials, which are widely used in many applications. In this context, the impact of measurements with the tracking station is significant in a much wider scope apart from the $\bar{\text{P}}$ANDA experiment.

The detector model developed includes active sensor elements, associated electronics, local and global support structures as well as a complete routing scheme for all services including cables and cooling pipes. The detector optimization performed, on the one hand, aims at a high acceptance in combination with a sufficient number of hit points delivered by the active sensor elements and a minimized material budget of the full detector. On the other hand, it warrants sufficient space for all passive elements and safety margins in addition to the very tight boundary conditions for the overall detector integration.

Finally, the MVD model has been integrated with all details into the simulation framework of $\bar{\text{P}}$ANDA. To the knowledge of the author this is the first time that such a comprehensive detector model has been migrated from a technical project into a complex simulation framework of a large experiment. In this way it is possible to directly check the impact of engineering solutions on the overall detector performance or, vice versa, to validate given technical specifications for different detector parts with simulations of the experimental conditions.

Extensive detector simulations have been carried out including a systematic check of basic detector parameters. As a result, it could be shown that the detector coverage is optimized

for a minimum number of four hit points inside the MVD. The overall material budget for the most part, taking into account the full routing of all services, stays well below 10% of one full radiation length. Apart from a detailed mapping of the material distribution, considerations about the potential impact of ongoing hardware developments are compiled in this thesis. Important information concerning the technical specifications of different detector components is given by the outcome of the count rate studies accomplished with the DPM generator. Obtained results are consistent with the specified limits on the average and the peak hit rate for the readout electronics, as well as the expected data rate to be handled in different detector parts.

The reliability of the DPM results has been checked carefully by a comparison with available experimental data. Special emphasis was put on the elastic scattering part, which is one of the dominating processes in the reaction. Therefore, a cut-off parameter must be set explicitly before starting the DPM generator. Based on systematic checks, a parameterization could be extracted linking the cut-off parameter to a corresponding four-momentum transfer. In this way it is possible to choose the cut-off parameter according to the physically interesting region. Because the DPM generator is particularly adapted to the needs of $\bar{\text{P}}$ANDA, it is used in various simulations focusing on the detector performance of individual subsystems. Hence, the evaluated parameterization of the DPM cut-off parameter is not only important for studies with the MVD.

In summary, cornerstone data of the MVD have been fixed within this work. Major parts of the presented detector model as well as associated detector simulations will contribute to the technical design report (TDR) of the $\bar{\text{P}}$ANDA MVD, which is currently under work and will be submitted at the end of this year. Furthermore, the detailed MVD model has been introduced into the physics simulation framework of $\bar{\text{P}}$ANDA. A collection of simulated benchmark channels concluding this thesis demonstrates that the physics performance with the developed detector model meets the given requirements. Based on the realistic detector description, a further optimization of the tracking algorithm for $\bar{\text{P}}$ANDA is facilitated. Moreover, parts of the presented work have impact in other detector subgroups as well as projects outside of $\bar{\text{P}}$ANDA.

Bibliography

[1] K. Nakamura et al. (Particle Data Group). Review of particle physics. *J. Phys.*, G 37:075021, 2010.

[2] A.V. Manohar and C.T. Sachrajda. Quark Masses - Updated review given in [1].

[3] K. Brinkmann, P. Gianotti and I. Lehmann. Exploring the Mysteries of Strong Interactions - The PANDA Experiment. *Nucl. Phys. News*, 16:15–18, 2006.

[4] B. Povh, K. Rith, Ch. Scholz and F. Zetsche. *Teilchen und Kerne - Eine Einführung in die physikalischen Konzepte*. Springer, 5. Auflage edition, 2001.

[5] PANDA collaboration. Physics Performance Report for: PANDA - Strong Interaction Studies with Antiprotons. arXiv:0903.3905v1 [hep-ex], 2009.

[6] D. H. Perkins. *Introduction to High Energy Physics*. Cambridge University Press, 4th edition edition, 2008.

[7] B. Richter. From the Psi to Charm - The Experiments of 1975 and 1976. Nobel Lecture, December 1976. Online available: http://nobelprize.org/nobel prizes/physics/laureates/1976/richterlecture. html.

[8] S. Ting. The Discovery of the J Particle: A Personal Recollection. Nobel Lecture, December 1976. Online available: http://nobelprize.org/nobel prizes/physics/laureates/1976/ting-lecture.html.

[9] Custom-made credit system for the classification of the experimental status:

Criterion	**	*(*)	*	(*)
$\pm\Delta M$ [MeV]	< 0.1	< 1	< 10	≥ 10
$\pm\Delta\Gamma/\Gamma$, $\Gamma < 1\,\text{MeV}$	≤ 0.1	-	> 0.1	-
$\pm\Delta\Gamma/\Gamma$, $\Gamma \geq 1\,\text{MeV}$ $\Delta\tau$ / τ, $\Gamma < 1\,\text{MeV}$	< 0.01	< 0.1	< 0.5	$\leq 1\,\text{MeV}$ upper limit
Quantum numbers	fully determined	favoured assignment	to be confirmed	quark model prediction, mass + width consistent with
$(\sum_{N_{\text{abs}}} \Gamma_i)/\Gamma$	$> 90\%$	$> 60\%$	$> 30\%$	$> 10\%$
N_{Γ_i} N_{ch}	> 100 > 100	> 25 > 50	≥ 5 > 25	≥ 0 / / > 0 ≥ 5 / > 0

Stars are awarded if the given criterion is fulfiled. The final number of stars results from a sum of all four criteria, with $2\times(*) = *$. A higher number of stars indicates a higher quality of the experimental data. The maximum number of stars is ten.

[10] M. Kreps. Charmonium Spectroscopy (X, Y, Z) at the B Factories. *Proc. of Science*, BEAUTY 2009(038), 2009. arXiv:0912.0111v1 [hep-ex].

[11] S. Godfrey. Topics in Hadron Spectroscopy in 2009. *Proc. of the DPF-2009 Conference*, 2009. arXiv:0910.3409v2 [hep-ph].

[12] T.V. Uglov. Recent results from Belle. arXiv:1011.3369v1 [hep-ex], 2010.

[13] Z. Metreveli. Charmonium Spectroscopy Below Open Flavour Threshold. *Proc. of the CHARM2007 Workshop*, 2007. arXiv:0710.1884v1 [hep-ex].

[14] M. Ablikim et al. (BES Collaboration). Determination of the $\psi(3770)$, $\psi(4040)$, $\psi(4160)$ and $\psi(4415)$ resonance parameters. *Physics Letters B*, 660(4):315 – 319, 2008.

[15] A. Zghiche. Charm Meson Spectroscopy at BABAR and CLEO-c. *Proc. of the CHARM2007 Workshop*, 2007. arXiv:0710.0314v2 [hep-ex].

[16] P. Colangelo and F. De Fazio. Open charm meson spectroscopy: Where to place the latest piece of puzzle. arxiv:1001.1089v1 [hep-ph], 2010.

[17] S. Godfrey and N. Isgur. Mesons in a relativized quark model with chromodynamics. *Phys. Rev. D*, 32:189–231, 1985.

[18] M. Di Pierro and E. Eichten. Excited heavy-light systems and hadronic transitions. *Phys. Rev. D*, 64(114004), 2001.

[19] C.G. Wohl. Charmed Baryons - Revised review given in [1].

[20] M. G. Oreglia et al. Study of the reaction $\psi' \to \gamma\gamma J/\psi$. *Phys. Rev. D*, 25(9):2259–2277, 1982.

[21] M. Ambrogiani et al. Study of the $\gamma\gamma$ decays of the $\chi_{c2}(1^3p_2)$ and $\chi_{c0}(1^3p_0)$ charmonium resonances. *Phys. Rev. D*, 62(5):052002, 2000.

[22] A. Abulencia et al. (CDF Collaboration). Analysis of the Quantum Numbers J^{PC} of the X(3872) Particle. *Phys. Rev. Lett.*, 98:132002, 2007.

[23] K. Seth. A New Analysis of the R Measurements: Resonance Parameters of the Higher Vector States of Charmonium. arXiv:hep-ex/0405007v2, 2005.

[24] T. Aaltonen et al. (CDF Collaboration). Precision Measurement of the $X(3872)$ mass in $J/\psi\pi^+\pi^-$ Decays. *Phys. Rev. Lett.*, 103(15):152001, 2009.

[25] I. Adachi et al. (Belle Collaboration). Study of X(3872) in B meson decays. arXiv:0809.1224v1 [hep-ex], 2008.

[26] B. Aubert et al. (BABAR Collaboration). Observation of a Broad Structure in the $\pi^+\pi^- J/\psi$ Mass Spectrum around 4.26 Gev/c^2. *Phys. Rev. Lett.*, 95(14):142001, 2005.

[27] C.Z. Yuan et al. (Belle Collaboration). Measurement of the $e^+e^- \to \pi^+\pi^- J/\psi$ Cross Section Via Initial-State Radiation at Belle. *Phys. Rev. Lett.*, 99(18):182004, 2007.

[28] Q. He et al. (CLEO Collaboration). Confirmation of the $Y(4260)$ resonance production in initial state radiation. *Phys. Rev. D*, 74(9):091104, 2006.

[29] R. Rameika. A Review of the Fermilab Fixed-Target Program. *SLAC-R-444*, 1993.

[30] D. Bettoni. The E835 experiment at Fermilab. *Hyperfine Interact*, 194:225–231, 209.

[31] W.R. Leo. *Techniques for Nuclear and Particle Physics Experiments*. Springer, 2nd edition, 1994.

[32] G. Lutz. *Semiconductor Radiation Detectors - Device Physics*. Springer, 2nd edition, 1999.

[33] G.F. Knoll. *Radiation Detection and Measurement*. John Wiley&Sons, 3rd edition, 2000.

[34] H. Bichsel, D.E. Groom and S.R. Klein. Passage of particles through matter - Updated review given in [1].

[35] Figures 13.34 and 13.35 at page 494 and 495 in [33] with the references therein.

[36] T. Mouthuy. Silicon pixel detector research and development. *Nucl. Instr. Meth.*, A 368:213–216, 1995.

[37] G. Lindström et al. Radiation hard silicon detector developments by the RD48 (ROSE) collaboration. *Nucl. Instr. Meth.*, A 466:308–326, 2001.

[38] M.Moll et al. Development of radiation hard sensors for very high luminosity colliders - CERN-RD50 project. *Nucl. Instr. Meth.*, A 511:99–107, 2003.

[39] C. Höppner, S. Neubert, B. Ketzer and S. Paul. A novel generic framework for track fitting in complex detector systems. *Nucl. Instr. Meth.*, A 620:518–525, 2010.

[40] R.E. Kalman. A New Approach to Linear Filtering and Prediction Problems. *Trans. of the ASME-Journal of Basic Engineering*, D 82:35–45, 1960.

[41] R. Frühwirt. Application of kalman filtering to track and vertex fitting. *Nucl. Instr. Meth.*, A 262:444–450, 1987.

[42] P. Yepes. A fast track pattern recognition. *Nucl. Instr. Meth.*, A 380:582–585, 1996.

[43] B. Lillekjendlie. Circular Arcs Fitted on a Riemann Sphere. *COMPUTER VISION AND IMAGE UNDERSTANDING*, 67(3):311–317, 1997.

[44] A. Fontana et al. Use of GEANE for tracking in Virtual Monte Carlo. *Journal of Phys. Conf. Series*, 119:03201, 2008.

[45] PANDA collaboration. Letter of intent for: PANDA - Strong Interaction Studies with Antiprotons. Technical report FAIR-ESAC, 2004.

[46] GSI Helmholtzzentrum für Schwerionenforschung. FAIR - An International Accelerator Facility for Beams of Ions and Antiprotons. Baseline technical report, 2006. [Online] Available: http://www.gsi.de/fair/reports/btr.html.

[47] P. Spiller and G. Franchetti. The FAIR accelerator project at GSI. *Nucl. Instr. Meth.*, A561:305–309, 2006.

[48] W. F. Henning. FAIR - recent developments and status. *Nucl. Instr. Meth.*, A805:502c–510c, 2008.

[49] PANDA collaboration. Technical progress report for: PANDA - Strong Interaction Studies with Antiprotons. FAIR-ESAC/Pbar/Technical Progress Report GSI, 2005.

[50] T.Barnes. Update on charmonium theory. arxiv:1003.2644v1 [hep-ph], 2010.

[51] E. Fioravanti. Charmonium rates. *XXXII. PANDA Collaboration Meeting, GSI Darmstadt*, March 2010.

[52] Belle Collaboration. Measurement of $D^0 - \bar{D}^0$ Mixing Parameters in $D^0 \to K_s\pi^+\pi^-$ Decays. *Phys. Rev. Lett.*, 99(13):131803, 2007.

[53] CLEO Collaboration. Determination of the $D^0 \to K^+\pi^-$ relative strong phase using quantum-correlated measurements in $e^+e^- \to D^0-\bar{D}^0$ at CLEO. *Phys. Rev. D*, 78(1):012001, 2008.

[54] CDF Collaboration. Evidence for $D^0 - \bar{D}^0$ Mixing Using the CDF II Detector. *Phys. Rev. Lett.*, 100(12):121802, 2008.

[55] BaBar Collaboration. Measurement of $D^0-\bar{D}^0$ Mixing Parameters in $D^0 \to K_s\pi^+\pi^-$ Decays. *Phys. Rev.*, D80(7):071103, 2009.

[56] V. Koch. Aspects of Chiral Symmetry. *Int.J.Mod.Phys.*, E6:203–250, 1997.

[57] see references given in [5], page 129, left column, 2nd paragraph.

[58] F. Klingl et al. Masses of J/ψ and η_c in the Nuclear Medium: QCD Sum Rule Approach. *Phys. Rev. Lett.*, 82:3396–3399, 1999.

[59] see references given in [5], page 129, right column, Chapter 4.4.1, 1st paragraph.

[60] J. Pochodzalla and A. Sanchez-Lorente. Roadmap for double hypernuclei spectroscopy at PANDA. *EPJ Web of Conferences*, 3(07008), 2010.

[61] A. Lehrach et al. Beam dynamics of the high-energy storage ring (HESR) for FAIR. *Int. J. Mod. Phys. E*, 18(2):420–429, 2009.

[62] C. Welsch and J. Ullrich. FLAIR – a facility for low-energy antiproton and ion research. *Hyperfine Interact*, 172(1-3):71–80, 2006.

[63] B. Lorentz et al. HESR Linear Lattice Design. *Proc. Of European Accelerator Conference EPAC, Genova*, "MOPPC"(112):325–327, 2008.

[64] F. Hinterberger. Beam-target Interaction and Intrabeam Scattering in the HESR. Technical Report FZJ 4206, 2006. ISSN: 0944-2952.

[65] D.M. Welsch et al. Closed Orbit Correction and Sextupole Compensation Schemes for the Normal-Conducting HESR. *Proc. Of European Accelerator Conference EPAC, Genova*, "THPC"(076):3161–3163, 2008.

[66] A. Lehrach et al. Beam performance and luminosity limitations in the high energy storage ring (HESR). *Nucl. Instr. Meth.*, A 561:289–296, 2006.

[67] O. Boine-Frankenheim et al. Cooling equilibrium and beam losses with internal targets in high energy storage rings. *Nucl. Instr. Meth.*, A 560:245–255, 2006.

[68] H. Stockhorst, D. Prasuhn, R. Maier and B. Lorentz. Cooling scenario for the hesr complex. *AIP Conf. Proc.*, 821:190–195, 2006.

[69] H. Poth. Electron cooling: Theory, experiment, application. *Physics Reports*, 196(3–4):135–297, 2006.

[70] I. Meshkov and A. Sidorin. Electron cooling. *Nucl. Instr. Meth.*, A532:19–25, 2004.

[71] D. Möhl, G. Petrucci, L. Thorndahl and S. van der Meer. Physics and technique of stochastic cooling. *Physics Reports*, 58:73–119, 1980.

[72] J. Marriner. Stochastic cooling overview. *Nucl. Instr. Meth.*, A532:11–18, 2004.

[73] D. Reistaad et al. Calculations on High-Energy Electron Cooling in the HESR. *Proc.of the Workshop on Beam Cooling and Related Topics COOL2007, Bad Kreuznach*, "MOA2C"(05):44–48, 2004.

[74] H. Stockhorst et al. Stochastic Cooling Developments for the HESR at FAIR. *Proc. of the European Accelerator Conference EPAC2008, GenoaProc. of the European Accelerator Conference EPAC2008, Genoa*, "THPP"(055):3491–3493, 2008.

[75] A. Smirnov, A. Sidorin and D. Krestnikov. Effective Luminosity Simulation for PANDA experiment at FAIR. *Proc. of COOL 2009, Lanzhou*, "THPMCP"(002):1–3, 2009.

[76] P. Abbon et al. (COMPASS Colaboration). The COMPASS experiment at CERN. *Nucl. Instr. Meth.*, A577:455–518, 2007.

[77] PANDA collaboration. Technical Design Report for the Solenoid and Dipole Spectrometer Magnets. arxiv:0907.0169v1 [physics.ins-det], 2009.

[78] P. Wintz. Status of the HW Developments and Achievements for the STT. *XXXVI. PANDA Collaboration Meeting, GSI*, March 2011.

[79] A. Costanza et al. The straw tube tracker of the PANDA experiment. *Nucl. Instr. Meth.*, A617:148–150, 2010.

[80] A. Sokolov, J. Ritman and P. Wintz. Application of the time-dependent charge asymmetry method for longitudinal position determination in prototype proportional chambers for the PANDA experiment. *Nucl. Instr. Meth.*, A574:50–56, 2007.

[81] Q. Weitzel et al. Development of a high-rate gem-based tpc for panda. *IEEE Nuclear Science Symposium Conference Record*, N12(1):227–233, 2007.

[82] L. Fabbietti et al. The PANDA GEM-based TPC Prototype. arxiv:1004.4079v2 [nucl-ex], 2010.

[83] B. Ketzer. A micropattern gaseous detectors in the COMPASS tracker. *Nucl. Instr. Meth.*, A494:142–147, 2002.

[84] B. Ketzer et al. Performance of triple GEM tracking detectors in the COMPASS experiment. *Nucl. Instr. Meth.*, A535:314–318, 2004.

[85] H. Staengle et al. Test of a large scale prototype of the DIRC, a Čerenkov imaging detector based on total internal reflection for BaBar at PEP-II. *Nucl. Instr. Meth.*, A397:261–282, 1997.

[86] C. Schwarz et al. The barrel DIRC of the PANDA experiment. *Nucl. Instr. Meth.*, A595:112–115, 2008.

[87] C. Schwarz et al. Development of the PANDA barrel DIRC. *JINST*, 4:"P12016", 2009.

[88] Peter Schönmeier et al. Disc DIRC endcap detector for PANDA at FAIR. *Nucl. Instr. Meth.*, A595:108–111, 2008.

[89] M. Düren et al. The PANDA time-of-propagation disc DIRC. *JINST*, 4:"P12013", 2009.

[90] PANDA collaboration. Technical Design Report for the PANDA Electromagnetic Calorimeter (EMC). arxiv:0810.1216v1 [physics.ins-det], 2008.

[91] N. Akopov et al. The HERMES Dual-Radiator Ring Imaging Cerenkov Detector. *Nucl. Instr. Meth.*, A479:511–530, 2002.

[92] G. S. Atoyan et al. Lead-scintillator electromagnetic calorimeter with wavelength shifting fiber readout. *Nucl. Instr. Meth.*, A320:144–154, 1992.

[93] G. S. Atoyan et al. Development of Shashlyk Calorimeter for KOPIO. *Nucl. Instr. Meth.*, A531:467–480, 2004.

[94] A. Täschner et al. Development of cluster-jet targets: From COSY-11 to FAIR. *AIP Conf. Proc.*, 950:85–88, 2007.

[95] M. Kühnel et al. Low-Z internal target from a cryogenically cooled liquid microjet source. *Nucl. Instr. Meth.*, A602:311–314, 2009.

[96] H. Orth. Status of targets for PANDA. *XXVIII. PANDA Collaboration Meeting, GSI Darmstadt*, March 2009.

[97] Chr. Bargholtz et al. Properties of the WASA pellet target and a stored intermediate-energy beam. *Nucl. Instr. Meth.*, A587:178–187, 2008.

[98] M. Büscher et al. The Moscow-Jülich Frozen-Pellet Target. *AIP Conf. Proc.*, 814:614–620, 2006.

[99] M. Büscher et al. Production of Hydrogen, Nitrogen and Argon Pellets with the MOSCOW-JÜLICH Pellet Target. *Int. J. Mod. Phys. E*, 18(2):505–520, 2009.

[100] G. Schepers et al. Particle Identification at PANDA. *Report of the PID TAG group*, 2009.

[101] F.Hügging. Development of a Micro-Vertex-Detector for the PANDA-Experiment at the FAIR facility. *IEEE Nuclear Science Symposium Conference Record*, N30(190):1239–1243, 2006.

[102] L. Schmidt. Recommendations from the FE-DAQ Workshop in Bodenmais. *PANDA Note*, DAT-001, 2009.

[103] D. Calvo. Private communication.

[104] D. Calvo, S. Coli and G. Giraudo. Cooling and mechanics. *XXXIII. PANDA Collaboration Meeting, MVD subgroup, Stockholm*, June 2010.

[105] D. Calvo et al. Hybrid pixel detector in the PANDA experiment. *Proc. of Science*, Rd09(015), 2009.

[106] Th. Würschig. Utilization of Double-Sided Silicon Strip Detectors within the PANDA Micro-Vertex-Detector. *IEEE Nuclear Science Symposium Conference Record*, N30(140):2215–2219, 2008.

[107] G. Beck and G. Viehhauser. Analytic model of thermal runaway in silicon detectors. *Nucl. Instr. Meth.*, A618:131–138, 2010.

[108] A. Pepatoa et al. The mechanics and cooling system of the ALICE silicon pixel detector. *Nucl. Instr. Meth.*, A565:6–12, 2006.

[109] P. Bonneau et al. Cooling system for the TILECAL hadron calorimeter of the ATLAS detector. *ATL-TILECAL-98-139*, 1998.

[110] Th. Würschig et al. Mechanics and detector integration in the PANDA Micro-Vertex-Detector. *JINST*, 5:C12024, 2010.

[111] Istituto Nazionale di Fisica Nucleare (INFN). Via P.Giuria 1, 10125 Torino Italy, Group coordinator: Daniela Calvo, Email: calvo@to.infn.it.

[112] D. Calvo et al. The silicon pixel system for the Micro Vertex Detector of the PANDA experiment. *Nucl. Instr. Meth.*, A617:560–562, 2010.

[113] A. Braghieri et al. Radiation damage effects on epitaxial silicon devices for the PANDA hybrid pixel detector. *IEEE Nuclear Science Symposium Conference Record*, N30(402):2539–2541, 2008.

[114] D. Calvo et al. Thinned epitaxial silicon hybrid pixel sensors for the PANDA experiment. *Nucl. Instr. Meth.*, A594:29–32, 2008.

[115] F. Antinori et al. The ALICE pixel detector readout chip test system. *Proc. of the Seventh Workshop on Electronics for LHC Experiments, Stockholm*, "CERN-LHC-2001"(034), September 2001.

[116] D. Calvo et al. A Silicon Pixel Readout ASIC in CMOS 0.13 µm for the PANDA Micro Vertex Detector. *IEEE Nuclear Science Symposium Conference Record*, N44(1):2934–2939, 2008.

[117] T. Kugathasan et al. A 15µw 12-bit dynamic range charge measuring front-end in 0.13µm cmos. *IEEE Nuclear Science Symposium Conference Record*, N56(3), 2010.

[118] D. Calvo et al. TOPIX: The first prototype of pixel readout for PANDA experiment. *Nucl. Instr. Meth.*, A596:96–99, 2008.

[119] D. Calvo et al. Hybrid pixel detector with epitaxial sensors and readout in 130nm CMOS technology for PANDA. *Nucl. Instr. Meth.*, A624:290–294, 2008.

[120] I. Kipnis et al. A time-over-threshold machine: the readout integrated circuit for the BaBar silicon vertex tracker. *IEEE Trans. Nucl. Sci.*, 44(3):289–297, 1997.

[121] I. Peric et al. The FEI3 readout chip for the ATLAS pixel detector. *Nucl. Instr. Meth.*, A565:178–187, 2006.

[122] C. Bozzi et al. The design and construction of the BaBar silicon vertex tracker. *Nucl. Instr. Meth.*, A447:15–25, 2000.

[123] D. Robinson et al. Silicon microstrip detectors for the ATLAS SCT. *Nucl. Instr. Meth.*, A485:84–88, 2002.

[124] J.-L. Agram et al. The silicon sensors for the Compact Muon Solenoid tracker- design and qualification procedure. *Nucl. Instr. Meth.*, A517:77–93, 2004.

[125] Prototype sensors specified for PANDA ordered at CiS, Forschungsinstitut für Mikrosensorik und Photovoltaik GmbH, Erfurt.

[126] A.S. Brogna et al. N-XYTER, a CMOS read-out ASIC for high resolution time and amplitude measurements on high rate multi-channel counting mode neutron detectors. *Nucl. Instr. Meth.*, A568:301–308, 2004.

[127] Th. Würschig et al. Setup of a test-station for double-sided silicon microstrip detectors. *Panda-MVD - note*, 005, 2010.

[128] M. French et al. Design and Results from the APV25, a deep Submicron CMOS Front-End Chip for the CMS Tracker. *Nucl. Instr. Meth.*, 466:359–365, 2001.

[129] D. Betta et al. Development of a fabrication technology for double-sided AC-coupled silicon microstrip detectors. *Nucl. Instr. Meth.*, 460:306–315, 2001.

[130] R. Schnell. Untersuchungen zu First-Level-Datenauslesestrukturen für den Siliziumstreifendetektor im Mikro-Vertex-Detektor von PANDA. Diplomarbeit, TU Dresden, 2009.

[131] L. Ackermann. Charakterisierung von Silizum-Streifensensoren für den Panda Micro-Vertex-Detektor. Diplomarbeit, TU Dresden, 2009.

[132] F. Krüger. Charakterisierung von Mikrostreifen-Sensormodulen. Diplomarbeit, TU Dresden, 2009.

[133] M. Becker. Aufbau und Inbetriebnahme einer Tracking-Station mit Silizium-Streifen-Detektoren. Diplomarbeit, Uni Bonn, 2010.

[134] K. Koop. FPGA-basierte Auslese von Silizium-Streifen-Detektoren. Diplomarbeit, Uni Bonn, 2010.

[135] R. Schnell et al. FPGA-based Readout for Double-Sided Silicon Strip Detectors. *JINST*, 6:C01008, 2011.

[136] S. Bianco. Characterization of the PANDA Micro-Vertex- Detector and Analysis of the First Data Measured with a Tracking Station. *IEEE Nuclear Science Symposium Conference Record*, N42(278), 2010.

[137] S. Bianco. Simulations for the evaluation of the coverage and the material budget of the Micro Vertex Detector of PANDA. Master thesis, Turin university, 2010.

[138] Rohacell®, Webpage: www.rohacell.com.

[139] D. Calvo, P. De Remigis, M. Mignone and R. Wheadon. An update on the low-mass cable. *XXXIII. PANDA Collaboration Meeting, MVD subgroup, Stockholm*, June 2010.

[140] G. Giraudo. Mvd updates on mechanics and cooling. *XXXII. PANDA Collaboration Meeting, MVD subgroup, GSI Darmstadt*, March 2010.

[141] Th. Würschig. Setup of a Mechanical Mock-up for the Micro-Vertex-Detector. *Panda MVD-note*, 002, 2008.

[142] Th. Würschig. Basic Conventions for the CAD-Modelling of the Micro-Vertex-Detector. *Panda MVD-note*, 003, 2008.

[143] Autodesk® Inventor™, Webpage: www.autodesk.de.

[144] S. Spataro (PANDA Collaboration). Simulation and event reconstruction inside the PandaRoot framework. *J. Phys. Conf. Ser.*, 119, 2008.

[145] R. Wheadon. Mvd pixel layout proposal. *XXIX. PANDA Collaboration Meeting, MVD subgroup, Turin*, June 2009.

[146] G.R. Lynch and O.I. Dahl. Approximations to multiple coulomb scattering. *Nucl. Instr. Meth.*, B58:6s–10s, 1991.

[147] Th. Würschig and H.-G. Zaunick. Frontend electronics specifications for the silicon strip detectors of the PANDA MVD. *CBM-XYTER Family Planning Workshop, GSI*, December 2008.

[148] According to the Bethe-Bloch formula, a minimum kinematic energy corresponding to a particle momentum of 93 MeV/c is needed to cross a layer of 200 µm beryllium, which represents the minimum path lenght in a pipe of the beam-target system (see page 51). A fast tool for the calculation of the stopping power can be found e.g. under: http://www.sgeier.net/tools/bbt.html.

[149] G. Giraudo et al. The SDD and SSD support structure for the ALICE Inner Tracking System. *JINST*, 4:P01003, 2009.

[150] J.J. Steijger. The lambda wheels, a silicon vertex detector for HERMES. *Nucl. Instr. Meth.*, A453(1.2):98–102, 2000.

[151] ROOT - A Data Analysing Framework, Webpage: http://root.cern.ch.

[152] CadConverter documentation, Webpage: http://panda-wiki.gsi.de/cgi-bin/view/Computing/CadConverter.

[153] Collision check after conversion: ROOT-function `CheckOverlaps -S` with 1 million events and an overlap threshold of 0.00001 cm.

[154] File upload to SVN trunk version, Location: https://subversion.gsi.de/trac/fairroot/browser/pandaroot/trunk/geometry.

[155] A. Capella et al. Dual parton model. *PHYSICS REPORTS*, 236(4 & 5):225–329, 1994.

[156] S.A. Bass et al. Microscopic Models for Ultrarelativlstic Heavy Ion Colllslons. *Prog. Part. Nucl. Phys.*, 41:255–369, 1998.

[157] M. Bleicher et al. Relativistic hadron–hadron collisions in the ultra-relativistic quantum molecular dynamics. *Nucl. Part. Phys.*, 25:1859—1896, 1999.

[158] V. Flaminio, W.G. Moorhead, D.R.O. Morrison and N. Rivoire. Compilation of cross-sections III: p and anti-p induced reactions. *CERN-HERA*, 84-01, 1984.

[159] P. Jenni et al. Anti-pp And pp Forward Elastic Scattering between 4 and 10 Gev/c. *Nucl. Phys.*, B129:232–252, 1977.

[160] T. Armstrong et al. Precision measurements of antiproton-proton forward elastic scattering parameters in the 3.7 to 6.2 gev/c region. *Phys.Let.*, B 385:479–486, 1996.

[161] A. Galoyan, J. Ritman, A. Sokolov and V. Uzhinsky. Parametrization of the $\bar{p}p$ Elastic Scattering Differential Cross Section Between $2 \leq p_{lab} \leq 16$ Gev/c. arxiv:0809.3804v1 [hep-ex], 2008.

[162] W. F. Baker et al. Antiproton-proton elastic scattering at 3.55 gev/c. *Nucl. Phys.*, B12:5–8, 1969.

[163] A. Berglund et al. K-p and anti-pp Elastic Scattering at 10.1 Gev/c. *Nucl. Phys.*, B176:346–354, 1980.

[164] S. Agostinelli et al. Geant4: A simulation toolkit. *Nucl. Instr. Meth.*, A506(3):250–303, 2003.

[165] J. Allison et al. Geant4: Developments and Applications. *Trans. Nucl. Sci.*, 53(1):270–278, 2006.

[166] A. Khoukaz. Update on targets. *XXXV. PANDA Collaboration Meeting, GSI Darmstadt*, November 2010.

[167] The density chosen for the carbon foam is more than a factor of two smaller compared to foams with high thermal conductivity, which are intended to be used for the pixel hybrids (e.g. POCOFoam [170], $\rho = 0.55$ g/cm^3). However, it delivers more realistic values for all other carbon support structures, which approximate a light foam (Rohacell [138], $\rho = 0.0513$ g/cm^3) as intermediate layer by applying a weighting between carbon and the so-defined carbon foam. Possible corrections are discussed in table 6.5.

[168] PDG group. Atomic and Nuclear Properties of Materials, [Online] Available: http://pdg.lbl.gov/2010/AtomicNuclearProperties/index.html.

[169] H. Bichsel, D.E. Groom and S.R. Klein. Passage of Particles Through Matter - Section 27 of [1].

[170] POCOFoam®, Webpage: www.poco.com.

[171] Y. Tian and C. Liu and D. Hutt and B. Stevens. Electrodeposition of indium for bump bonding. *58 th Electronic Components and Technology Conference*, ECTC 2008:2096–2100, 2008.

[172] A.P. de Haas. Very low mass microcables for the ALICE silicon strip detector. *CERN-ALICE-PUB-99-20*, 1999.

[173] R. Jäkel. *Resolution Studies for the Micro-Vertex-Detector of the PANDA Experiment and the Reconstruction of Charmed Mesons for Specific Hadronic Channels.* PhD thesis, TU Dresden, 2009.

[174] BaBar collaboration. Workbook for BaBar users - online documentation. Webpage: http://www.slac.stanford.edu/BFROOT/www/doc/workbook/workbook.html.

[175] Kinematic vertex fit "PndKinVtx"implemented in [144].

[176] A. Pitka. Simulationen zum Nachweis angeregter D-Mesonen mit dem PANDA Detektor. Diplomarbeit, Uni Bonn, 2011.

[177] R. Jäkel. Charmed meson reconstruction with the PANDA detector. *Int. J. Mod. Phys.*, A 24:467–470, 2009.

[178] See chapter 4.2.2.5, page 77 in [5].

[179] See chapter 4.2.4, page 103 in [5].

[180] M. C. Mertens. *Der PANDA Mikro Vertex Detektor: Entwicklung eines Labormesssystems, Simulation der MVD-Betriebsparameter sowie Untersuchungen zur Auflösung der Breite des $D^*_{s0}(2317)$.* PhD thesis, Ruhr Universität Bochum, 2010.

[181] S. Lange. Update on X(3872) at Panda. *XXXIII. PANDA Collaboration Meeting, MVD subgroup, Stockholm*, June 2010.

[182] G.Y. Chen and J. P. Ma. Production of $X(3872)$ at panda. *Phys. Rev.*, D 77:097501, 2008.

[183] J.S. Lange et al. Prospects for X(3872) Detection at PANDA. arxiv:1010.2350v2 [hep-ex], 2010.

List of Figures

List of Tables

Danksagung

An dieser Stelle möchte ich die Gelegenheit nutzen, mich für die Unterstützung bei all jenen zu bedanken, die immer für mich da waren und mir wichtigen Rückhalt gaben:

Rita, dedico-te este trabalho. Eu sei que tiveste de fazer sacrifícios por mim, muito obrigado pelo teu amor e pela tua ajuda! As perspectivas agora são melhores para caminharmos sempre juntos!

Auch meinen Eltern und meiner Schwester gilt ein ganz großer Dank. Sie haben mir sehr viele Dinge abgenommen, sodass ich mich ganz auf die Arbeit konzentrieren konnte. Dies gilt besonders für die letzte Zeit, in der ich bei den seltener werdenden Besuchen mit viel Arbeit und wenig Zeit nach Dresden kam.

Bei Prof. Dr. Jochen Dingfelder möchte ich mich für die freundliche Übernahme der Betreuung des Gutachtens bedanken. In unseren Treffen habe ich ihre Offenheit und das wache Interesse an dem von mir vorgelegten Thema sehr geschätzt.

Ein spezieller Dank auch an Prof. Dr. Wolfgang Enghardt dafür, dass er sich als externes Mitglied für die Prüfungskomission bereitgestellt hat.

Im weiteren möchte ich mich nun speziell an jene wenden, die im besonderen Maße zum Gelingen dieser Arbeit beigetragen habe:

Mein ganz besonderer Dank gilt meinem Doktorvater Prof. Dr. Kai-Thomas Brinkmann für die sehr gute fachliche und persönliche Betreuung meiner Arbeit. In den vielen Diskussionen erhielt ich wertvolle Hinweise und Denkanstöße. Besonders wichtig war mir, dass ich mich in allen Belangen auf seine Unterstützung verlassen konnte. Das große mir entgegengebrachte Vertrauen gab mir die Sicherheit, auf dem eingeschlagenen Weg weiterzugehen. Speziell innerhalb eines so großen Projektes wie $\bar{\text{P}}$ANDA war dies wichtig für eine gute und effektive Zusammenarbeit mit verschiedenen Forschungsgruppen.

Ich möchte mich auch bei allen Mitgliedern der partizipierenden MVD Gruppen aus Turin, Jülich und Bonn bedanken, ohne die diese Arbeit in dieser Qualität nicht zustande gekommen wäre.

My special acknowledgements I would like to give to Daniela Calvo and Beppe Giraudo for their good collaboration and the warm welcome during my various stays in Torino.

Dr. Tobias Stockmanns danke ich für die Hilfe bei der Bereitstellung des CAD-Konverters.

Voglio dire “Grazie mille!”particolare a Simone Bianco. Starting from his master thesis, he became the “in-situ” expert of the CAD converter here in Bonn. Thanks a lot for his patience to answer all my little questions. Really great teamwork and I think it was helpful for both of us!

Zum Schluss möchte ich mich bei allen jetzigen und ehemaligen $\bar{\text{P}}$ANDAs in Bonn und Dresden bedanken: René Jäckel, Ralf Kliemt, Hans-Georg Zaunick, Robert Schnell, Max Becker, Karsten Koop, Andreas Pitka ... und alle hier nicht namentlich aufgeführten. Es war und ist eine sehr nette und angenehme Zusammenarbeit mit euch!